LOW-VELOCITY IMPACT DAMAGE TOLERANCE OF COMPOSITE LAMINATES WITH INTERLAMINAR HYBRID TOUGHENING VIA CORE-SHELL-RUBBER PARTICLES AND NON-WOVEN THERMOPLASTIC FIBRE VEILS

A thesis submitted to The University of Manchester for the degree of Doctor of Philosophy
in the Faculty of Science and Engineering

2022

Mehmet Çağatay Akbolat

Department of Mechanical, Aerospace and Civil Engineering

The University of Manchester

TABLE OF CONTENTS

LIST OF FIGURES

LIST OF TABLES

LIST OF ABBREVIATIONS

BSE	Backscattered
BVID	Barely visible internal damage
CAI	Compression after impact
CC	Compliance calibration
cm	Centimetre
CNT	Carbon nano tubes
CSR	Core-shell rubber particles
dB	Decibel
DCB	Double cantilever beam
ETFE	Ethylene tetrafluoroethylene
g	Gram
g/m^2	Gram by centimetre square
Hz	Hertz
ILFT	Interlaminar fracture toughness
J	Joule
kg	Kilo gram
kHz	Kilo hertz
kJ	Kilo joule
kN	Kilo newton
kPa	Kilo pascal
MBT	Modified beam theory
MCC	Modified compliance calibration
MHz	Mega hertz
mm	Millimetre
MPa	Mega pascal
MWCNT	Multi-walled carbon nano-tubes
N	Newton
NCF	Non-crimp fabric

NL	Non-linearity
PA66	Polyamide 6’6
PAI	Polyamide-imide
PCL	Polycaprolactone
PEI	Polyetherimide
PES	Polyether sulfone
PPS	Polyphenylene sulphide
RTM	Resin transfer moulding
SE	Secondary electron
SEM	Scanning electron microscopy
SI	Structural integrity
T_g	Glass transition temperature
UD	Unidirectional
VARI	Vacuum assisted resin infusion
VIS	Visual observation
µm	Micro meter
2D	Two dimensional
3D	Three dimensional
3-ENF	Three-point bend end notched flexure
4-ENF	Four-point bend end notched flexure
°C	Celsius degree

ABSTRACT

Advanced polymer composite laminates have recently been widely used as a structural component in many engineering applications (*e.g.* aerospace) due to their high specific strength and stiffness over metallic materials. However, polymer composite laminates are vulnerable to impact events due to the weak delamination resistance. Several toughening strategies (*i.e.* bulk resin toughening, interlaminar thermoplastic veil toughening, 3-dimensional fibre reinforcement and through-thickness reinforcement) have been developed up to date to address the lack of delamination resistance for composite laminates. Thermoplastic veil and bulk resin toughening approaches are easy to apply and cost-effective strategies compared to the 3-dimensional and through-the-thickness reinforcement methods as not requiring complex and expensive manufacturing processes. In this regard, this study focuses on enhancing interlaminar fracture, impact and post-impact properties with the hybrid use of core-shell rubber particles (CSR) and thermoplastic non-woven veils.

The fracture, impact and post-impact properties of composite laminates (*i.e.* combination of carbon fibre non-crimp fabrics and two-part low-viscous epoxy) are investigated and toughened with Polyetherimide (PEI) veils, Polyphenylene sulphide (PPS) veils, CSR particle content and the hybrid use of PPS veils and CSR particle content in this study. The mode-I and mode-II fracture resistance of the laminates were examined prior to the impact and post-impact compression tests. It is indicated that energy dissipation toughening mechanisms via PPS veils is more efficient compared the PEI veils. However, crack tip migration within the veils to the neighbouring lamina reduce the crack resistance of the laminates with veils during crack propagation. The use of PPS veils with CSR particles together changed the crack tip propagation path and provide further improvement in the mode-I fracture properties. However, the CSR particle content adversely affected the mode-II fracture properties of the laminates. Thus the CSR particle content also slightly reduced the mode-II fracture properties of the laminates toughened with the hybrid approach when compared to the laminates toughened with PPS veils. Followingly, impact tests demonstrated that the hybrid use of the PPS veils and CSR particles significantly suppressed the impact damage as the induced impact energy was mostly absorbed until the delamination threshold is reached. Then, the crack tip migrated to the resin-rich region between the veil and carbon fibre surfaces and the limited contribution of the impact resistance via toughening mechanisms obtained from the PPS veils and CSR particles to impact resistance was observed. The impact resistance is governed by mode-I initiation fracture properties until the delamination threshold is reached, then the propagation fracture properties were not transferred to the impact resistance. The performed compression after impact test results indicate that there is a correlation between mode-I initiation fracture energies and residual compressive strength of the laminates.

The use of PPS veils and CSR particles together suppressed the impact damage area and improved the post-impact properties for the composite laminates with no additional thickness penalty. However, the transfer of the toughening properties to the impact and post-impact properties obtained from the hybrid approach is limited, which can be due to the crack tip migration and the high strain rate occurred under impact loading.

Declaration

No portion of the work referred to in the thesis has been submitted in support of an application for another degree or qualification of this or any other university or other institute of learning.

Copyright Statement

Dedication

I would not make my journey from sparkling to becoming fire happen without the help of my family. That's why I would like to dedicate my work;

to my mother (her loving memory is forever in my heart), as teaching me to be patient against tough times and stubborn to achieve my aims;

to my father, as being a source of inspiration to me and for his encouragement throughout my life;

to my sisters, for their support and care.

Acknowledgement

I would like to present my appreciation to Dr Kali Babu Katnam and Prof Prasad Potluri for their guidance and help during my PhD.

I would like to thank the technical staff in the Northwest Composite Centre for their assistance and advice in my experimental work. I would also thank my friends and colleagues for providing friendly, social and academic environment.

I would like to acknowledge The Ministry of National Education of the Republic of Türkiye for their financial support.

CHAPTER 1: Introduction

1.1 Research Background

Composite laminates have recently been used as a structural component for lightweight critical applications (*e.g.* aerospace industry) because of their high specific strength/stiffness, corrosion resistance, fatigue properties and reparability [1,2]. However, the vulnerability of composite laminates to out-of-plane impact loading (*e.g.* tool dropping onto composite-based structures during maintenance or manufacturing and stones or debris hitting during take-off or landing of aircraft) is a highly critical design problem due to their inherent brittle intralaminar (*e.g.* matrix cracking and fibre breakage) and interlaminar failure modes (*e.g.* delamination), which threatens the structural integrity of composite laminates [3,4]. Low-velocity transverse impact loading with a blunt projectile can generate barely visible sub-laminar damage (*i.e.* requires non-destructive testing to detect), which causes a significant reduction in residual mechanical properties of composite laminates [5]. In this regard, this study aims to enhance fracture, impact and post-impact properties with a hybrid toughening approach (*i.e.* the combination of thermoplastic veil interleaving and bulk resin toughening).

In the concern of the impact resistance of composite laminates, mode-I and mode-II interlaminar fracture properties are of the utmost importance [6–10]. Researches have been shown that significant enhancement in interlaminar toughness properties of composites can be provided with 3D-fibre reinforcement (*e.g.* weaving [11–13]) and through the thickness reinforcements (*e.g.* stitching [14–16] and z-pinning [17–20]). Although these reinforcement methods offer significant enhancement in interlaminar fracture toughness of composite laminates, in-plane properties of composite laminates are generally jeopardised because of fibre crimping, the reduction in fibre volume fraction, fibre breakage and misalignment [18,21–25]. The requirement of the complex and expensive manufacturing processes of 3D-fibre reinforcement and through the thickness reinforcement methods is another disadvantage of them compared to material based toughening techniques such as bulk resin and interlaminar toughening methods [26,27].

In the area of bulk resin toughening, rubber particles as a modifier in the epoxy resin are one of the most commonly used and effective methods of enhancing fracture

properties of epoxies [28–33]. Rubber particles can contribute to the fracture properties of composites due to plastic growth and shear band yielding initiated by cavitation mechanisms [30,31,34–37]. Pre-formed core-shell rubber (CSR) particles (*i.e.* structured core-shell latex particles with a rubbery core covered by a glassy shell) are the second generation of rubber modifiers, which can keep their structure in epoxies unlike liquid rubber particles (*i.e.* using liquid rubber particles in epoxies can lead incomplete phase separation) [28]. In CSR particle toughening, fracture properties of composites can be promoted without affecting the glass transition temperature of epoxies (T_g) and the volume fraction of CSR particles can easily be controlled [37–39]. However, blending rubber particle agents as a secondary phase into epoxy resin can increase the initial viscosity of the mixed resin system, which might reduce the resin flow during the infusion process in manufacturing and brings difficulty in achieving void-free laminate due to incomplete fibre wet-out [38,40]. Therefore, the volume fraction of CSR particles needs carefully to be selected, especially for vacuum-assisted resin infusion manufacturing.

Interlaminar veil toughening (*i.e.* introduction of tough and ductile thermoplastic non-woven fibre network between laminae as an additional layer in laminates) creates tortuous crack paths which maintain mechanical links between crack interfaces by bridged fibres [41,42]. Up to date, numerous researchers have reported that interlaminar thermoplastic veil toughening based on micro- or nano-fibres can provide significant enhancement in fracture properties of composite laminates [27,43–48]. In interlaminar veil toughening, the areal weight of veils is the highly critical parameter, which directly influences the toughening performance of interleaved composite laminates. Numerous researches demonstrated that higher areal weight of veils often leads to higher interlaminar fracture toughness until a certain value is reached [27,48–50]. However, toughening veils with a dense areal weight might have detrimental effects on the in-plane properties of composite laminates, particularly for micro-fibre veil interleaving [27,51].

Several strategies have recently been offered to promote the fracture properties of veil toughened laminates by using veils with low areal weights (*i.e.* without considerably reducing in-plane and out-of-plane laminate properties), *e.g.* hybrid veil toughening [47,52–54], improvement in adhesion properties between thermoplastic fibres and matrix via ultra-violet light treatment [55] and particle doping on veils [56]. The

literature manifested here indicates that bulk resin toughening and interlaminar veil toughening strategies are promising methods for laminates to enhance fracture, impact and post-impact properties. The use of core-shell-rubber particle content and thermoplastic micro fibre veils together can influence the energy dissipation mechanisms of laminates. Also, any study has not shown the influence of the hybrid use of bulk resin toughening and interlaminar veil toughening strategies on fracture, impact and post-impact properties of laminates up to date. In this context, this study proposes the hybrid use of core-shell-rubber particle content and thermoplastic micro fibre veils to provide further improvement in the fracture, low-velocity impact and post-impact properties of laminates by using veils with low areal weight.

1.2. Research Aim and Objectives

Composite laminates present brittle behaviour under impact loading, especially when the matrix material is highly cross-linked epoxies. Low-velocity out-of-plane impact loading with a blunt projectile can generate barely visible sub-laminar damage (*i.e.* matrix cracking, fibre breakage, and delamination), which causes a significant reduction in residual mechanical properties of composite laminates. Among these failure mechanisms, delamination failure causes significant loss in the load-bearing capability of composite laminates. Therefore, this study aims to enhance the delamination resistance, thus low-velocity impact and post-impact properties of laminates using a hybrid toughening approach (*i.e.* combination of bulk resin toughening and thermoplastic veil interlaminar toughening). To investigate the influence of the hybrid toughening strategy, the following objectives are investigated:

- The influence of the thermoplastic veils on the delamination resistance of composite laminates,
- The influence of the core-shell rubber particle in the matrix on the delamination resistance of composite laminates,
- The influence of the hybrid toughening approach on the delamination resistance of composite laminates,
- The influence of the hybrid toughening approach on the low-velocity impact resistance of composite laminates,

- The influence of the hybrid toughening approach on the low-velocity impact damage tolerance of composite laminates.

1.3. Thesis Outline

This thesis is divided into 9 chapters:

Chapter 2 presents a literature review. First, a brief introduction to composite laminates is given. Then, the low-velocity impact resistance is introduced and the relationship between low-velocity impact and delamination resistances for composite laminates is given. The toughening strategies are presented and their advantages and disadvantages are discussed.

Chapter 3 describes the materials, manufacturing, and experimental processes which are applied to characterise the delamination resistance, impact resistance and impact damage tolerance of the composite laminates.

Chapter 4 investigates the interlaminar fracture resistance of the interleaved composite laminates with Polyetherimide (PEI) and Polyphenylene sulphide (PPS) veils under mode-I loading. The influence of the fibre material on the fracture performance for interleaved composite laminates is discussed.

Chapter 5 investigates the interlaminar fracture resistance of the hybrid toughened composite laminates under mode-I loading. The mode-I fracture performance of the laminates with/without CSR particle content, PPS veils and the hybrid use of CSR particle and PPS veils are compared.

Chapter 6 investigates the interlaminar fracture resistance of the hybrid toughened composite laminates under mode-II loading. The mode-II fracture performance of the laminates with/without CSR particle content, PPS veils and the hybrid use of CSR particle and PPS veils are compared.

Chapter 7 presents the drop-weight low-velocity impact test results. In this chapter, the low-velocity impact response of the laminates with/without CSR particle content, PPS veils and the hybrid use of CSR particle and PPS veils are compared.

Chapter 8 illustrates the compression after impact test results of the laminates with/without CSR particle content, PPS veils and the hybrid use of CSR particle and PPS veils. The influence of the hybrid toughening approach on the post-impact properties is investigated in this chapter.

Chapter 9 concludes this thesis. Also, future research works are suggested.

CHAPTER 2: Literature Review

2.1. Introduction

Advanced composite laminates (*e.g.* carbon fibre reinforced polymers), which can offer high specific strength and stiffness compared to conventional structural materials, are widely being used in many structural applications, including safety-critical aerospace structures (*e.g.* wings and fuselage in Airbus A350) but it is well known that composite structures are inherently brittle, especially when the matrix material is a highly cross-linked polymer (*e.g.* epoxy), and vulnerable to in-service impact loading (*e.g.* tool dropping onto composite-based structures during maintenance or manufacturing and stones or debris hitting during take-off or landing of aircraft) [57]. In this regard, enhancing out-of-plane low-velocity impact damage tolerance of composite laminates by exploring toughening approaches, which are cost-effective and easy-to-manufacture, is highly critical to ensure the safety and structural integrity of composite structures during their service life.

From this point of the view, this chapter reviews the literature on impact damage tolerance of composite laminates and how delamination resistance affects the impact and post-impact properties of composite laminates starting with a brief background on composite materials. This review highlights the importance of toughening properties on the low-velocity impact damage tolerance for composite laminates and introduces various toughening strategies for composite laminates. The reviewed literature discusses the advantage and disadvantages of the toughening strategies. Finally, it offers a cost-effective hybrid toughening approach (*i.e.* combination of interlaminar thermoplastic veil toughening and bulk resin toughening strategies) as a promising toughening strategy to improve delamination resistance, thus low-velocity impact response and impact damage tolerance of composite laminates.

2.2. Fibre Reinforced Composite Laminates

Fibre-reinforced composite laminates are the mechanical structural components containing fibres of high strength and modulus surrounded in or bonded to a matrix. Both fibre and matrix retain their physical and chemical identities in composite form,

but both cannot provide the mechanical properties obtained from the composite form by itself alone [57,58].

Composite laminates have recently been gaining importance in light-weight critical structural applications such as aerospace, marine, and renewable energy industries. For example, a systematic increase in demand for composite materials for several Boeing programs can be seen in Figure 2. 1 [59]. In comparison to conventional metallic materials, fibre reinforced polymer composite materials provide higher specific strength and stiffness, improved fatigue life, better corrosion resistance, and tailorability for optimum strength and stiffness [60].

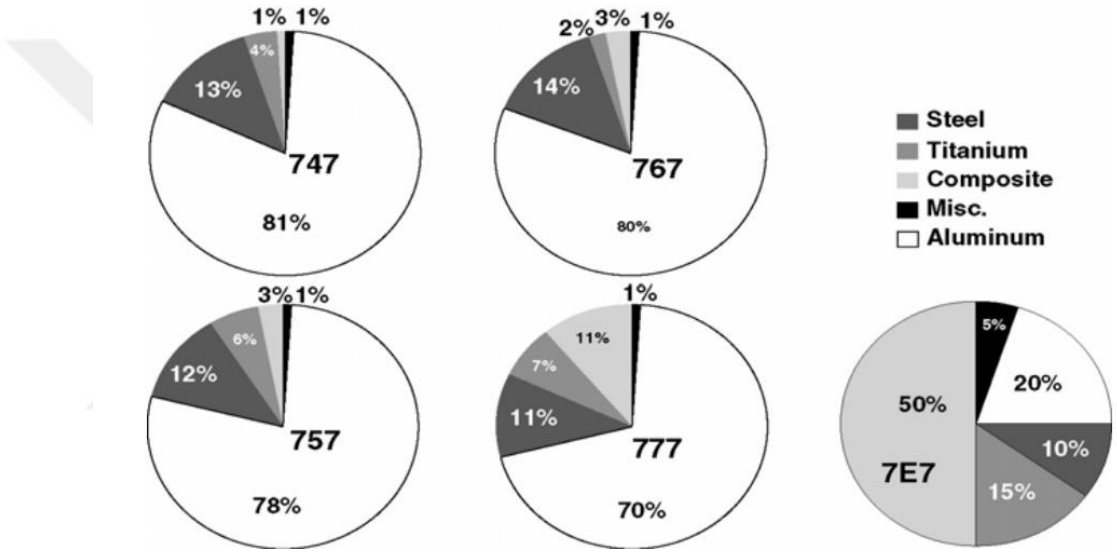

Figure 2. 1| The combination of materials used in Boeing aircraft [59].

2.2.1. Continuous Phase

The continuous phase, known as matrix, holds the reinforcement phase together by surrounding them and transfers loads through the interface to the reinforcing fibres and the composite from external sources [61]. The selection of matrix materials takes critical importance for advanced composite materials because the matrix materials dominantly determine the transverse load carrying capability for composite structures [62]. In the fibre reinforced polymer composites, thermoplastic (*e.g.* polyolefin, polyester, and polyamides) and thermoset (*e.g.* epoxy, vinyl ester and phenolic)

polymers can be used as a matrix material [63]. Thermoplastic polymers comprise long molecular chains which are held in a place by strong intra-molecular covalent bonds and weak intermolecular bonds as schematically represented in Figure 2. 2a [57]. Thus, thermoplastic polymers are recyclable (*i.e.* provide easiness in repair), which can be heated into a deformable plastic state and re-solidify upon cooling [64]. The primary advantages of thermoplastic polymers over thermosets regarding structural design concerns are their impact and fracture properties, which outcomes of high damage-tolerant composite structures [2,65,66]. However, the relatively high viscosity of thermoplastic polymers compared to thermosets complicates the manufacturing process because of requiring high temperature and pressure [67]. In thermoset polymers, molecules are connected with cross-links as schematically shown in Figure 2. 2b. Cross-links in thermoset polymers provide structural integrity by making difficult for sliding molecules to pass one on another one [57]. Thermoset polymers cannot be melted once polymerised as they are chemically bonded together by cross-links in thermosets, thus repair in thermoset composites is a complex process when compared to thermoplastic-based composites [68]. The major drawback of using thermoset polymers as a matrix material for composites is their weakness to transverse impact loads due to the inherently brittle behaviour of thermosets [69].

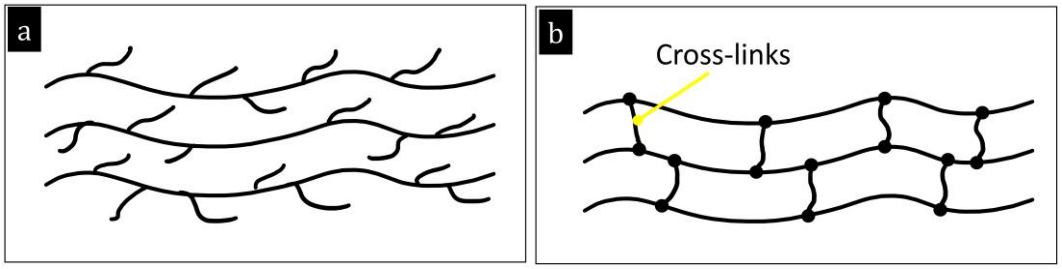

Figure 2. 2| Schematic representations of molecular structures of polymer matrices: (a) thermoplastics and (b) thermosets [57].

Thermoset polymers have been dominantly used in continuous fibre reinforced polymer composites due to their higher stiffness and strength to weight ratio compared to conventional metallic materials [70]. The main advantage of thermoset polymers over thermoplastics is the relatively lower viscosity, which brings easiness in manufacturing [71]. However, thermoset-based composite laminates might contain

interlaminar failure under impact loading because of the brittle nature of thermosets, which can deteriorate the residual strength and stiffness of composite structures [66,72]. Hence, improving the delamination resistance of composite laminates made of thermoset resins, thus the impact and post-impact properties, is vitally important to ensure the structural integrity of thermoset-based composite components.

2.2.2. Reinforcement Phase

The reinforcement phase of composites carries a major load on composite structures and provides strength and stiffness. Continuous fibres are generally used in lightweight critical applications and the orientation of fibres can be adjusted depending on principal stresses acting on composite based structural components. The reinforcement selection of composites primarily depends on physical property requirements (e.g. density), mechanical property requirements (*e.g.* tensile strength and stiffness, compressive strength and stiffness, fatigue strength) and the cost of reinforcements [73,74].

In structural applications, the most commonly used fibres are glass, aramid and carbon fibres [75]. Glass fibres (*i.e.* usually preferred as a structural component for renewable energy applications such as wind turbines, marine applications, and non-critical aerospace applications such as antenna enclosures, engine cowlings) provide high chemical resistance, impact resistance with low cost [58]. However, their relatively low fatigue, tensile modulus and high density are the limiting factors for glass fibre reinforced composites compared to other types of structural reinforcement fibres [76,77]. Aramid fibres (*e.g.* Kevlar), highly crystalline aromatic polyamides, offer stiffness between glass and carbon fibres, and are mostly used in the military industry (*e.g.* protective clothing and helmet due to heat and flame resistance) and aerospace industry due to their excellent impact properties [78]. However, their disadvantages are weakness in bending, buckling, compression loading and transverse tension [79]. Carbon fibres are the most widely used reinforcement fibres in high-performance lightweight critical structural applications such as the aerospace industry due to their high tensile modulus, specific tensile strength, fatigue strength and thermal conductivity with very low coefficient of linear thermal expansion over other types of reinforcing fibres [57,75]. However, their drawbacks are a low strain to failure, low

impact resistance, and relatively higher cost compared to other reinforcement fibres [80].

Arrangement of fibres such as fibre orientation, crimp and yarn interlacement can influence the final mechanical properties of composite laminates [81]. The architecture of reinforcement fibres commonly used in structural applications can be classified as woven, braided, and unidirectional. In the weaving process, two sets of continuous fibres (*i.e.* warp and weft yarns) are interlaced at the right angle [82]. There are three main weaving structures (*e.g.* plain, twill and satin) as illustrated in Figure 2. 3. Plain woven fabrics are the simplest and most commonly used woven fabrics in comparison to another type of woven fabric architectures. The strength and stiffness of composite laminates manufactured with plain woven fabric are compromised because of high crimping [83,84]. In twill weaves, the degree of crimps is relatively lower than that of plain weaves [84]. Thus, composite manufacturing with twill woven fabrics results in a smoother surface finish as it is easier to wet the fabrics out. Also, the in-plain mechanical properties of composites with twill woven fabrics are relatively better than composites including plain woven fabrics [83]. The satin weave is fundamentally twill weave with fewer intersections, thus the composite laminates consisting of satin woven fabrics can translate better strength properties in all directions compared to composites with plain and twill woven fabrics [83–85]. In addition, three sets of yarns are interlaced to form 3D woven structures (see, Figure 2. 4) to enhance the damage tolerance of composites and interlaminar properties of composite laminates [86]. 3D woven preforms can provide significant improvement in the delamination resistance of composites due to binder fibres located through-the-thickness direction [87].

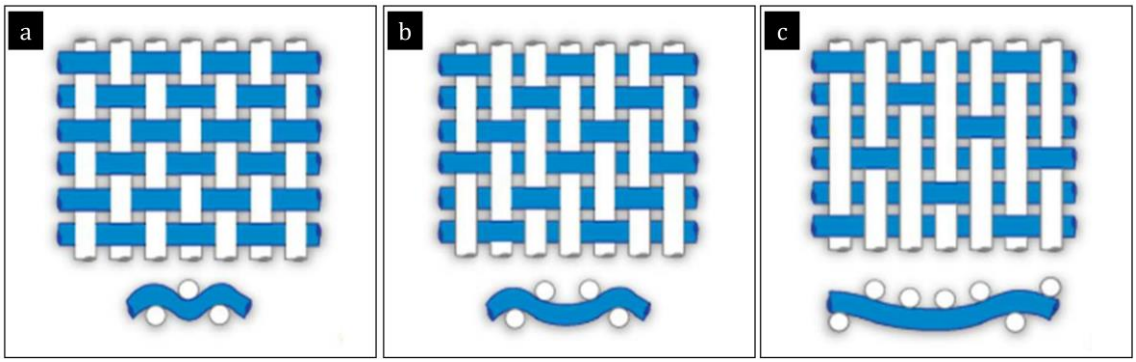

Figure 2. 3| Representations of 2D textile weaves: (a) plain, (b) twill, and (c) satin weaves [88].

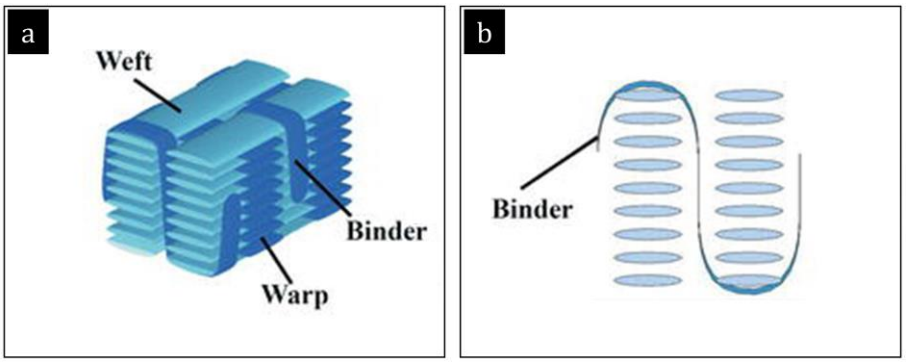

Figure 2. 4| A Representation of (a) a 3D woven fabric and (b) a binder path [89].

In the braiding process, the threads are intertwined by transporting one half of them in one direction, while the other half is moved in the opposite direction of the impeller wheels, see schematically braiding process in Figure 2. 5 [90]. Composite laminates with braided fibre structure provide excellent impact properties, damage tolerance and shear properties and the ability to form complex shapes compared to conventional fibre preforms. However, the requirement of expensive equipment, complex and long process duration, and high cost limit the use of braided fibre preforms.

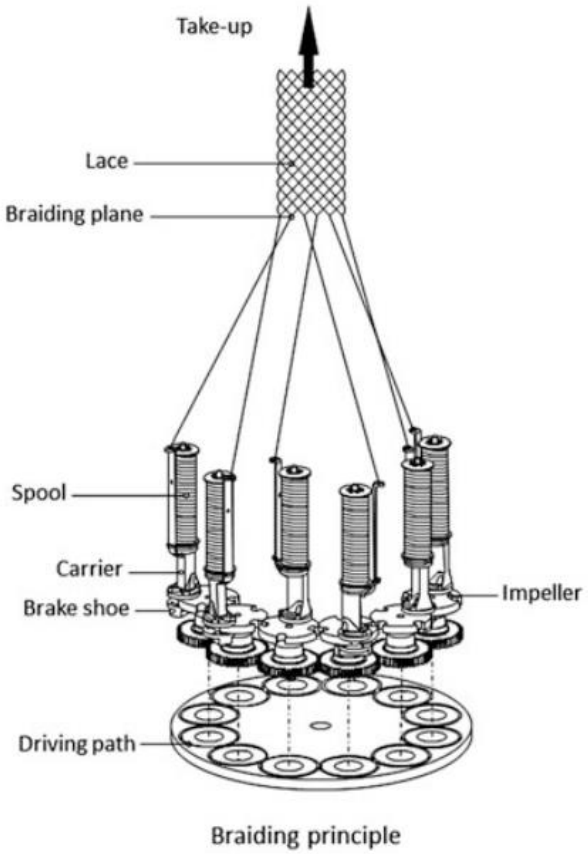

Figure 2. 5| An illustration representing the principle of the braiding process [90].

In unidirectional (UD) fibre alignment, all reinforcement fibres stay in a single and parallel direction. Using unidirectional fibres in composite materials maximises the fibre volume ratio while minimising fibre crimping and provides extremely high in-plane properties. However, composites with unidirectional fibres suffer from out-of-plane loading due to a lack of through-the-thickness reinforcement fibres [91,92]. In unidirectional prepreg (*i.e*. impregnated with a resin system) composites, fibres are straight and uniformly distributed as shown in Figure 2. 6a. Alternatively, non-crimp fabrics (NCF) include one layer of parallel tows woven together with thin weft yarns, see Figure 2. 6b [93]. Unidirectional NCF fabrics exhibit moderate waviness unlike unidirectional fibre prepregs, which can result in relatively lower mechanical properties compared to UD reinforced composites.

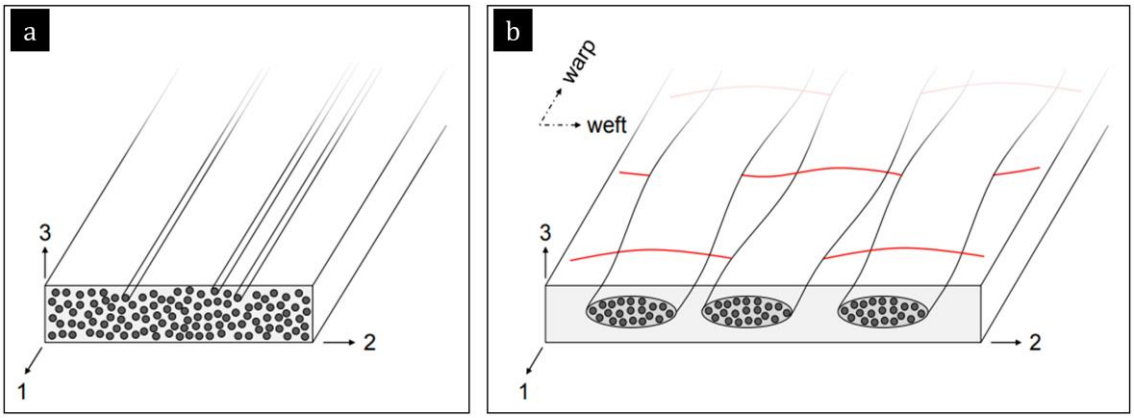

Figure 2. 6| Schematics of (a) an unidirectional and (b) a NCF composites [93].

2.3. Composite Manufacturing

Composite laminates are commonly manufactured with prepreg moulding and resin transfer moulding techniques. Prepreg fabrics usually comprise of a single layer of fibres, unidirectional or woven, embedded in a partly cured resin system. Prepreg fabrics are required to be stored in an environment at ~-18° to maintain the longest shelf life, which increases the cost of composite laminates with prepreg fabrics. Prepreg composite laminates can be manufactured with auto-clave ovens. Stacked prepreg fibres on a mould are first covered with a vacuum bag and cured under applied heat and pressure in an autoclave or a pressure [71,73].

In resin transfer moulding (RTM), several layers of fibre fabric are placed in the half bottom of a two-part mould as shown in Figure 2. 7. Then, resin is injected into a dry fibre preform inside a closed mould under vacuum pressure of 3.5-7 bar [94]. The injected resin fills the gaps between fibre yarns in the dry preforms by spreading throughout the mould. The major advantage of resin transfer moulding is the manufacturability of complicated shapes and the elimination of trimming operations [57].

Vacuum-assisted resin infusion (VARI) technique (see, Figure 2. 8) is a cost-effective way to manufacture composite laminates with no required high-cost investments such as an autoclave oven [71]. Composite manufacturing with VARI technique results in a relatively low fibre volume fraction (*e.g.* ~55%) compared to composite manufacturing with RTM due to relatively lower vacuum pressure used in VARI (~1 bar) [57]. In

manufacturing with VARI, low-viscous resins are preferred to achieve adequate impregnation of the preform with a resin [71].

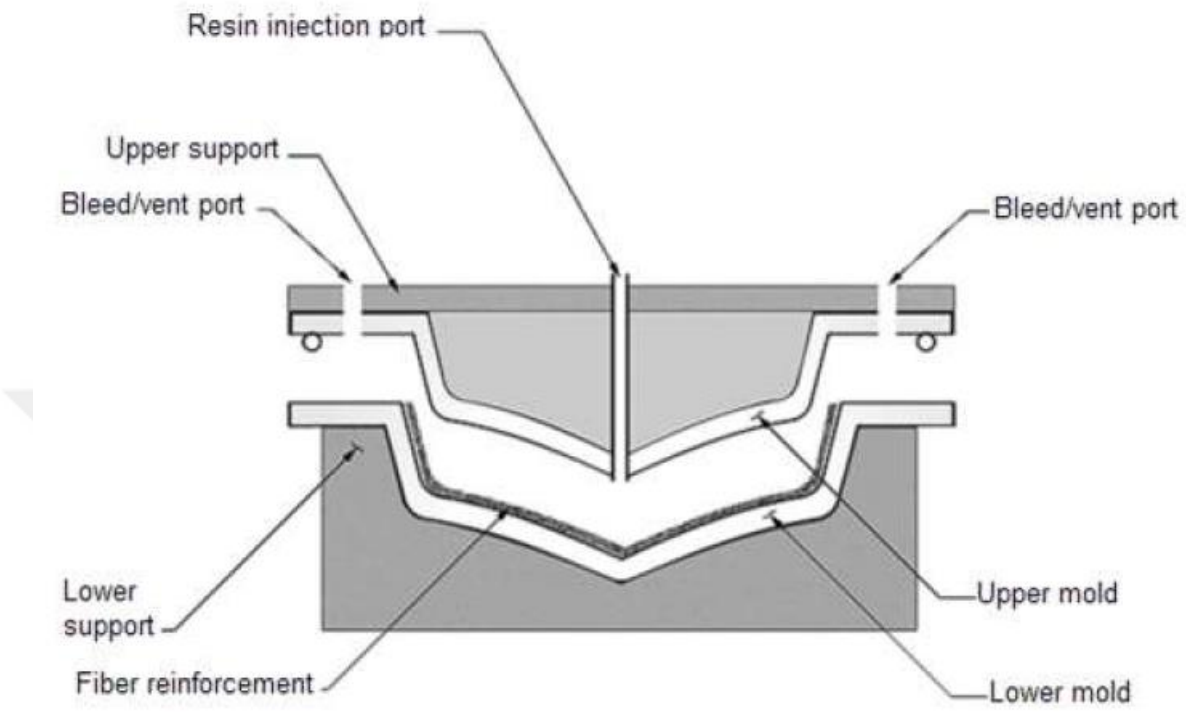

Figure 2. 7| A schematic of resin transfer moulding [71].

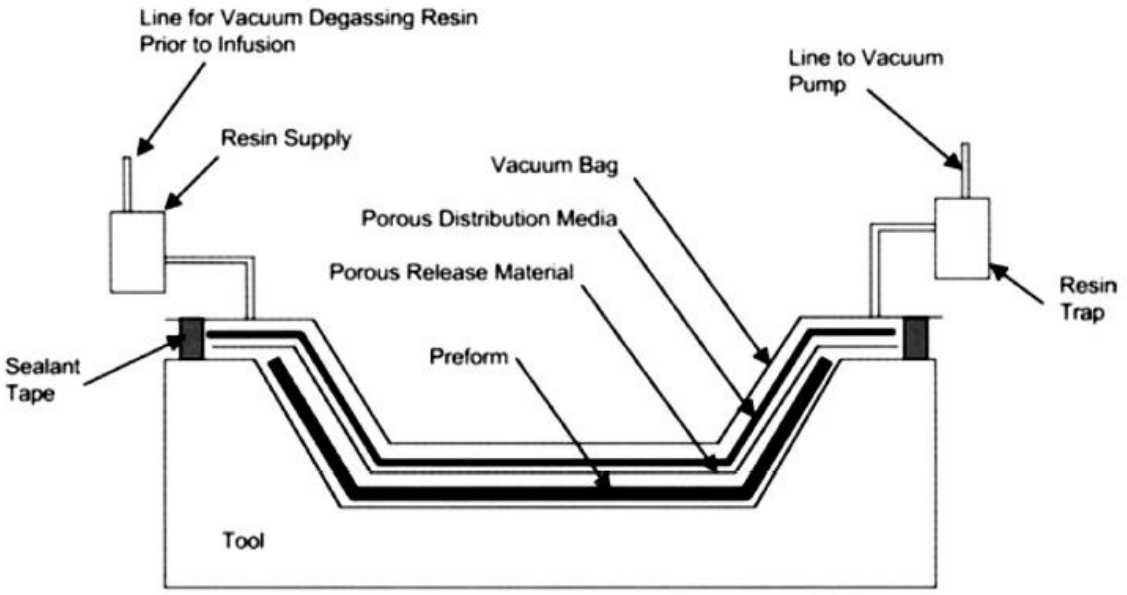

Figure 2. 8| A schematic of vacuum-assisted resin infusion moulding [71].

2.3.1. Composite Curing

The heat transfer process for composite curing occurs either in the autoclave or out-of-autoclave. Autoclave (see, Figure 2. 9) is a pressurised oven in which pre-forms with vacuum bagging are located under high pressure (*e.g.* 4-7 bar) and at a temperature varying from 120 to 180 for typical epoxy prepregs [95]. The high pressure of autoclave ovens offers ply compaction, eliminates surplus resin which provides an increase in fibre volume ratio, and suppresses void formation [73]. Thus, autoclave curing is commonly preferred to achieve composite components with a high-quality finish including low void content. However, long process time (*i.e.* due to low heating rate at ~3°C requiring extensive cure cycle) and high investment cost (*i.e.* due to size of autoclaves, temperature/pressure requirements and safety needs) are the main drawbacks of autoclave curing [71].

Out-of-autoclave (*i.e.* oven) curing is the simplest and cheapest method of composite curing. The moulded composite laminates with RTM and VARI techniques can be cured in a simple oven. The major disadvantage of out-of-autoclave curing is the relatively low-quality of final composite laminates (*e.g.* lower fibre volume fraction and high void content) than those cured in an autoclave due to lack of applied pressure [57,71].

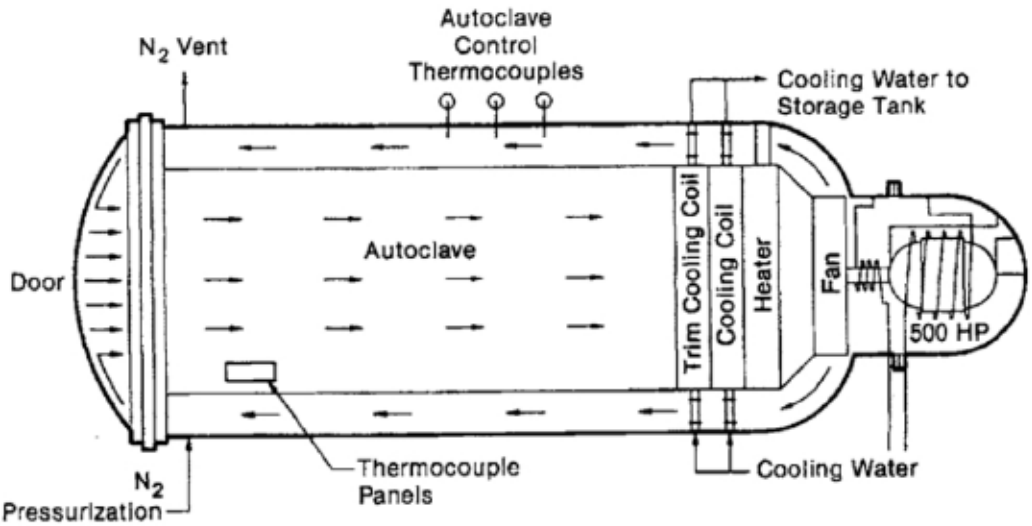

Figure 2. 9| A schematic of an autoclave oven [71].

2.4. Impact Damage Tolerance of Composite Laminates

Damage tolerance describes the ability of the structure to withstand further loads after damage formation which might arise during the manufacturing process and in-service loading [96,97]. In damage tolerant design concept for aerospace applications, two main categories need to be satisfied: a) slow crack growth (*i.e.* structure is required to sustain the growth of the initial damage for a specified period of service while sustaining a minimum level of residual static strength and not achieve a size large enough to cause rapid unstable crack propagation) and b) fail-safe (*i.e.* the ability of mechanical structures to be operated safely with partial failure prior to inspection and the maintenance of specified static strength throughout the service period) [98].

Impact events, which can introduce internal failure mechanisms for particularly composite-based structural applications, are a typical phenomenon and one of the major concerns in the design of composite structures. For example, the study performed on repairs of Boeing 747 demonstrated that 13% of repairs are because of foreign object impacts, which shows a high possibility of impact events during the in-service life of aerospace structural applications and the importance of investigating the impact behaviour of composite structures for the damage tolerant composite design [99]. Numerous studies demonstrated that impact events (*e.g.* runway debris, bird strikes, hailstones, and tool drop during maintenance) are responsible for the reduction of the residual properties for composite laminates up to ~60% [100–105].

For out-of-plane low energy impact events, composite laminates suffer a much larger degree of strength reduction in compression than in tension. Cantwell et al. [106] conducted a study using composite laminates containing high-strain carbon fibres (*i.e.* system A) and high-strength carbon fibres (*i.e.* system B) to evaluate their post-impact residual properties of them (see Figure 2. 10). This study reveals that composite laminates can experience significant loss in compressive strength after impact damage is introduced. A decreasing trend with an increase in impact energy in post-impact compressive strength of two composite systems is shown in Figure 2. 10a. On the other hand, no linear trend with increasing impact energy was observed for the post-impact tensile properties (see Figure 2. 10b). Cantwell et al. [106] stated that the fracture of 0° fibres results in a rapid reduction in the post-impact tensile strength of composite

laminates. Therefore, this study presents that compression after impact properties of laminates are a critical design problem.

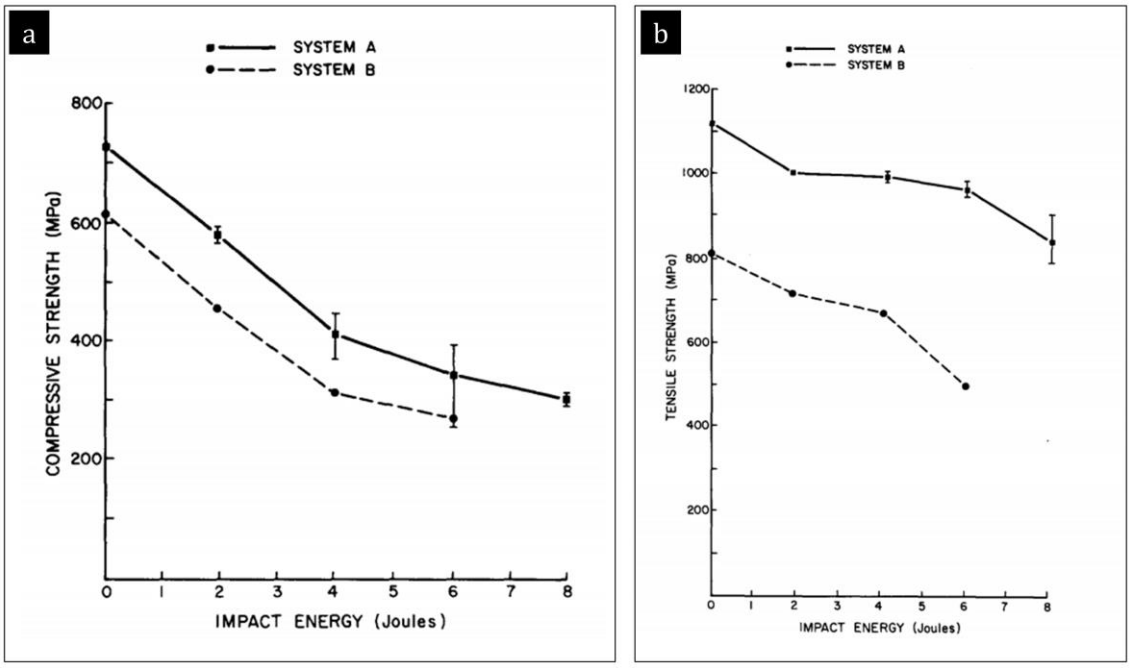

Figure 2. 10| (a) The residual compressive and (b) tensile strengths after impact for the material systems A and B [106].

In this respect, compression loading is more critical compared to tension loading after impact damage. The impact damage tolerance of composite laminates can experimentally be evaluated with the compression after impact (CAI) test methodology. In CAI testing, a drop-weight impact test (*i.e.* representative of physical scenarios of transverse impact to a composite laminate such as tool drop can be produced) is first performed, then a compression test is applied to investigate residual strength. In general, sublaminar failure modes in composite laminates are captured with SEM and the damage area in composite laminates is detected with the non-destructive ultrasonic evaluation technique (*e.g.* ultrasonic C-scan and computed tomography) [107,108].

2.4.1. Low-Velocity Impact Behaviour of Composite Laminates

Fibre-reinforced composite laminates are extremely vulnerable to transverse impact loads and impact events can create visible or barely visible internal damage (BVID) in composite laminates [72]. This study focuses on low velocity impact damage tolerance of composite laminates. In this regard, it is highly critical to understand how the impact energy and stress waves control the failure mechanisms of composite laminates to evaluate their behaviour of them under impact loading.

Impact events can be classified depending on the velocity of the impactor as low-velocity impact (*i.e.* large mass) and high-velocity impact (*i.e.* small mass) [109]. However, researchers categorised impact events with different approaches. For example, Sjoblom et al. [110] and Shivakumar et al. [111] described low-velocity impact events as impact loading up to 10 m/s inducing a quasi-static load in structural composite laminates depending on the target stiffness, material properties and mass and stiffness of impactors. Cantwell and Morton [66] also characterised low-velocity impact as impact loading up to 10 m/s. Abrate [112] suggested that low-velocity impact events occur on composite laminates for impact speeds of lower than 100 m/s. Alternatively, Liu and Malvern [113] recommended that impact events are classified depending on the damage generated by impact in composite laminate (*i.e.* high-velocity impact is defined by penetration failure induced fibre breakage while low-velocity impact by delamination and matrix cracking). On the other hand, Olsson [114] suggested that the response of composite laminates to impact events can be described depending on the behaviour of elastic waves which are initiated by impact and propagated from the point of impact. Energy dissipation mechanisms and corresponding vibration of the target, related to wave propagation induced by the impact, can lead to degradation of the post-impact properties of composites. Therefore, the duration of impact is the significant parameter governing the impact response of composite laminates. When contact time is in the order of the transition time for through-the-thickness waves, the response of composite laminates is dominantly controlled by transverse waves, as shown in Figure 2. 11a. For longer impact durations, the response of composite laminates to the impact is governed by flexural and shear waves, as shown in Figure 2. 11b. When the duration of impact is much longer than the time elastic waves reach the structure boundaries, the response of composites to the impact becomes quasi-static and boundary controlled as shown in Figure 2. 11c [114].

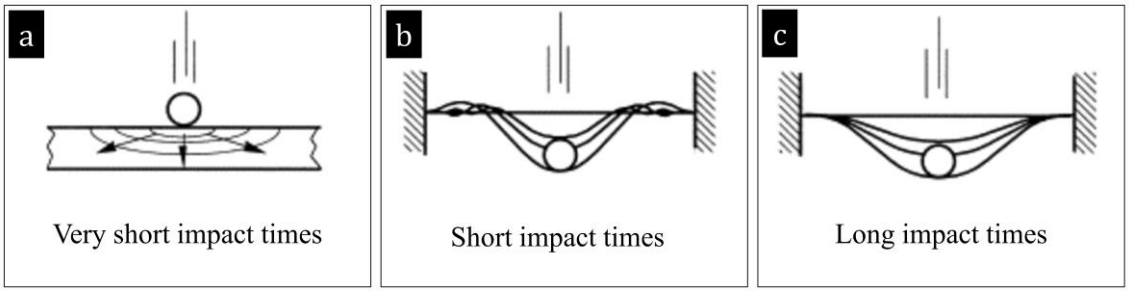

Figure 2. 11| Impact responses of composite laminates: (a) dominated by transverse dilatational waves, (b) dominated by flexural and shear waves and (c) quasi statical response [114].

In conclusion, the response of high-velocity impact is related to transverse waves, thus deformation of high-velocity impact is localised at the region where the impact is induced on laminates and easily detectable. Wave-controlled and boundary-controlled impact responses can be introduced in composite laminates by low-velocity impact loading. In this study, the focus will be on the low-velocity impact response of composite laminates.

2.4.2. Low-Velocity Impact Damage Mechanisms of Composite Laminates

The response of composite laminates under impact loading is different and complicated because of the inhomogeneous and anisotropic nature of laminated composite material systems compared to metallic materials. While metallic materials absorb impact energy in elastic-plastic deformation, composite materials dissipate impact energy with intralaminar (*e.g.* matrix cracking and fibre breakage) and interlaminar (*e.g.* delamination) failure modes [115,116].

The response of composite laminates under impact loading can be defined with absorbed energy, peak force, peak deformation, a period of impact contact and resulting damage forms [117]. Representative low-velocity blunt impact histories of force-time and energy-time curves are given in Figure 2. 12. The load-time curve demonstrates that the contact load steadily rises until reaching a critical force (F_{cr}) and then suddenly drops. This sudden reduction in the typical load-time history explains that composite laminates under impact loading suffer from sublaminar failures (*e.g.*

matrix cracks and delamination failures) which result in a reduction in transverse stiffness of composites [118]. After the sudden drop, contact load increases up to maximum peak value (F_{max}) with reduced stiffness, then contact load goes to zero as the impactor rebounds from the specimen without penetrating [119]. Parallel to force-time history, energy time history also indicates that some amount of energy is absorbed through the failure mechanisms. Also, the whole impact energy induced to composite laminates is not dissipated via damage mechanisms and some of that is elastically used for rebounding when the composite laminates are under transverse impact loading [120].

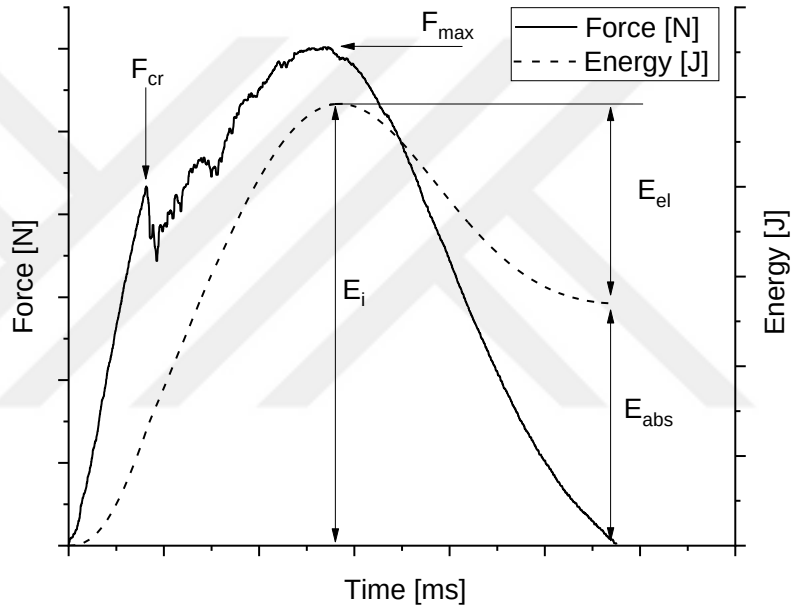

Figure 2. 12| A representative force-time and energy-time histories of composite laminates subjected to low-velocity impact indicating critical force (F_{cr}), maximum contact force (F_{max}), impact energy (E_i), rebounded elastic energy (E_{el}) and absorbed energy (E_{abs}) [118,119].

Low-velocity blunt impact events can generate barely visible internal damage, which degrades the load-carrying capability for composite laminates [122]. In most cases, typical damage modes of composites under low-velocity blunt impact loading are matrix crack, delamination, and fibre breakage as shown in Figure 2. 13 [123].

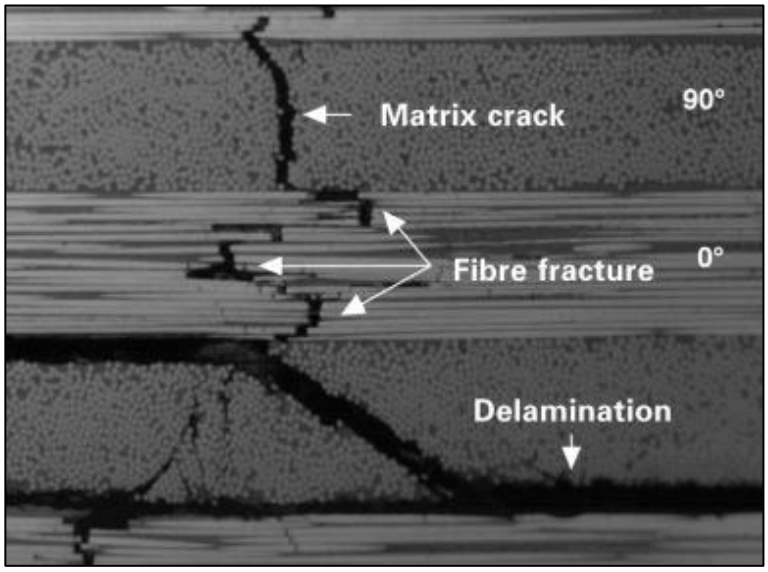

Figure 2. 13| Typical microstructural failure mechanisms of composite laminates demonstrating matrix crack, fibre fracture and delamination failure [123].

The representation of a composite laminate with typical failure mechanisms is also schematically given in Figure 2. 14. The initial failure mechanism is matrix cracking for composite laminates under impact loading [123]. Shear matrix cracks, which are commonly located in planes parallel to fibre directions in unidirectional fibre composites, occur by transverse shear stresses through composite laminates [124]. Also, matrix cracks at bottom layers, namely bending cracks, are generated by the tensile component of bending stresses (*i.e.* related to flexural deformation of composite laminates) and they are characteristically vertical [72,124,125]. Delamination failure (*i.e.* separation of layers) governed by interlaminar shear stresses is introduced in composite laminates as a result of matrix crack propagation into the weak interlaminar region of adjacent layers because of bending stiffness mismatch [126,127]. Fibre breakages occur when impact energy increases to a limit where matrix cracking and delamination failures are not able to dissipate energy. Fibre breakages at the bottom layers of composite laminates (*i.e.* non-impacted face) occur because of excessive tensile bending stress. On the other hand, the generation of fibre buckling at the top layers of composite laminates (*i.e.* impacted face) is the consequence of high local stress and high indentation effects of the impactor. [109].

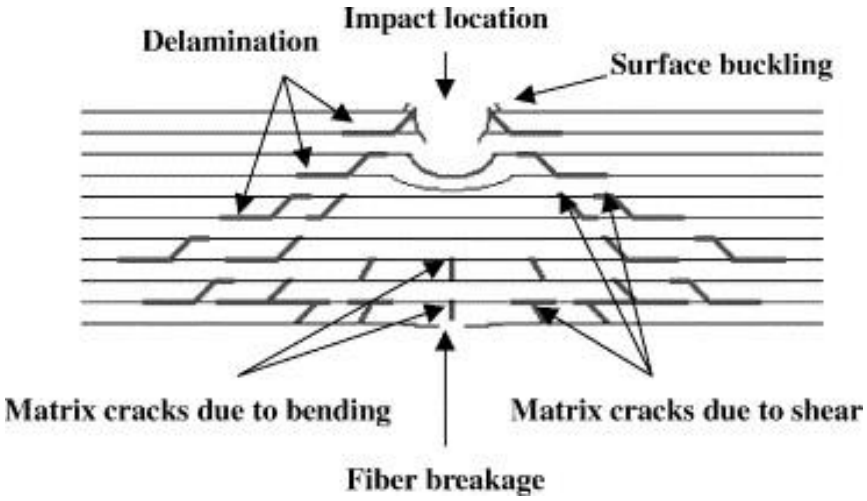

Figure 2. 14| A schematic representation of a composite laminate with the typical damage modes [119].

Among the failure mechanisms abovementioned, delamination failure is the most dominant failure mechanism which significantly causes degradation in the post-impact properties of composite laminates [2]. From this point of view, understanding delamination generation and what mechanisms play a role in leading delamination resistance in a composite material system is a vital consideration for damage tolerant composite structure design.

2.5. Interlaminar Fracture Toughness: Influence on Impact Behaviour of Composites

Delamination, the predominant failure mechanism decaying the properties of composite laminates because of a large reduction in composite stiffness and strength, may occur due to impact events or interlaminar stress creating design required imperfections, which are developed because of discontinuities at stress-free edges such as free edges, notches, ply drop-offs, bonded joints and bolted joints (see Figure 2. 15) [2,128]. Failure to detect delamination may severely reduce the structural durability of composite laminates. For example, barely visible delamination failure occurred due to the transverse impact, which is the concern of this study, can decrease the residual compressive strength of composite laminates by 60% [129].

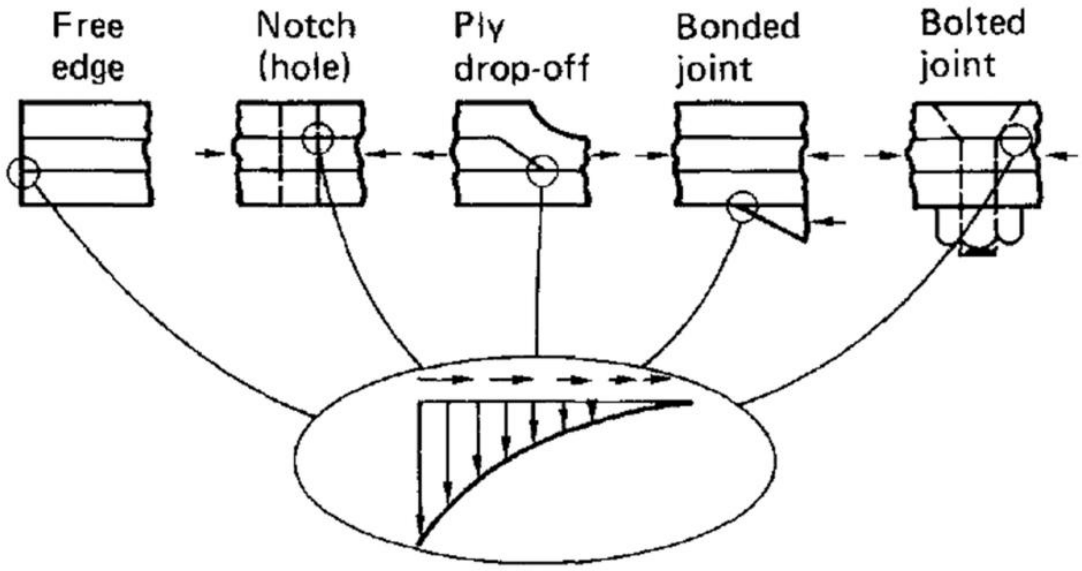

Figure 2. 15| The sources of out-of-plane stressing from load path discontinuity [2].

Fracture toughness defines the ability of a material system containing a crack to withstand loading [130]. The interlaminar toughness behaviour of composite laminates including the stress fields near crack tips can be explained with the three basic modes (see Figure 2. 16). Mode-I is the opening crack mode which is characterised by the displacement of two crack surfaces moving directly apart from each other, mode-II is the sliding crack mode which occurs when the two crack surfaces are displaced by sliding over each other, and mode-III is the tearing mode which arises when the two crack surfaces slide with respect to one another parallel to the leading edge [131,132].

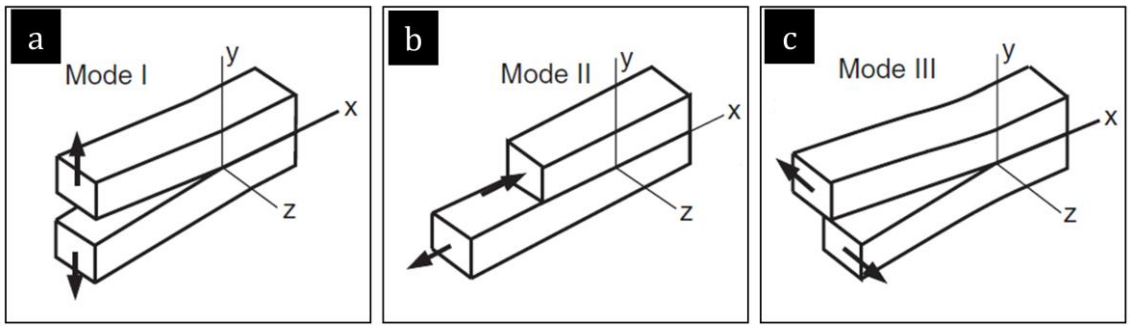

Figure 2. 16| Modes at the stress fields near crack-tips: a) Mode-I, b) Mode-II, and c) Mode-III [131].

Mode-I and mode-II fracture toughness of composite laminates are of the utmost importance with respect to the impact behaviour of composite laminates as both loading conditions can govern the delamination resistance of composites under impact loading [8,134,135]. For example, the experimental study conducted by Masters [136] on mode-I, mode-II delamination resistance and the post-impact properties of different types of epoxy and bismaleimide-based carbon fibre composites toughened with interleaf films clearly demonstrates that an increase in G_I and G_{II} can deliver enhancement in post-impact properties in each carbon fibre composite material systems as seen in Figure 2. 17.

When laminates are subjected to the impact loading, initial damage mode is matrix cracks and delamination is induced by the transverse matrix cracking. Also, matrix cracks exist along lamina interfaces, which can suggest that mode-II fracture properties govern the delamination initiation. However, the presence of matrix at the interface of lamina undergoes tension stress to the principal tension stress direction [137,138]. The study performed by Choi et al. [125] indicates that mode-I and mode-II fracture properties are key parameters for the laminates under impact loading. Also, it is demonstrated that delamination initiation can predominantly be dominated by mode-I fracture properties while mode-II fracture becomes increasingly essential for the delamination propagation once delamination is initiated. Another study reported by Liu et al. [139] was performed to understand the delamination initiation and growth for composite laminates under transverse loading. This study indicates that mode-I fracture predominantly govern the delamination initiation while mode-II toughness properties primarily dominates the delamination propagation. Salpekar [137] also indicated that mode-I fracture properties are an important parameter for delamination growth while mode-II fracture properties dominate the delamination propagation.

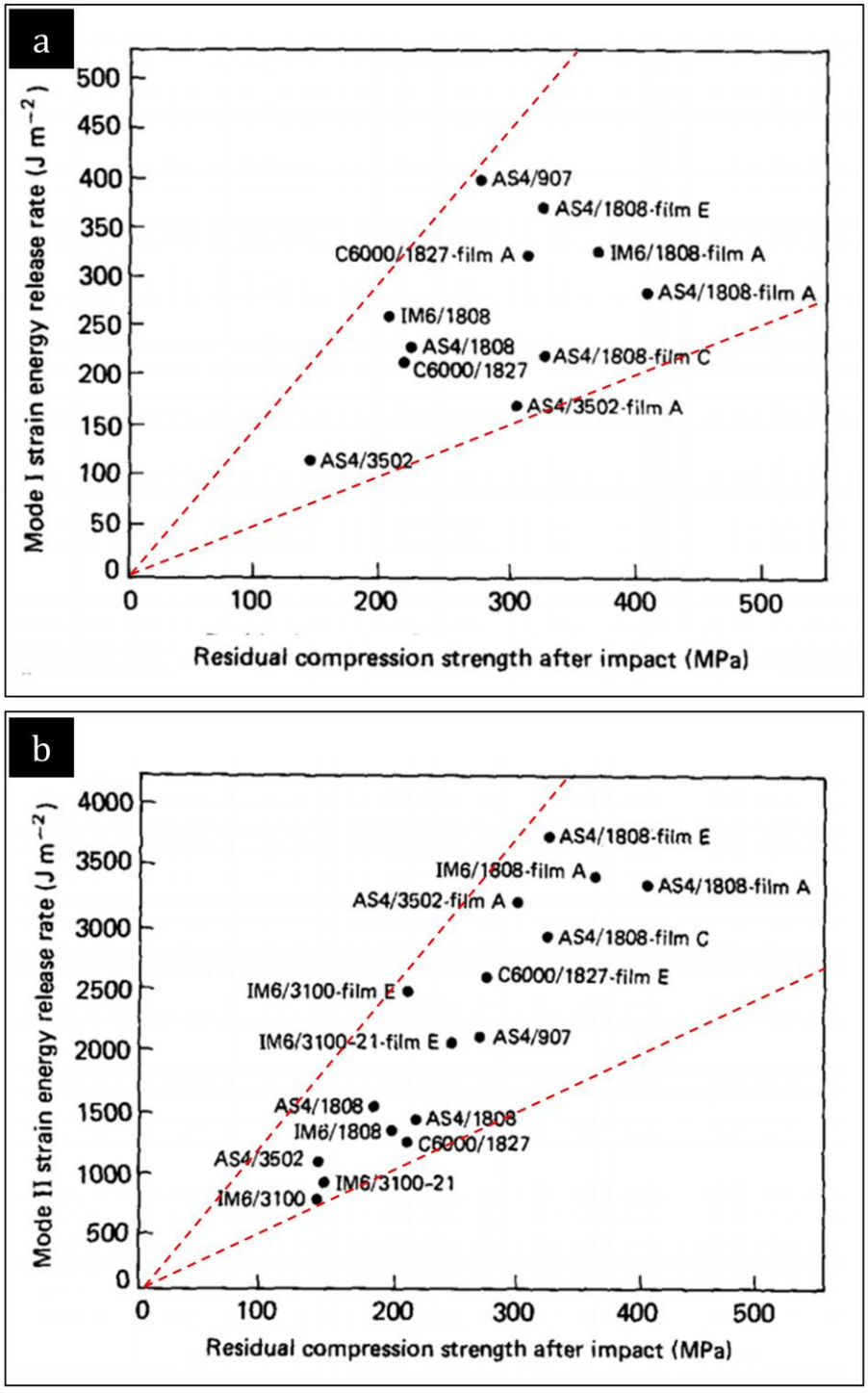

Figure 2. 17| The results of the experimental study performed by Masters [136] showing the correlation between impact and delamination resistance in interleaved laminates under (a) mode-I and (b) mode-II loading conditions.

In laminated composite structures, micro-mechanisms mainly responsible for energy absorption during mode-I and mode-II loading (schematically represented in Figure 2. 18) are these [140]: (i) formation of fracture surfaces, (ii) plastic deformation and/or microcracking of the matrix in the damage zone around the crack tip, and (iii) crack bridging by fibres or fibre bundles resulting in fibre peeling and fractures. In mode-I loading, delamination resistance is initially developed by intrinsic properties of composites as the crack tip first interacts with matrix and matrix/reinforcement interface. Then, resistance to crack propagation is dominantly established by fibre bridging mechanisms [141,142]. On the other hand, mode-II fracture behaviour of composite laminates is highly dependent on matrix properties. [143,144]. Therefore, any improvements on matrix, fibre-matrix interface properties and fibre bridging mechanisms would contribute to the impact and post-impact properties of composite laminates.

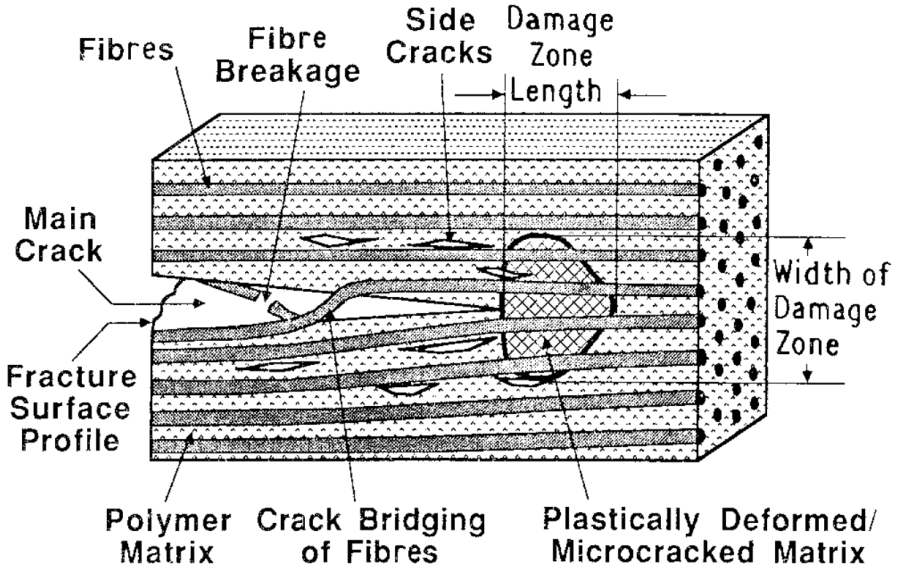

Figure 2. 18| A schematic illustration of micromechanisms of energy absorption during interlaminar fracture of unidirectional composites [140].

2.6. Strategies to Improve Interlaminar Fracture Toughness of Composite Laminates

Susceptibility of composite laminates to impact results in poor impact damage tolerance in structural composites because of primarily delamination failure, and the

behaviour of composite laminates under impact loading is related to mode-I and mode-II fracture properties as discussed in Section 2.3. In this section, the toughening strategies of fibre-reinforced composite laminates will be defined, and the advantages and disadvantages of each toughening method will be discussed.

2.6.1. Toughening with Textile Preform

The arrangement of fibre reinforcement significantly influences the mechanical properties of fibre reinforced composite material systems as transferring of fibre properties to composites is determined by geometry, distribution and tortuosity of the fibre paths [81]. Fibre reinforcement architectures can be categorised as unidirectional, two dimensional (2D) woven and three dimensional (3D) woven fabric [145].

Several studies demonstrated that 3D woven fabric composites present greater delamination resistance compared to 2D woven and unidirectional fabric composites because of the difficulty for cracks to propagate through the three-dimensional adjustment of reinforcement fibres in 3D woven composites [11–13,146]. Mouritz et al. [147] performed an extensive study to investigate the influence of 2D fabrics (*e.g.* braided and knitted) and 3D fabrics (lightly stitched, heavily stitched, orthogonally woven and layer-interlock woven) on the mode-I fracture behaviour of the fibreglass composites. The results of this study demonstrate that the fracture toughness properties of composites can significantly be enhanced with 3D fabric composites compared to unidirectional composites as shown in Figure 2. 19. The highest improvement was achieved from braided and knitted fabric composites due to extensive crack branching (*i.e.* the interlaminar crack was forced to follow a tortuous path through the complex fibre architectures, see Figure 2. 20).

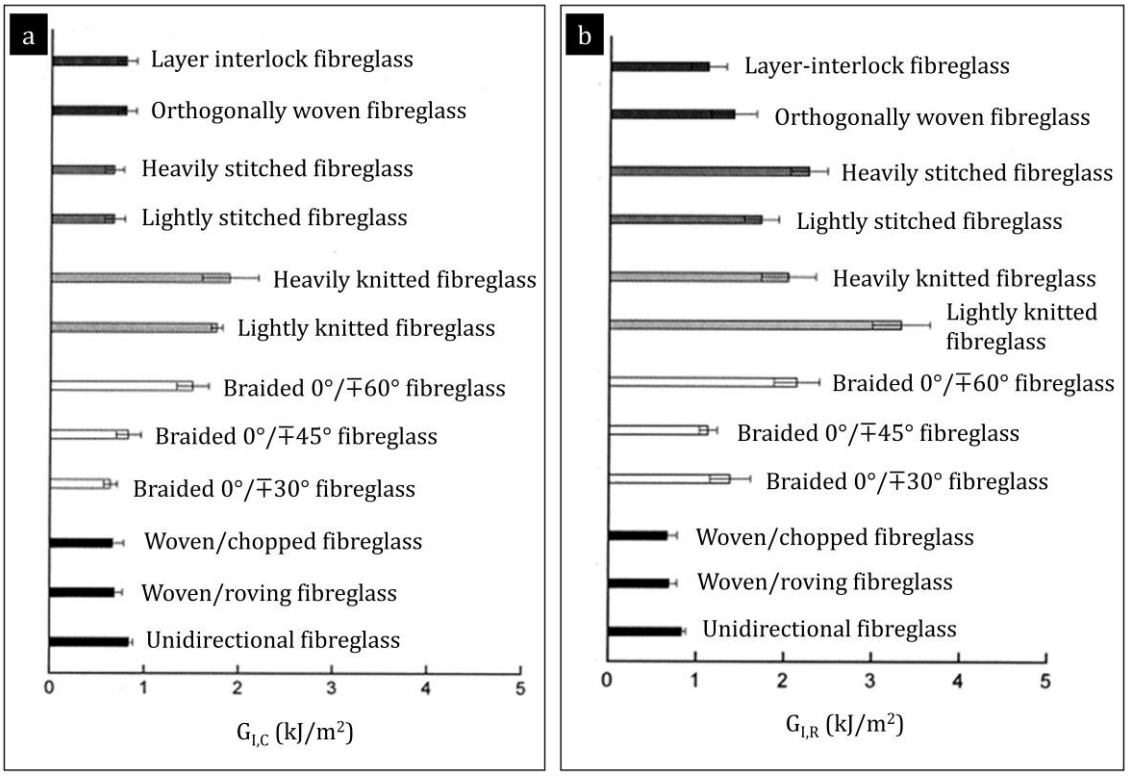

Figure 2. 19| (a) Initiation, *i.e.* $G_{I,C}$, and (b) propagation, *i.e.* $G_{I,R}$, interlaminar mode-I fracture energies of composite laminates based on a different type of fibre [147].

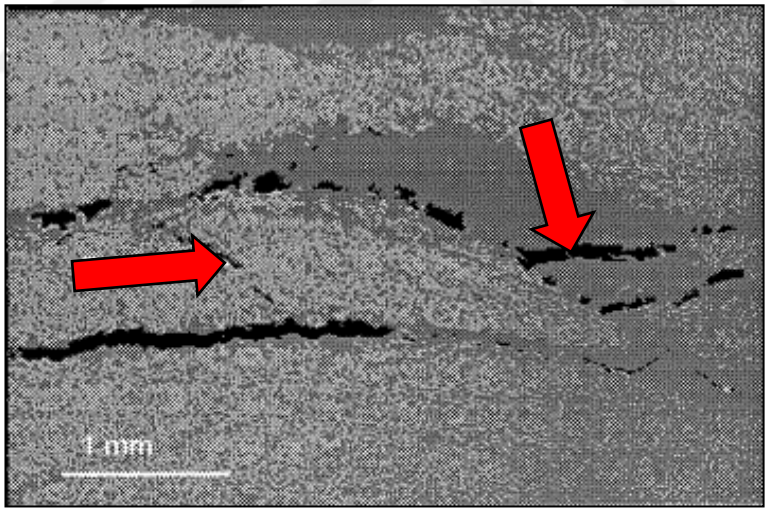

Figure 2. 20| The micrograph indicating an interlaminar crack propagation following a tortuous path in the braided fabric composite [147].

In a comparison of woven and unidirectional fibre composites, it can explicitly be said that woven fabrics composites provide better impact and damage tolerance with increased energy absorption capability compared to unidirectional fabric composites

with the reduction in impact damage by benefiting from yarn interlacement of woven fibre architectures[23,92]. However, relatively poor in-plane shear and reduced tensile and compressive properties of woven composites are their major drawbacks compared to unidirectional composite systems due to inadvertent geometric defects such as misalignment of in-plane fibres, the introduction of weak resin-rich pockets, lower fibre volume ratio [22,23,148].

2.6.2. Through-the-Thickness Reinforcement

The damage tolerance of composite laminates can be improved with through-the-thickness reinforcement methods such as stitching [149], z anchoring [17], and tufting [150,151]. Z-anchoring (*i.e.* microstructure of the composite laminate with z-pin reinforcement is shown in Figure 2. 21a) is the through the thickness reinforcement technique which can only be applied for pre-preg composites. Z-anchoring is applied by inserting a metal or fibrous pins into the uncured pre-preg stack acting as fine nails that lock the laminate plies together with a combination of friction and adhesion, with the help of a collapsible polymer foam carrier and air horn [17]. Experimental fracture studies demonstrated that z-anchoring can enhance the delamination resistance of composites in both mode-I and mode-II loading [18,19,152–154]. Fracture mechanisms of z-pinned composites responsible for energy absorption under mode-I loading are defined as breakage, debonding, and frictional pull-out of the z-pins, while those under mode-II loading are shear deformation, debonding, snubbing, and shear-induced pull-out of the z-pins [19,20,152,155–157]. Some studies also showed that Z-anchoring can provide improvement in impact damage tolerance of composite laminates by suppressing delamination failure due to bridging traction forces generated by the Z-pins [17,121]. However, the insertion of z-pins into composite laminates may generate some microstructural damage such as fibre crimping, fibre distortion, the cluster of broken fibres, fibre waviness and the presence of resin-reach zone as seen in Figures 2. 21b and -c [21].

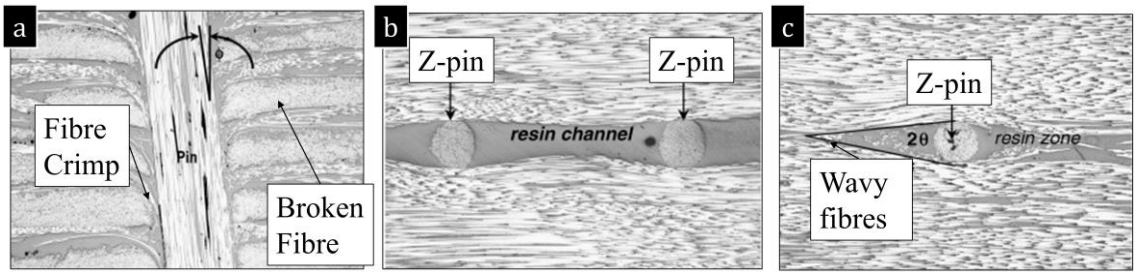

Figure 2. 21| The microstructural defects due to z-pin insertion in the composites: (a) fibre crimping and breakage, (b) presence of the resin-reach zone and (c) fibre waviness [17].

Stitching is the other type of through the thickness reinforcement technique which consists of sewing high tensile fibre thread through stacked dry or pre-preg layers to produce a 3D fibre preform [158]. Numerous studies demonstrate that the presence of stich patterns in the fibre stacks can significantly improve delamination resistance of composite laminates in mode-I and mode-II with the fracture mechanisms coming from stitch yarns such as interfacial debonding, slack absorption, fibre breakage, pull-out friction and stitch yarn ploughing through the matrix [15,159–161]. For example, Velmurugan and Solaimurugan [162] performed an experimental study to investigate the effect of Kevlar stitches on the fracture properties of the glass fibre reinforced composite laminates. It is reported that Kevlar stitch yarns increased the mode-I interlaminar fracture toughness of the composites from 0.580 kJ/m^2 to 9.394 kJ/m^2 as the stitch fibres underwent tensile breakage during the crack propagation phase as shown in Figure 2. 22.

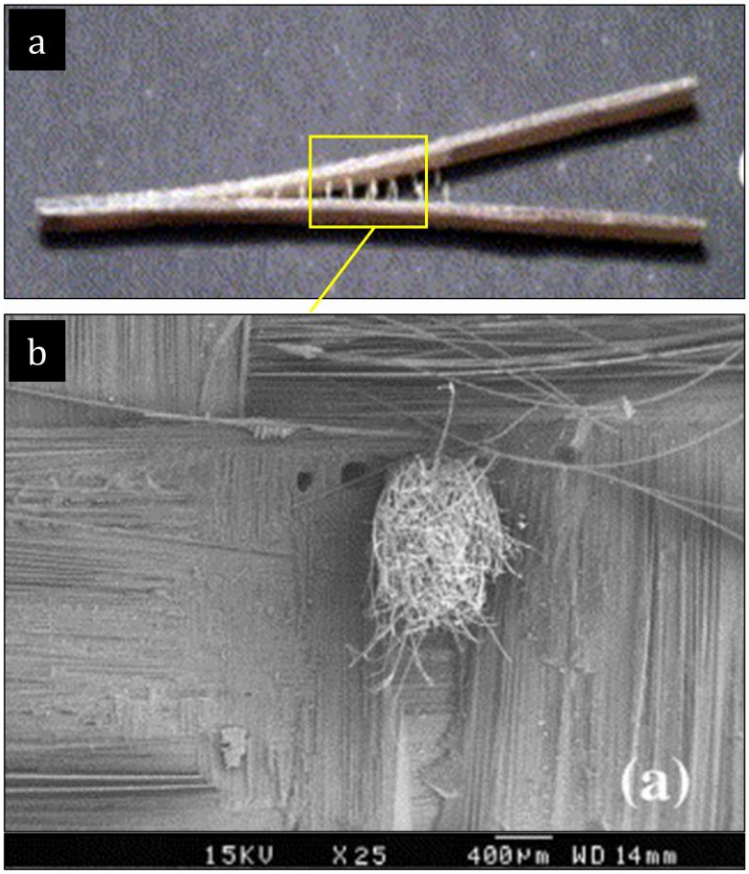

Figure 2. 22| The stitch fibres undergo tensile breakage in the fracture plane: (a) DCB specimen with the broken stitch fibres, (b) microstructure of stitch fibres [157].

Although transverse stitching is a promising method to toughen composite laminates, the penetration of needles into fabric stacks can generate some impregnation defects (*i.e*. in-plane fibre crimping, misalignment of in-plane fibres, distortion of through-thickness stitching threads and formation of resin pockets, see Figure 2. 23). These defects can act as a stress riser and reduce the in-plane strength and stiffness of composite laminates [14,24,25].

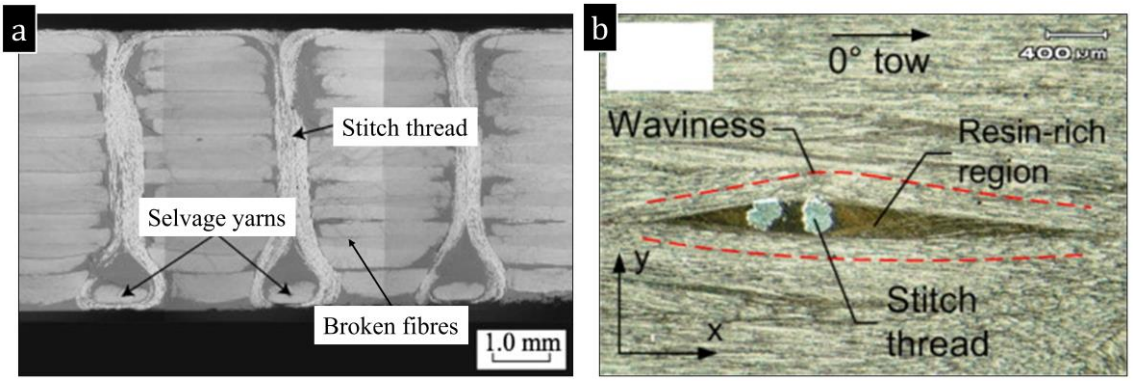

Figure 2. 23| The impregnation defects of stitching reinforcement: (a) broken fibres due to the presence of stitch yarns in the composites and (b) introduction of fibre bundle waviness and resin-rich zone [158,159].

Tufting, which is the process of the presence of loose loops staying in the position due to the natural friction between the fabric and the thread penetrated by a needle (see Figure 2. 24a), is also used as through-the-thickness reinforcement in the composite laminate [26,151]. Dell'Anno [165] performed an experimental study on 5 harness satin woven carbon fibre/epoxy composites tufted with glass threads and illustrated significant improvement in mode-I fracture energy of composite laminates with tufting threads by a factor of ~15 at the crack propagation phase. However, a drop-down in the ultimate tensile strength from 477 MPa to 430 MPa was reported because of resin pockets and impregnation defects due to the needle penetration (see Figures 2. 24b and -c).

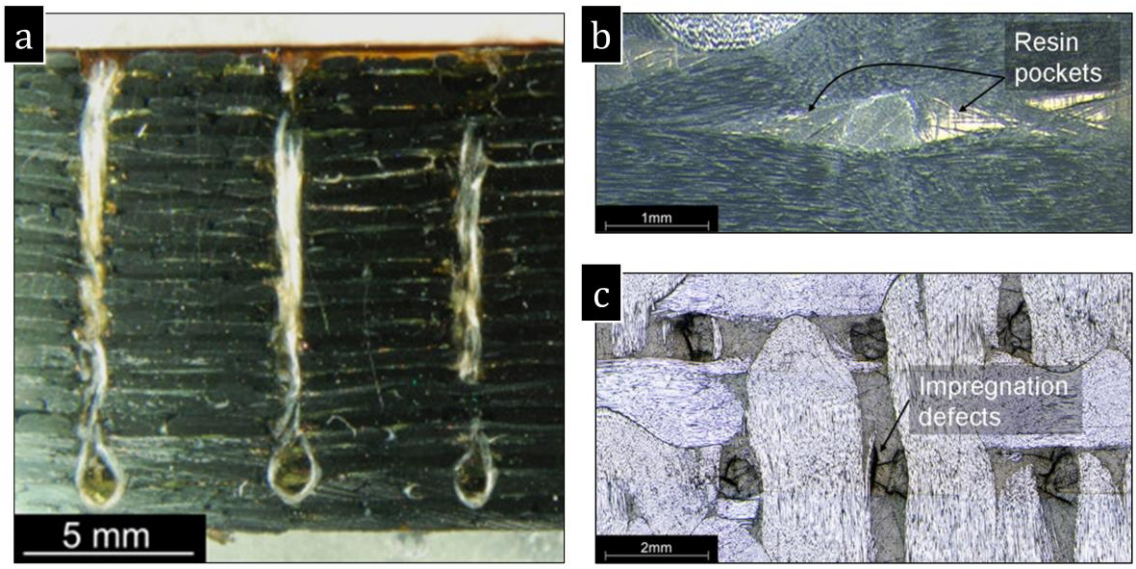

Figure 2. 24| (a) A composite laminate with tufting loops, (b) a resin pocket because of through-the-thickness loop presence and c) impregnation defects due to needle penetration [151,165].

2.6.3. Matrix Modification

Epoxy resins have been used as primary matrix material in structural applications due to their high strength, stiffness, thermal properties, and chemical resistance but intrinsically poor fracture toughness and impact resistance of epoxies due to high crosslinking density make epoxy-based composite laminates vulnerable to micro-cracks which can be introduced in-service loading and limits their applications [166–168]. In this regard, this section discusses the modification of epoxies with different types of fillers.

Improving crack growth resistance with rubbery particulate phase to overcome the brittleness of epoxy resins was first proposed by Sultan et al. in 1971 [169]. In liquid rubber toughening, the phase separation of reactive polymers occurs during the epoxy resin curing process. The cured elastomer modified epoxy resins include dispersed rubber domains (~0.1-5 μm) which are chemically bonded to the epoxy polymers [2]. As a consequence of liquid rubbery particle-phase modification of epoxy resins, improvement in fracture toughness of epoxies can be achieved by several orders of magnitude via cavitation of rubber particles (see Figure 2. 25) [170,171]. However, modification of epoxies with the addition of a liquid rubbery phase may result in a reduction in the glass transition temperature (T_g) of the epoxies because of incomplete phase separation of elastomers. Therefore, the second generation of rubber particles,

which is structured core-shell latex particles with a rubbery core and a thin layer of a glassy shell, have been proposed to overcome these drawbacks [28]. Using particles with core-shell structures provides better thermomechanical properties as shell structured particles do not bring incomplete phases in the matrix [31,38,172]. The other advantage of using core-shell rubber (CSR) particles for bulk resin modification is to control the size of rubber particles and volume fraction. The size of CSR particles influences the fracture properties of epoxy resins as large particles may lie outside the plastic zone while small particles can be cavitated within the plastic zone. For example, Pearson and Yee [30] performed a study to evaluate the influence of CSR particle size (*i.e.* ranging from 0.2 μm to 200 μm) on toughening mechanisms of epoxies. They reported that relatively large particles provide a modest improvement in fracture toughness of epoxies by particle bridging and crack deflection mechanisms as they are outside of the plastic zone (*i.e.* thus particles are not cavitated) while smaller particles significantly enhance the fracture toughness of epoxies by cavitating and the shear banding (*i.e.* initiated by cavitation) mechanisms. Similarly, Kim et al. conduct an experimental study on epoxies modified with CSR particles ranging in size from 0.16 μm to 1.2 μm [34]. They demonstrate that the highest fracture toughness is achieved using particles with the size of 0.4 μm. It is also reported that using particles smaller than 0.2 μm decreases the toughening effectiveness as small particles are hard to cavitate.

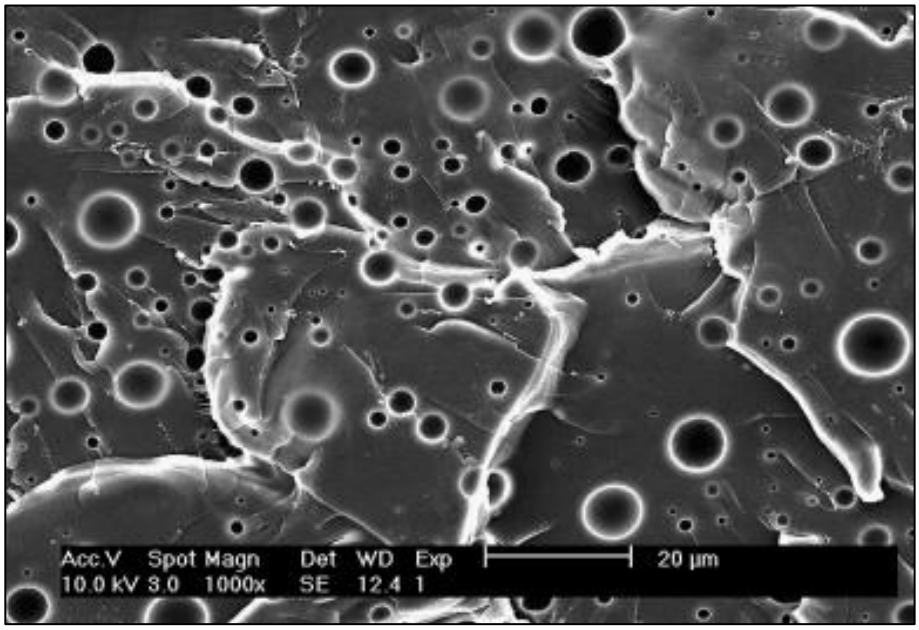

Figure 2. 25| The micrograph of the epoxy resin blended with rubber particles showing cavitation [170].

Thermoplastic particle toughening is another alternative way offering improvement in the fracture toughness of highly brittle epoxy resins [173–175]. Thermoplastic particles as modifiers can be preferred due to their ductility, thermal and chemical stability and high T_g [176]. The study conducted by Cahudhary et al. [177] explored the amine-functionalized poly(styrene) microspheres as a toughener for the epoxy resin. It is reported that G_I increased by ~33% with the use of 3% amino-poly(styrene) with the fracture mechanisms of crack pinning, crack bowing, microcracking, particle bridging, crack path deflection and particle yielding as shown in Figure 2. 26. In thermoplastic particle toughening, defining the weight ratio of thermoplastic particles takes high importance as explained in the study performed by Kinloch and Yuen [178]. In this study, polyether sulphone was added into a two-part brittle epoxy system and showed that thermoplastic incorporation up to 8 phr (parts per hundred rubber) dissolved in the epoxy and achieved no contribution to the crack growth resistance. Improvement in crack resistance from 75 J/m^2 to 500 J/m^2 with the ~100 phr concentration of the epoxy was provided when phase separation of particles is achieved with the incorporation of thermoplastic particles. Moreover, Park et al [179] showed that 15 wt% addition of polyethersulfone (PES) in the epoxy enhanced the fracture toughness of the final blend by ~20% due to the depression of crack growth upon formation of the branches by PES particles. However, complex manufacturing

processes with the use of hazardous solvents limit the application of thermoplastic modifiers as bulk resin tougheners [180,181].

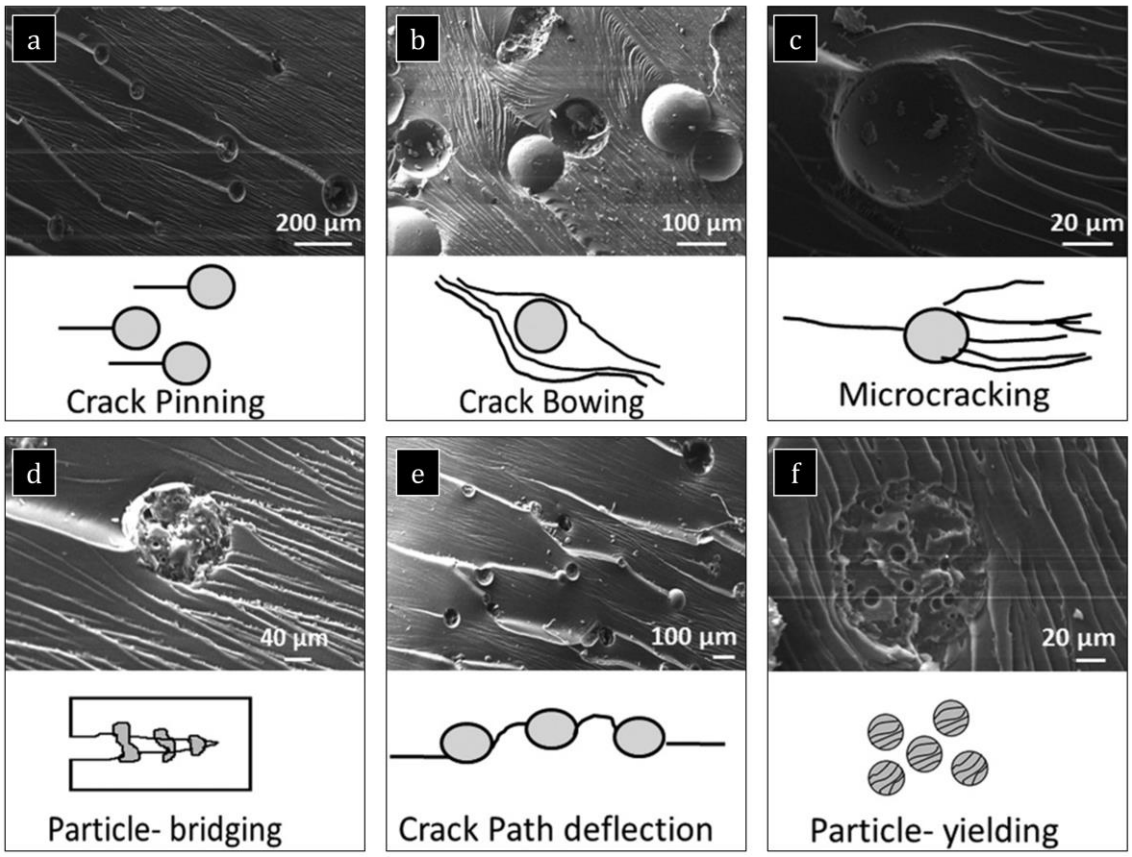

Figure 2. 26| Schematics of the underlying toughening mechanisms along with SEM images of fracture surface revealing (a) crack pinning, (b) crack bowing, (c) microcracking, (d) crack path deflection, (e) particle bridging, and (f) particle yielding [177].

Researchers have also paid significant attention to enhancement in fracture toughness of epoxies using nano-sized particle fillers such as silica particles and carbon nanotubes (CNT) due to the unique mechanical properties of these fillers [182,183]. Nano-size filler can be distinguished into three groups depending on dimensions: a) nano-particulate fillers (*e.g.* silica nanoparticles [184], alumina particles [185]) b) nano-fibrous fillers (*e.g.* CNTs [186,187]) and c) single or multiple nanolayer fillers (*e.g.* nano clays [188,189]). Each type of fillers contributes to the fracture resistance of epoxy resins with different failure mechanisms. For nano-particulate materials, debonding of nanoparticles and subsequent plastic void growth are the mechanisms which can provide improvement in the fracture properties of epoxies [190]. For nano-

fibrous materials, nano-fibrous bridging can increase fracture toughness by suppressing the growth of nanopores and crack growth propagation [191]. Also, pulled-out nanotubes with high interface might lead significant increase in fracture energy [192]. For nanolayered fillers, the main toughening mechanism is identified as massive micro-cracks which cause stress concentration and increase fracture surface due to crack deflection [193]. However, achieving homogeneous nanofiller dispersion is a major obstacle because nanofillers with a high specific surface area may encourage the formation of agglomeration due to intermolecular interactions such as van der Waals forces [192,194,195].

2.6.4. Interlaminar Thermoplastic Veil Toughening

Interlaminar thermoplastic veil toughening is a method of introducing tough, ductile polymers or adhesive at the fibre interface as an additional layer [42,50]. Interleaving of thermoplastic veils between fibre layers offers an affordable toughening route [47,49,196], and also does not complicate the manufacturing route. For example, veils with their fibrous structures do not restrict resin flow and do not influence resin properties such as T_g [197–199].

Interlaminar thermoplastic veil toughening based on either nano- or micro-scale fibre can significantly enhance interlaminar fracture toughness (ILFT) of composite laminates under mode-I and mode-II loading [27,43–48,54]. Fibre bridging via thermoplastic veils, associated with progressive fibre debonding and pull-out, is a promising toughening mechanism. Areal weight is an adjustable parameter in the interlaminar toughening via thermoplastic veils and significantly influences the toughening performance of veils [27,48–50]. For example, the study performed by Ramirez [49] indicates that interlaying veils with higher areal weight leads to a higher increase in the interlaminar fracture energies of laminates until a certain value (~30 g/m^2) is reached. Quan et al. [48,50] performed experimental studies for mode-I and mode-II fracture energy of composite laminates using different types of micro-veils (*e.g.* Polyethylene-terephthalate (PET), Polyphenylene-sulfide (PPS) and Polyamide-12 (PA)) in varying areal weights from 5 g/m^2 to 15 g/m^2 and inserted them in the carbon fibre reinforced composite laminates with different fibre architectures (*e.g.* unidirectional prepreg, 5 harness prepreg and non-crimp fabric). In these studies, an increase in fracture energy with increasing areal weight is observed. Similarly,

Beylergil et al. [27,46] interleaved carbon fibre epoxy laminates with electrospun Polyamide 6,6 (PA66) nano veils with an areal weight of 0.525, 1.05, 17 and 50 g/m^2. They found that the G_{IC} of composite laminates increased by ~24% using nano veils with ~0.525 g/m^2, and by ~737% with interleaving nano veils with 50 g/m^2. The material type of veils can also affect the performance of interlaminar thermoplastic veil toughening. For example, Beckerman and Pickering [43] investigated the performance of various electrospun nanofiber (*e.g.* Polyamide 6'6 (PA66), Polyvinyl butyral (PVB), Polycaprolactone (PCL), Polyethersulfone (PES) and Polyamide-imide (PAI)) on interlaminar toughness of prepreg composite laminates and showed that PA66 interleaved laminates performed better by ~156% in G_I and 69% in G_{II} as PA66 have a higher elongation to break properties compared to another type of veils. Also, the study conducted by Quan et al. [48] using micro veils confirms that different type of veils influences the toughening of performance of thermoplastic veil toughened laminates.

Moreover, the interaction between veils and host materials (*e.g.* resin and fibre prepreg or preform) is a parameter directly affecting the toughness improvement by changing the fracture mechanisms in veil-toughened laminates. Quan et al. [55] enhanced the veil/epoxy adhesion with the ultraviolet-irradiation technique and found that improving the interface between matrix and thermoplastic veil in NCF composite laminates resulted in an increase in both mode-I and mode-II properties because the bonded interface of the veils influenced the energy dissipation behaviour of the laminates and resulted in additional carbon fibre and PPS fibre bridging mechanisms during fracture process. In another study performed by Quan et al. [56], enhancement in the interface between matrix and veils was increased by doping multi-walled carbon nanotubes (MWCNT) on veils. It is reported that further enhancement was provided by doping a small amount of MWCNTs with an additional interaction coming from MWCNTs such as MWCNT pull-out and breakage between thermoplastic veil and epoxy, thus relatively improved interface absorbed more energy with fracture mechanisms.

As mentioned above, thermoplastic veil interleaving with nano- or micro-fibres is a cost-effective and promising toughening method for composite laminates. Veils with nano-size fibres allow the interface to accommodate more fibres without increasing the thickness of composite laminates and nanofiber interleaving can provide significant improvement in the fracture properties of composites without hardly

affecting their in-plane properties of them [46]. However, the production of veils with nano-size fibres via the electrospinning technique is a complicated process. For example, the use of highly hazardous and volatile chemicals needs to be carefully considered as these chemicals create health and safety issues [200]. The production of electrospun nanofibers with uniform diameter and thickness is another critical concern as the diameter and thickness of electrospun nanofibers are the parameters influencing the toughening performance of nanofiber interleaved laminates [43,201]. Also, producing uniform nanofiber interlayers requires a long time and clogging or blockage of the nozzles is another problem because of the solidification of polymeric solutions during the manufacturing process. The clogging of the nozzles can cause the loss of stability, which results in non-uniform dispersion in the thickness and diameter of nanofibers. In comparison to nanofibers, production of non-woven thermoplastic veils based on micro-fibres via wet-laid web formation technique (*i.e.* can be easily applied for commercial production) is cost-effective and there is a large number of suppliers in the market [202]. However, micro-fibre veil interleaving with dense areal weight might affect in-plane properties due to a reduction in reinforcing fibre volume fraction. For example, PA66 veils based on microfibres were interleaved with the areal weight of 17 g/m^2 and 50 g/m^2 in the study performed by Beylergil. It was reported that ~349% and ~718% improvement in G_{IC} and G_{IR}, respectively, was achieved using veils with 50 g/m^2. In addition, interleaving PA66 veils with 17 g/m^2 provided enhancement by ~84% and ~171% in G_{IC} and G_{IR}, respectively. The investigations on in-plane mechanical properties in this study showed that interleaving veils with an areal weight of 50 g/m^2 reduced tensile modulus by ~30% while that was ~10% for the veils with 17 g/m^2. On the other hand, Garcia-Rodriguez performed an experimental study using co-polyamide veils with 4 g/m^2 areal weight and demonstrated that improvement in G_I by ~200% was achieved with no substantive compromise in the in-plane properties of carbon-epoxy laminates [51]. Thus, the selection of areal weight is a prominent parameter in thermoplastic veil toughening, especially for microfibre based veils with dense areal weight.

2.7. Conclusions

Chapter 2 reviews the literature and draws conclusions below:

- Composite laminates with prepreg fabrics can achieve high mechanical properties. However, the need of high-cost equipment for manufacturing and storage conditions of prepreg fabrics generate high cost. Cost-effective composite laminates can be manufactured with preform fabrics and low-viscous epoxies with vacuum-assisted resin infusion and out-of-autoclave curing.
- Significant improvement can be achieved with 3D-fibre reinforcement (*i.e.* weaving) through the thickness reinforcements (*e.g.* z-pinning, stitching, and tufting). However, these reinforcement methods generally reduce the in-plane properties of composite laminates because of impregnation effects (*e.g.* fibre crimping, fibre breakage and misalignment)
- Bulk resin and thermoplastic veil offer cost-effectiveness over 3D-fibre and through the thickness reinforcements reinforcement methods and these toughening approaches can be applied easily with vacuum resin infusion.
- Core-shell rubber particles can significantly improve the delamination resistance of epoxies and composite laminates. However, blending the secondary phase in epoxies can increase the viscosity of the mixed resin system and brings complications for achieving void-free laminate. Therefore, the volume fraction of core-shell rubber particles carefully needs to be selected.
- Interlaminar thermoplastic veil toughening can significantly improve delamination resistance by introducing fibre bridging mechanisms at an interface for composite laminates, especially for the low-delamination resistant composite laminates such as unidirectional composites. This toughening technique is easy to apply and does not require modifications in manufacturing. However, the presence of veils can increase the thickness of laminates and cause a reduction in in-plane properties. Therefore, the areal weight of veils carefully needs to be selected, especially for microfibre veils.

The literature review here manifests that thermoplastic veil toughening can significantly improve the delamination resistance of composite laminates. However, an increase in thickness due to the presence of veils at interlaminar regions can reduce the in-plane properties of composite laminates. In this regard, this study proposes the

hybrid use of thermoplastic veils and core-shell rubber particles together to provide further enhancement in delamination resistance, low-velocity impact and post-impact responses of laminates by using veils with low areal weight without considerable reduction in in-plane properties of laminates.

CHAPTER 3: Methodology

3.1. Introduction

This chapter provides an insight into the material system and the experimental details used in this study to characterise the delamination resistance and low-velocity impact behaviour and impact damage tolerance of the manufactured composite laminates. First, the material system and manufacturing method applied in this study are introduced. Then, the methods used to characterise the interlaminar fracture toughness for the composite laminates in this study are described. After that, the drop-weight impact tests and compression after impact test protocols are presented. Also, the fracture surface observation with scanning electron microscopy and non-destructive test performed to detect impact damage are explained.

3.2. Materials

The base composite laminates chosen for this study are a combination of two-part low viscous epoxy resin and carbon fibre non-crim fabric (NCF) preform. The epoxy resin used as matrix material is a blend of Araldite LY564/Aradur 2954 (epoxy/hardener) with a mix ratio of 100:35 by weight supplied by Hunstman, see Table 3. 1 for the mechanical properties of Araldite LY564/Aradur 2954 mixed resin. The reinforcement phase is a unidirectional carbon fibre non-crimp fabric (NCF) preform supplied from the Saertex with a total areal weight of 314 g/m^2 (*i.e.* consists of 300 g/m^2 carbon fibre tows, 11 g/m^2 stabilizing E-glass fibre bundles and 3 g/m^2 polyester non-structural stitching thread) as shown in Figure 3. 1.

Table 3. 1| Mechanical properties of Araldite LY564/Aradur 2954 blend with a mix ratio of 100:35 released by the supplier.

Properties	Araldite LY564/Aradur 2954
Mixed Resin Viscosity	500-700 MPa s at 25 °C
Glass Transition Temperature	150-153 °C
Fracture Toughness	0.69-0.76 MPa√m
Fracture Energy	149-181 J/m^2

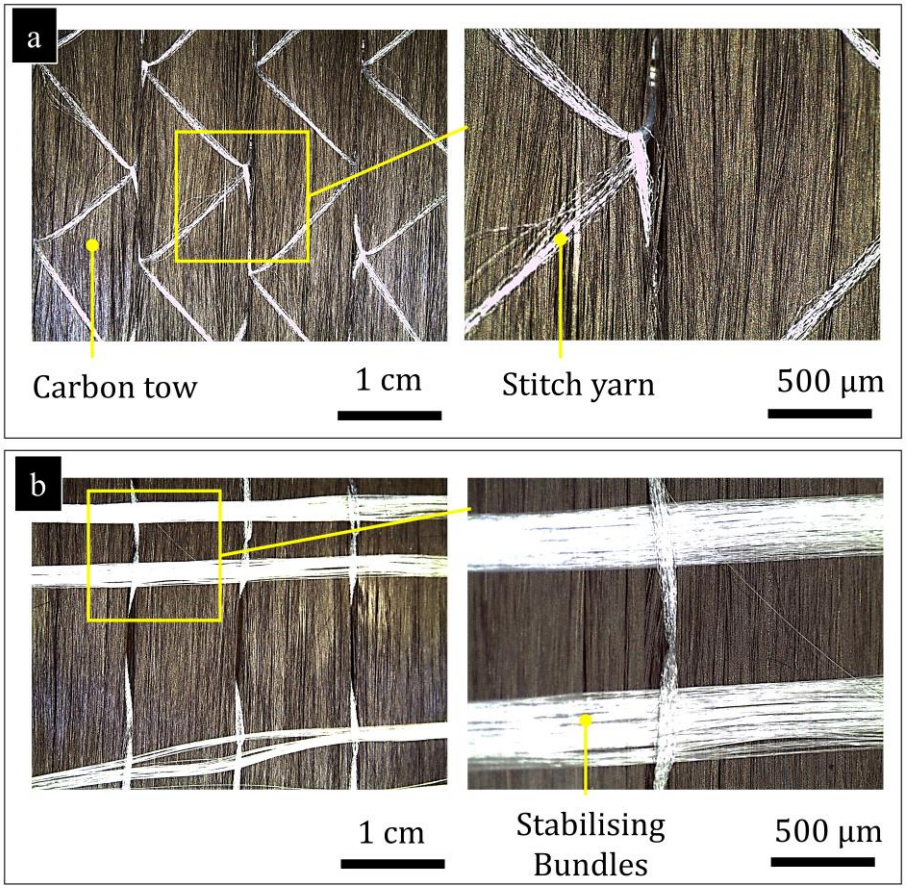

Figure 3. 1| The digital images indicating carbon fibre NCF fabric taken from (a) front and (b) back faces.

Composite laminates were toughened with thermoplastic veils and core-shell rubber particle (CSR) content. Core-shell rubber particle toughener used in this study is Albidur EP 2240 A (with 40 wt% near-spherical particles with a polysiloxane core and diameters ranging from 100 nm to 3 µm in Bisphenol A diglycidyl ether) supplied from the Evonik (Germany). Polyetherimide (PEI) and Polyphenylene sulphide (PPS) microfibre veils were supplied by Technical Fibre Products. The binder of the PEI (with

a nominal areal weight of 10 g/m^2) and PPS (with a nominal areal weight of 5 g/m^2 and 10 g/m^2) veils are cross-linked polyester and cross-linked styrene acrylic binder, respectively. The microstructural features obtained from 10 g/m^2 PEI and PPS veils are shown in Figure 3. 2. The average diameter of the thermoplastic veils was defined using micrographs obtained from different locations of the veils by neglecting fibre intersections and overlaps (*i.e.* the diameter of 100 individual fibres was measured using ImageJ software). Then, the specific surface area (S_f) of the veils was calculated using Equation 3. 1, where ρ_f is the fibre density and d_f is the fibre diameter.

$$S_f = \frac{4}{\rho_f d_f} \qquad \text{Equation 3. 1}$$

The physical properties of the veils are given in Table 3. 2. Both PEI and PPS fibres are 6 mm in length. When compared to non-woven veils with 10 g/m^2, the measured diameter of PPS fibres (9.19 μm) is relatively smaller than the diameter of PEI fibres (13.74 μm). Therefore, the specific surface area of PPS fibres is significantly higher than that of PEI fibres. The specific surface area of the 10 g/m^2 PEI and 10 g/m^2 PPS veils were measured as 227 m^2/kg and 322 m^2/kg, respectively. The micrographs of the PEI and PPS veils are compared in Figure 3. 2. This figure exposes the denser fibre network of the PPS veils compared to the PEI veils.

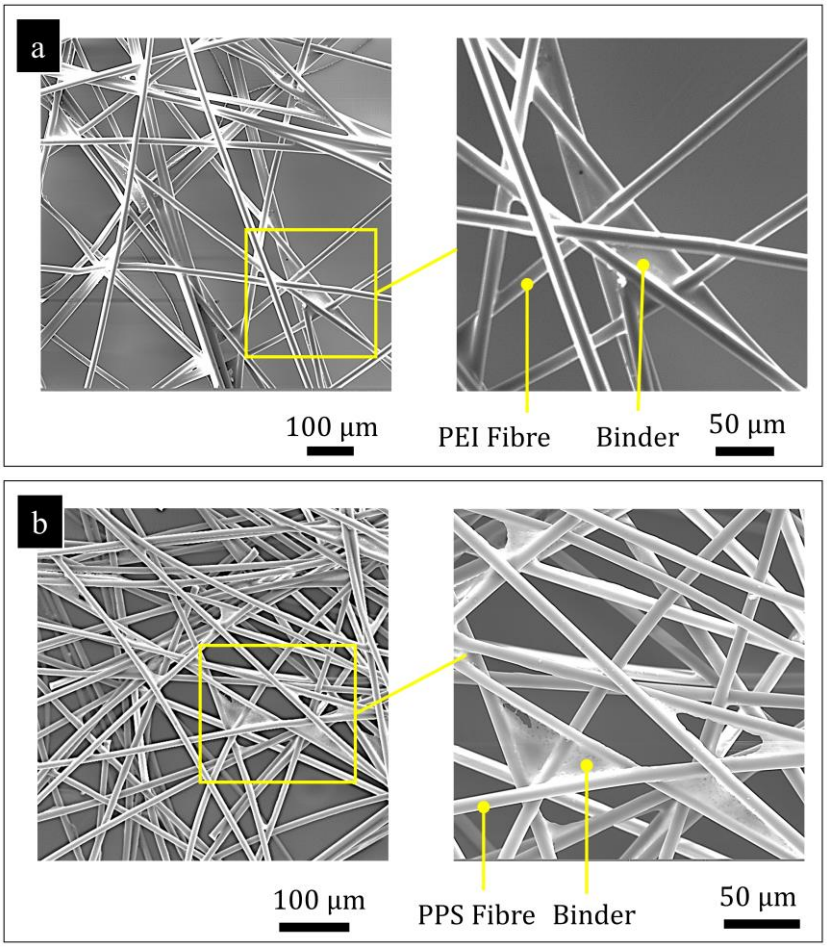

Figure 3. 2| The micrographs of the (a) PEI veil and (b) PPS veil with 10 g/m² areal weight.

Table 3. 2| The physical properties, dry veil thickness, fibre density (ρ_f), individual fibre length, average fibre diameter (d_f) and specific surface area (S_f) of the PEI and PPS non-woven veils.

Veil material	Dry veil thickness (µm)	ρ_f (kg/m³)	Fibre length (mm)	d_f (µm)	S_f (m²/kg)
PEI (10 g/m²)	76.3 ± 1.00	1280	6	13.74 ± 1.04	227.44
PPS (10 g/m²)	65.7 ± 2.98	1350	6	9.19 ± 0.98	322.41
PPS (5 g/m²)	40. 4 ± 2.13				

3.3. Composite Manufacturing

Composite laminates with/out toughеners were manufactured with vacuum-assisted resin infusion at room temperature and out-of-autoclave curing in this study. The prepared mould for vacuum-assisted resin infusion is indicated in Figure 3. 3. Toughened laminates were manufactured with 5 wt% CSR particle content (CSR5), 10 wt% CSR particle content (CSR10), 10 g/m^2 PEI veil (PEI10), 10 g/m^2, 15 g/m^2 and 20 g/m^2 PPS veil (PPS10, PPS15 and PPS20, respectively) and the use of 10 wt% CSR particle content and 20 g/m^2 PPS veil together (hybrid). A stack of carbon fibre NCF fabrics (with an orientation of $[0^0]_{10}$ for interlaminar fracture toughness tests and $[0^0/90^0]_2/0^0{}_2/[90^0/0^0]_2$ for low-velocity impact and compression after low-velocity impact tests) was used to manufacture the laminates. Thermoplastic veils were located at the symmetry plane for the fracture toughness test specimens and each interlaminar region of carbon fibres for the low-velocity impact and compression after impact tests. Only one layer of PPS veil was used for the laminates with 10 g/m^2 PPS veils. To achieve laminates with 15 g/m^2 PPS veils, one layer of 5 g/m^2 PPS veil and one layer of 10 g/m^2 PPS veil were located at the same interlaminar region. To achieve laminates with 20 g/m^2 PPS veils, two layers of 10 g/m^2 PPS veil were located at the same interlaminar region.

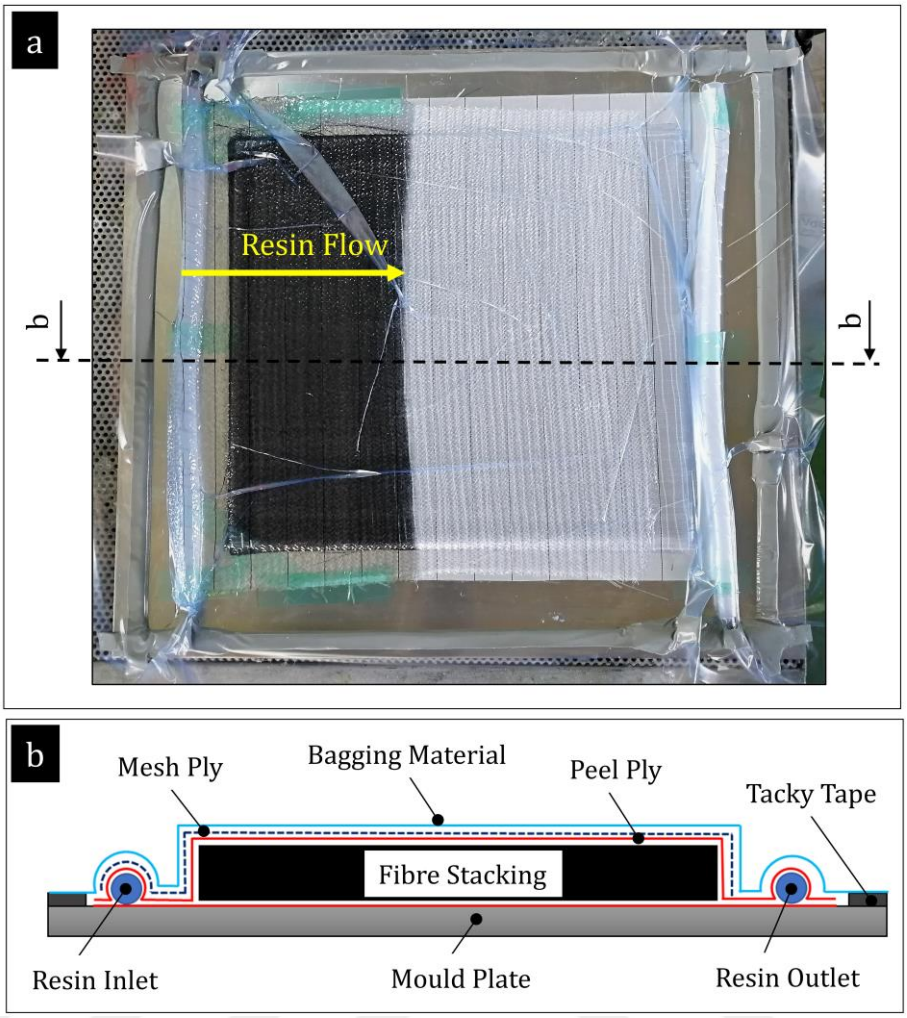

Figure 3. 3| Composite laminate manufacturing with vacuum resin infusion: (a) vacuum bag layup and (b) a schematic indicating the whole setup, *i.e.* resin infusion pipes, fibre stacking, peel ply, mesh ply and bagging material, placed on a flat mould.

The resin preparation phase is schematically indicated in Figure 3. 4. For incorporating CSR particles into the two-part epoxy resin system, Araldite 564 epoxy and Albidur EP 2240 A (with 40% concentration in DGEBA) were measured and mixed in a clean container, then sonicated in an ultrasonic water bath at 38 kHz and 50 °C for 30 minutes to achieve a homogenous distribution of the CSR particles in the epoxy. Followingly, Aradur 2954 hardener (with a 1:0.35 mix ratio) was added into the blend of the Araldite 564 and Albidur EP 2240 A and the final resin blend was mixed manually. For example, 155 g of Albidur 564, 70 g of Aradur 2954 and 75 g of Albidur EP 2240 A were mixed to obtain a modified resin mixture of 300 g with 10 wt% CSR particle content. Subsequently, the final resin mixture was degassed in a vacuum at -100 kPa for 30 minutes before resin infusion. Composite laminates were cured in an

oven using recommended cure cycle by the resin supplier: heating from room temperature (~20 °C) to 80 °C with 1 °C/min rate for 1 hour, dwell at 80 °C for 2 hours, heating from 80 °C to 140 °C with 1 °C/min rate for 1 hour, dwell at 140 °C for 8 hours, then cooled down to room temperature as seen in Figure 3. 5. After the curing was completed, the manufactured laminates were sectioned into the desired dimensions with a Compcut 200 CNC plate saw.

The laminates were aimed to be manufactured with cost-effective strategy as abovementioned. With the manufacturing route applied in this study, the homogenous distribution of the CSR particle content was successfully achieved as seen in Figure 3. 6.

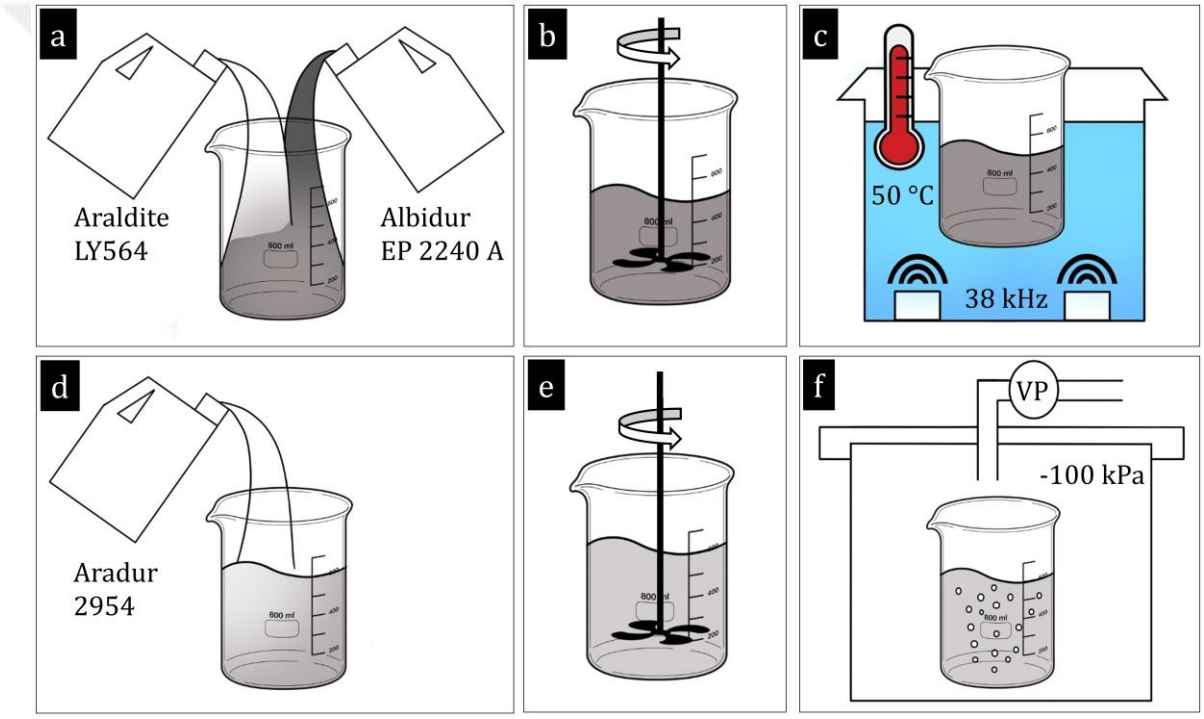

Figure 3. 4| A schematic showing the resin preparation process: (a) blending of the epoxy (Araldite LY564) with the CSR particle content (Albidur EP 2240 A), (b) mechanical mixing of the blend, (c) sonication of the blend with an ultrasonic water bath at 38 kHz and 50 °C for 30 minutes, (d) adding hardener (Aradur 2954) in the blend, (e) mechanical mixing of the final blend and (f) degassing of the resin mixture at 100 kPa vacuum pressure for 30 minutes.

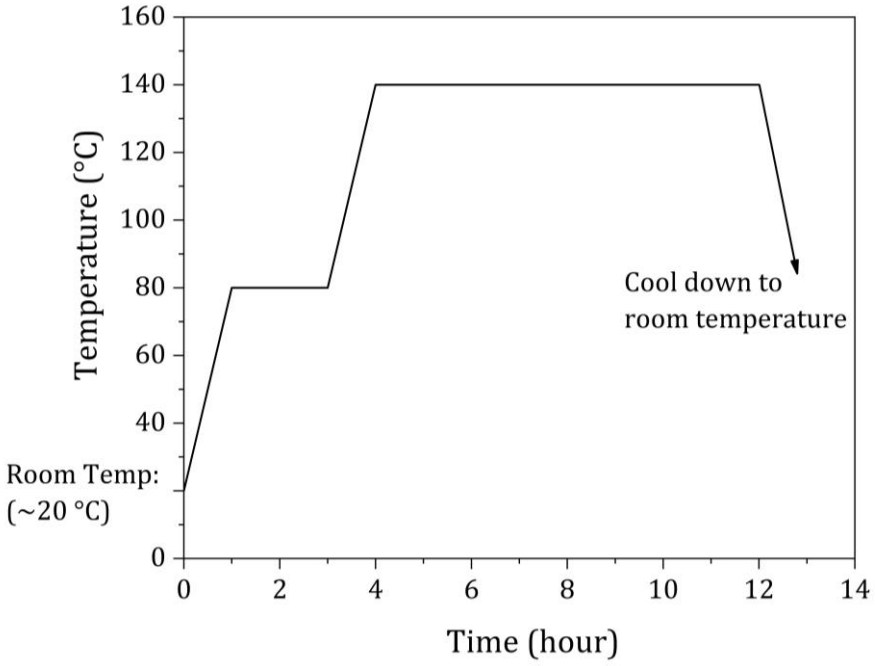

Figure 3. 5| The cure cycle of the epoxy resin system, *i.e.* heating for 1 hour at 80 °C with 1 °C/min rate, dwelling for 2 hours at 80 °C, heating for 1 h to 140 °C with 1 °C/min rate, dwelling 8 hours at 140 °C, and cooled down to room temperature (~20 °C).

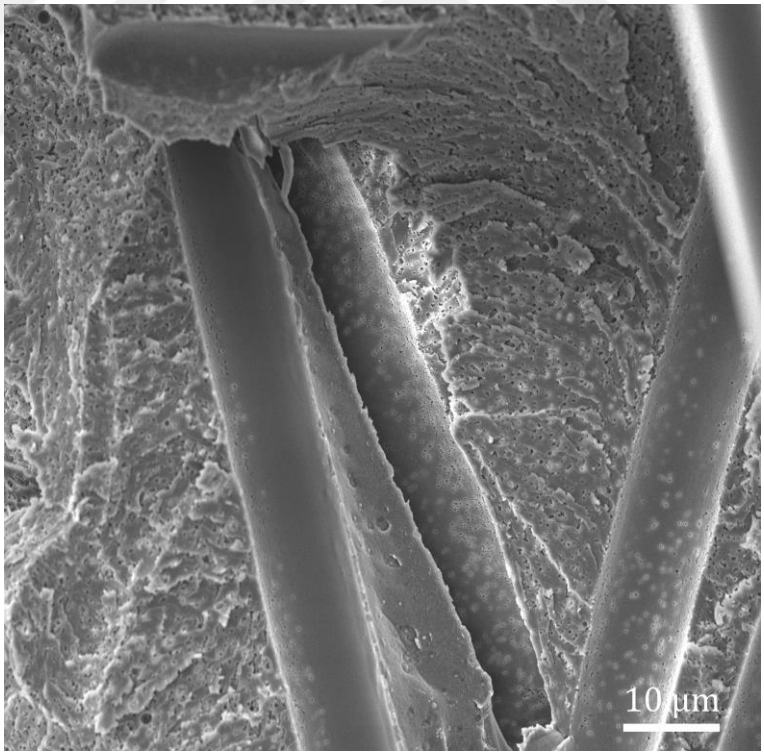

Figure 3. 6| The micrograph indicating the homogenous distribution of the CSR particles on the fracture surface obtained from the hybrid toughened laminate.

3.4. Interlaminar Fracture Toughness Testing

The mode-I and mode-II fracture toughness energies of the composite laminates were characterised as described in Section 3.4.1. and 3.4.2.

3.4.1. Mode-I Interlaminar Fracture Toughness Testing

The mode-I interlaminar fracture energies (G_I) of the composite laminates were measured with double cantilever beam (DCB) testing according to ASTM D-5528 [203]. Figure 3. 7 indicates the experimental test setup, a schematic indicating the dimensions of the test samples and the stacking sequence used for composite manufacturing for DCB test specimens. A release film (*i.e.* Ethylene tetrafluoroethylene (ETFE) film with a thickness of ~10 μm) was inserted at the symmetry plane of the laminates (with the dimensions of 180 mm x 25 mm x ~3.5 mm) to introduce pre-crack with a length of 55 mm in the composite laminates during the lay-up process. For the thermoplastic veil and hybrid toughened composite laminates, thermoplastic veils were interleaved at the mid-plane after the release film. The loading hinges were also bonded on the specimen using Araldite 2000+ structural adhesive. Then, the sides of the manufactured composite laminates were coated with a white marker and a scale was marked every 1 mm for 55 mm. The DCB tests were performed using three specimens for each batch at a crosshead speed of 5 mm/min using for loading and 25 mm/min for unloading with an Instron 5969 universal mechanical testing machine and crack tip propagation was observed using a glass magnifier from the coated side of the DCB specimens. During the manufacturing of the laminates, a resin pocket was introduced due to the presence of the film insert and the presence of a resin pocket leads to the existence of a blunt crack tip. Therefore, a sharp pre-crack of approximately 3 mm in length to represent the cracks that occurred in structural applications was generated in order to extend the resin pocket at the behind of the film insert for each specimen before DCB tests. After a sharp pre-crack was generated, the DCB tests were performed.

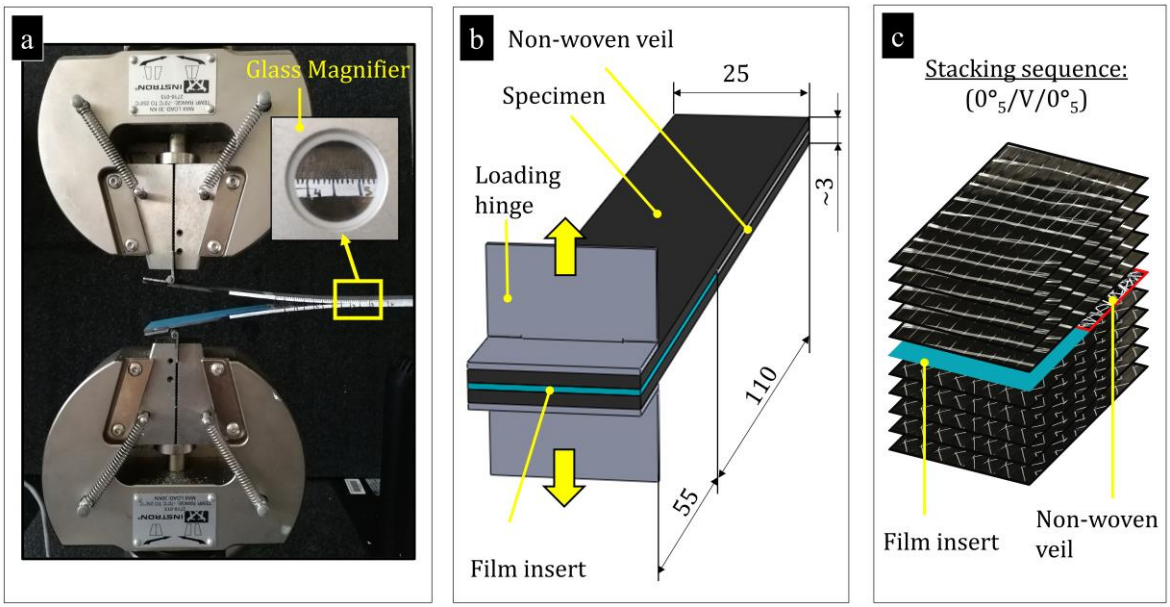

Figure 3. 7| Mode-I ILFT test procedure: (a) the experimental test setup indicating DCB test specimen and the glass magnifier used to follow crack tip, (b) a schematic indicating the standard DCB test specimen dimensions and (c) the details of the laminate stacking (Note that V indicates the veils. The schematic only demonstrates 1 layer of veils. The composite laminates with PPS veils were manufactured with three different areal weights, *i.e.* a layer of 10 g/m^2 PPS veil was inserted for the laminates toughened with 10 g/m^2 PPS veil laminates, a layer of 10 g/m^2 and 5 g/m^2 PPS veils were inserted together for the laminates toughened with 15 g/m^2 PPS veil, 2 layers of 10 g/m^2 PPS veil were inserted together for the laminates toughened with 20 g/m^2 PPS veil laminates. Also, all dimensions are in mm).

The mode-I fracture energies of composite laminates can be measured with three different methods (*e.g.* a compliance calibration (CC), a modified compliance calibration (MCC) and a modified beam theory methods (MBT)) as mentioned in ASTM D-5528 [203]. The round-robin test conducted to evaluate data reduction methods demonstrated that mode-I fracture energies calculated with the different methods differed only by 3%, thus none of these methods is superior to the other ones [204]. This study indicates that the MBT method yielded more conservative values of G_I for 80% of the specimens tested and ASTM D-5528 recommends the use of the MBT method. Depending on the MBT method, the G_I of composite laminates with DCB testing according to ASTM D-5528 is calculated as shown below:

$$G_I = \frac{3P\delta}{2b(a + |\Delta|)}$$ Equation 3. 2

Using Equation 3. 2, where P is the load, δ is the displacement, b is the specimen width, a is the crack length and Δ is the crack length correction factor. Δ is derived from the slope of the cubic root of the compliance (*i.e.* $C^{1/3}$, where $C = \delta/P$) as a function of crack length as illustrated in Figure 3. 8.

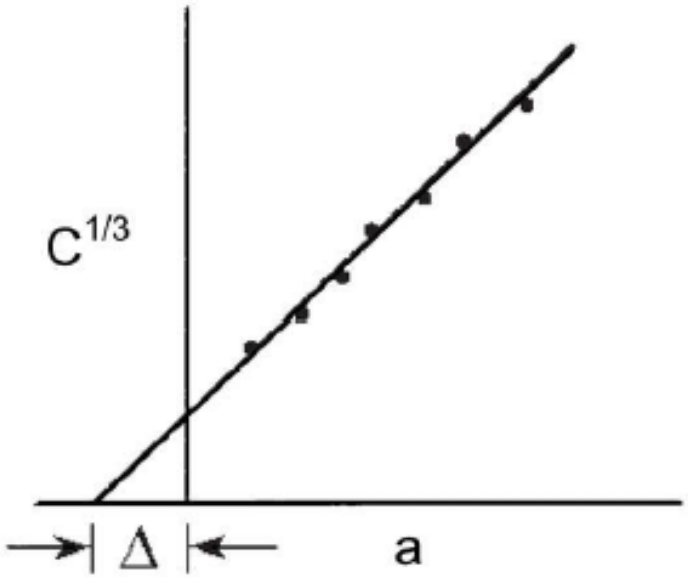

Figure 3. 8| Detection of the crack length factor with a curve derived from the slope of the cubic root of the compliance (*i.e.* $C^{1/3}$, where C = δ/P) as a function of crack length [199].

According to ASTM D-5528, initiation or onset fracture energies ($G_{I,C}$) can be calculated based on three different approaches, *e.g.* deviation from linearity (NL), visual observation (VIS) and 5 % offset/maximum load (5 %/Max) as seen in Figure 3. 9. The NL value for $G_{I,C}$ is calculated from the load-displacement curve at the point of deviation from linearity. The NL approach accepts that the crack tip starts to propagate from the insert in the interior of the specimen at this point and NL represents a lower bound value for $G_{I,C}$ compared to VIS and 5 %/Max approaches. VIS value for $G_{I,C}$ is determined using the load-displacement values at which the delamination is visually observed to grow from the insert on either edge using the microscope. $G_{I,C}$ value obtained using the 5%/Max approach is calculated by determining from the intersection of the load-deflection curve, once it has become nonlinear with a line drawn from the origin and

offset by a 5% increase in compliance from the original linear region of the load-displacement curve. If the intersection occurs after the maximum load point, the maximum load is used to calculate this value.

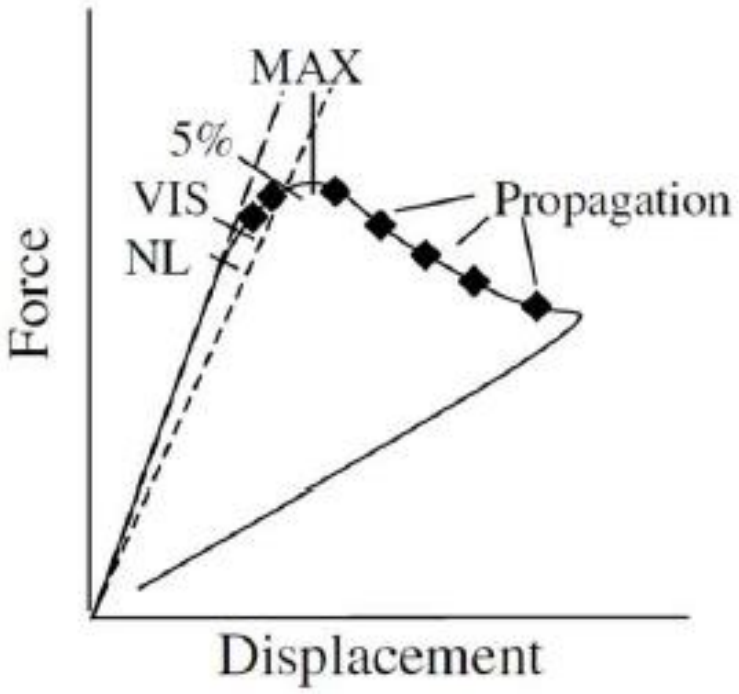

Figure 3. 9| Defining the initiation fracture energy using three different approaches, *e.g.* deviation from linearity (NL), visual observation (VIS) and 5 % offset/maximum load (5 %/Max) from a force-displacement curve [199].

The initiation mode-I fracture energies were calculated with 5%/Max approach and those demonstrate the fracture energies required to initiate the crack. The propagation mode-I fracture energies are the mean values of the linear region of R-curves (*i.e.* with crack extension between 25 mm and 55 mm in this study) and those represent the fracture energy required for initiated cracks to propagate. Figure 3.10 indicates the initiation point and steady-state region in R-curves obtained from laminates under mode-I loading.

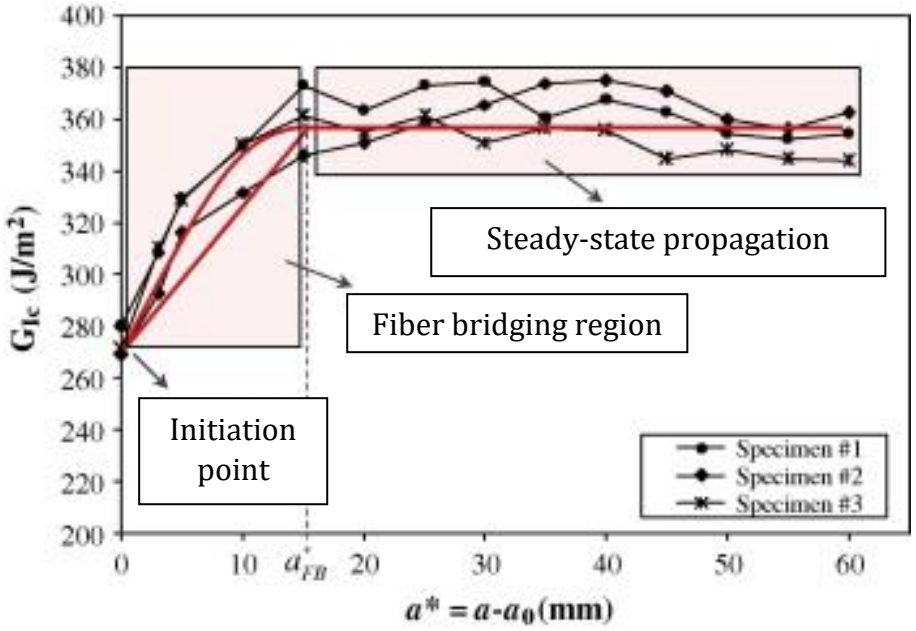

Figure 3. 10| R-curve response of laminates under mode-I loading indicating initiation and steady-state propagation region [205].

3.4.2. Mode-II Interlaminar Fracture Toughness Testing

The mode-II interlaminar fracture energies (G_{II}) of composite laminates can be measured with the three-point bend end-notched flexure (3-ENF) testing. However, a vertical shear force acting within the delaminated region and at the crack tip may cause friction that can influence the toughness values measured from the tests. Therefore, the four-point bend end-notched flexure (4-ENF) testing method was proposed to address the lack of stability of the crack growth examined from 3-ENF tests [206,207]. In this respect, 4-ENF testing was used in this study. The dimensions (*i.e.* 180 mm x 25 mm x ~3.5 mm) and the stacking sequences (*i.e.* consisting of 10 plies of the NCF fabrics at 0°, and thermoplastic veils presence at the symmetry plane after the release film for the composite laminates toughened with thermoplastic veils) of the composite laminates manufactured for 4-ENF tests are the same as the laminates for DCB tests. The configurations of the 4-ENF fixture are shown in Figure 3. 11. The span of the loading rollers is 60 mm and that of the loading roller is 100 mm. Thus, the initial delamination length is 30 mm. The sides of the manufactured composite laminates for 4-ENF tests were coated with a white marker and marked every 1 mm for 40 mm. The 4-ENF tests were conducted using three specimens for each batch at a crosshead speed of 5 mm/min using for loading and 25 mm/min for unloading with an Instron 5969 universal mechanical testing machine and crack tip propagation was observed using a

glass magnifier from the coated side of the 4-ENF specimens. Prior to 4-ENF tests, a sharp pre-crack of approximately ~3 mm long was generated to extend the resin pocket at the behind of the film insert under shear loading. Then, the initial delamination length of 30 mm was expanded until achieving 70 mm. Mode-II fracture energies for initiation values, $G_{II,C}$, of the composite laminates were calculated using a non-linear point approach and propagation values for mode-II fracture energies, $G_{II,R}$ of the composite laminates were determined from the plateau region of the R-curves (*i.e.* with crack extension between 20 mm and 40 mm). Equation 3. 3 was used to calculate the G_{II} values of the composite laminates.

$$G_{II} = \frac{P^2}{2b}\frac{\partial C}{\partial a}$$ Equation 3. 3

Where P is load, b specimen is the specimen width, a is the crack length and $\partial C/\partial a$ is the gradient from a compliance curve as seen in Figure 3. 12.

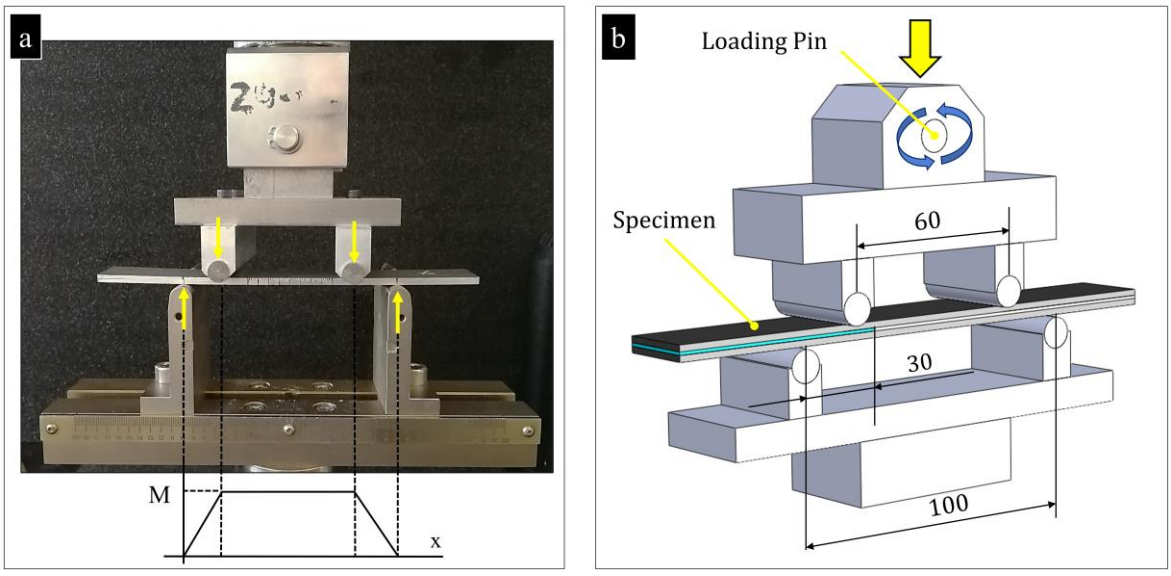

Figure 3. 11| Mode-II ILFT test procedure: (a) 4-ENF experimental test setup with moment distribution and (b) a schematic indicating test dimensions (the laminate stacking sequence and the specimen dimensions are the same with the DCB test specimen, see Figures 3. 7b and -c. Also, all dimensions are in mm).

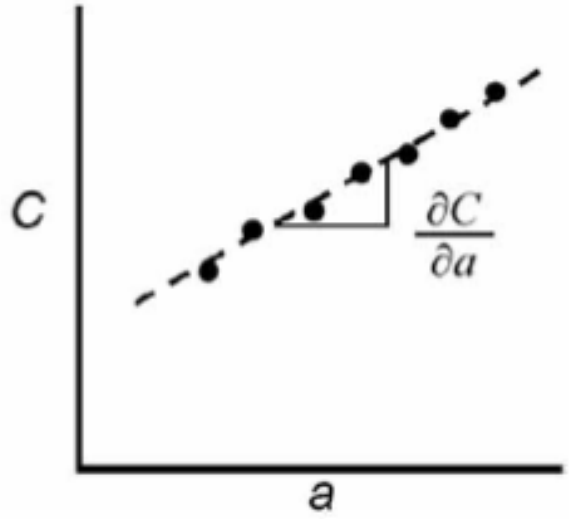

Figure 3. 12| The graph used to define the gradient of compliance (C = δ/P) and the crack length [199].

3.5. Low-Velocity Impact Damage Tolerance

The low-velocity impact damage tolerance of the composite laminates was evaluated in two phases: low-velocity drop-weight impact testing and compression after low-velocity impact testing as explained in Sections 3.5.1 and 3.5.2, respectively.

3.5.1. Low-Velocity Drop-Weight Impact Testing

The low-velocity impact (LVI) response of the composite laminates manufactured with/out toughening agents were investigated for low-velocity impact loading with an Instron Ceast 9350 drop-weight impact tower controlled by CeastVIEW 5.94 3C software based on the Prichard and Hogg protocol [129]. The impact tests were performed at different impact levels (*i.e*. 2 J, 2.5 J, 3 J, 4 J, 5 J, 7.5 and 10 J) by varying the height of the impactor (100 mm, 126 mm, 150 mm, 199 mm 252 mm, 378 mm and 505 mm, respectively) with the impactor velocities (*i.e.* 1.4 m/s, 1.56 m/s, 1.7 m/s, 1.98 m/s, 2.22 m/s, 2.72 m/s and 3.15 m/s, respectively), at the moment of impact. The impact test procedure, with a clamping system, schematic and stacking sequence for the laminates with veils, is given in Figure 3. 13. The specimens (*i.e.* 89 mm x 55 mm) were inserted between two metal plates with a circular opening with a diameter of 40 mm. Then plates were clamped with rubber tips and composite laminates were subjected to impact loading. The impact tower is equipped with a data acquisition

system, a piezoelectric transducer, and an anti-rebound system. The contact force-time data was collected with a sampling frequency of 500 kHz during impact. Impact tests were repeated at least three times for each specimen. The velocity, displacement, and absorbed energies were calculated using Equations 3. 4, 3. 5, and 3. 6.

$$v(t) = v_0 + gt - \int_0^t \frac{F(t)}{m} dt \qquad \text{Equation 3. 4}$$

$$\delta(t) = v_0 + \frac{gt^2}{2} - \int_0^t \left[\int_0^t \frac{F(t)}{m} dt \right] dt \qquad \text{Equation 3. 5}$$

$$E(t) = \frac{m[(v_0)^2 - \left(v(t)\right)^2]}{2} + mg\delta(t) \qquad \text{Equation 3. 6}$$

Where v, g, t, F, m and δ are the velocity of the impactor, the gravitational acceleration (9.81 m/s^2), the time of the impact (t = 0 when the impact is initiated), the contact force, the mass of the impactor (2.02 kg), and displacement, respectively. After the impact tests were performed, the laminates were scanned using C-scanning with transmission mode to detect the sublaminar impact damage area and the damage mechanisms were detected with scanning electron microscopical observation, as explained in Sections 3.6 and 3.7, respectively.

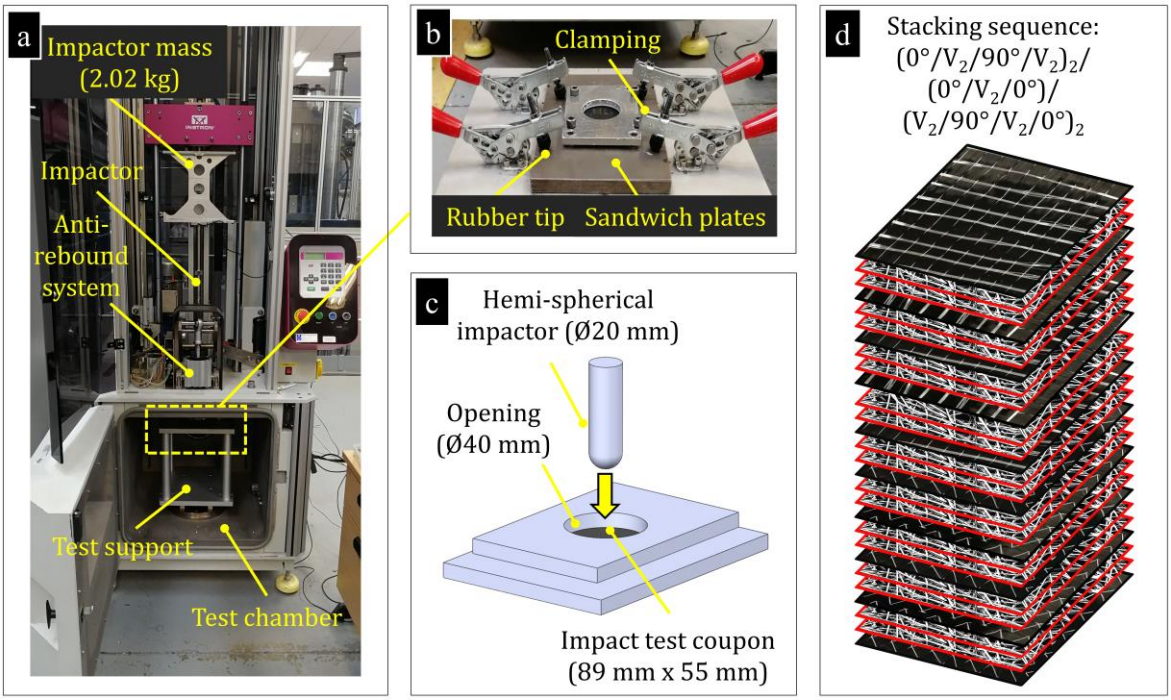

Figure 3. 13| Drop-weight impact test procedure: (a) the experimental test setup indicating the impactor, impactor mass, anti-rebound system, tests support and test chamber, (b) clamping system with rubber tip and sandwich plates, (c) a schematic indicating dimensions of the test setup and (d) the stacking sequence of the manufactured composite laminates used for low-velocity impact tests (V indicates 1 layer of PPS veil, and 2 layers of 10 g/m^2 PPS veil were interleaved at each interface for the impact tests).

3.5.2. Compression After Impact Testing

Compression after impact (CAI) tests were performed to determine the residual compressive strength of the composite laminates. Delamination, which is the typical internal failure that occurs under impact loading, leads to the premature collapse for composite laminates under compression loading. The layup orientation and the width of composite laminates can influence the behaviour of composites under compression loading, thus these parameters are required to be maintained consistently [208]. Thin samples are generally used to measure the residual compressive strength of composite laminates to ensure that compressive failure is initiated by the introduced internal impact damage. However, the use of thin composite laminates for the CAI tests can result in global buckling of the composite laminates prior to failure under in-plane compression load. Therefore, the CAI test fixtures include the anti-buckle supports to impede the buckling of the composite laminates.

In this study, the CAI tests were performed according to Prichard and Hogg's protocol [129]. Figure 3. 14 demonstrates the digital image of the experimental test setup indicating a miniature Boeing CAI fixture and a schematic of the test fixture. The composite laminates were manufactured with a length of 89 mm, a width of 55 mm and a thickness of ~3.5 and ~4 mm depending on the material systems and loaded at 5 mm/min.

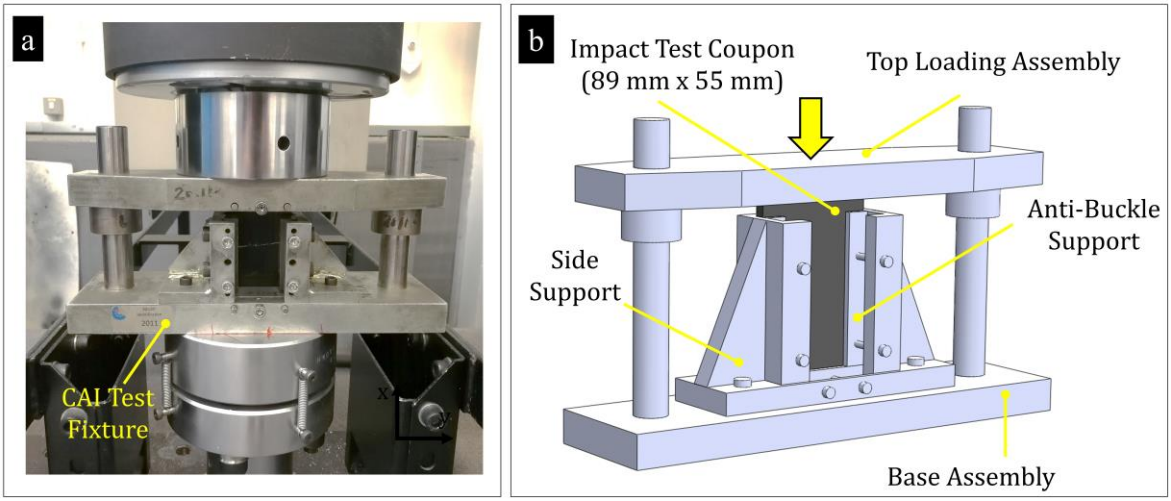

Figure 3. 14| (a) The compression after impact test setup with the miniature Boeing CAI test fixture and (b) a schematic of miniature Boeing CAI test fixture indicating the impact test coupon (89 mm x 55 mm x ~3.5 - 4 mm), top assembly, side support, anti-buckle support and base assembly (see, Figure 3. 13d for the stacking sequence of the composite laminates used for CAI tests).

3.6. Non-Destructive Testing

Ultrasonic testing is a non-destructive test (NDT) method widely used in industrial applications and academic studies on materials to detect internal flaws or discontinuities such as delamination after impact loading or void occurrence after manufacturing. There are three main varieties of NDT methods which are commonly used. An A-scan gives only one-dimensional information about the time history of the echoes received by the transducer. B-scanning is used to detect cross-sectional defects (*i.e.* the vertical axis is the time axis of the A-scanning whereas the horizontal axis gives positional information of defects). In C-scanning, the amplitude of a particular echo is monitored at each point on the surface of the samples. Measurements at each point are obtained using a scanning mechanism which generates a plan of the defect positions.

However, C-scanning is not able to generate information about the depth of the samples [209].

In this study, impact damage introduced in the composite laminates was detected with a Midas NDT Systems C-scan system controlled by the Zeus v3.0 software, see Figure 3. 15. The composite laminates were scanned using a 5 MHz transducer (probe) in transition mode. The tests were performed at the scanning speed of 150 mm/s with a 250 µm grid size and 250 µm index step. C-scans generate qualitative data for the detection of the defects such as delamination and void content. The transmitter signals are attenuated, and the amplitude of the received signals differs due to defects. Then, the received signals are processed with the software.

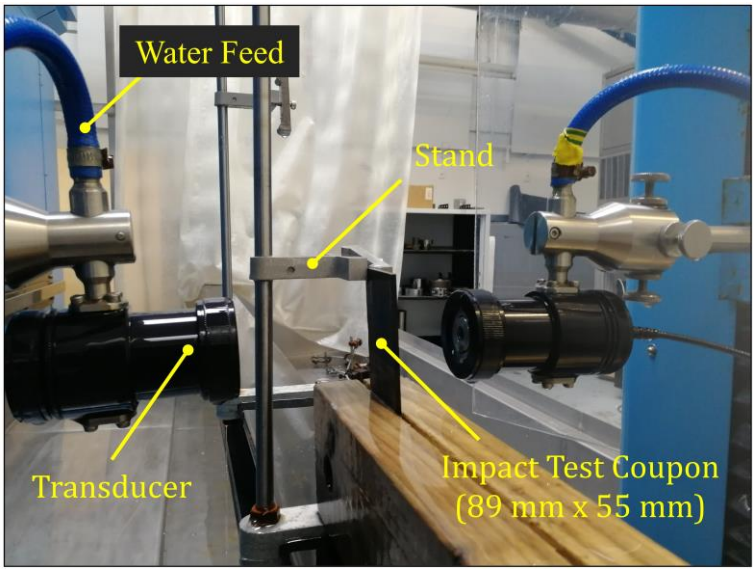

Figure 3. 15| A digital image of C-scanning equipment indicating through transition mode scanning with water feed, stand, transducers and impact test coupon.

3.7. Fractography

Fractographic investigations were performed using scanning electron microscopy (SEM) in this study to obtain the failure mechanisms from the fracture surfaces of the composite laminates. Electron guns generate a steady flow of electrons. Electron beams are then accelerated by the positive-charged anodes. The electron beams passing through the lenses are focused to ensure that electrons reach up to the sample precisely. SEMs usually include two types of magnetic lenses. The condenser lenses,

which define the resolution, are the first lenses electrons pass through and the electron beams then meet the objective lenses, which define the level of focus, before reaching the sample. After the electrons converge by magnetic lenses, scanning coils raster the electron beam onto the sample. Depending on the interaction of the beam with the samples, electrons are transmitted from the sample and electron detectors collect the transmitted electrons. Backscattered (BSE) electrons indicate high sensitivity based on the atomic numbers of materials (*i.e.* the higher the atomic number for material the brighter appearance achieved). Secondary electrons (SE) are detected from the electron passing from the surface of the samples and they are used to generate detailed information from the surface of the samples. Detection of X-rays generated from the electron beams is used to identify the elements which the samples contain. After electron beams are transmitted from the surface of the samples, the image processor receives the signals and processes the image.

In this study, SEM investigations were performed to define the fracture failure mechanisms introduced to the untoughened and toughened composite laminates under mode-I, mode-II and impact and compression after impact loadings. The fracture surfaces of the DCB and 4-ENF test specimens were only coated with gold-palladium (Au-Pd) (~10 nm thick) and investigated with a SEM. The impact and CAI test coupons were machined with a diamond cutter through the length and the machined surfaces were ground to remove machining induced surface undulations, scratches or near-surface micro-damage with 1200, 2400 and 4000 grit papers for SEM. Then the ground surfaces were coated with gold-palladium (Au-Pd) (~10 nm thick).

CHAPTER 4: Mode-I Interlaminar Fracture Energies of Composite Laminates Interleaved with Thermoplastic Veils

4.1. Introduction

This chapter is to investigate the influence of non-woven thermoplastic veils on the interlaminar fracture resistance of composite laminates under mode-I loading conditions. The mode-I fracture energies of the composite laminates toughened with two different non-woven veils are compared in this chapter. Composite laminates were toughened with 10 g/m^2 Polyetherimide (PEI) veils with cross-linked polyester binder and 10 g/m^2 Polyphenylene sulphide (PPS) veils with cross-linked styrene acrylic and the fracture energies of the laminates are compared in this section.

The average diameter of the PEI fibres and PPS fibres is ~13.74 and ~9.19 μm, respectively. Also, the specific surface areas of the PEI and PPS veils are ~227 m^2/kg and ~322 m^2/kg, respectively. The dry veil thickness is measured as ~76.3 μm for PEI veils and ~65.7 μm for PPS veils. Therefore, the PPS veils have a denser network compared to the PEI veils.

Double Cantilever Beam (DCB) specimens were manufactured with vacuum-assisted resin infusion. The mode-I fracture energies of the composite laminates were characterised following ASTM D5528 [203]. Interlaminar fracture toughness of the composite laminates at the onset of crack propagation ($G_{I,C}$) was calculated based on a 5%/max load approach and interlaminar fracture energies for crack propagation ($G_{I,R}$) were obtained by taking the average of the fracture energy values calculated from the increment of crack length between 25 mm and 55 mm where the R-curve becomes flat for all the specimens. The effect of PEI and PPS veil veils on the delamination resistance of the composite laminates under mode-I loading are compared in this chapter.

4.2. DCB Test Results

The mode-I fracture energies of the untoughened epoxy (base), epoxy with 10 g/m^2 PEI veil (PEI10) and epoxy with 10 g/m^2 PPS veil (PPS10) laminates are measured and the representative load-displacement (P-δ) and the crack growth resistance curves (R-

curves) of the base, PEI10 and PPS10 laminates are compared in Figure 4. 1. The P-δ curves (Figure 4. 1a) indicate that the response of the PPS10 laminates considerably differs compared to the response of the base laminates in mode-I —while the effect of PEI veils can be negligible. All the composite laminates experienced gradual crack growth under mode-I loading. A higher peak load was generated from the PPS10 laminates compared to the base and PEI10 laminates, which offers that PPS veils improved the resistance to crack initiation. The comparison of R-curves (Figure 4. 1b) demonstrates that $G_{I,C}$ is considerably higher for the PPS10 laminates compared to the other laminates. A marginally increasing trend in the R-curve of the base laminates is observed. The $G_{I,R}$, which is dependant on both intrinsic (*i.e.* ahead of the crack front) and extrinsic toughening (*i.e.* behind the crack front) mechanisms, is somewhat constant and close to $G_{I,C}$. This indicates that the fracture resistance of the base laminates is predominantly governed by the intrinsic toughening mechanisms for both crack tip initiation and propagation. Similarly, PEI10 laminates exhibited a marginally rising R-curve and $G_{I,C}$ of the PEI10 laminate is slightly higher compared to the base laminates (Figure 4. 1b). In contrast, the R-curve of the PPS laminates experienced decreasing trend, which suggests that PPS veils introduced the beneficial toughening mechanisms immediately after the crack initiation whereas PPS fibres played only a minor role on further crack propagation.

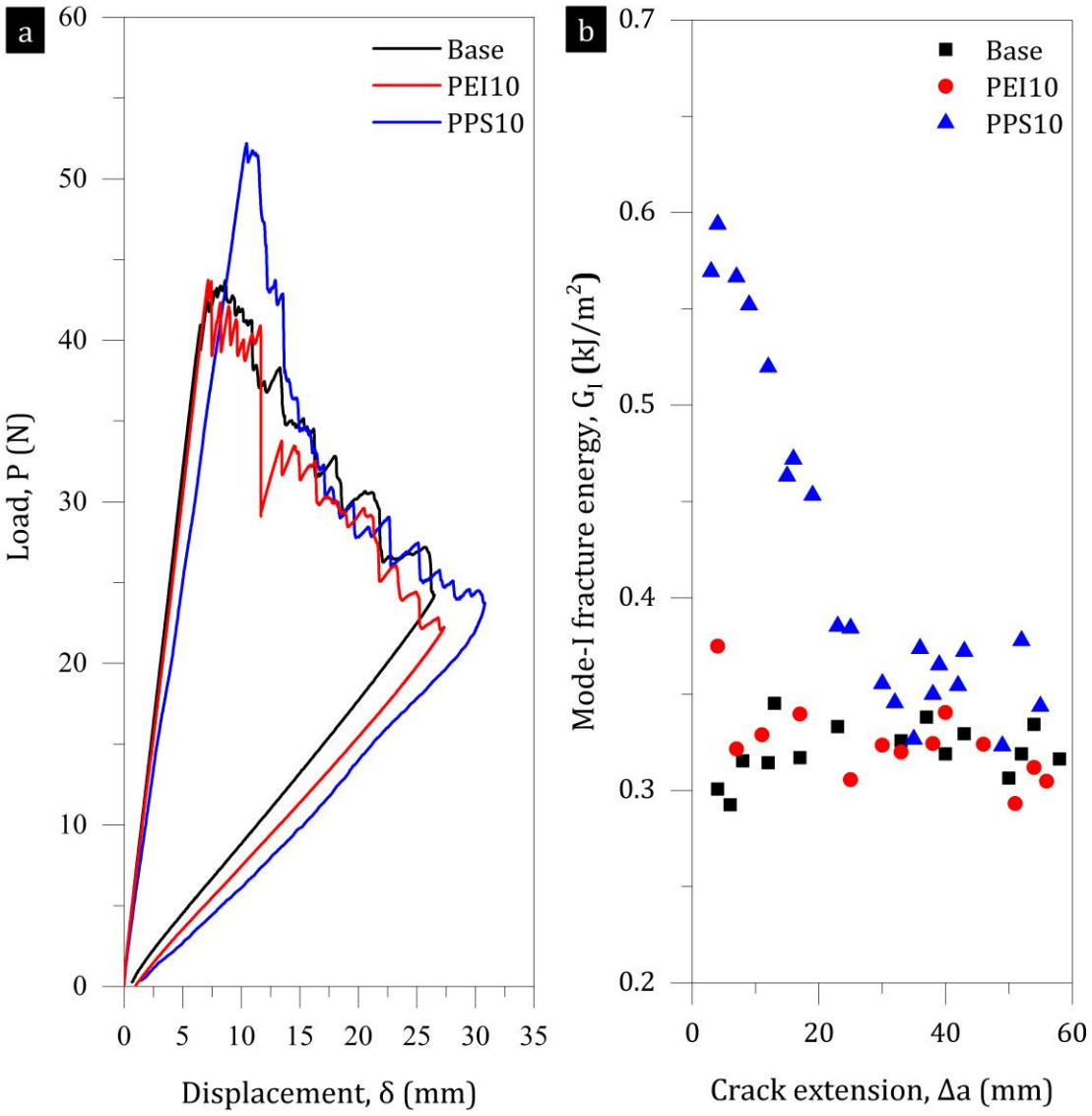

Figure 4. 1| Comparison of the mode-I fracture behaviour of the base, PEI10 and PPS10 laminates: (a) load-displacement, *i.e.* P-*δ*, curves and (b) the R-curves, *i.e.* mode-I fracture energies vs crack extension, G_I vs Δa.

4.3. Mode-I Toughening Mechanisms

The fracture surfaces of the base, PEI10 and PPS10 laminates were examined after the DCB tests were performed (see, Figures 4. 2 – 4. 4). The fracture surfaces of the base laminate expose the stitch yarn pattern of the NCF preform as shown in Figure 4. 2a, which demonstrates that the crack growth was mainly in the interlaminar region ahead of the initial crack front. Then, the crack propagated in both inter- and intralaminar regions after substantial growth, with partially visible stitch yarn patterns. The micrographs for the crack initiation and propagation obtained from the base laminate are given in Figures 4. 2b and -c, respectively. The stitch yarns and carbon fibre-rich

regions (Figure 4. 2b) just ahead of the crack front show that the crack path was initially predominantly interlaminar. The micrograph of the base laminate obtained from the propagation region shows the carbon fibre-rich surface patches with some broken carbon fibres, and intralaminar fracture with carbon fibre bridging, as seen in Figure 4. 2c. The crack growth path for the base laminate is schematically given in Figure 4. 2d. The fracture surfaces of the PEI10 laminates are shown in Figure 4. 3a and expose cloudy surfaces ahead of the release film due to PEI veil presence, and carbon fibre strips for the crack extension > ~10 mm. This indicates that the crack tip was initiated from the PEI toughened interlaminar region, then propagated through the neighbouring lamina. The micrograph obtained from the initiation region of the PEI10 laminate (Figure 4. 3b) indicates the PEI fibre-rich regions (and the fibre impressions). This suggests that the crack growth was initially within the PEI toughened interlaminar region. The micrograph taken from the propagation region of the PEI10 laminate indicates that the crack growth was partly interlaminar (within the PEI veil) and partly intralaminar (with carbon fibre-rich patches) as seen in Figure 4. 3c. Broken and pulled-out PEI fibres and broken carbon fibres prove the bridging phenomenon during the crack opening. However, the contribution of the generated fibre bridging mechanisms to the crack resistance is highly limited. Also, the crack growth path for PEI10 laminate is schematically represented in Figure 4. 3d. Furthermore, Figure 4. 4a indicates the fracture surfaces of the PPS10 laminate and exposes the stitch pattern yarns only ahead of the crack initial crack front. This confirms that the crack tip was predominantly within the PPS veil toughened interlaminar region. However, the crack propagation was both inter- and intralaminar regions without stitch yarn pattern on the fracture surfaces. The micrograph obtained from the initiation region of the PPS10 laminate (Figure 4. 4b) indicates the PPS fibre rich patches. Loose fibres with the smooth surface of PPS fibres confirm that adhesion between the PPS fibre-matrix interface is relatively lower when compared to the PEI and matrix interface adhesion (Figure 4. 3b). Also, the initial high peak load in the load-extension curve suggests that fibre bridging mechanisms were successfully established for the PPS10 laminates. On the other hand, Figure 4. 4c represents the SEM image obtained from the propagation region of the PPS10 laminates and exposes that crack growth was partly from the interlaminar PPS toughened region (with a PPS fibre-rich patch) and partly from the intralaminar untoughened region (with carbon fibre-rich patch). Broken and pulled-out PPS fibres and the broken carbon fibres suggest the fibre bridging mechanisms

during crack growth, similar to the crack propagation path obtained from the PEI10 laminate (see Figure 4. 3d). The crack propagation path is schematically given in Figure 4. 4d.

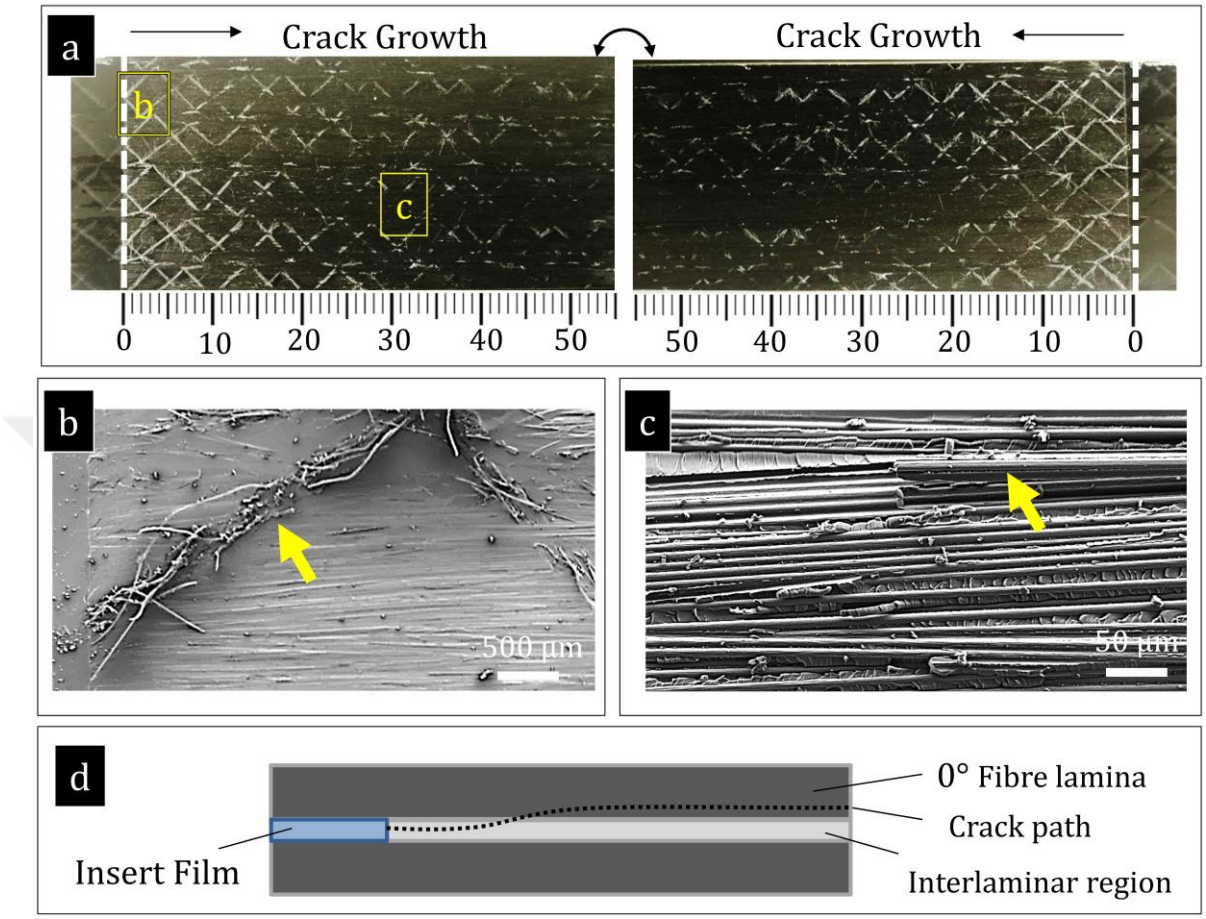

Figure 4. 2| The mode-I fracture surface features of the base laminate: (a) a pair of fracture surfaces, (b) the crack initiation region with stitch yarns and carbon-fibre rich interlaminar surface, (c) the crack propagation region with debonded and broken carbon fibres, and (d) a schematic representation of the crack path.

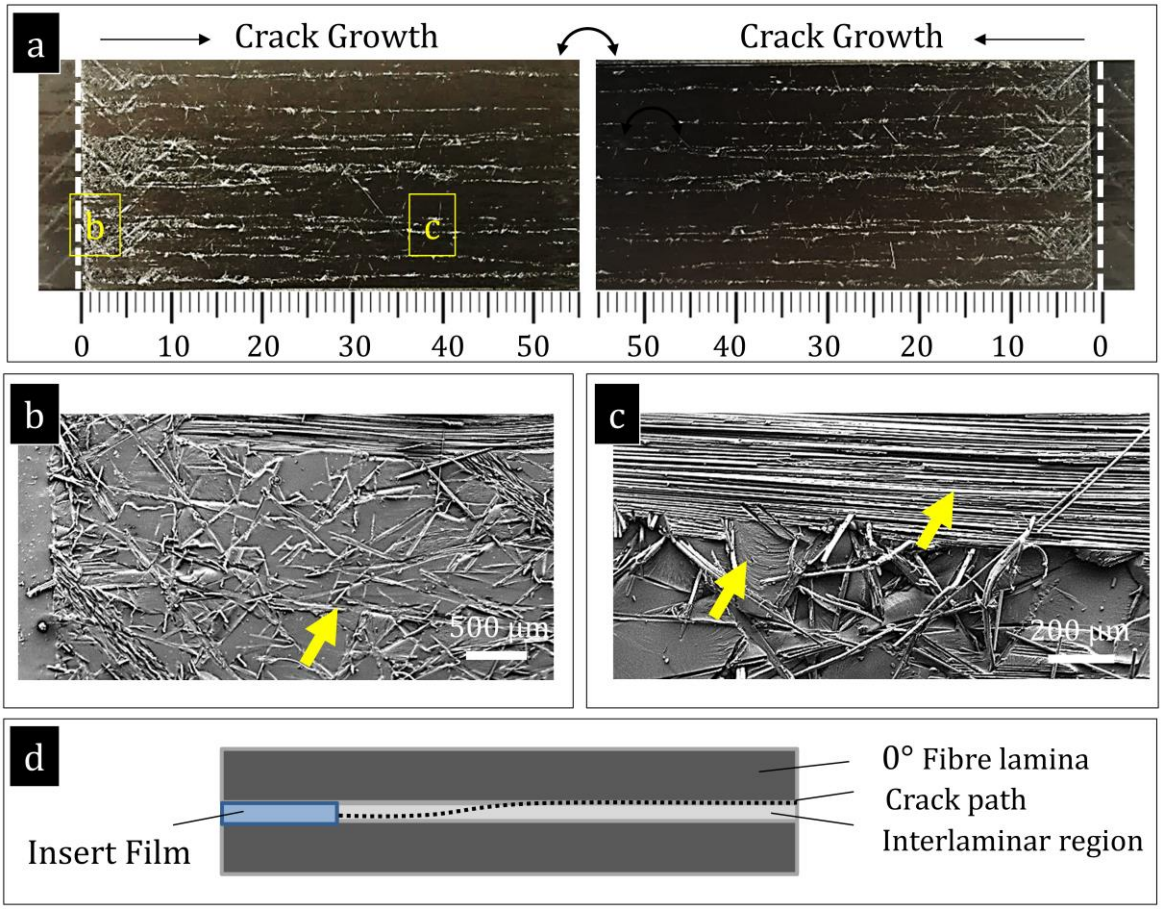

Figure 4. 3| The mode-I fracture surface features of the PEI toughened laminate: (a) a pair of fracture surfaces, (b) the crack initiation region with PEI fibre imprints, (c) the crack propagation region with broken carbon and PEI fibres, and (d) a schematic representation of the crack path.

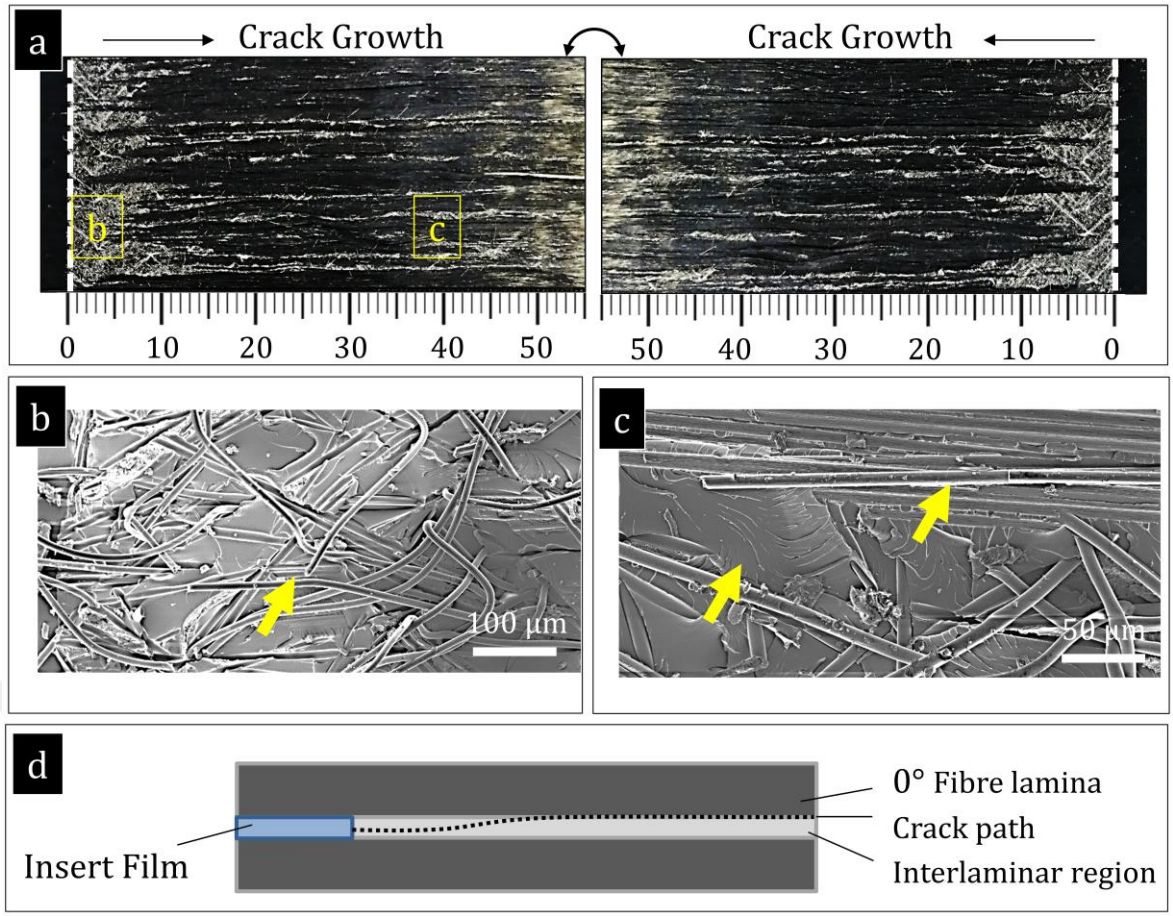

Figure 4. 4| The mode-I fracture surface features of the PPS toughened laminate: (a) a pair of fracture surfaces, (b) the crack initiation region with debonded and broken PPS fibres, (c) the crack propagation region with broken carbon and PPS fibres, and (d) a schematic representation of the crack path.

4.4. Discussions

The composite laminates, consisting of the 10 plies of the unidirectional carbon fibre NCF preform and the low-viscous epoxy resin (Araldite 564/Aradur 2954), were manufactured with vacuum resin infusion at ambient conditions and cured out-of-autoclave with no additional pressure. 10 g/m^2 PEI and PPS veils were interleaved at the symmetry plane of the NCF fabrics in the fabric layup process. The mode-I fracture properties of the composite laminates were measured to understand the influence of the veils on the fracture resistance for the crack initiation and propagation.

Table 4. 1 demonstrates the comparison of the mode-I fracture properties of the PEI10 and PPS10 laminates. The initiation and propagation fracture energies of the base laminates are 294 and 315 J/m^2, respectively. The fracture energies of the PEI10 and

PPS10 laminates are higher by ~12% and ~80% at the onset of crack propagation and by ~3% and ~18% for the crack propagation, respectively.

Table 4. 1| The mode-I fracture initiation and propagation energies (*i.e.* $G_{II,C}$ and $G_{II,R}$, respectively) of the base, PEI10 and PPS10 laminates.

Material system (Acronym)	$G_{I,C}$ (J/m^2)	$G_{I,R}$ (J/m^2)	Variation in $G_{I,C}$	Variation in $G_{I,R}$
Epoxy (Base)	294 ± 7	315 ± 8	-	-
Epoxy + 10 g/m^2 PEI veil (PEI10)	330 ± 38	326 ± 38	+12%	+3%
Epoxy + 10 g/m^2 PPS veil (PPS10)	526 ± 38	371 ± 26	+80%	+18%

The base laminate experienced crack tip migration from the interlaminar region to the neighbouring lamina (Figure 4. 2). This could be a result of the compaction of the NCF fabrics (*i.e.* introduces in-plane and out-of-plane fibre bundle waviness primarily originated by the stitches) [210,211]. The test results also indicate that both PEI10 and PPS10 laminates experienced falling R-curves (see Figure 4. 1b). This indicates that PEI and PPS fibre energy dissipation toughening mechanisms were obtained just behind the release film. For the crack propagation, the toughening mechanisms via the PEI and PPS fibres were not efficiently promoted. Similar to the base laminates, the micrographs of the fracture surfaces obtained from the PEI10 (see Figure 4. 3) and PPS10 (see Figure 4. 4) laminates confirm the crack tip migration within the veils to the neighbouring lamina.

In addition, the $G_{I,C}$ of the PPS10 laminates is significantly higher than that of the PEI10 laminates. The micrographs confirm loose and broken PPS fibres (Figure 4. 4) whereas PEI fibres were embedded within the epoxy (Figure 4. 3). This indicates that relatively high adhesion of the PEI fibres and the epoxy interfaces suppressed the fibre bridging mechanisms. On the other hand, it is shown that easily debonded PPS fibres can stimulate the fibre bridging mechanisms and significantly enhanced the fracture resistance by establishing PPS fibre toughening mechanisms (*e.g.* debonding and breakage, see Figure 4. 4).

The PPS toughened laminates are compared with the aerospace grade composite material systems as seen in Table 4.2. This study indicates that the laminates with poor intrinsic fracture properties can be successfully toughened with thermoplastic veils. Also, cost effective material systems (manufactured with room temperature infusion and out-of-autoclave curing with no external pressure) can provide fracture properties as high as aerospace grade material systems. On the other hand, thermoplastic veils with relatively strong fibre adhesion and low specific surface area might not be helpful as observed in the PEI toughened laminates. Also, such detrimental factors may decrease the fracture properties of laminates [44,56].

Table 4. 2| A comparison of the mode-I fracture energies obtained from the PPS toughened laminates with that of T700/Cycom 890, HYE/1034E, T300/RTM6-2 and HTA/6376C aerospace-grade laminates [48,212–214].

Material system	$G_{I,C}$ (J/m^2)	$G_{I,R}$ (J/m^2)	Variation in $G_{I,C}$	Variation in $G_{I,R}$	References
Epoxy + 10 g/m^2 PPS veil (PPS10)	526 ± 38	371 ± 26	-	-	-
T700/Cycom 890	369 ± 28	463 ± 15	42%	-20%	[48]
HYE-1034E (Prepreg)	181 ± 9	171 ± 8	190%	117%	[48]
T300/RTM6-2	245 ± 22	313 ± 29	115%	18%	[212]
GTA/6376C (Prepreg)	260 ± 10	258 ± 20	102%	44%	[213,214]

4.5. Conclusions

Chapter 4 compares the fracture performance of the composite laminates interleaved with PEI and PPS veils in mode-I and draws the conclusions below:

- *The influence of the PEI veil:* The PEI veils marginally improved the mode-I fracture energies (by ~12% for $G_{I,C}$ and ~3% for $G_{I,R}$ compared to the base laminate). The micrographs indicate that relatively high adhesion of the PEI fibre-epoxy interface suppressed the fibre bridging mechanisms (see embedded PEI fibres within the epoxy due to the high adhesion from Figure 4. 3).

- *The influence of the PPS veil:* The PPS toughened laminates performed better than the PEI toughened laminates (by ~80% and ~18% in $G_{I,C}$ and $G_{I,R}$, respectively). Weakly debonded PPS fibres successfully promoted the fibre bridging mechanisms (see debonded and broken fibres due to the fibre bridging on the fracture surface with the smooth surface of the PPS fibres from Figure 4. 4).

This chapter indicates that the veil fibres with relatively weak adhesion to the matrix (PPS) can easily debond from the matrix and promote fibre bridging mechanisms. As the benefit achieved from the veils was lowered due to the crack tip migration from the veil toward the neighbouring lamina (see Figure 4. 1b for the decreasing crack resistance with the crack growth), the PPS veils significantly improved the mode-I initiation fracture energies, whereas slight improvement in mode-I propagation fracture energies.

CHAPTER 5: Mode-I Interlaminar Fracture Energies of Hybrid Toughened Composite Laminates

5.1. Introduction

The previous chapter indicated that PPS veil toughened composites outperformed the PEI veil toughened laminates under mode-I loading conditions. In this chapter, the influence of the hybrid use of the PPS veils and CSR particle content on the mode-I fracture properties for the carbon fibre NCF/epoxy laminates is investigated.

The hybrid laminates were manufactured with vacuum-assisted resin infusion. The mode-I fracture energies of the manufactured composite laminates were measured following ASTM D5528 [203]. The initiation fracture energies ($G_{I,C}$) of the composite laminates were calculated based on the 5%/max load approach. The propagation fracture energies ($G_{I,R}$) were measured taking the average of the fracture energy values calculated from the increment of crack length between 25 mm and 55 mm, where the R-curve becomes flat for all the specimens. The fracture surfaces of the DCB specimens were obtained with scanning electron microscopy (SEM) to investigate the fracture mechanisms leading to the mode-I fracture resistance for the composite laminates.

5.2. DCB Test Results

The representative load-displacement (P-δ) curves and the crack growth resistance curves obtained from the DCB tests on the untoughened epoxy (base), the epoxy with 5% CSR particle content (CSR5), the epoxy with 10 wt% CSR particle content (CSR10), the epoxy with 10 g/m^2 PPS veil (PPS10), the epoxy with 15 g/m^2 PPS veil (PPS15), the epoxy with 20 g/m^2 PPS veil (PPS20) and the epoxy together with 10 wt% CSR particle content and 20 g/m^2 PPS veil (hybrid) laminates are presented in Figure 5. 1. The P-δ curves indicate that all laminates experienced gradual crack growth with no significant load drops and mode-I crack growth (*i.e.* the peak load at the onset of crack growth and the area enclosed by the loading and unloading paths) varies depending on the toughening approach. The P-δ curves indicate that the hybrid toughened laminates sustained a relatively high load during crack growth, which suggests significantly high fracture at the onset of crack growth and during crack growth under mode-I loading.

The P-δ curve also indicates that interlaminar toughening with PPS veil incorporation initially provided significant improvement, then resulted in a gradual decrease with increasing crack path growth. This suggests that PPS interleaving mostly enhanced the crack resistance of the composite laminates at the onset of the crack propagation but the fracture toughness performance of the laminates with PPS veils for the crack propagation is not as high as that for the crack initiation. Also, the peak load generation is increasing with increasing the areal weight of veils. Therefore, the crack resistance of the PPS veil toughened laminates is dependent on the areal weight. Moreover, P-δ curves indicate 5 wt% and 10 wt% CSR particles had not considerably affected the peak load at the onset of the crack growth but a higher load compared to the base laminates is observed.

Figure 5. 1b indicates the variation in mode-I fracture energies with respect to crack extension. The base, CSR5 and CSR10 laminates experienced a marginally increasing trend. This shows that the energy dissipation mechanisms are dependent on intrinsic toughening mechanisms (*i.e.* ahead of the crack tip), which are associated with the matrix and carbon-matrix interface properties. However, the energy dissipation via extrinsic toughening mechanisms (*i.e.* behind the crack front) such as fibre breakage and bridging for these laminates is limited. In contrast, the PPS10, PPS15 and PPS20 laminates exhibited decreasing R-curves, which could signify that toughening mechanisms introduced due to the presence of PPS veils were predominantly effective at the onset of crack growth and then became ineffective during crack growth. However, the hybrid laminates with the presence of 20 g/m^{2}PPS veils and 10 wt% CSR particles exhibited rising R-curve with significant enhancements in mode-I fracture energies for crack initiation and propagation.

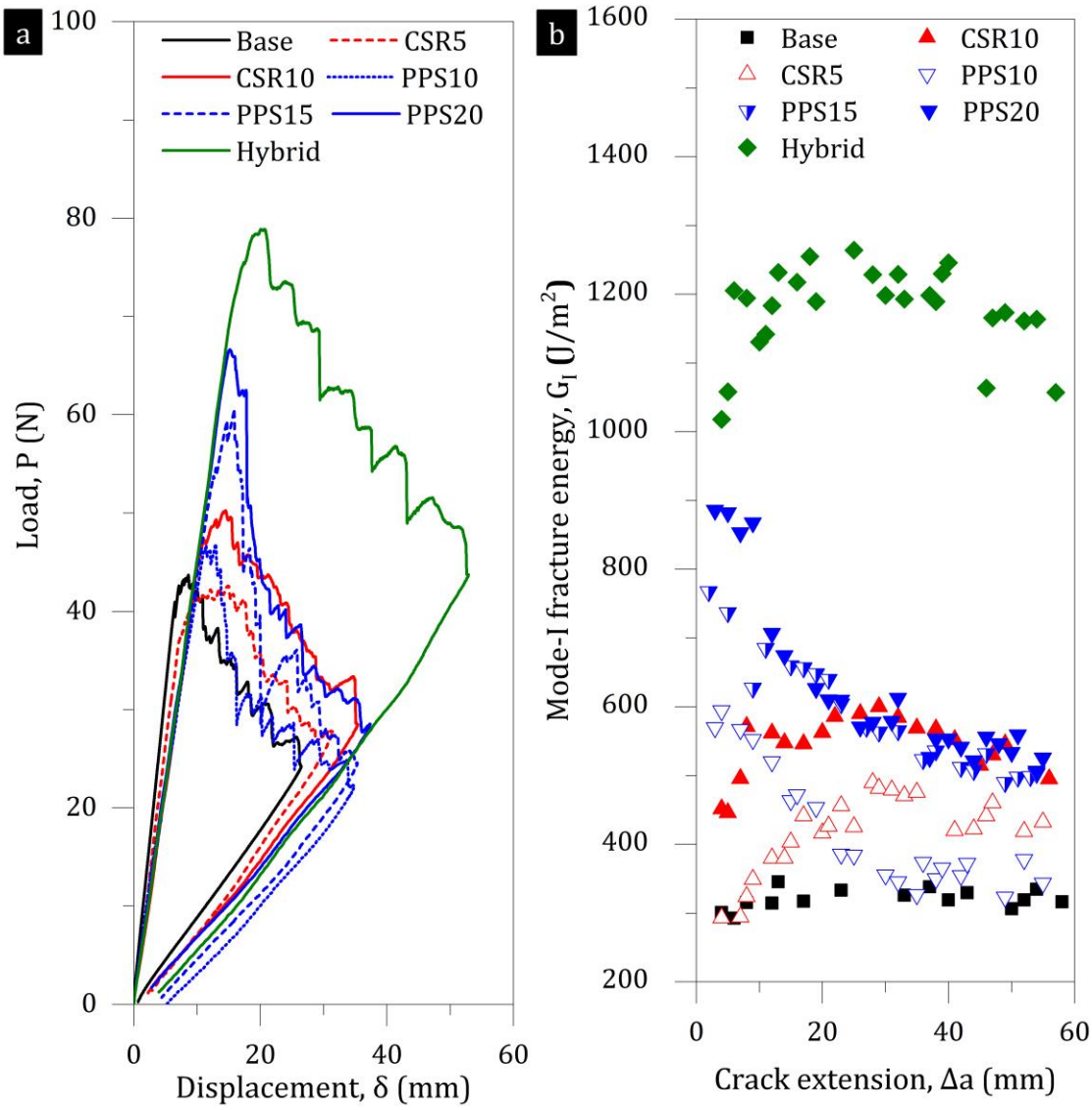

Figure 5. 1| Comparison of the mode-I fracture behaviour of the base, PPS10, PPS15, PPS20 and hybrid laminates: (a) load-displacement, *i.e.* P-δ, curves and (b) the R-curves, *i.e.* mode-I fracture energies vs crack extension, G_I vs Δa.

5.3. Mode-I Toughening Mechanisms

The fracture surfaces of the base, CSR10, PPS20 and hybrid toughened laminates were examined to understand the failure locus and toughening mechanisms, as seen in Figures 5. 2 – 5. 5. A pair of mode-I fracture surfaces obtained from a representative base laminate is given in Figure 5. 2a. The stitch patterns are clearly visible on the fracture surfaces for crack extension up to 20 mm but less visible because of some carbon fibre for the crack extension of more than 20 mm. This indicates that the crack front, introduced with release film, initially propagated along the resin-rich interlaminar region between NCF lamina, then migrated through the neighbouring

lamina with further crack propagation. The micrograph taken from the initiation region shows the stitch yarns (see Figure 5. 2b), and that taken from the propagation region exposes broken carbon fibres (Figure 5. 2c). The schematic demonstrates the crack locus for the base laminate, see Figure 5. 2d. As the mode-I initiation fracture energy is related to the intrinsic energy dissipation mechanisms ahead of the pre-crack front, the fracture surface indicates that energy dissipation is limited. The R-curve and the micrographs taken from the propagation region together demonstrate the resistance to the crack propagation reaches the steady-state with fibre bridging mechanisms [141,142]. The mode-I propagation fracture energies are slightly higher than the mode-I initiation fracture energies, which indicates that extrinsic toughening mechanisms via fibre bridging (*i.e.* with weak interface adhesion) marginally contribute to the energy dissipation during crack growth [215].

A pair of the mode-I fracture surface from the representative CSR10 laminate with micrographs is given in Figure 5. 3a. The stitch patterns are less visible, indicating crack migration, and fracture surfaces appear rough compared to the base laminate. The stitch pattern is partly visible and partly covered with the carbon fibres starting from the onset of the crack propagation to the full crack extension. The micrograph obtained from the crack initiation region of the CSR10 laminate confirms the rough surface features with exposed carbon fibres and the particle-toughened epoxy with river lines and loose stitch yarns (see Figure 5. 3b). The micrograph taken from the propagation region of the CSR10 laminate indicates broken and loose carbon fibres along with the rough matrix surface features as seen in Figure 5. 3c. The observed crack locus is given in Figure 5. 3d.

The fracture surfaces and micrographs of the PPS20 laminate are shown in Figure 5. 4. The surface features indicate that the crack growth was initially predominantly within the PPS veil, then partly within the PPS veil and partly migrated into the neighbouring lamina, as seen in Figure 5. 4a. The micrograph taken from the initiation region, see Figure 5. 4b, confirms the crack growth within the PPS veil, indicating debonded PPS fibres on the fracture surface while pulled-out PPS fibres as a result of PPS fibre bridging during crack growth. The glassy matrix surface around the PPS fibres with the smooth surface shows the brittle behaviour of the epoxy and the weak fibre-matrix adhesion. The micrograph taken from the propagation region indicates that crack growth was partly within the PPS veil (with debonded PPS fibres) and partly from the

neighbouring lamina. The crack migration observed adversely affected the fracture propagation energy as a significant falling R-curve is observed (see Figure 5. 1b) for the PPS laminates. The schematic indicates the crack tip migration in Figure 5. 4d.

The fracture surfaces and micrographs obtained from the representative hybrid laminate are shown in Figure 5. 5. A pair of the fracture surfaces (see Figure 5. 5a) demonstrates that the crack initiation and propagation were partly within the PPS veil and partly within the neighbouring lamina. The crack path appeared to have remained more or less unchanged with crack growth (without considerably migrating into the neighbouring lamina). The micrographs taken from the crack propagation region indicate exposed and broken carbon fibres as well as debonded and pulled-out PPS fibres, as seen in Figure 5. 5c. The micrographs taken from the crack propagation region show debonded and pulled-out PPS fibres with cavitated epoxy rich regions between fibres. The mode-I crack path observed in the hybrid laminates is schematically shown in Figure 5. 5d. The enhanced fracture energy and rising R-curve (see Figure 5. 1b) observed in the hybrid laminates, along with micrographs presented in Figures 5. 5b and -c, show that the combination of PPS veils and CSR particles introduced toughening mechanisms and led to significantly higher energy dissipation via fibre debonding, fibre bridging and epoxy cavitation while promoting crack growth path within PPS veils.

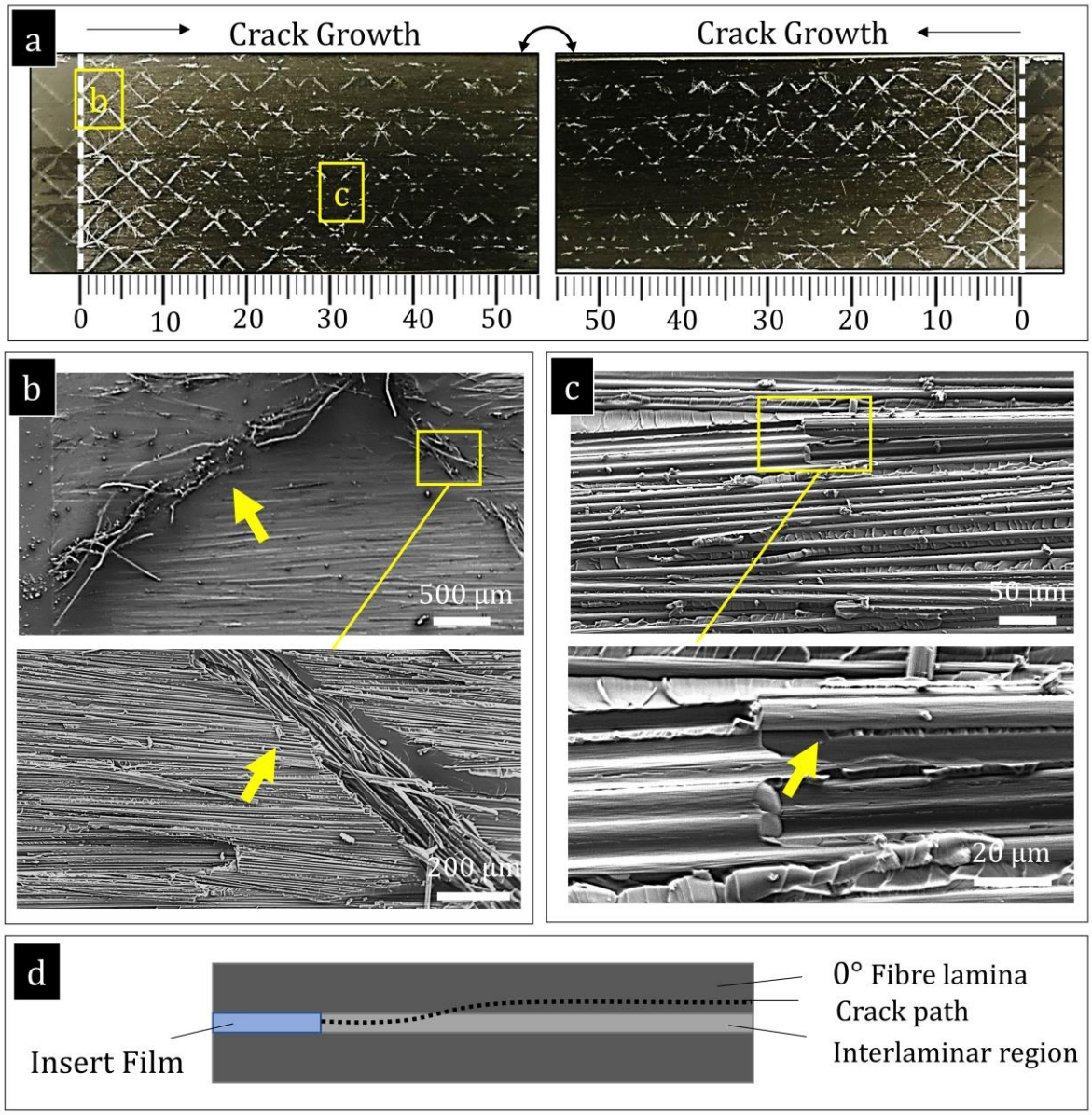

Figure 5. 2| The fracture surface features of the base laminate: (a) a pair of fracture surfaces, (b) the crack initiation region with stitch yarns and carbon-fibre rich interlaminar surface, (c) the crack propagation region with some broken carbon fibres, and (d) a schematic representation of the crack locus.

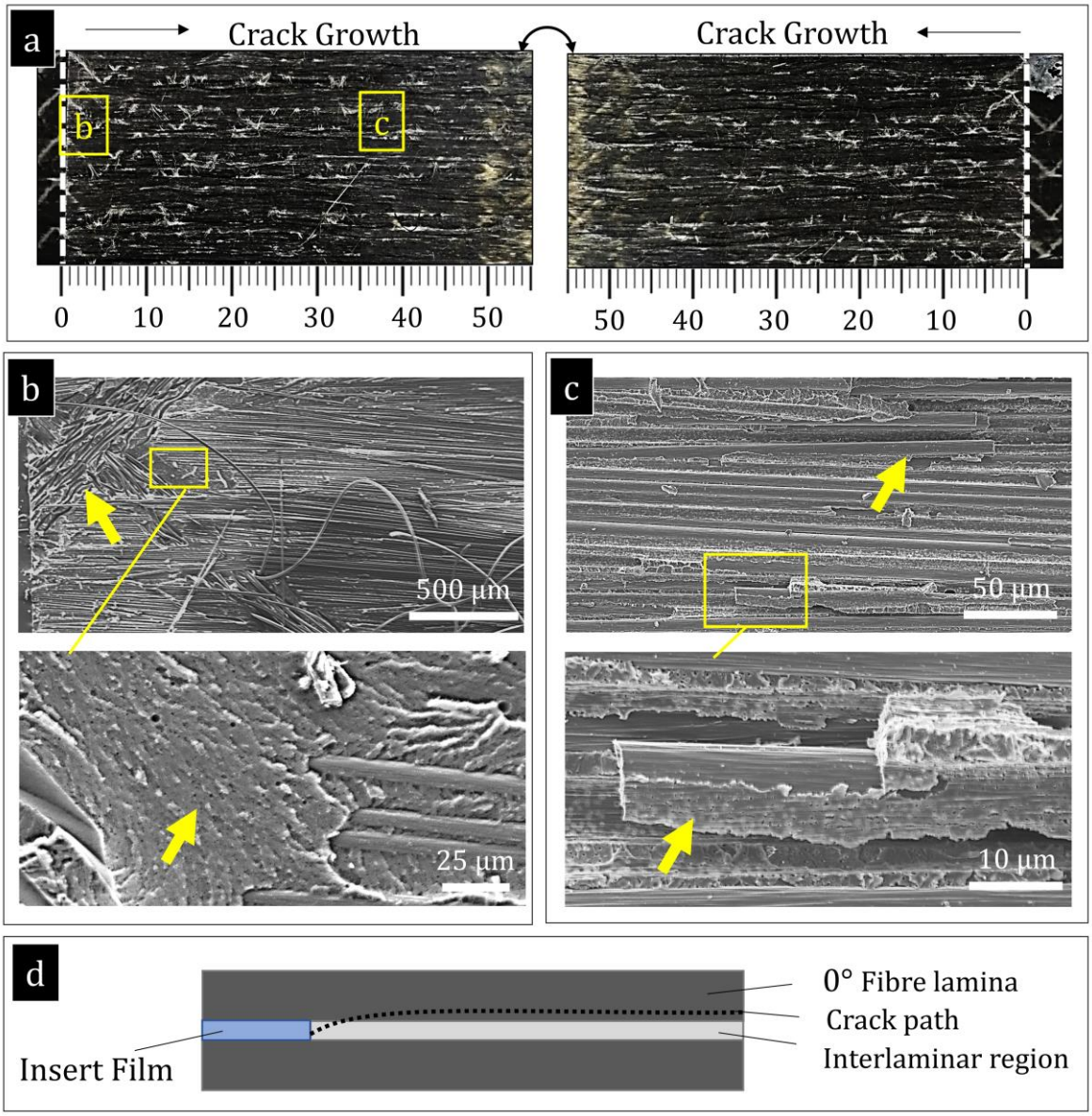

Figure 5. 3| The fracture surface features of the CSR10 laminate: (a) a pair of fracture surfaces, (b) the crack initiation region with debonded stitch yarns and rough resin-rich surface with CSR particle, (c) the crack propagation region with broken carbon fibres and residual matrix on the fibres and (d) a schematic representation of the crack locus.

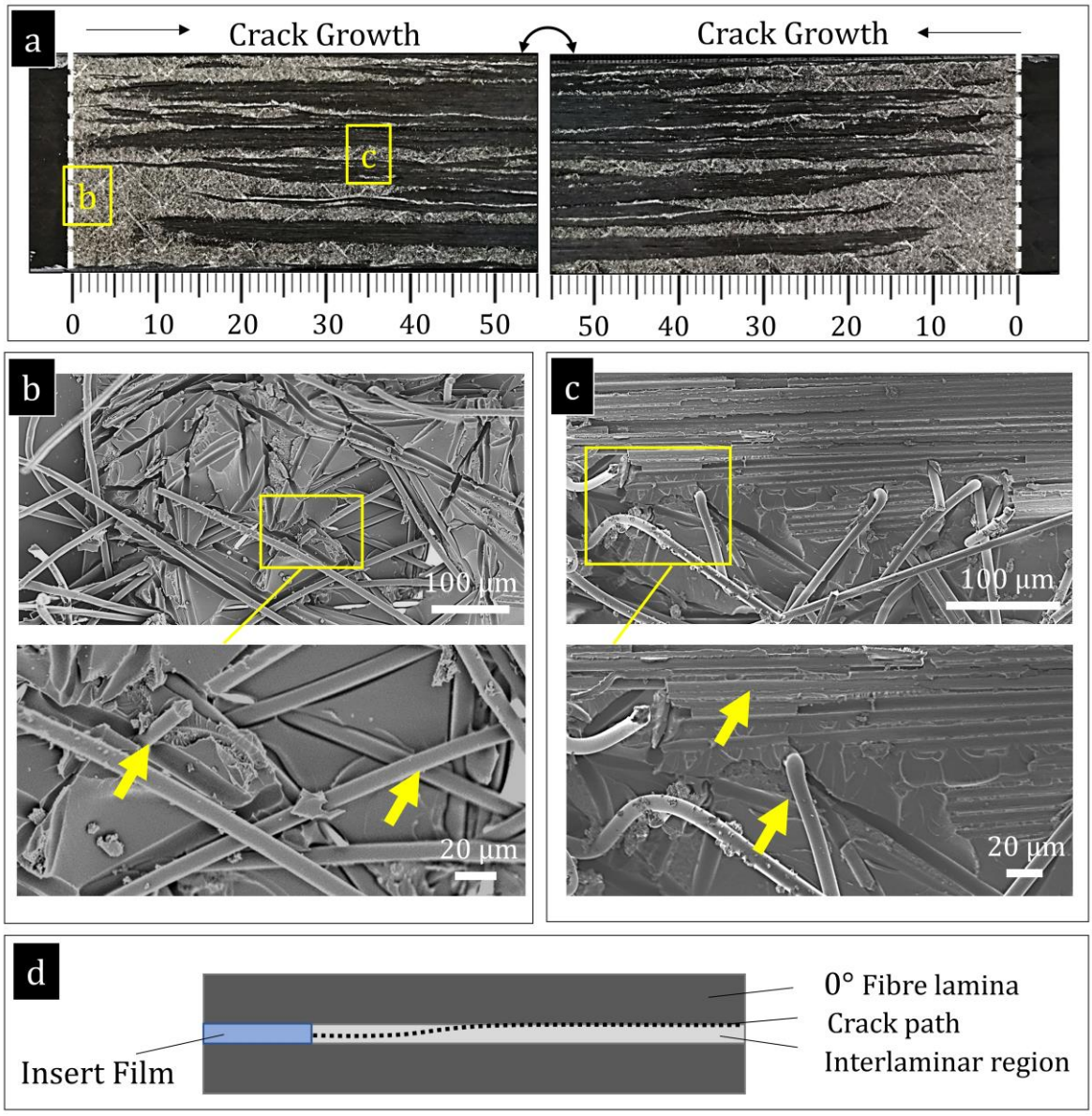

Figure 5. 4| The mode-I fracture surface of the PPS20 laminate: (a) a pair of fracture surfaces, (b) crack initiation region with debonded, pulled-out and broken PPS fibres, (c) crack propagation region with debonded and pulled-out PPS fibres, and exposed and broken carbon fibres, and (d) a schematic representation of the crack locus.

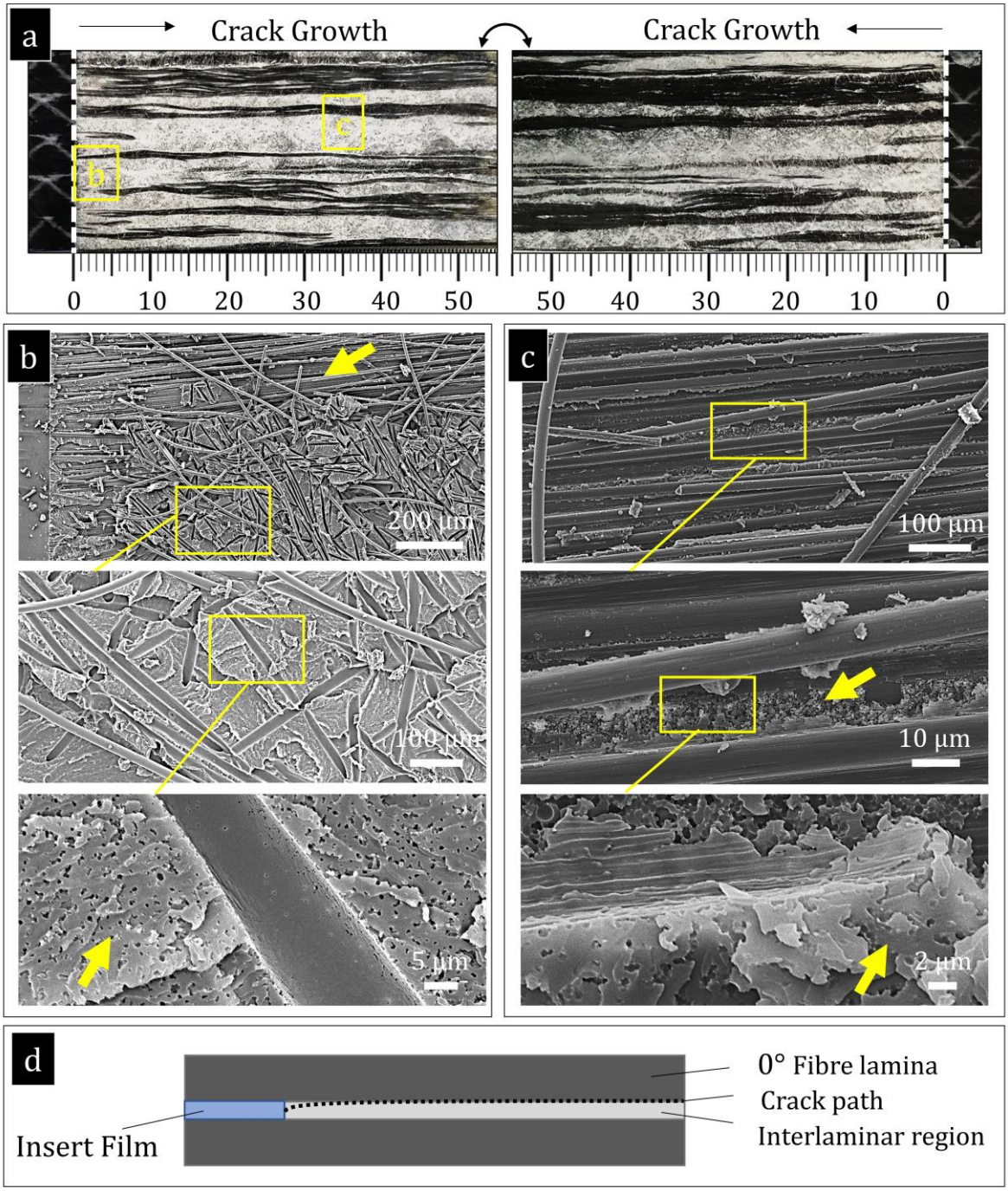

Figure 5. 5| The mode-I fracture of the hybrid toughened laminate: (a) a pair of fracture surfaces, (b) crack initiation region with cavitated epoxy and debonded/pulled-out carbon and PPS fibres, (c) crack propagation region with cavitated epoxy and debonded/pulled-out carbon and PPS fibres, and (d) a schematic of the crack locus.

5.4. Discussions

The mode-I fracture initiation and propagation energies of the base, CSR5, CSR10, PPS10, PPS15, PPS20 and hybrid laminates are compared and presented in Table 5. 1. In comparison with the base laminates, the enhancement in $G_{I,C}$ and $G_{I,R}$ observed with

CSR particles, PPS veils and their combination is also presented. With 5 wt% CSR content, $G_{I,C}$ is hardly influenced, while a 55% increase in $G_{I,R}$ is observed. But, with 10 wt% CSR content, both $G_{I,C}$ and the $G_{I,R}$ are enhanced by 50% and 70%, respectively. In addition, with 10, 15, and 20 g/m^2 PPS veils, the $G_{I,C}$ are increased by 80%, 160% and 215%, respectively, while the $G_{I,R}$ is increased by 18%, 67% and 75%, respectively. Although a significant improvement in the $G_{I,C}$ values, the crack migration is adversely affected $G_{I,R}$ (*i.e.* falling R-curves) and decreased the $G_{I,R}$ values in comparison with the $G_{I,C}$ values. However, the incorporation of CSR particles influenced the crack path (*i.e.* constrained mode-I crack path within the PPS veil) and significant improvement was achieved for both the $G_{I,C}$ and $G_{I,R}$ values (by 245% and 275%, respectively).

Table 5. 1| The mode-I fracture initiation and propagation energies (*i.e.* $G_{I,C}$ and $G_{I,R}$) of the base, CSR5, CSR10, PPS10, PPS15, PPS20 and hybrid laminates.

Material system (Acronym)	$G_{I,C}$ (J/m^2)	$G_{I,R}$ (J/m^2)	Variation in $G_{I,C}$	Variation in $G_{I,R}$
Epoxy (Base)	294 ± 7	315 ± 8	-	-
Epoxy + CSR 5 wt% (CSR5)	289 ± 6	487 ± 37	-2%	+55%
Epoxy + CSR 10 wt% (CSR10)	445 ± 21	544 ± 29	+50%	+70%
Epoxy + 10 g/m^2 PPS veil (PPS10)	526 ± 38	371 ± 26	+80%	+18%
Epoxy + 15 g/m^2 PPS veil (PPS15)	763 ± 55	526 ± 38	+160%	+67%
Epoxy + 20 g/m^2 PPS veil (PPS20)	830 ± 49	550 ± 10	+215%	+75%
Epoxy + CSR 10 wt% + 20 g/m^2 PPS veil (Hybrid)	1016 ± 80	1179 ± 5	+245%	+275%

The initiation and propagation fracture energies of the laminates are compared under mode-I loading, see Figure 5. 6. The data points associated with PPS10, PPS15 and PPS20 laminates below the diagonal line indicate that fracture propagation energies are lower than the fracture initiation energies (representing falling R-curves). In addition, the data points associated with CSR5 and CSR10 laminates are above the diagonal line, which represents the rising R-curves (fracture propagation energies are higher than the fracture initiation energies). When compared to PPS20 laminates, the data point associated with the hybrid laminate is above the diagonal line with a

significant positive vertical shift, which represents rising R-curves and the beneficial influence of hybrid toughening on mode-I fracture energies.

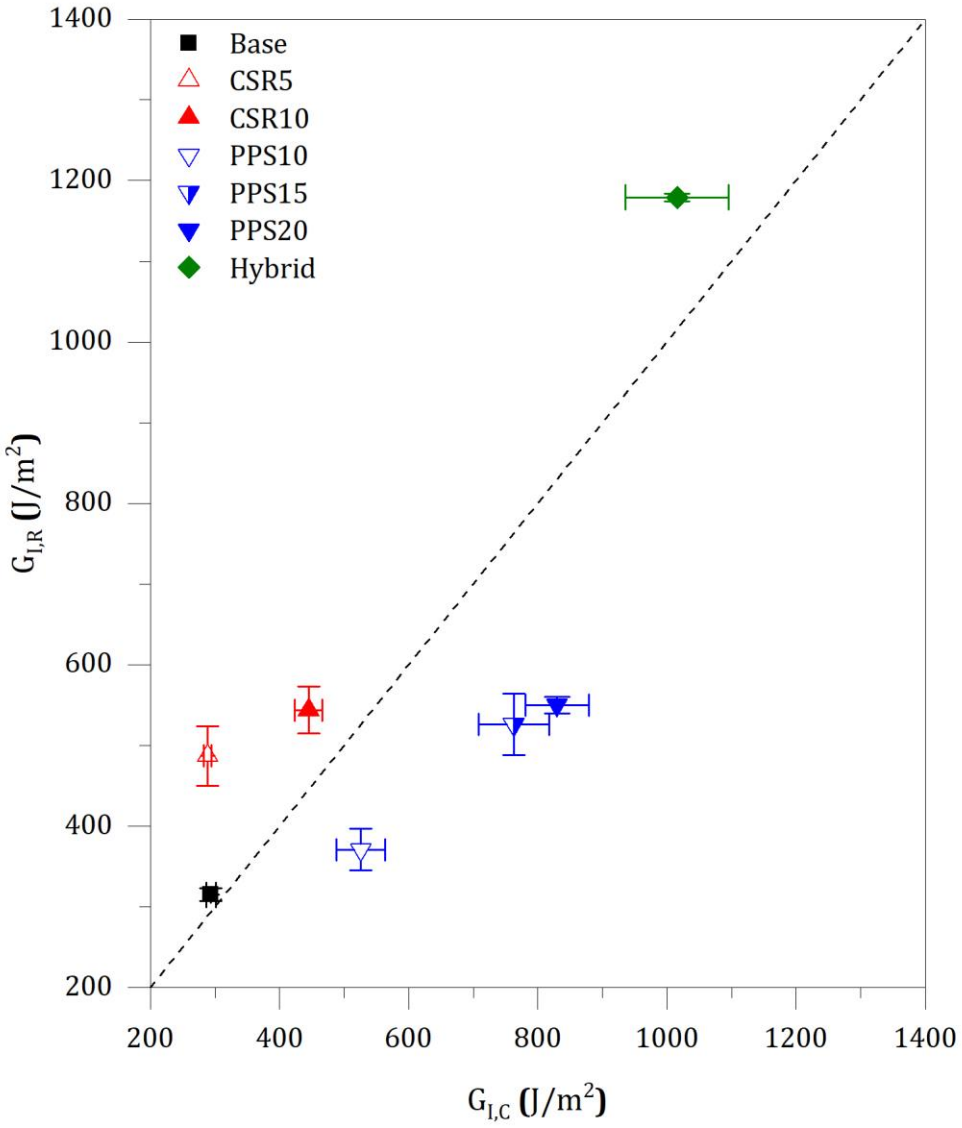

Figure 5. 6| Correlation between $G_{I,C}$ vs $G_{I,R}$ in the base, CSR5, CSR10, PPS10, PPS15, PPS20 and hybrid laminates.

Several studies demonstrated that the fracture performance of the veil toughened composite laminates is dependent on the areal weight of veils [27,49,51]. The fracture initiation and propagation fracture energies with respect to the areal weight of PPS veils are shown in Figure 5. 7. A significant improvement in $G_{I,C}$ is seen with increasing areal weight, which indicates the energy dissipation with toughening mechanisms via PPS fibres (~530 J/m^2 with 10 g/m^2, ~770 J/m^2 with 15 and ~830 J/m^2 with 20 g/m^2).

However, the fracture propagation energies of PPS toughened laminates are lower compared to the achievement obtained for the initiation. For the hybrid toughened laminates, considerable increases in G_{IC} and G_{IR} are obtained and fractographical observations indicate that the CSR particles incorporation changed the crack locus (crack tip predominantly was within the PPS veils). Therefore, this study indicates that the hybrid toughening approach is a beneficial route to enhance mode-I fracture energies further and does not require an additional increase in areal weight and a complicated manufacturing route.

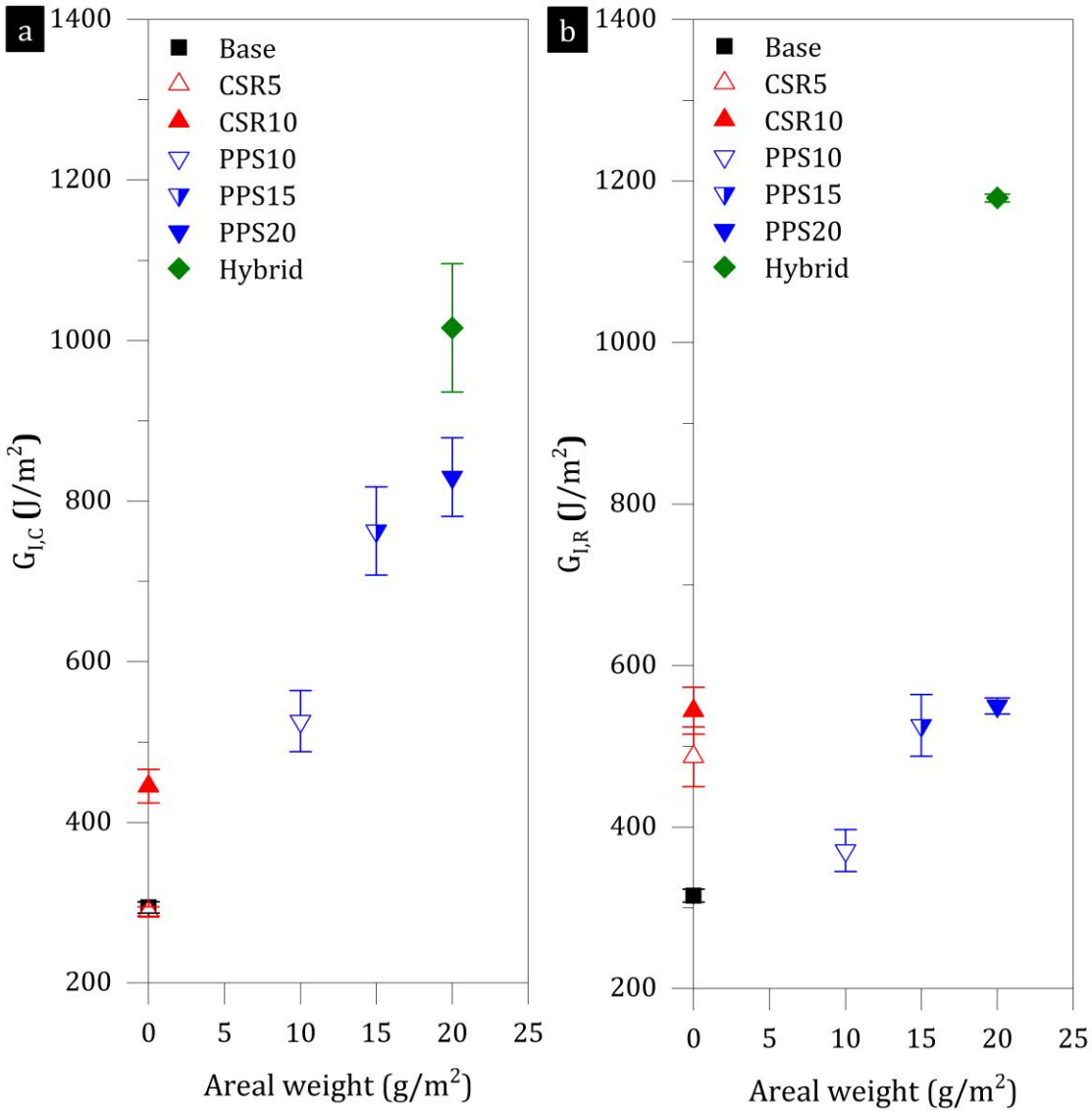

Figure 5. 7| The effect of the areal weight of PPS veils on (a) $G_{I,C}$, and (b) $G_{I,R}$.

5.5. Conclusions

Chapter 5 investigates the hybrid toughened laminates and how the use of PPS veils with CSR particles content influence the crack tip migration and R-curves under mode-I loading condition. The conclusions below are drawn in this chapter:

- *The influence of the CSR particle content:* Marginally rising R-curves were obtained from the composite laminates with 5wt% and 10 wt% CSR particle content (Figure 5. 1b). With 5 wt% particle content, the $G_{I,C}$ is hardly changed and the $G_{I,R}$ is enhanced by 50%. The $G_{I,C}$ and $G_{I,R}$ are increased by 55% and 75% with 10 wt% particle content. The micrographs indicate cavitated matrix between fibres and carbon fibre bridging, also exposed crack tip migration into the adjacent lamina (Figure 5. 3).
- *The influence of the PPS veil:* PPS veils significantly improved the mode-I fracture energies of the PPS10, PPS15 and PPS20 laminates. The $G_{I,C}$ is increased significantly, by 80%, 160% and 215% with 10, 15 and 20 g/m^2 areal weights, respectively (see Table 5. 1). However, the enhancement in $G_{I,R}$ is considerably lower compared to that of $G_{I,C}$ (*i.e.* 18%, 67% and 75% with 10, 15 and 20 g/m^2 areal weights, respectively). The micrographs expose PPS fibre-based fracture mechanisms (*e.g.* PPS debonding and PPS fibre pull-out during initiation) just behind pre-crack, and considerable crack migration into the neighbouring lamina with carbon fibre debonding and bridging during crack growth (Figure 5. 4). Increasing areal weight increased the mode-I fracture energies of PPS toughened laminates.
- *The influence of the CSR particle content and PPS veil together:* The PPS veils with CSR particle content positively influenced the mode-I fracture energies of the hybrid laminates (The $G_{I,C}$ and $G_{I,R}$ are increased by 245% and 275%, respectively). A considerably rising R-curve was obtained from the hybrid laminates. The micrographs confirmed PPS fibre debonding, carbon fibre debonding, fibre bridging and matrix cavitation without considerable crack migration into the neighbouring laminae with carbon fibre debonding and bridging during crack growth.

This chapter indicates that a hybrid effect with the CSR particle content and PPS veils was developed for composite laminates under mode-I loading. Thus, the hybrid toughening approach can help manufacture significantly toughened laminates using

veils with low areal weight without significant reduction in in-plane properties for the loading conditions related to the mode-I loading.

CHAPTER 6: Mode-II Interlaminar Fracture Energies of Hybrid Toughened Composite Laminates

6.1. Introduction

The previous chapter indicates that the hybrid toughening strategy provides a synergistic improvement in mode-I fracture properties for the investigated composite material system. Followingly, this chapter investigates the influence of the hybrid toughening approach on mode-II fracture properties for the composite material system.

The mode-II interlaminar fracture energies of the composite laminates were calculated with the 4-point bend end-notched flexure test method (4-ENF) following the procedures as explained in the Refs [206,207]. Initiation mode-II fracture energies, $G_{II,C}$, of the composite laminates were determined using a non-linear point approach, and propagation values for mode-II fracture energies, $G_{II,R}$ were determined by taking the average values obtained from the plateau region (*i.e.* where crack extension is between 20 and 40 mm) of the R-curves.

After the mechanical tests, fracture surfaces of the composite laminates were examined with SEM and the fracture mechanisms governing the fracture resistance under mode-II loading for the composite laminates were investigated.

6.2. 4-ENF Test Results

The P-δ curves and the R-curves of the base, CSR5, CSR10, PPS10, PPS15, PPS20 and hybrid laminates obtained from 4-ENF mechanical tests are presented in Figure 6. 1. As can be seen from Figure 6. 1a, all laminates exhibited gradual mode-II crack growth. However, the mode-II crack behaviour and the energy required for crack initiation and propagation vary depending on the toughening route (see Figure 6. 1a). Variations in the peak load generation and the area enclosed by the loading and unloading path are noticeably different. In comparison to the base laminate, the P-δ curves of CSR5 and CSR10 show that CSR particle content adversely affected peak load and the load sustained during mode-II crack growth. The adverse effect is more visible for the

CSR10 laminate. The P-δ curves of PPS10, PPS15, and PPS20 laminates indicate that the presence of PPS at the interlaminar region increased the load generation at the onset of crack growth and the area enclosed by the loading and unloading path indicates fracture energy is significantly enhanced with PPS veils compared to the base laminate. The P-δ curves of the PPS10, PPS15, and PPS20 laminates also demonstrate that the increase in areal weight has a marginal effect on mode-II crack behaviour. Moreover, the P-δ curve of the hybrid laminate shows that the load generation at the onset of crack growth and the area enclosed by the loading and unloading path marginally decreased compared to the PPS20 laminate. The adverse effect of the CSR particle content in the epoxy adversely affected the mode-II fracture properties of the hybrid laminates, as expected.

The R-curves of composite laminates indicate the variation of mode-II fracture energies with respect to crack extension as shown in Figure 6. 1b. The R-curve of the base laminate shows a decreasing trend and the behaviour of the CSR5 laminate is also similar to the base laminate. However, the CSR10 laminate exhibited a linear R-curve. These indicate that the base, CSR5 and CSR10 laminates present no significant energy dissipation mechanisms during crack growth.

Moreover, the PPS10, PPS15, and PPS20 laminates exhibited considerably falling R-curves, although significantly higher initiation and propagation are higher. Figure 6. 1b indicates that fracture initiation and propagation energies increase with the increasing areal weight of PPS veils, yet the R-curves follow a similar trend (*i.e.* initially increasing followed by falling trend until reaching steady-state segment). It indicates that energy dissipation mechanisms were effective at the onset of the crack growth, then the efficiency of the energy dissipation mechanisms slightly decreases with further crack growth. However, the hybrid laminate exhibited increasing R-curves with significant enhancement in fracture initiation and propagation energies in mode-II compared to the base laminate.

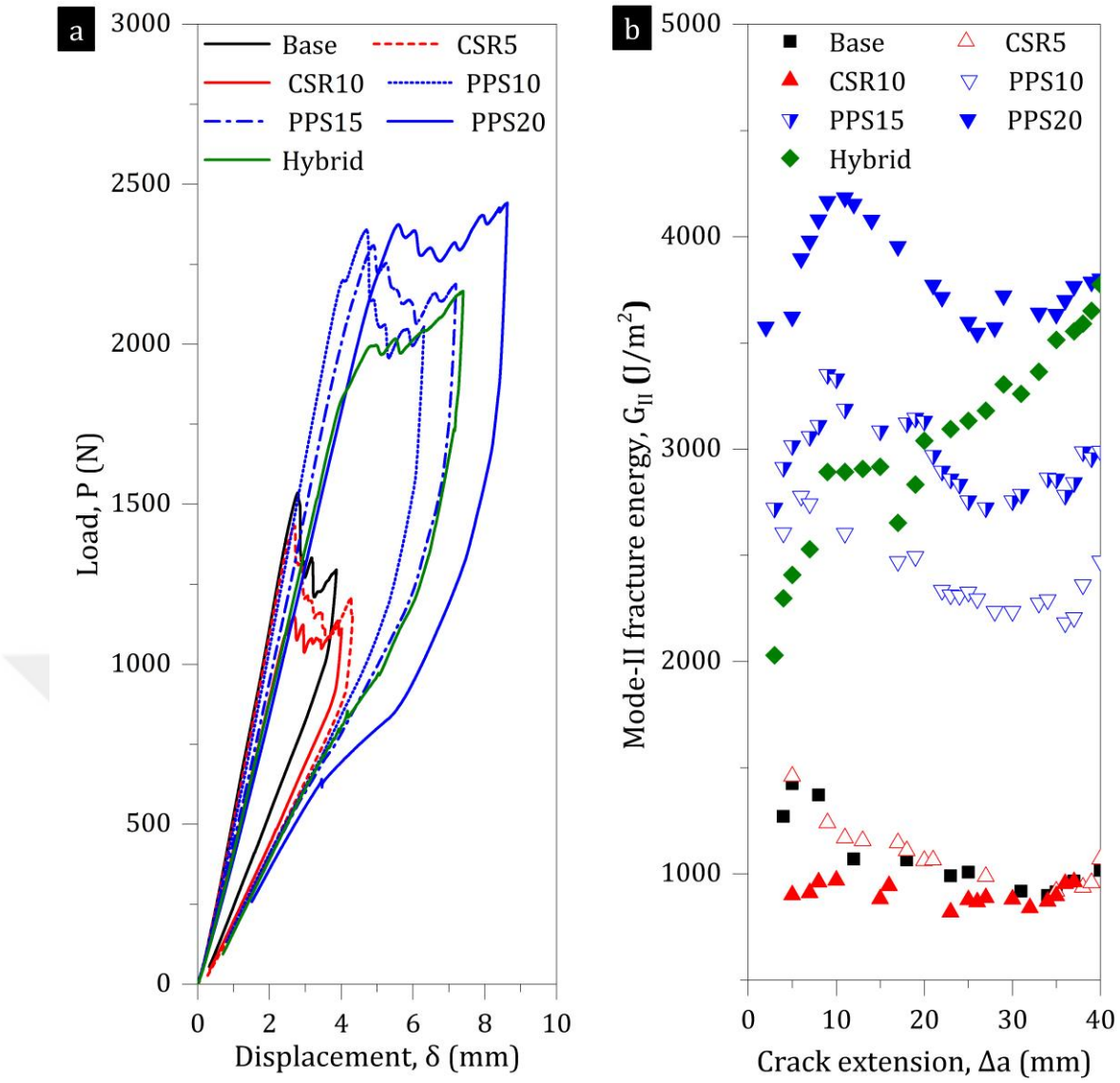

Figure 6. 1| Comparison of the mode-II fracture behaviour of the base, PPS10, PPS15, PPS20 and hybrid laminates: (a) load-displacement, *i.e.* P-δ, curves and (b) the R-curves, *i.e.* mode-I fracture energies vs crack extension, G_I vs Δa.

6.3. Mode-II Toughening Mechanisms

The fracture surfaces of the laminates were investigated with a SEM to understand toughening mechanisms leading to the fracture resistance and crack path of the composite laminates under mode-II loading. The pair of the fracture surfaces with micrographs obtained from the initiation and propagation regions of the base, CSR10, PPS20 and hybrid toughened laminates were presented in Figures 6. 2 – 6. 5.

Figure 6. 2a shows the pair of the fracture surfaces of the base laminate. The stitch patterns are visible on the fracture surfaces for the crack extension of up to ~20 mm.

For the crack extension of more than 20 mm, the stitching yarn patterns are less visible, covered with carbon fibres. This indicates that the crack tip was initiated from the resin-rich region between the adjacent layers, then migrated into the neighbouring laminae with further crack growth, exposing carbon fibres. The micrographs taken from the initiation and propagation regions (see Figure 6. 2a and -b, respectively) indicate stitch yarns and exposed carbon fibres. A schematic given in Figure 6. 2d demonstrates the crack path for the base laminate under mode-II loading. As the mode-II fracture initiation energy (*i.e.* $G_{II,C}$) is associated with intrinsic energy dissipation mechanisms ahead of the pre-crack front, the micrographs from the initiation region (see Figure 6. 2b) indicate considerable energy dissipation with debonded and pulled-out stitch yarn fibres and matrix cusps (which are typical in mode-II fracture developing from the coalescence of sinusoidal shaped micro-cracks occurred perpendicular to maximum principal tensile stress in the resin-rich region [216]). The micrographs from the propagation region (see Figure 6. 2c) exposes that the crack migrated into the neighbouring lamina with exposed carbon fibres and matrix cusps. The R-curve for the base laminate (Figure 6. 1b), together with the observations made from the micrographs (Figure 6. 2), indicate that the resistance to crack growth marginally decreased with crack migration and reached a steady state. The mode-II fracture propagation energy (*i.e.* $G_{II,R}$) values from the base laminate are marginally lower than the $G_{II,C}$ values, indicating that no significant extrinsic toughening mechanisms were introduced.

A pair of fracture surfaces from the CSR10 laminate is given in Figure 6. 3a. The stitch yarns on the fracture surface are visible, which indicates that crack propagation was within the interlaminar region. The micrograph obtained from the initiation region (see Figure 6. 3b) demonstrate the debonded stitch yarn and exposed carbon fibres with cavitated cusps. The micrograph taken from the propagation region (Figure 6. 3c) also indicates cavitated cusps and carbon fibres. The R-curves of laminate indicated that the incorporation of the CSR particles decreases the load generation at the onset of crack growth and during crack growth. Although the cavitated matrix cusps were observed on the fracture surfaces, the energy dissipation mechanisms due to the CSR particle incorporation did not enhance the mode-II fracture energies. Also, Figure 6. 3d schematically indicates the crack growth path for the CSR10 laminate in mode-II.

The fracture surfaces of PPS20 laminates with micrographs obtained from the initiation and propagation regions are given in Figure 6. 4. The fracture surface features indicate the PPS veil (cloudy white finish) on one surface and exposed stitch patterns on another, see Figure 6. 4a. This indicates that the crack initially propagated within the PPS veil, then grew further along the neighbouring lamina while predominantly remaining within PPS veils. The micrograph taken from the initiation region (see Figure 6. 4b) indicates the crack growth was within PPS veils with matrix cusps on the fracture surface. Also, the smooth and clean surfaces of PPS fibres demonstrate the weak adhesion fibre-matrix interface. The weak fibre-matrix adhesion could have initiated fibre debonding and influenced the crack growth. Considering R-curves (see Figure 6. 1b), it can be suggested that toughening mechanism obtained via PPS fibres significantly improved the mode-II fracture initiation and propagation energies. However, the R-curves of the PPS veil toughened laminates initially experienced a rising segment followed by a falling segment, which indicates that the initial crack growth within the PPS veil is associated with the rising R-curves. Then, crack migration towards the neighbouring laminae surface reduced the fracture propagation energies. Figure 6. 4d schematically indicates the crack growth path for PPS20 laminates in mode-II.

Figure 6. 5 indicates the a pair of fracture surfaces obtained from the hybrid laminates with micrographs taken from the initiation and propagation regions. A pair of fracture surfaces indicates that the crack growth was predominantly within PPS veils, see Figure 6. 5a. Unlike the PPS20 laminate, the crack path appeared to have remained within PPS veils without considerable migration along the neighbouring lamina. The micrographs from the crack initiation region demonstrate debonded and loose PPS fibres and expose the carbon fibres with cavitated epoxy cusps as seen in Figure 6. 5b. Similarly, the micrographs from the crack propagation region also reveal debonded and loose PPS fibres, and exposed carbon fibres with cavitated epoxy cusps, see Figure 6. 5c. The crack path is schematically given in Figure 6. 5d.

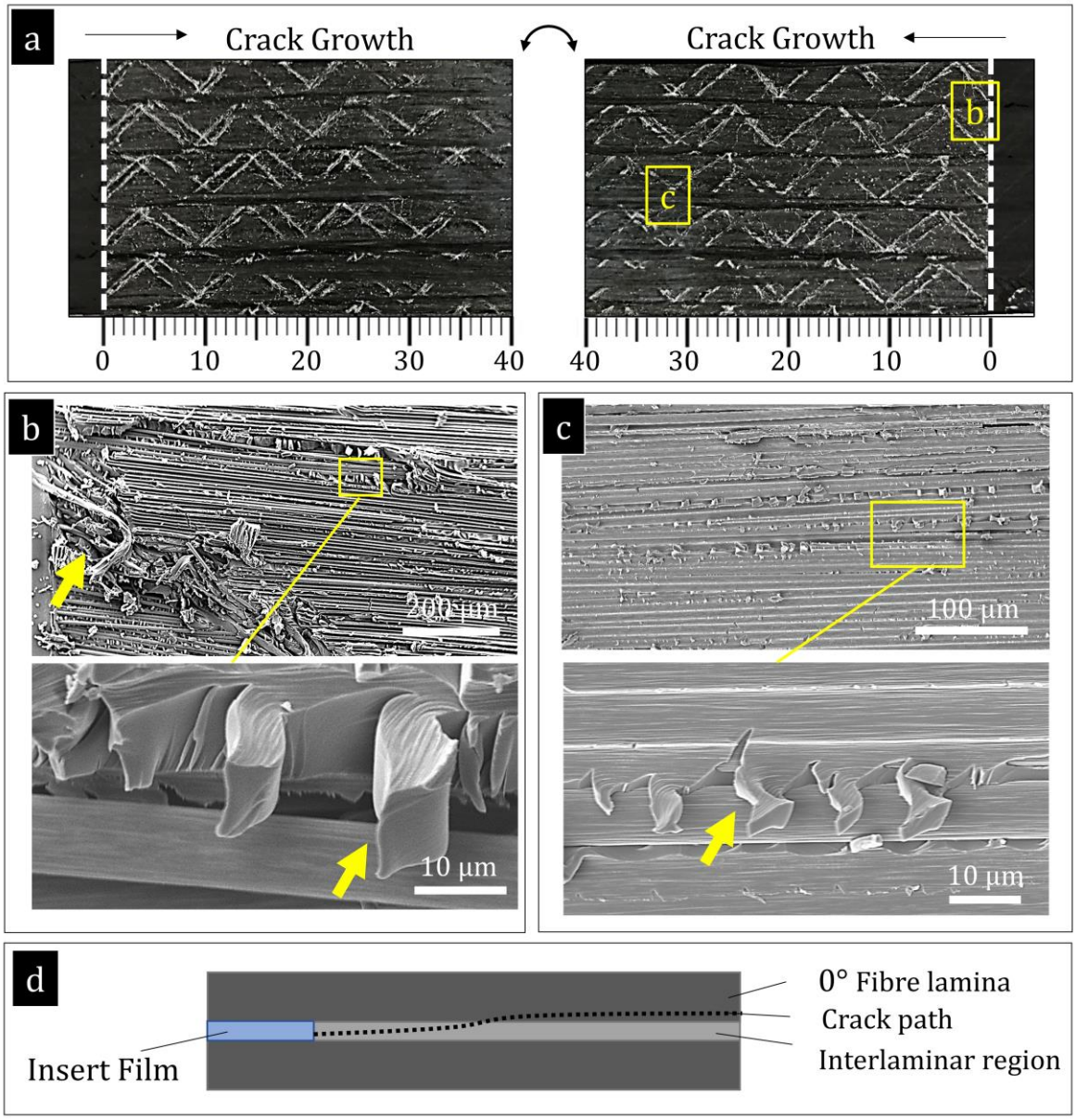

Figure 6. 2| The mode-II fracture surface features of the base laminate: (a) a pair of fracture surfaces, (b) the crack initiation region with debonded stitch yarn, exposed carbon fibres with matrix cusps, (c) the crack propagation region with the exposed carbon fibres and matrix cusps, and (d) a schematic representation of the crack growth locus.

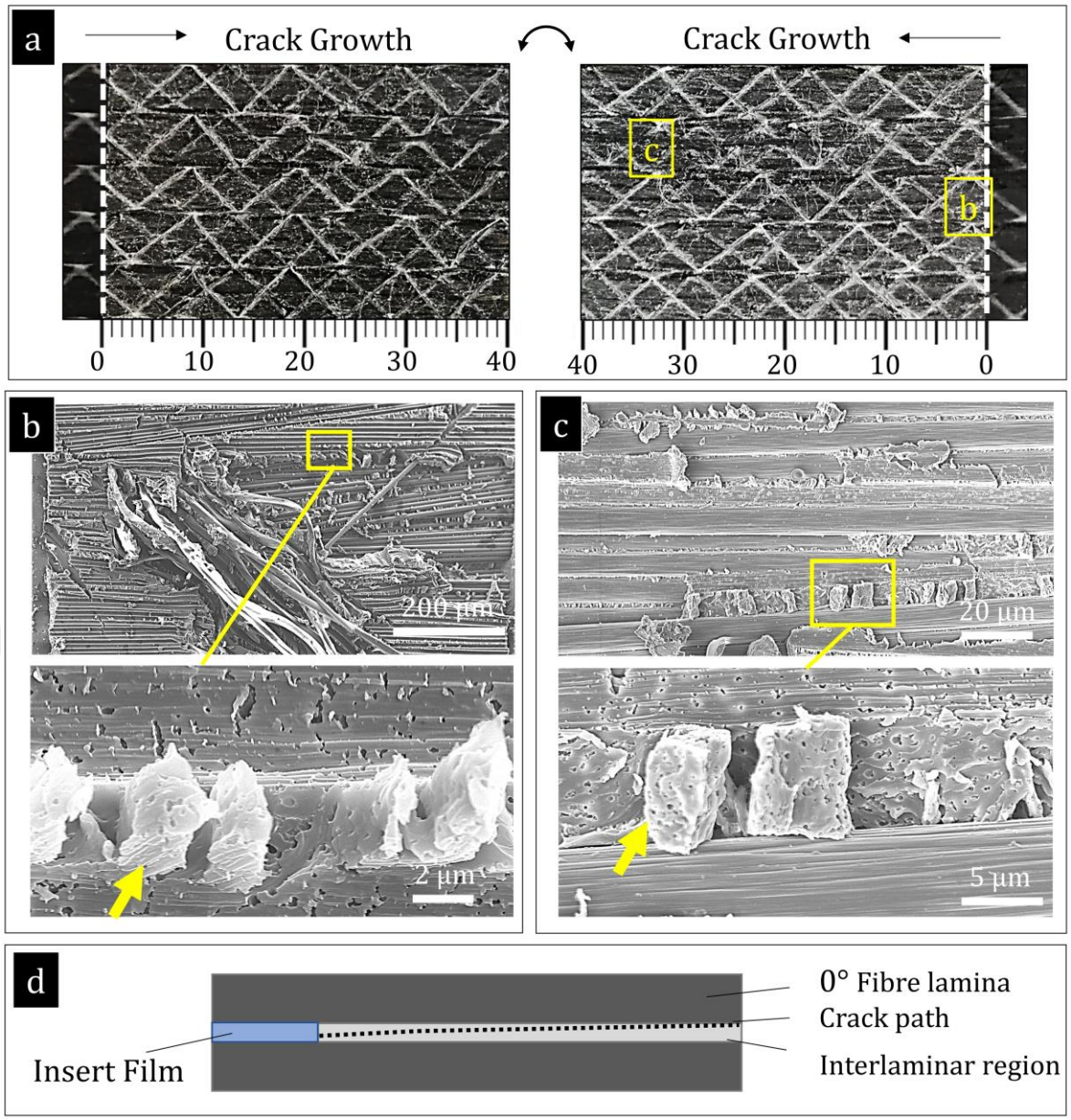

Figure 6. 3| The mode-II fracture surface features of the CSR10 laminate: (a) a pair of fracture surfaces, (b) the crack initiation region with the debonded stitch yarn, exposed carbon fibres and cavitated matrix cusps, (c) the crack propagation region with exposed carbon fibres and matrix cusps, and (d) a schematic representation of the crack growth locus.

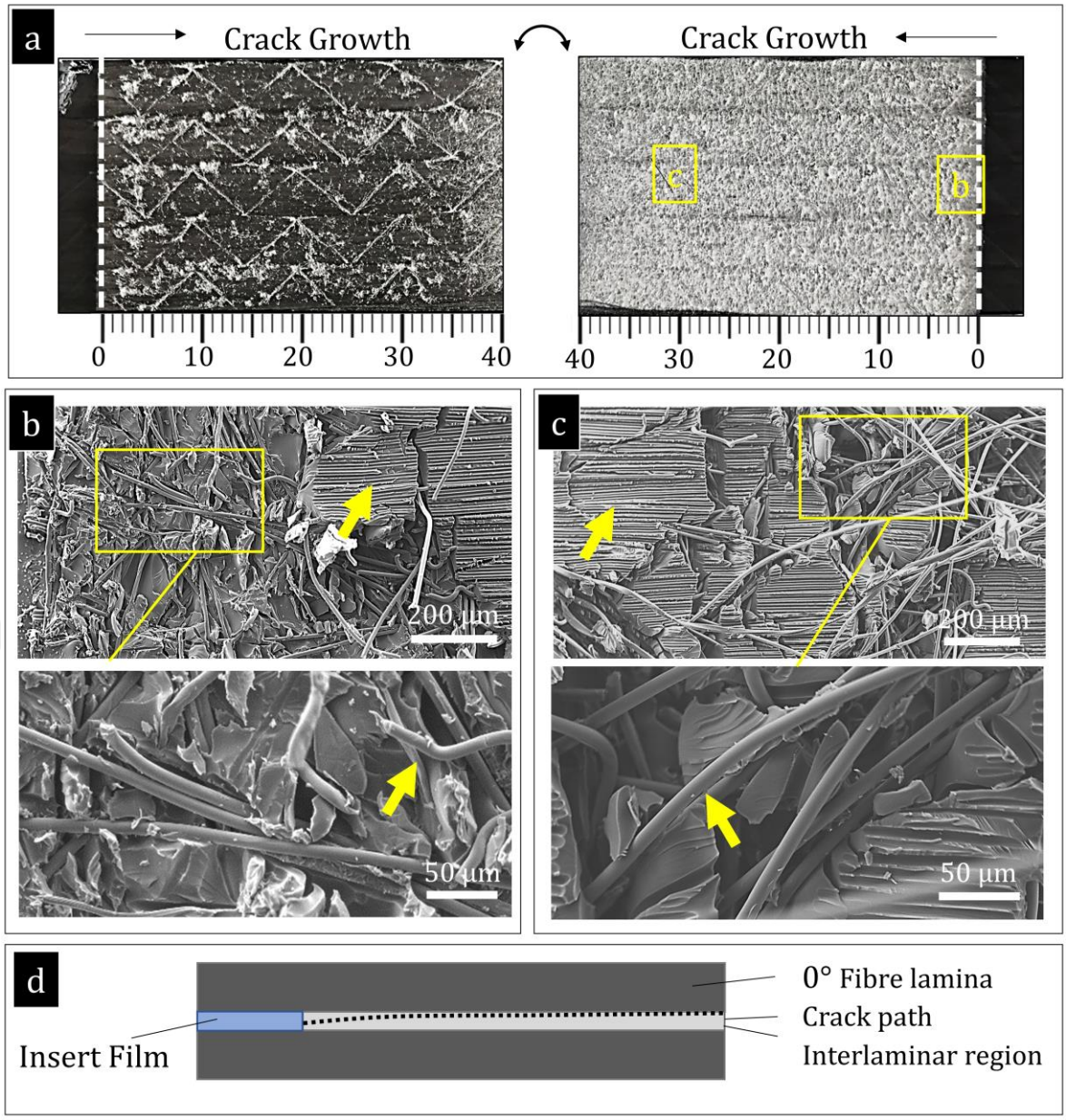

Figure 6. 4| The mode-II fracture surface features of the PPS20 laminate: (a) a pair of fracture surfaces, (b) crack initiation region with debonded PPS fibres and matrix cusps, and (c) crack propagation region with debonded PPS fibres, exposed carbon fibres and matrix cusps, and (d) a schematic representation of the crack growth locus.

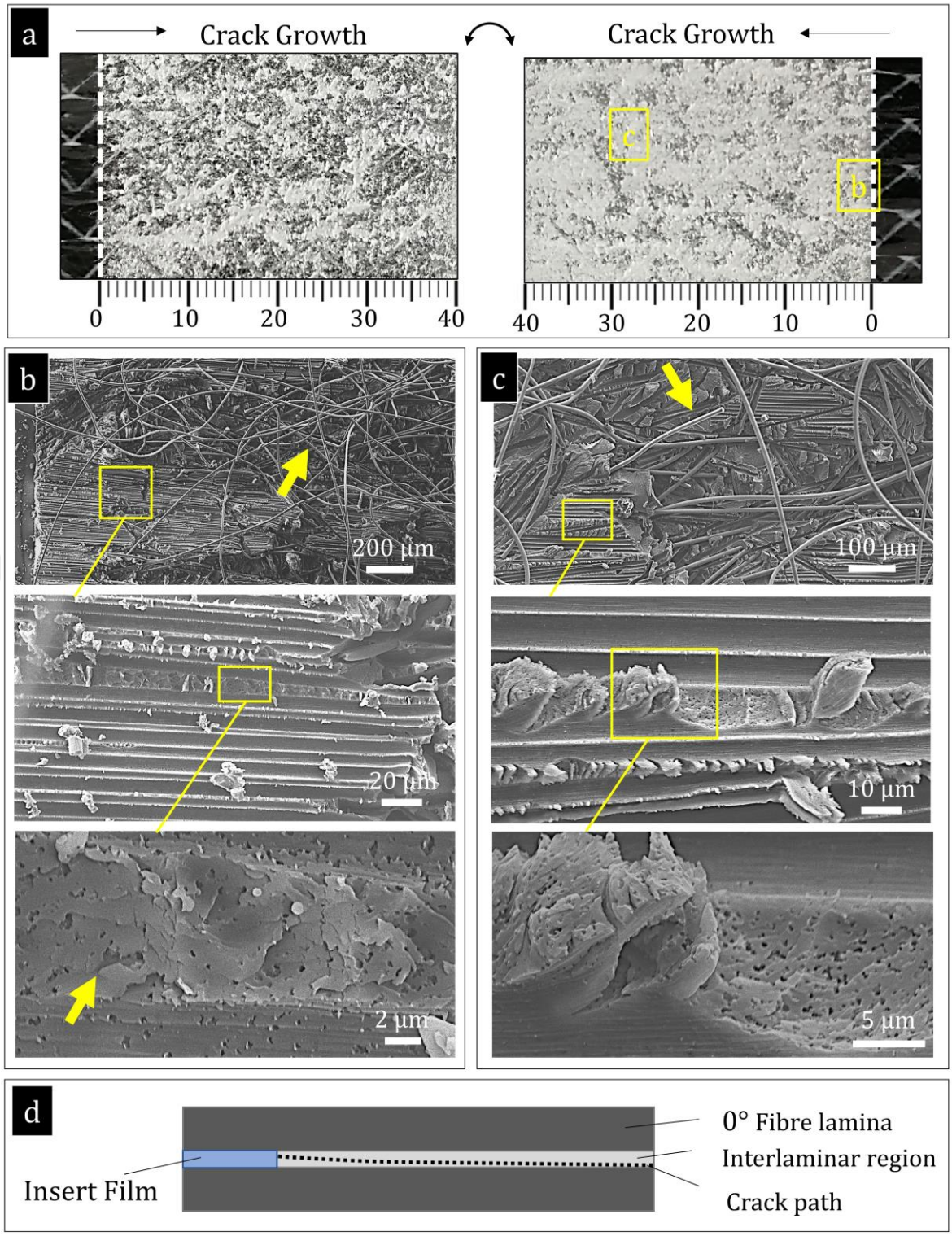

Figure 6. 5| The mode-II fracture surface features of the hybrid laminate: (a) a pair of fracture surfaces indicating, (b) crack initiation region with debonded PPS fibres, exposed carbon fibres and cavitated matrix, (c) crack propagation region with debonded PPS fibres, exposed carbon fibres and cavitated matrix cusps, and (d) a schematic representation of the crack growth locus.

6.4. Discussions

The $G_{II,R}$ and $G_{II,C}$ of the base, CSR5, CSR10, PPS10, PPS15, PPS20 and hybrid laminates are given in Table 6. 1. This table also includes the variation of fracture energies in comparison with the fracture energies of the base laminate. With 5 wt% CSR content, no significant change in $G_{II,C}$ and $G_{II,R}$ was observed. With 10 wt% CSR content, both $G_{II,C}$ and $G_{II,R}$ decreased by 35% and 15%, respectively. This indicates the negative influence of CSR particle content on mode-II fracture energies. With 10, 15, and 20 g/m^2 PPS veils, the $G_{II,C}$ values are increased by 97%, 110% and 150%, respectively, while the $G_{II,R}$ values are increased by 155%, 190% and 255%, respectively. It shows that the enhancement in $G_{II,C}$ and $G_{II,R}$ values increased with increasing the areal weight of PPS veils. With the 20 g/m^2 PPS veils and 10 wt% CSR content, $G_{II,C}$ and $G_{II,R}$ values of the hybrid laminates are increased by 64% and 215%, which indicates the adverse of CSR particles on the hybrid laminates. However, it is worth noting that the hybrid laminates exhibited a rising R-curve, while PPS laminates exhibited a falling R-curve (see Figure 6. 1b).

Table 6. 1| The mode-II fracture initiation and propagation energies (*i.e.* $G_{II,C}$ and $G_{II,R}$) of the base, CSR5, CSR10, PPS10, PPS15, PPS20 and hybrid toughened composite laminates.

Material system (Acronym)	$G_{II,C}$ (J/m^2)	$G_{II,R}$ (J/m^2)	Variation in $G_{II,C}$	Variation in $G_{II,R}$
Epoxy (Base)	1340 ± 65	1022 ± 97	-	-
Epoxy + CSR 5 wt% (CSR5)	1331 ± 129	1058 ± 33	-1%	+3%
Epoxy + CSR 10 wt% (CSR10)	881 ± 48	877 ± 39	-35%	-15%
Epoxy + 10 g/m^2 PPS veil (PPS10)	2641 ± 128	2604 ± 307	+97%	+155%
Epoxy + 15 g/m^2 PPS veil (PPS15)	2821 ± 88	2970 ± 296	+110%	+190%
Epoxy + 20 g/m^2 PPS veil (PPS20)	3315 ± 248	3621 ± 366	+150%	+255%
Epoxy + CSR 10% + 20 g/m^2 PPS veil (Hybrid)	2201 ± 366	3203 ± 158	+64%	+215%

The comparison of the $G_{II,C}$ and $G_{II,R}$ values are shown in Figure 6. 6. The data points associated with the PPS10, PPS15 and PPS20 laminates are more or less along the diagonal line, which demonstrates that both fracture initiation and propagation energies are significantly enhanced. The data point associated with the CSR10 laminates represents falling R-curves, showing the adverse effect of CSR particle content on fracture energies. The data point associated with the hybrid laminate is above the diagonal line with a considerable negative shift along the horizontal axis, representing a rising R-curve and showing the adverse effect of CSR particle content on energy dissipation.

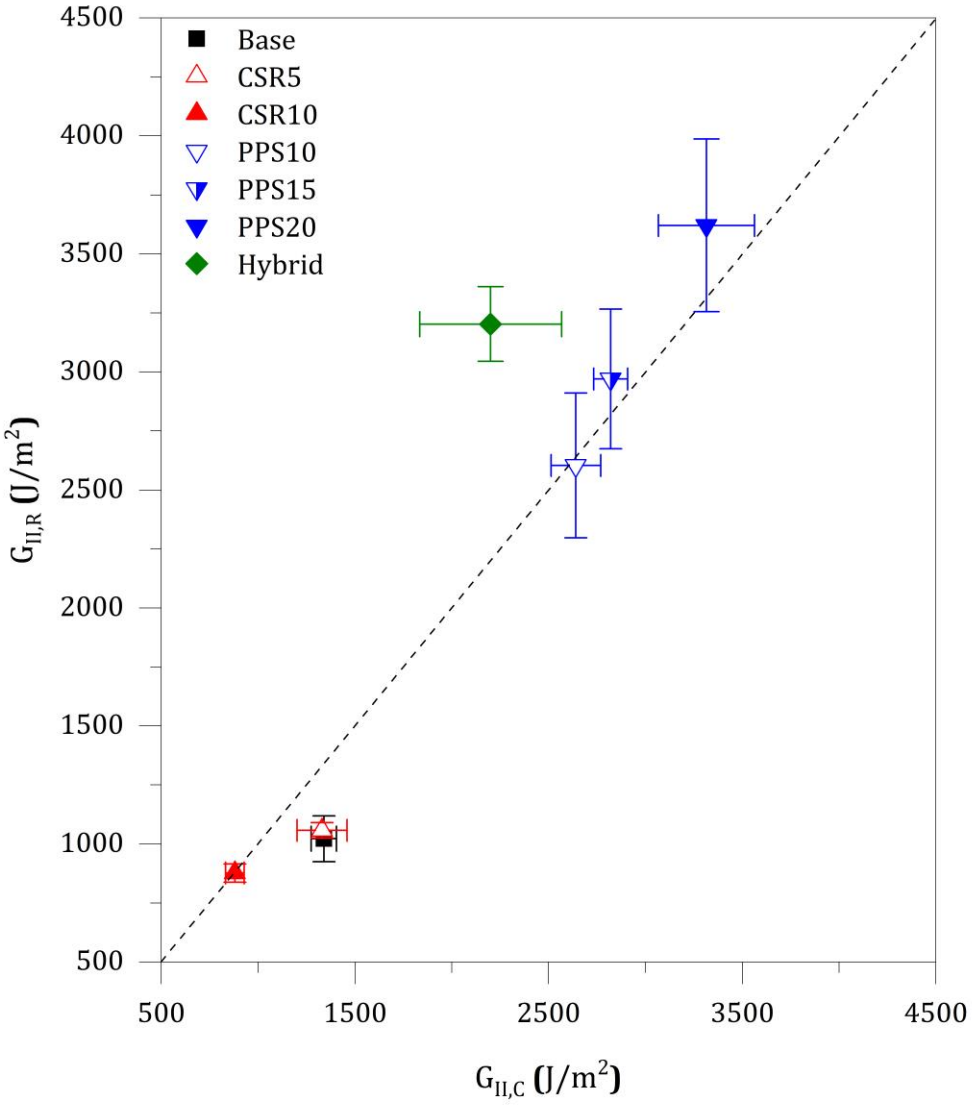

Figure 6. 6| Correlation between $G_{II,C}$ vs $G_{II,R}$ in the base, CSR5, CSR10, PPS10, PPS15, PPS20 and hybrid laminates.

Figure 6. 7 indicates the fracture initiation and propagation energies of the composite laminates with respect to the areal weight of PPS veils. A considerable increase in $G_{II,C}$ is observed with increasing areal weight from the PPS10, PPS15 and PPS20 laminates. The data points indicate a non-linear variation (~2650 J/m^2 with 10 g/m^2, ~2850 J/m^2 with 15 and ~3400 J/m^2 with 20 g/m^2). The data point associated with the hybrid laminate shows a significant reduction in $G_{II,C}$ with hybrid toughening. In addition, a considerable increase in $G_{II,R}$ is seen with increasing areal weight from the PPS10, PPS15 and PPS20 laminates (see Figure 6. 7b). The data points indicate a non-linear variation (~2700 J/m^2 with 10 g/m^2, ~3000 J/m^2 with 15 and ~3650 J/m^2 with 20 g/m^2). The data point associated with the hybrid laminate shows significant additional improvements in $G_{II,R}$ with hybrid toughening.

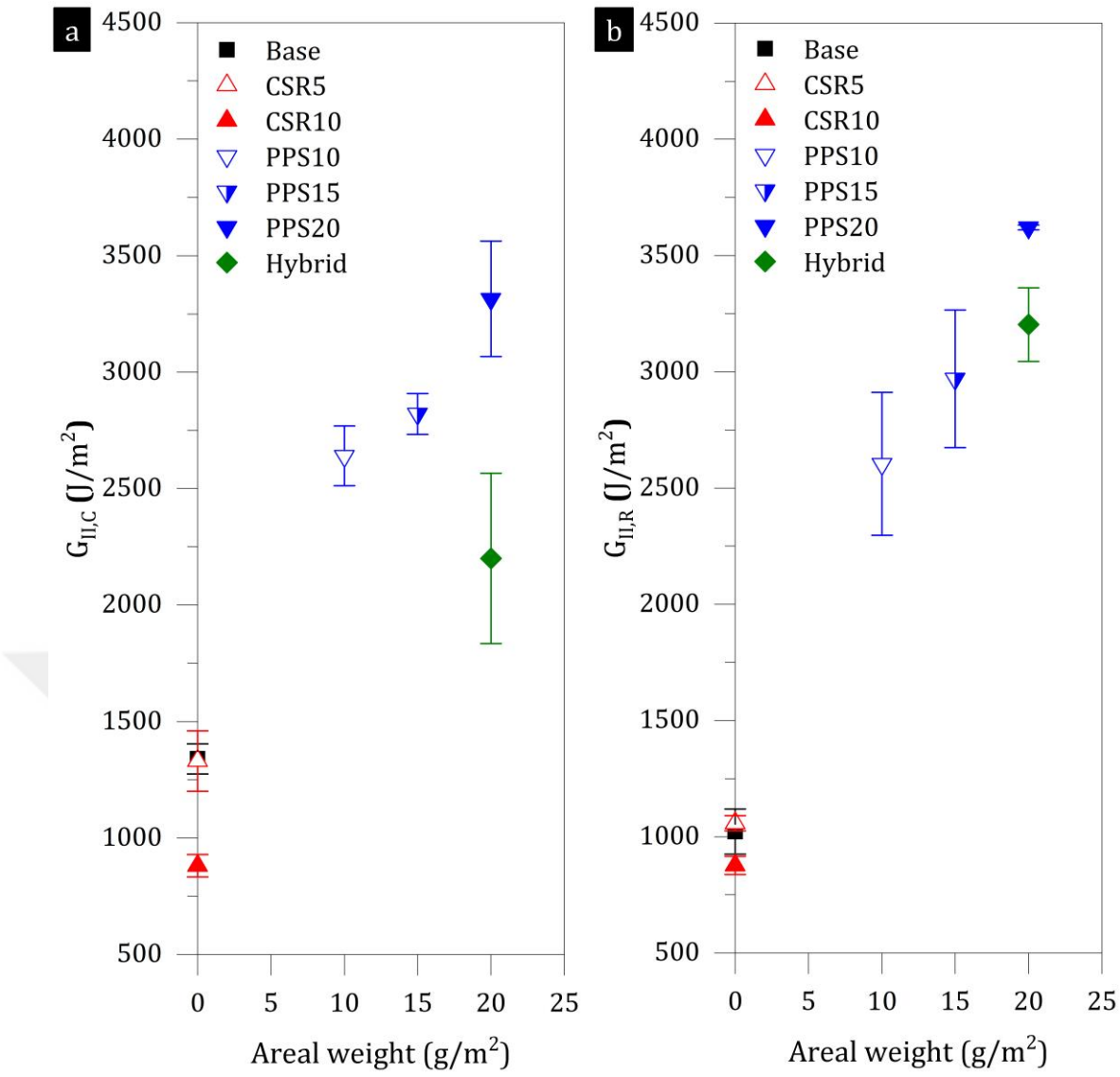

Figure 6. 7| The effect of the areal weight of PPS veils on (a) $G_{II,C}$, and (b) $G_{II,R}$.

For composite laminates, the mode-II fracture properties are usually 3-4 times greater than their mode-I fracture properties. Table 6. 2 indicates the ratio of the mode-II fracture properties to the mode-I fracture for initiation and propagation for the material system investigated in this study. It is shown in this study that the hybrid use of the PPS veils and CSR particles can decrease the imbalance between mode-I and mode-II fracture properties by achieving considerable improvement in mode-I and mode-II. This indicates that the hybrid use of the PPS veils and CSR particle content offers damage tolerant composite laminates using veils with low areal weight for the loading conditions related to both mode-I and mode-II loadings, *e.g.* low-velocity transverse impact and post-impact compression loading.

Table 6. 2| The fracture toughness ratios (G_{II}/G_I) of the laminates for crack initiation and propagation.

Material system (Acronym)	$G_{II,C}/G_{I,C}$	$G_{II,R}/G_{I,R}$
Epoxy (Base)	4.56	3.24
Epoxy + CSR 5 wt% (CSR5)	4.60	2.17
Epoxy + CSR 10 wt% (CSR10)	3.05	1.61
Epoxy + 10 g/m2 PPS veil (PPS10)	5.02	7.02
Epoxy + 15 g/m2 PPS veil (PPS15)	3.70	5.65
Epoxy + 20 g/m2 PPS veil (PPS20)	3.99	6.58
Epoxy + CSR 10% + 20 g/m2 PPS veil (Hybrid)	2.17	2.72

6.5. Conclusions

Chapter 6 investigates the hybrid toughened laminates and how the use of PPS veils with CSR particles content influence the crack tip migration and R-curves under mode-II loading condition. The conclusions below are drawn in this chapter:

- *The influence of the CSR particle content:* CSR5 laminates with 5% CSR particle content demonstrated no significant change in mode-II compared to the base laminates. 10 wt% CSR particle content exhibited an adverse effect on mode-II fracture properties of the CSR10 laminates ($G_{I,C}$ and $G_{I,R}$ are decreased by ~35% and ~155%). The micrographs confirmed (see Figure 6. 3) cavitated matrix cusps between fibres, and also revealed no significant crack migration into the neighbouring lamina.

- *The influence of the PPS veil:* PPS10, PPS15 and PPS20 laminates exhibited marginally increasing R-curves (see Figure 6. 1b). The $G_{II,C}$ is improved by ~97%, ~110% and ~150% with 10, 15 and 20 g/m^2 areal weights, respectively; and the $G_{II,R}$ is enhanced by ~155%, ~190% and ~255% with 10, 15 and 20 g/m^2 areal weights, respectively (see Table 6. 1). The micrographs confirmed PPS fibre debonding with no considerable crack migration into the neighbouring lamina. Increasing areal weight increased the mode-II fracture energies of the PPS toughened laminates.

- *The influence of the CSR particle content and PPS veil together:* Although a considerably rising R-curve was obtained from the hybrid laminates (see Figure 6. 1b), mode-II fracture energies of the hybrid laminates showed a reduction compared to the PPS20 laminate (The $G_{II,C}$ and $G_{II,R}$ are improved by ~64% and ~215% compared to the base laminates, respectively). The adverse effect of the CSR particle content (examined from the CSR10 laminates) also adversely affected the mode-II fracture energies of the hybrid laminates. The micrographs confirmed PPS fibre debonding, carbon fibre debonding and cavitated matrix cusps between fibres without considerable crack migration into the neighbouring laminae during crack growth (Figure 6. 5).

It is shown that the hybrid use of the CSR particle and PPS veils can affect the behaviour of the R-curves for the laminates and successfully incorporated in vacuum infused laminates to enhance mode-I and mode-II fracture energies. The beneficial effect of hybrid toughening on mode-I fracture energy (which is often critical) shows that further enhancement can be achieved with the hybrid toughening approach. Although a slight reduction was observed from the hybrid laminates compared to the PPS laminates in mode-II, the hybrid toughened laminates only exhibited the rising R-curve, which is highly important for damage tolerant laminates. When evaluating the improvement achieved for mode-I and mode-II fracture properties, the hybrid use of the CSR particle and PPS veils can allow manufacturing damage tolerant composite laminates using veils with low areal weight.

CHAPTER 7: Low-Velocity Impact Response of Hybrid Toughened Composite Laminates

7.1. Introduction

The behaviour of the composite laminates under impact loading is predominantly related to their fracture performance of them under mode-I and mode-II loading [8,134,135]. The fracture performance of the hybrid toughened composite laminates under mode-I and mode-II loading conditions was characterised as reported in Chapters 5 and 6. This chapter presents the investigation of the out-of-plane low-velocity impact performance of the base, CSR10, PPS20 and hybrid laminates and how the fracture toughness properties influence the impact resistance of the laminates.

The drop-weight low-velocity impact was performed following to Prichard and Hogg protocol at varying impact levels (*i.e*. 2 J, 2.5 J, 3 J, 4 J, 5 J, 7.5 and 10 J) [129]. Then, the impact damage areas of the composite laminates were detected using a through-transmission ultrasonic scanner. After that, the composite laminates were sectioned and the failure mechanisms were investigated with an SEM to detect the sublaminar damage modes.

The low-velocity impact tests were performed in two different phases. In the first phase, the impact response of the laminates was investigated close to the delamination threshold region at 2J, 3J and 4 J impact levels. Then, the impact resistance of the composite laminates was investigated at varying ranges (*i.e.* 2.5 J, 5 J, 7.5 J and 10 J impact levels). Also, the fracture and impact properties of the composite laminates are correlated in this chapter.

7.2. Drop-Weight Impact Test Results

7.2.1. Impact Damage Threshold

The low-velocity impact tests were first performed at 2 J, 3 J and 4 J impact levels to investigate the response of the base, CSR10, PPS20, and hybrid laminates at the impact levels close to the delamination threshold and one sample was used for each test.

Force-time and force-displacement curves of composite laminates subjected to 2 J, 3 J and 4 J impact levels are given in Figure 7. 1 and Figure 7. 2, respectively. The unstable sudden drops in the loading path of the force-time and force-displacement curves indicate the critical contact load (*i.e.* delamination threshold) for the laminates under impact loading. Figure 7. 1 indicates that the base and CSR10 laminates exhibit a sudden drop at each impact level. For the PPS20 and hybrid laminates, the force-time curves include sudden drop only at the 4 J impact level. The force-time curves (see Figure 7. 1) also demonstrate that there is no significant increase in the loading path after the base and CSR10 laminates exhibited the sudden drops at the 2 J impact level. These findings suggest that the critical impact load is close to the 2 J impact for the base and CSR10 laminates. For 4 J impact, the force-time curves of the PPS20 exhibit the load increase after the sudden drop whereas the curve of the hybrid laminate experienced a slight increase after the sudden drop. This indicates that the impact damage threshold of the hybrid toughened laminate is close to 4 J and slightly higher when compared to the PPS20 laminate. The force-displacement curves of the laminates are enclosed as seen in Figure 7. 2, which suggests that the impactor did not penetrate through the composite laminates. Some of the kinetic energy of the impactor was absorbed via sublaminar damage modes of the laminates and some of that was used to rebound the impactor.

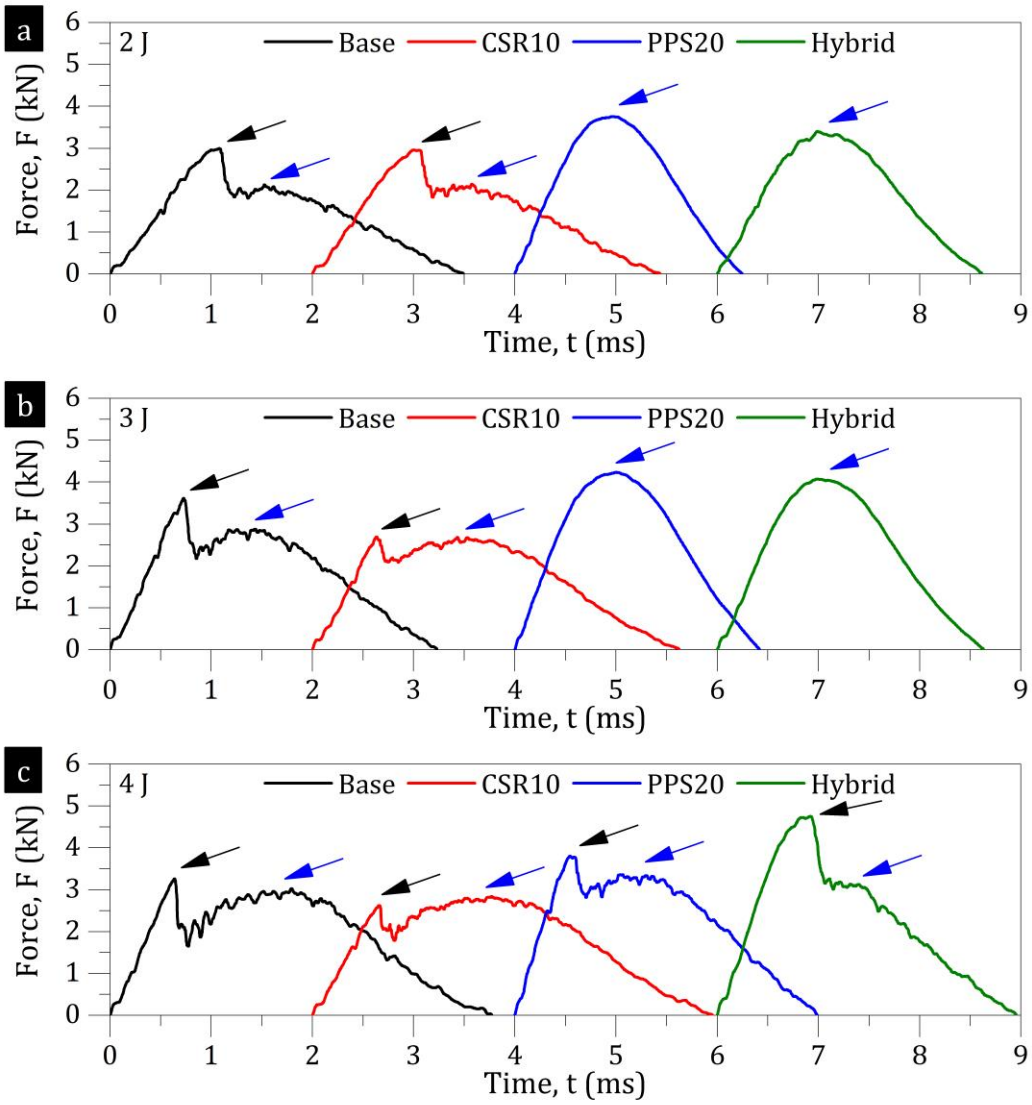

Figure 7. 1| The force-time curves of the composite laminates at (a) 2 J, (b) 3 J, and (c) 4 J impact levels (Note that the curves are given with 2 ms offset for a better clarity. Black and blue arrows indicate the threshold contact forces and maximum contact forces after the threshold, respectively.)

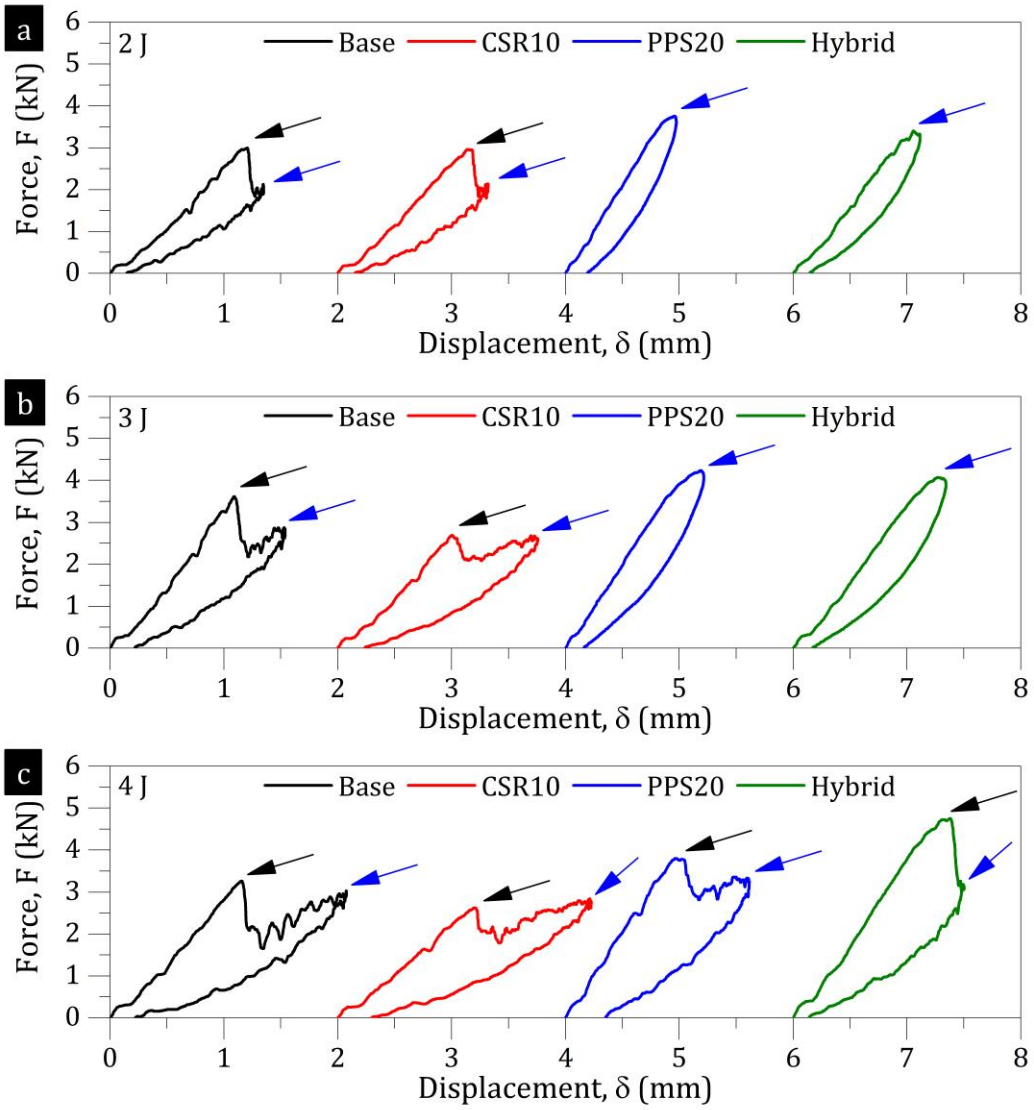

Figure 7. 2| The force-displacement curves of the composite laminates at (a) 2 J, (b) 3 J, and (c) 4 J impact levels (Note that the curves are given with 2 mm offset for a better clarity. Black and blue arrows indicate the threshold contact forces and maximum contact forces after the threshold, respectively).

For a better understanding, the projected damage areas were non-destructively detected using an ultrasonic C-scan in through the transmission mode after the impact damage was introduced to the laminates. Also, fracture surface features were investigated to understand the sublaminar damage modes occurred due to the impact loading. Figures 7. 3 – 7. 6 demonstrate the projected impact damage area obtained from the laminates and the fracture surface features with micrographs obtained with SEM. Prior to ultrasonic scanning of the composite laminates subjected to the impact loading, the composite laminates with no impact damage were scanned. The attenuation levels for the undamaged base, CSR10, PPS20 and hybrid laminates were

measured as 8.60 ± 2.30 dB, 11.22 ± 2.29 dB, 11.40 ± 3.00 dB and 15.02 ± 2.61 dB, respectively. The attenuation levels above these values for each composite laminate were accepted as a damaged region. C-scan images of the laminates also cover the attenuation profiles through the cross-sectional length of the laminates. Different profiles in attenuation values of the composite laminates were observed: (i) progressive decrease and (ii) sharp decreases depending on the growth of delamination failures. Progressive decreases in the attenuation profiles refer to the conical shape of the impact damage and sharp decreases in the profiles refer to the cylindrical shape of the impact damage. Figure 7. 3a indicates that the projected damage area of the base laminate is 1.44 cm^2, 1.74 cm^2 and 4.13 cm^2 at 2 J, 3 J and 4 J impact levels, respectively. At 2 J and 3 J impact levels, a progressively decreasing trend in the attenuation profiles were observed. This suggests that the delamination failure is expanded in larger area at the bottom layers as a result of shear matrix cracks undergoing the tension component of the bending moment under impact loading. A sharper decrease in the Y-attenuation profile of the base laminate subjected to impact loading at 4 J was observed, which suggests the delamination failure expanded within the damaged area at the multiple interlaminar regions. The cross-sectional observation of the base laminate (see Figure 7. 3b) shows the growth of the shear matrix cracks resulting in the delamination failure at multiple interlaminar regions expanded along a similar region within the area of the impact damage. Figure 7. 3c also confirms the shear cracks and delamination failures. Figure 7. 4a indicates the C-scan results of the CSR10 laminates. The CSR10 laminate includes a slightly lower damage area compared to the base laminate at the 2 J impact level. Also, attenuation profiles through the length of the CSR10 laminates indicate progressive decreases at 2 J and 3 J, which suggests that delaminated regions are larger in the bottom layers. At 4 J impact levels, the Y-attenuation profile of the CSR10 laminates exhibits a relatively sharper decrease. The cross-sectional observation of the CSR10 laminates indicates the multiple delamination failure extended within the damaged area as seen in Figure 7. 4b. The micrographs obtained from the CSR10 laminates confirm shear cracks and delamination failures as shown in Figure 7. 4c. Figure 7. 5a indicates the C-scan results obtained from the PPS20 laminates. For 2 J impact, no significant damage was observed (Note that ultrasonic C-scanning may not detect transverse damage modes such as micro-cracks in a matrix or single fibre breakage). For PPS20 laminate with 3 J transverse impact damage, slightly higher attenuation values are observed at the

impact point when compared to the values obtained from the unimpacted region. This can suggest that PPS20 laminate includes shear matrix cracks beneath the impact point but the delamination formation was not initiated yet (*i.e.* no sharp decrease was obtained from the force-time and force-displacement curves for the PPS20 laminate subjected to 3 J impact level, as seen Figure 7. 1 and Figure 7. 2, respectively). At the 4 J impact level, the attenuation profile of the PPS20 laminate reaches up to ~30 dB and decreases progressively until ~10 dB, which confirms that the shape of the impact damage is conical. The microstructural observation of the PPS20 laminate also indicates the conical impact damage profile, as seen in Figure 7. 5b. Figure 7. 5c also confirms shear cracks and delamination failures. The hybrid laminates hardly include the impact damage at 2 J and 3 J impact levels (see Figures 7. 1 and 7. 2) and C-scan images also confirm that shear matrix cracks accumulated beneath the impact point for the hybrid laminate with 2 J impact, see Figure 7. 6a. The cross-sectional fracture surface features of the hybrid laminate are given in Figure 7. 6b. The delamination failure was just initiated for the hybrid toughened laminate at the 4 J impact level (*i.e.* no significant contact load increase after the force-time and force-displacement curves exhibit the sudden load drop in the loading path, as seen in Figures 7. 1 and 7. 2, respectively). In parallel, the attenuation profile of the hybrid toughened laminate experiences a progressive decrease. Figure 7. 6c also confirms a larger delaminated interface at the lowest interlaminar region of the hybrid laminate as the introduced shear matrix cracks underwent the highest tension component of the bending moment at the lowest layer.

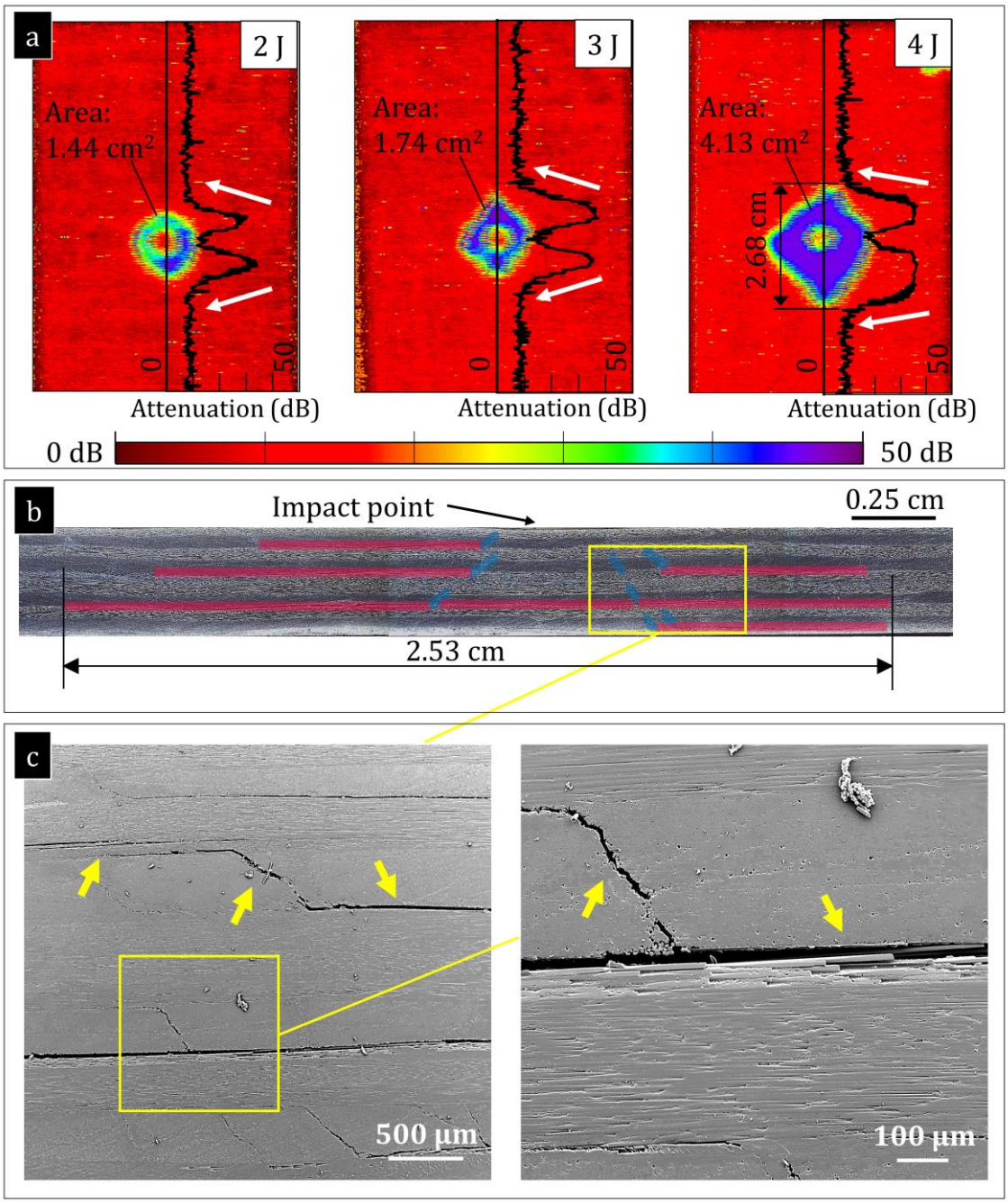

Figure 7. 3| (a) The projected damage area of the base laminates at 2 J, 3 J and 4 J impact levels with attenuation profiles (b) the cross-sectional fracture surface of the base laminate subjected to 4 J impact loading and (c) micrographs indicating shear cracks and delamination failures (For a better visibility, shear matrix cracks and delamination failures are indicated with blue and red markers, respectively).

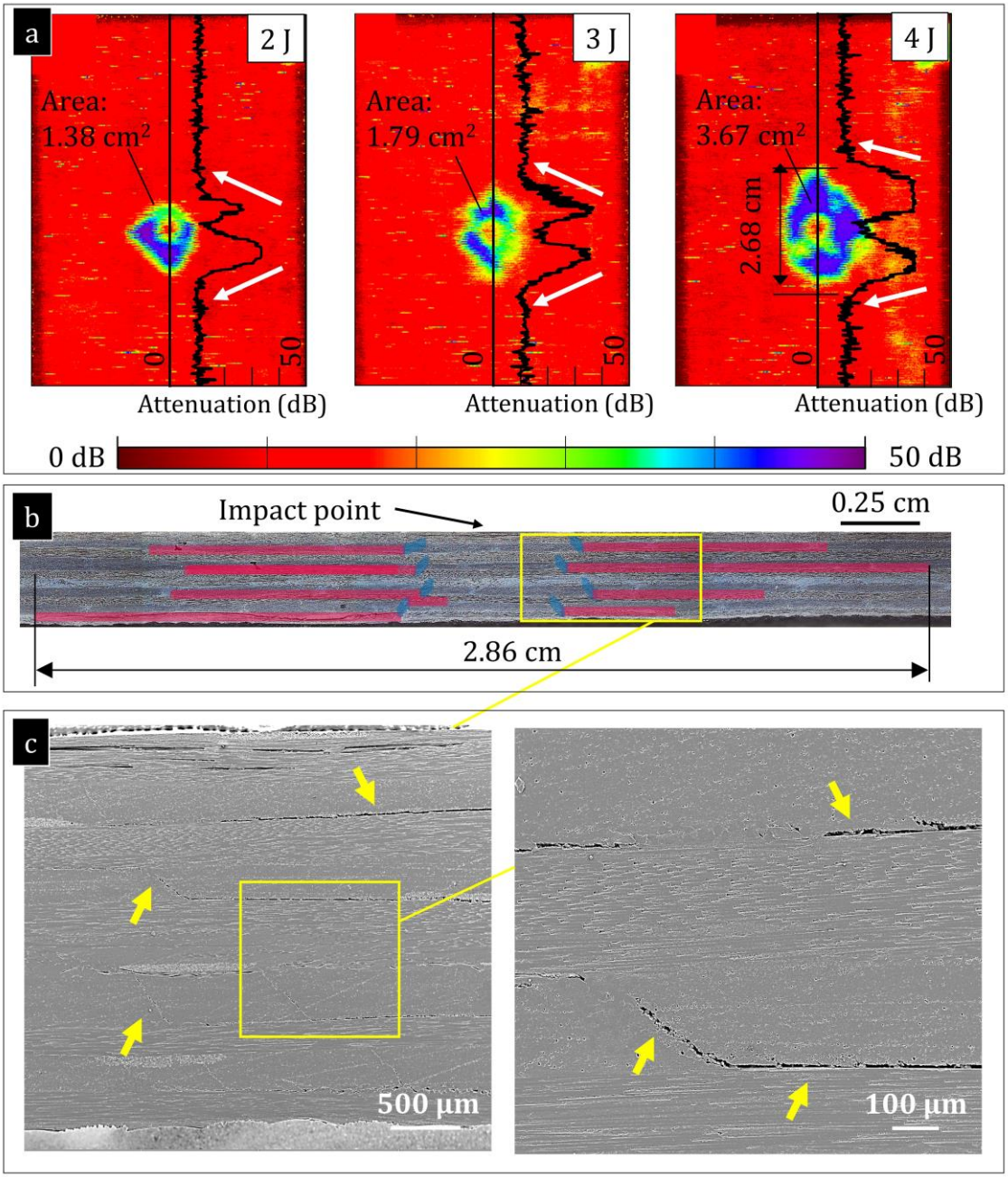

Figure 7. 4| (a) The projected damage area of the CSR10 laminates at 2 J, 3 J and 4 J impact levels with attenuation profiles (b) the cross-sectional fracture surface of the CSR10 laminate subjected to 4 J impact loading and (c) micrographs indicating shear cracks and delamination failures (For a better visibility, shear matrix cracks and delamination failures are indicated with blue and red markers, respectively).

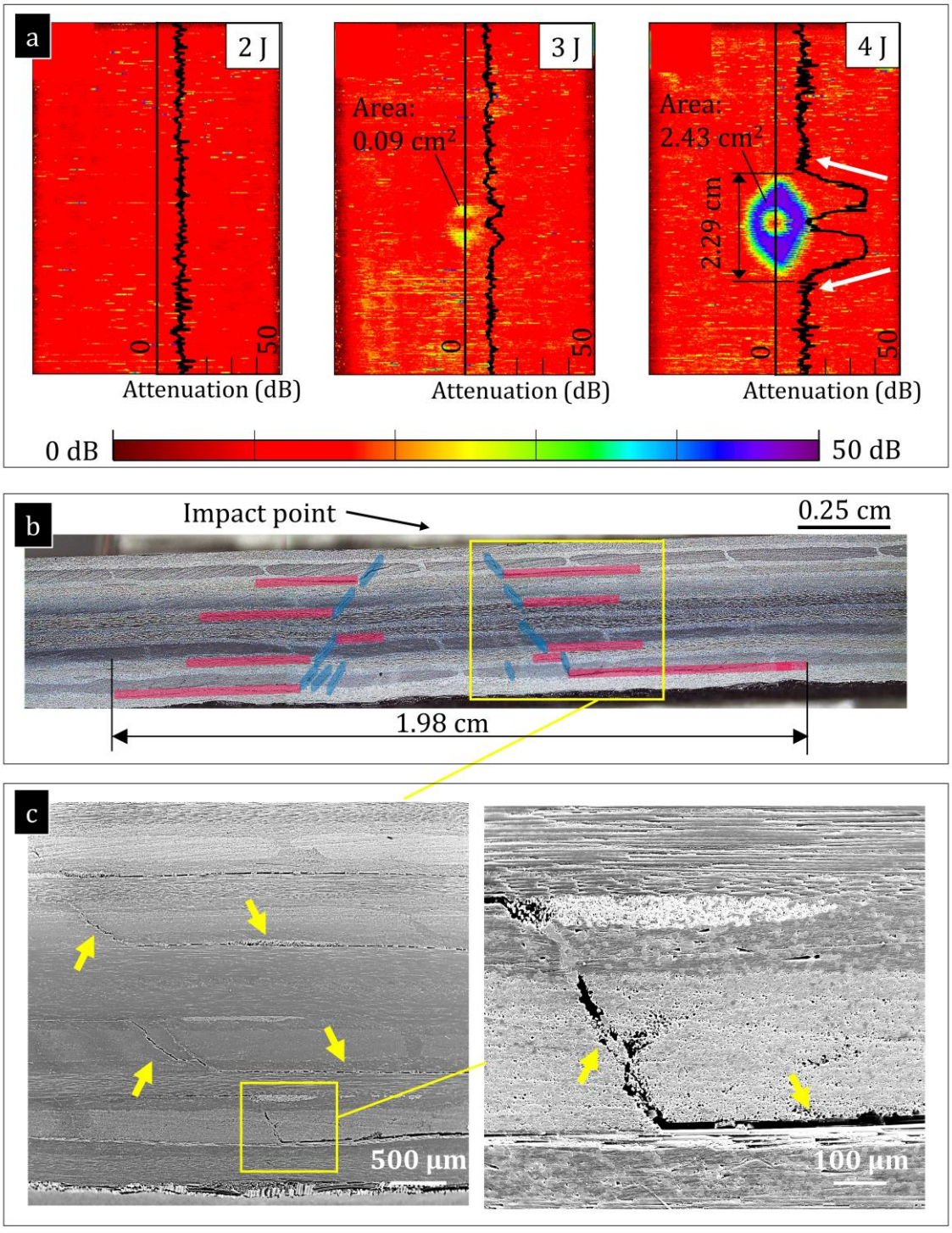

Figure 7. 5| (a) The projected damage area of the PPS20 laminates at 2 J, 3 J and 4 J impact levels with attenuation profiles (b) the cross-sectional fracture surface of the PPS20 laminate subjected to 4 J impact loading and (c) micrographs indicating shear cracks and delamination failures (For a better visibility, shear matrix cracks and delamination failures are indicated with blue and red markers, respectively).

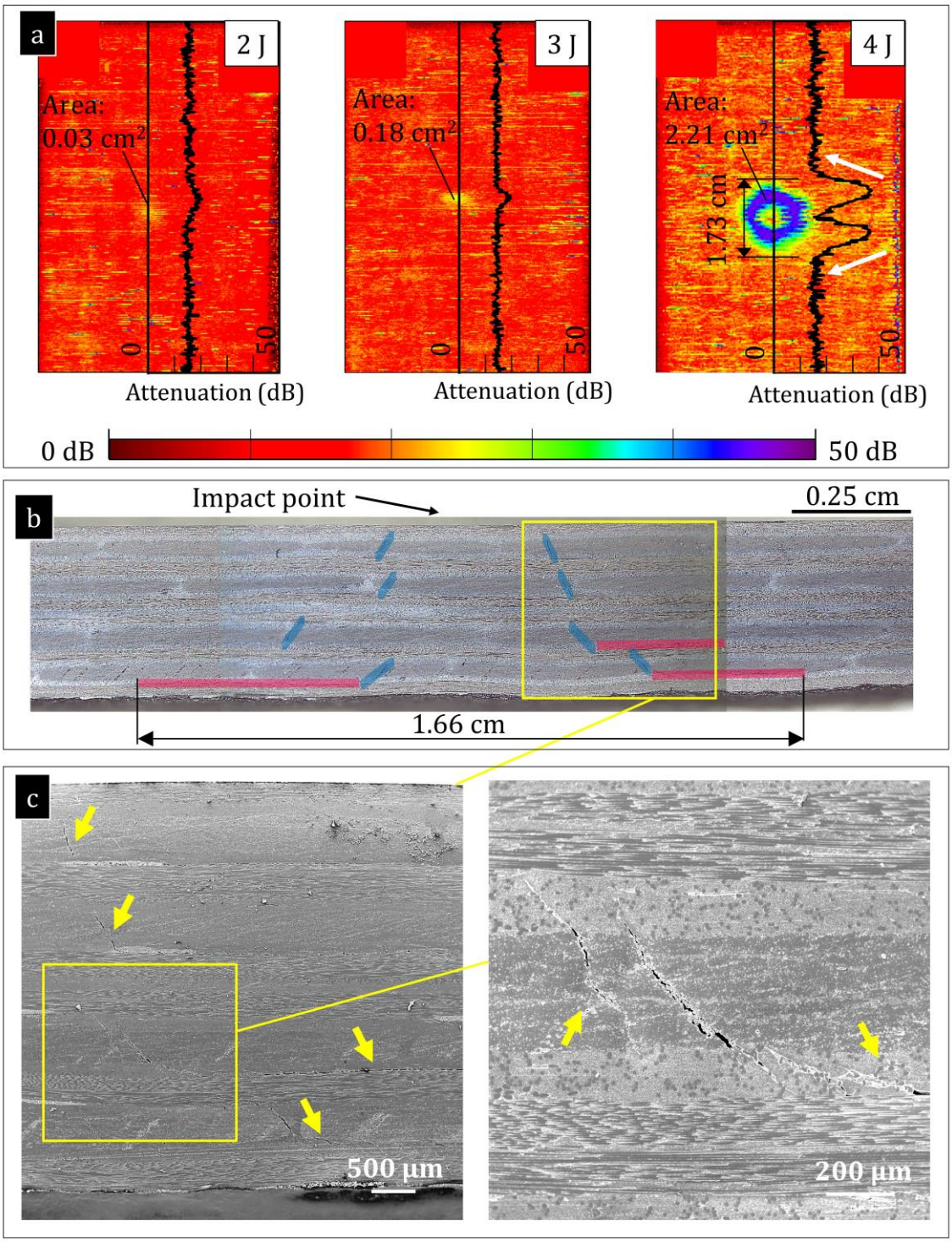

Figure 7. 6| (a) The projected damage area of the hybrid laminates at 2 J, 3 J and 4 J impact levels with attenuation profiles (b) the cross-sectional fracture surface features of the hybrid laminate subjected to 4 J impact loading and (c) micrographs indicating shear cracks and delamination failures (For a better visibility, shear matrix cracks and delamination failures are indicated with blue and red markers, respectively).

7.2.2. LVI Response of the Composite Laminates

The impact tests were carried out to examine the impact resistance of the composite laminates at varying ranges (*e.g.* 2.5 J, 5 J, 7.5 J and 10 J impact levels) to identify the behaviour of the composite laminates under impact loading using at least 3 samples at each impact level. The representative force-time and force-displacement curves of the base, CSR10, PPS20 and the hybrid toughened composite laminates obtained from the drop-weight low-velocity impact tests are given in Figure 7. 7 and Figure 7. 8, respectively. The unstable sudden drops in the loading path of the force-time and force-displacement curves refer to the delamination threshold for the composite laminates under impact loading. Figure 7. 7a demonstrates that the PPS20 and hybrid toughened composite laminates did not exhibit sudden drops in the loading path and these laminates absorbed impact energy with minor damage modes (*e.g.* matrix cracks) at 2.5 J. Both laminates experienced sudden drops at the impact level starting from 5 J. The load levels corresponding to the initiation of the sudden drops are between ~3 and ~3.5 kN for the base and CSR10 laminates whereas those are between ~4 and ~4.5 kN for the PPS20 and hybrid laminates as seen in Figure 7. 7. The force-displacement curves of the base, CSR10, PPS20 and hybrid toughened laminates clearly indicate that the impactor did not penetrate at 2.5 J, 5 J, 7.5 J and 10 J impact levels, see Figure 7. 8. Also, these curves manifest that the base and PPS20 laminates are stiffer under impact loading compared to the CSR10 and hybrid toughened composite laminates.

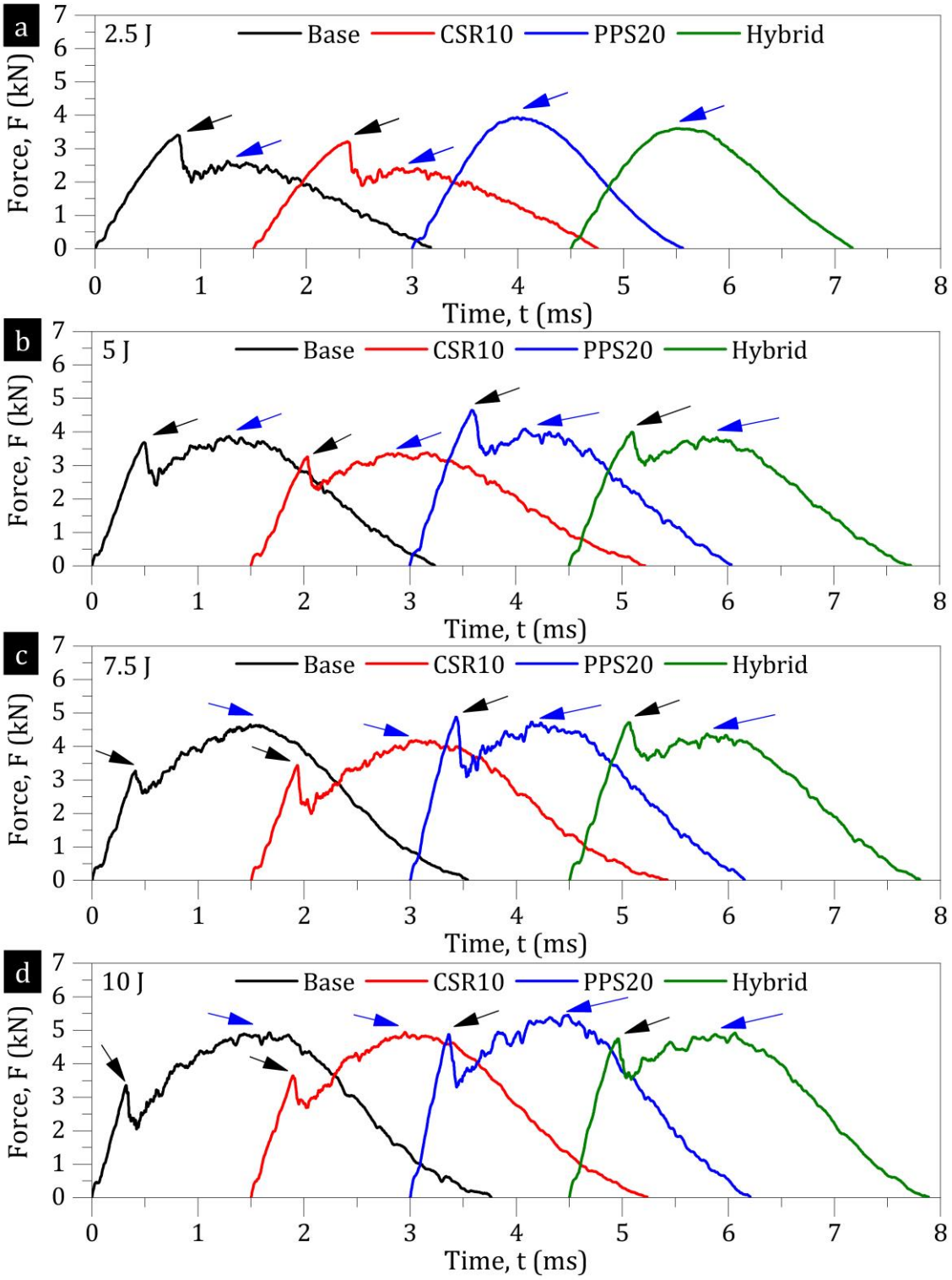

Figure 7. 7| The force-time curves of the composite laminates at (a) 2.5 J, (b) 5 J, (c) 7.5 J and (d) 10 J impact levels (Note that the curves are given with an offset for a better clarity. Black and blue arrows indicates the threshold contact forces and maximum contact forces after the threshold, respectively).

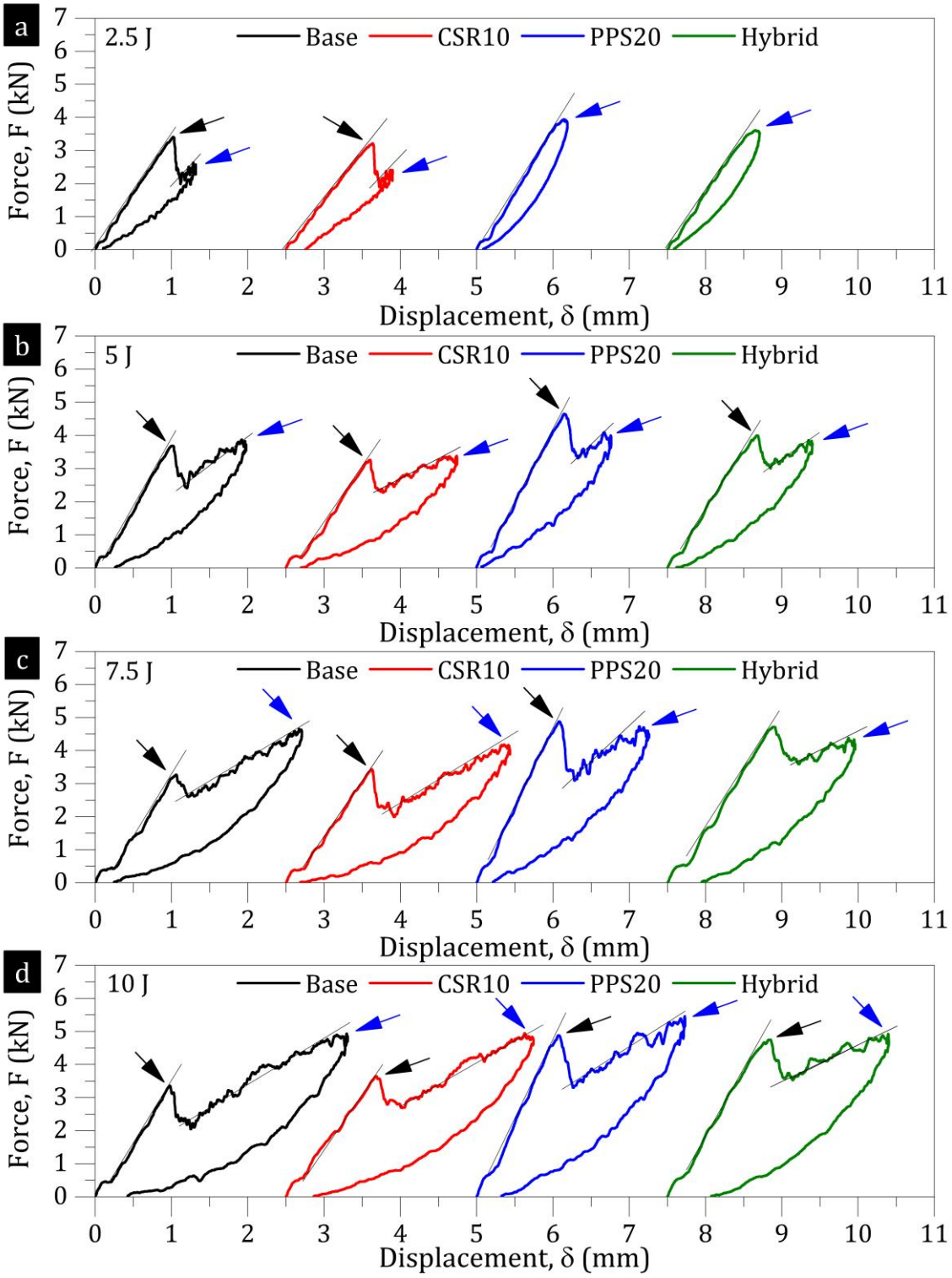

Figure 7. 8| The force-displacement curves of the composite laminates at (a) 2.5 J, (b) 5 J, (c) 7.5 J and (d) 10 J impact levels (Note that the curves are given with an offset for a better clarity. Black and blue arrows indicate the threshold contact forces and maximum contact forces after the threshold, respectively and thin black lines on the curves indicate the stiffness of the composite laminates under transverse impact).

Figure 7. 9 indicates the maximum displacement obtained from the composite laminates under impact loading and the structural integrity factor (SI) (*i.e.* the difference between the maximum displacement, d_{max}, and the displacement values corresponding to the threshold contact force, and lower values for SI factors offer lower loss in structural integrity [217]). Figure 7. 9a indicates the maximum values for d_{max} were obtained from the CSR10 laminates compared to other laminates at each impact level. On the other hand, d_{max} values for the PPS20 laminates are the lowest at 2.5 J, 5 J and 7.5 J impact levels and are similar to the hybrid toughened laminates at 10 J impact level. The structural integrity factor was also calculated and presented in Figure 7. 9b. This figure demonstrates that the highest structural integrity loss was obtained from the CSR10 laminates compared to the other composite laminates. Both the PPS20 and the hybrid laminates maintained the structural integrity for a 2.5 J impact. At the 5 J impact level, the loss in structural integrity factor for the PPS20 and hybrid toughened composite laminates is significantly lower than the base laminate. The difference between the PPS20 and the hybrid toughened laminates becomes distinguishable at 7.5 J and 10 J impact levels and the structural integrity factor is lower for the hybrid toughened laminates although the d_{max} for the hybrid toughened laminates is higher compared to the PPS20.

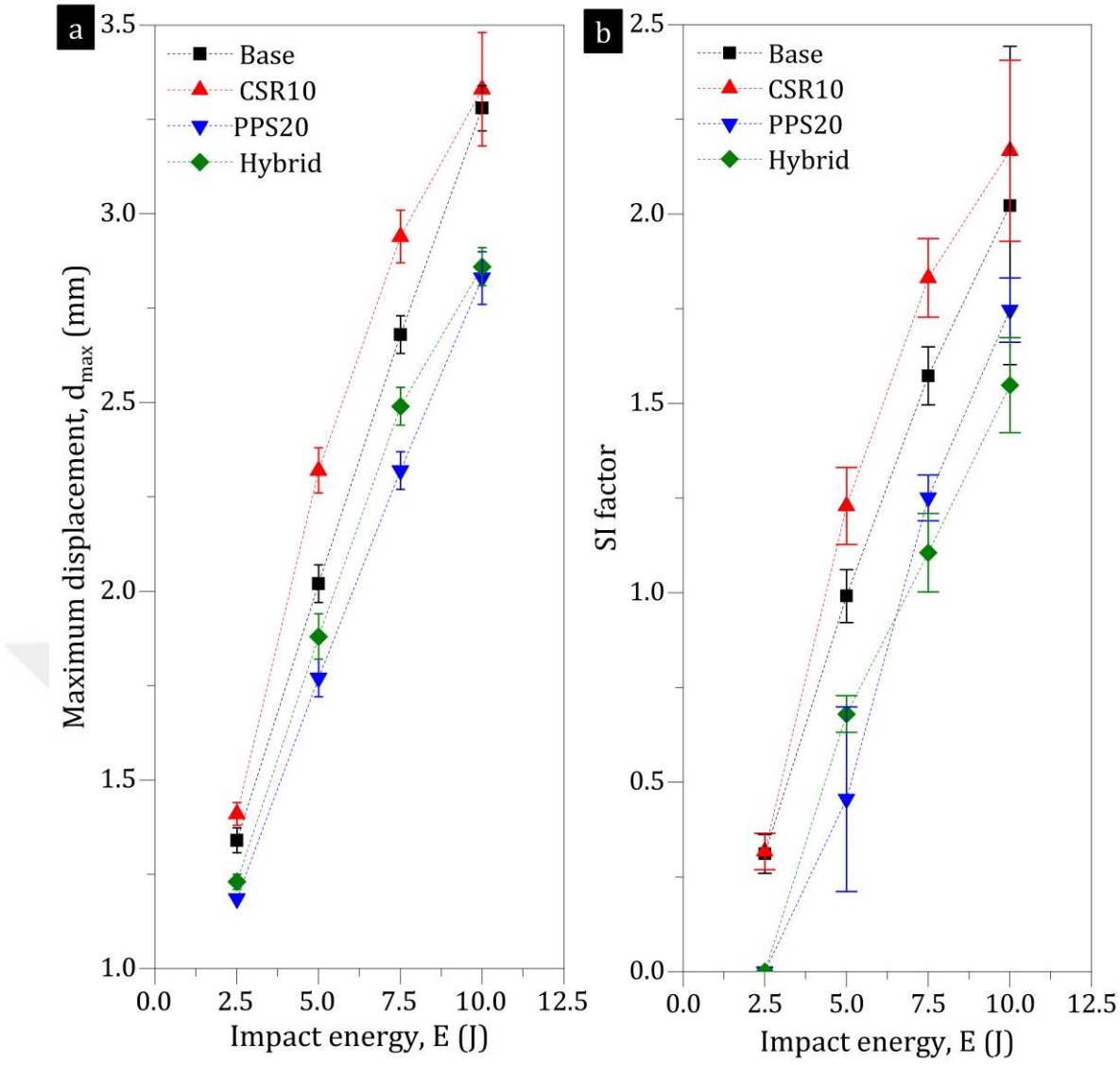

Figure 7. 9| (a) The maximum displacement, *i.e.* d_{max}, values of the base, CSR10, PPS20 and hybrid laminates under transverse impact at 2.5 J, 5 J, 7.5 J and 10 J and (b) the comparison of the structural integrity (SI) factor calculated from the composite laminates.

During impact loading, some amount of induced impact energy to composite laminates is absorbed via the damage modes (*i.e.* inelastic energy, E_i) whereas some amount of the impact energy rebounds the impactor (*i.e.* elastic energy, E_e). The area below the loading path of the force-displacement curves corresponds to the introduced impact energy and the area below the unloading path of the force-displacement curves refers to the elastic energy which is used to rebound the impactor. The difference between these areas below loading and unloading paths indicates the inelastic impact energy which is absorbed impact energy to generate sublaminar damage modes. Figure 7. 10 demonstrates the elastic and inelastic energies at each impact level. This figure

indicates that inelastic energies are increasing with increasing impact loading as expected. At the 2 J impact level, the inelastic energies of the base and CSR10 laminates are ~1.25 J whereas those of the PPS and hybrid toughened laminates are ~0.9 J. The differences in the inelastic energies for the composite laminates with/without veils are related to the delamination initiation. As the PPS20 and hybrid toughened laminates maintain their structural integrity with no suffering from delamination failure (see Figure 7. 9b), the majority of the induced impact energy was predominantly spent to rebound the impactor for a 2.5 J impact. At the 5 J impact level, each laminate absorbed a similar amount of impact energies (~2.5 J). After the 5 J impact, the response of the hybrid toughened laminates differentiates with increasing impact levels compared to the other type of composite laminates. For a 7.5 J impact, the base, CSR20 and PPS20 laminates absorbed ~4 J impact energy whereas the hybrid toughened laminates absorbed ~4.3 J impact energy. For a 10 J impact, the inelastic energy levels are ~5.5 J for the base, CSR10 and PPS laminates and ~6 J for the hybrid toughened laminates.

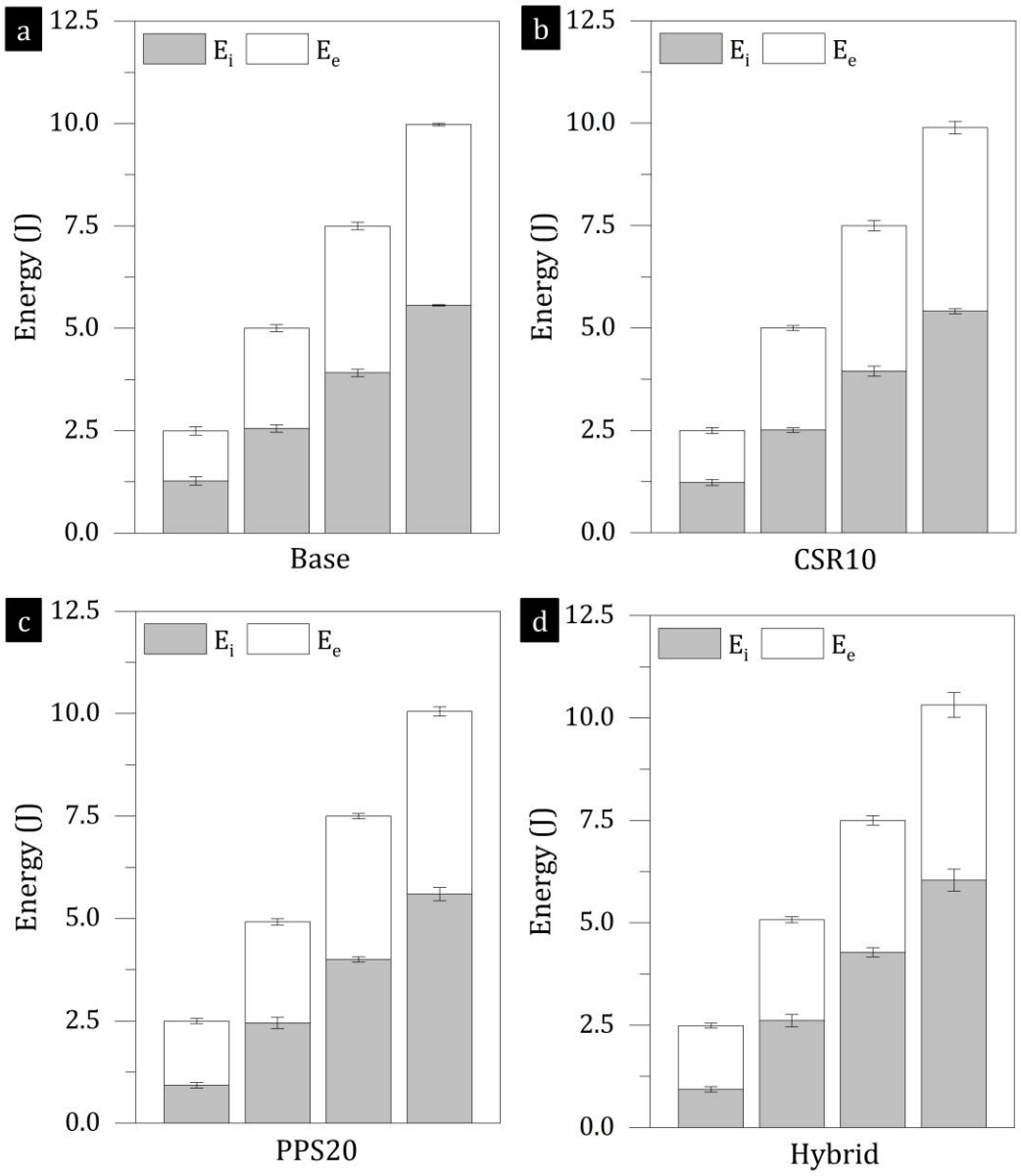

Figure 7. 10| Comparison of the inelastic, *i.e.* E_i, and elastic, *i.e.* E_e, energies for the (a) base, (b) CSR10, (c) PPS20 and(d) hybrid laminates.

After the impact tests, the projected damage area of the composite laminates subjected to impact loading was detected with ultrasonic through transmission C-scanning as mentioned in the previous section. Figures 7. 11a and -b indicate the projected damage area corresponding to the impact energy and the inelastic impact energy. The projected damage areas for the base laminates are 1.53 cm^2, 3.59 cm^2, 6.122 cm^2, and 9.52 cm^2 at 2.5 J, 5 J, 7.5 J and 10 J impact levels, respectively. Also, the highest damage areas were obtained from the CSR10 laminates at each impact level (*i.e.* 2.61 cm^2, 5.90 cm^2, 9.62 cm^2, 10.66 cm^2 at 2.5 J, 5 J, 7.5 J and 10 J impact levels, respectively). The lowest

projected damage area was detected from the hybrid laminates (*i.e.* 0.1 cm^2, 3.1 cm^2, 4.47 cm^2, 8.14 cm^2 at 2.5 J, 5 J, 7.5 J and 10 J impact levels, respectively). The projected damage areas of the PPS20 laminates are slightly higher compared to the hybrid laminates (*i.e.* 0.18 cm^2, 3.37 cm^2, 5.42 cm^2, 8.48 cm^2 at 2.5 J, 5 J, 7.5 J and 10 J impact levels, respectively). On the other hand, Figure 7. 11b indicates that the hybrid laminates absorbed slightly higher inelastic energies compared to the other laminates at 5 J, 7.5 J and 10 J impact levels. Also, the lowest projected damage areas were detected from the hybrid laminates compared to the other composite laminates.

Figures 7. 12a to -d give the C-scan results with attenuation profiles (*i.e.* ranging between 10 dB and 50 dB depending on the sub-laminar damage which the composite laminates include) along the length of the composite laminates. The base laminates exhibited progressive decreases in the attenuation profile for 2.5 J impact and the maximum attenuation level is lower than the base laminates subjected to the impact loading at 5 J, 7.5 J and 10 J impact levels as seen in Figure 7. 12a. For the CSR10 laminates, the attenuation level is relatively higher at the impact point compared to the base laminates for each impact as seen in Figure 7. 12b. Also, sharp decreases were observed from the CSR10 laminates at each impact level, which indicates CSR10 laminates include delamination failure at multiple interfaces for the impact levels from 2.5 J to 10 J. For the PPS20 laminates, no significant impact damage area was measured from the C-scanning observation at the 2.5 J impact level. However, the attenuation levels obtained around the impact point are slightly higher than the attenuation levels obtained from the region where the PPS20 laminate does not contain sublaminar damage modes as seen in Figure 7. 12c. For a 5 J impact, the progressive decrease in attenuation profile was obtained, which indicates delamination formation at the bottom layers due to the tension component of the bending moment. The attenuation profile of the PPS20 laminates subjected to the impact loading at 7.5 J and 10 J impact loading experienced sharp decreases. For the hybrid toughened laminates, the peak attenuation level is ~20 dB at the 2.5 J impact level (see Figure 7. 12d), which is slightly higher compared to the PPS20 laminates. Also, sharp decreases were observed from the attenuation profiles for each impact, which indicates a localised damage profile occurred for the hybrid laminates under transverse impact.

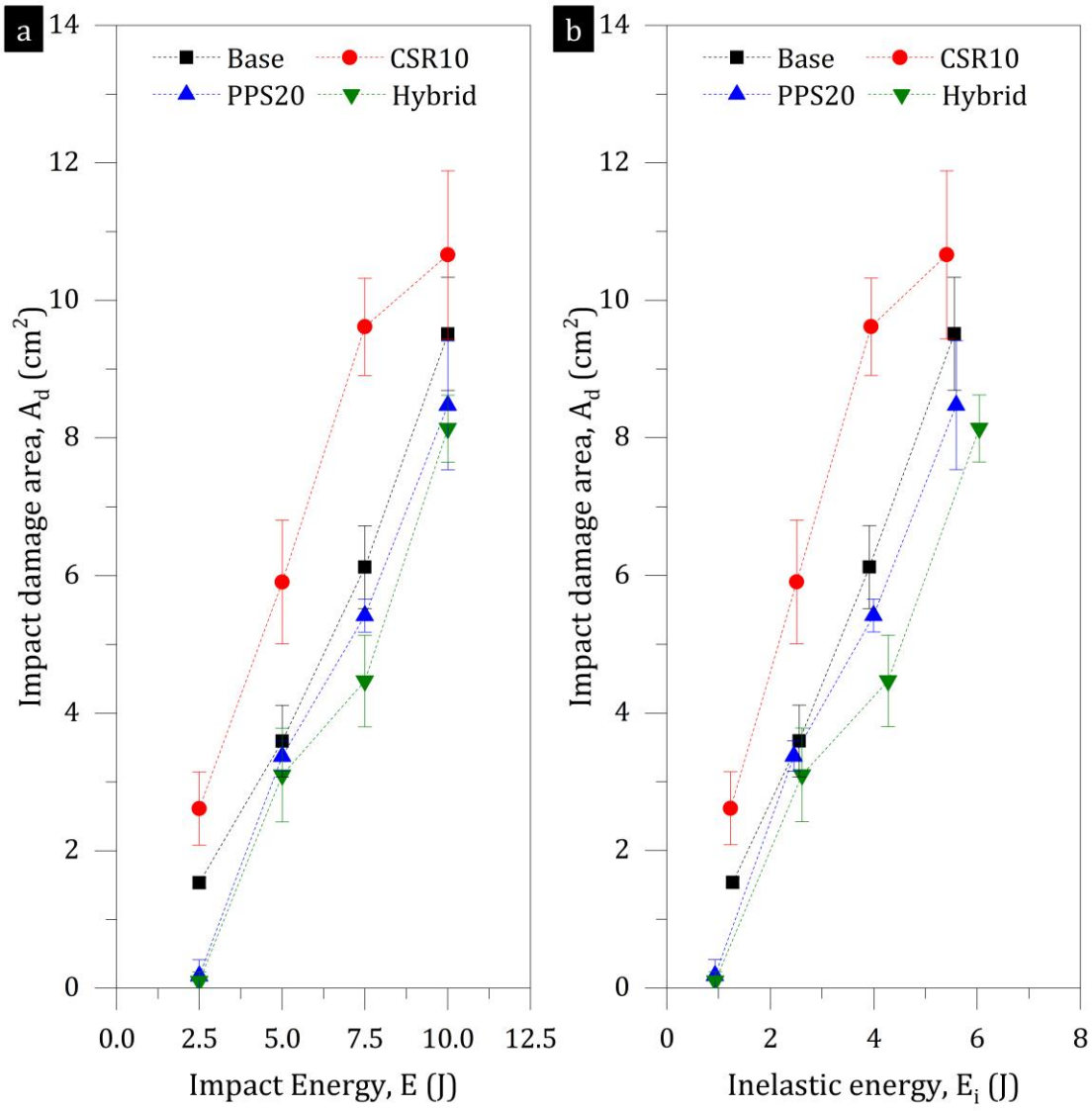

Figure 7. 11| Comparison of the total impact damage area, *i.e.* A_d, obtained from the base, CSR10, PPS20 and hybrid laminates with respect to (a) impact energies and (b) inelastic energies.

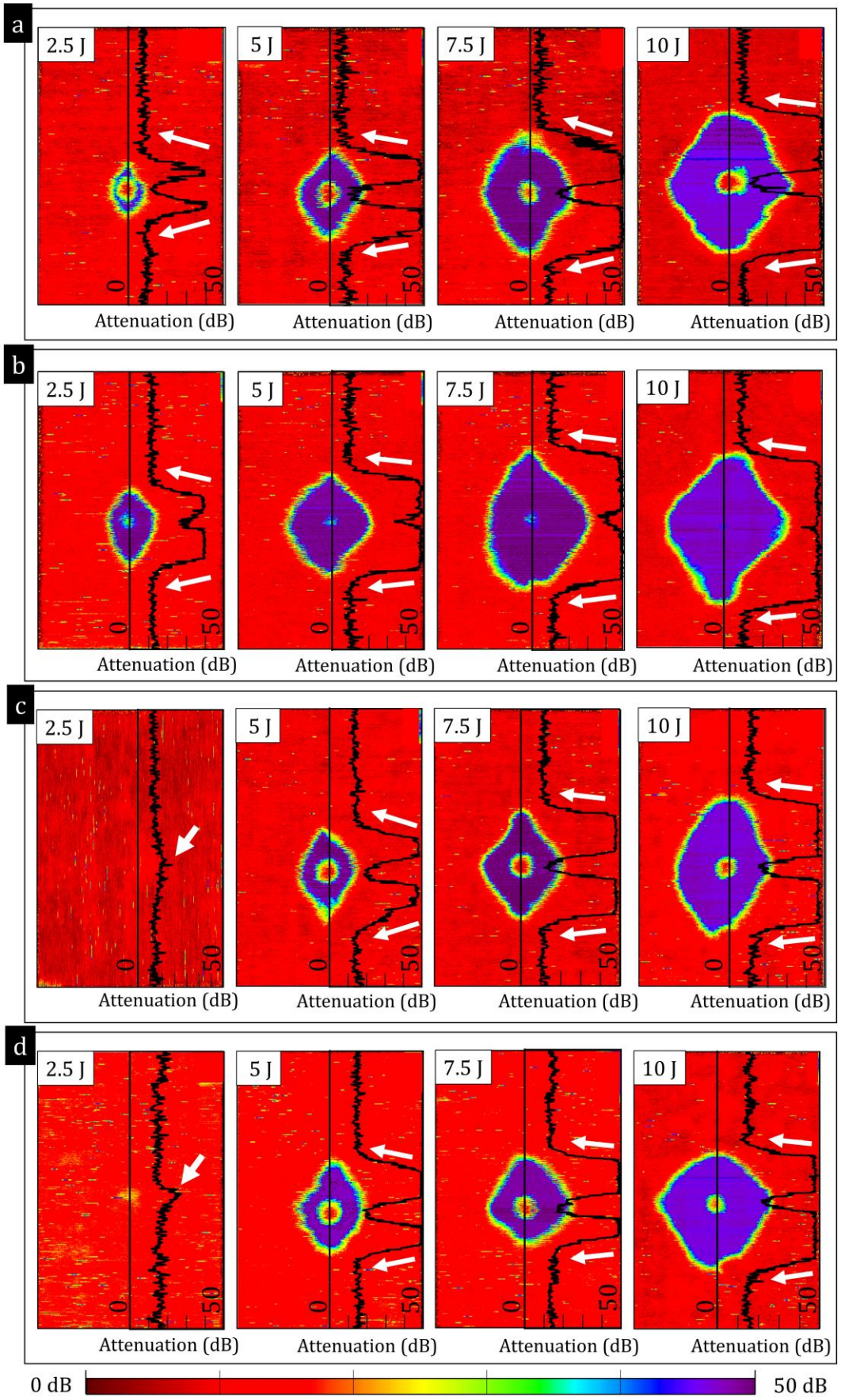

Figure 7. 12| The C-scan results with attenuation profile along the length of the (a) the base, (b) CSR10, (c) PPS20 and (d) hybrid laminates with transverse impact at 2.5 J, 5 J, 7.5 J, and 10 J.

7.3. Impact Toughening Mechanisms

The composite laminates subjected to the 10 J impact loading were sectioned and the cross-sectional fracture surface features were captured with SEM, see Figures 7. 13 – 7. 16. Figure 7. 13 indicates the cross-sectional fracture surface features of the base laminate. The digital image taken from the base laminate indicates shear matrix cracks and delamination failures, see Figure 7. 13a. The micrographs taken from the base laminate (see 7. 13b) demonstrates the glassy surface of the epoxy indicating the brittle characteristic of the base laminate under the transverse impact, and the clean surface of the carbon fibres indicating weak adhesion between the carbon-fibre matrix interface.

The fracture surface and micrographs obtained from the CSR10 laminates are given in Figure 7. 14. Figure 7. 14a indicates the shear matrix cracks and delamination failures. This figure also exposes that the delamination failures extended beneath the impact point for the CSR10 laminates, which also confirms the C-scan results (see Figure 7. 12b). The micrographs taken from the CSR10 laminate indicate the cavitated epoxy as seen in Figure 7. 14b.

Figure 7. 15 shows the cross-sectional fracture surface features of the PPS20 laminate. Figure 7. 15b exposes that PPS fibres can generate toughening mechanisms (*e.g.* fibre debonding) with shear matrix cracks. However, the crack tip was not propagated within the veils when delamination failure was initiated.

The cross-sectional fracture surface of the hybrid toughened composite laminate is given in Figure 7. 16. Similarly, the hybrid toughened laminates experienced PPS fibre toughening mechanisms during the formation of shear matrix cracks and the crack tip followed the resin-rich region along with the veils and the carbon fibre-matrix interfaces. Compared to the PPS20 laminates (Figure 7. 15c), Figure 7. 16c also exposes that the crack tip experienced branching during shear matrix development, which stimulates the PPS fibre toughening mechanisms (*e.g.* debonding) for the hybrid toughened laminates. Therefore, it could be said that the use of CSR particles together with the PPS veils can alter the energy dissipation mechanisms and influence the impact properties of the composite laminates. However, the PPS veils did not contribute to the impact response of the PPS20 and hybrid laminates due to the crack tip migration towards the resin-rich region between the veils and carbon fibre surfaces once delamination was initiated.

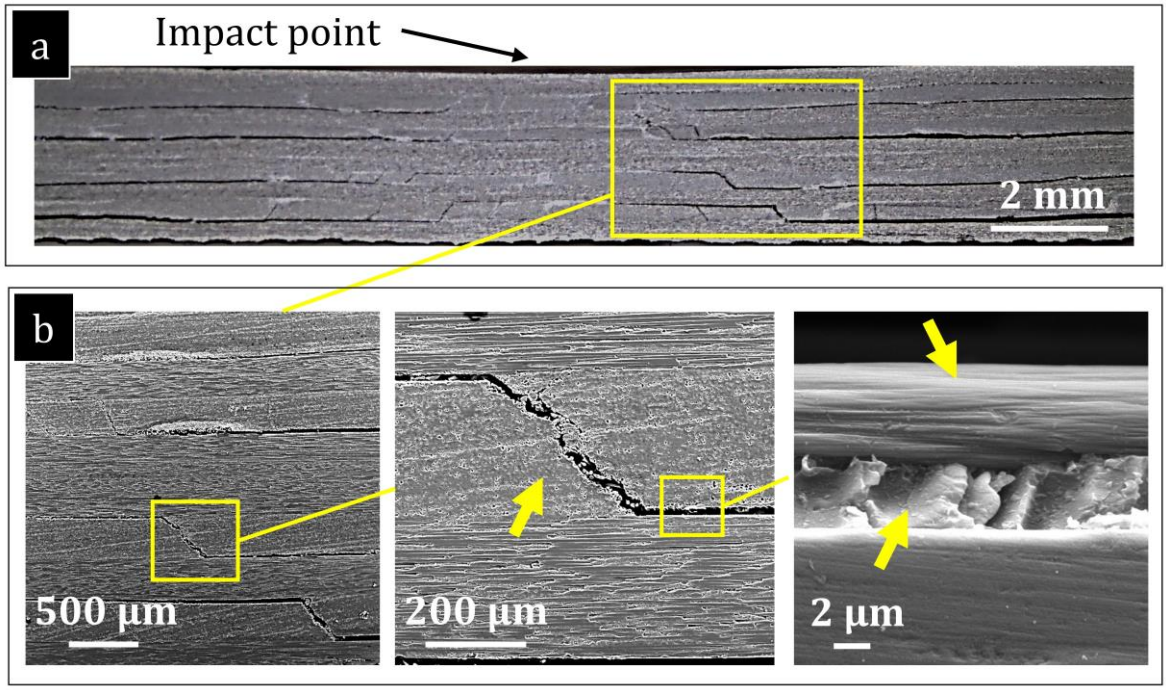

Figure 7. 13| The microstructural observations of the base laminate under transverse impact with 10 J energy: (a) the cross-sectional fracture surface features of the base laminate, (b) micrographs indicating the shear matrix cracks and delamination failures with the glassy surface of the epoxy and the carbon fibre surface.

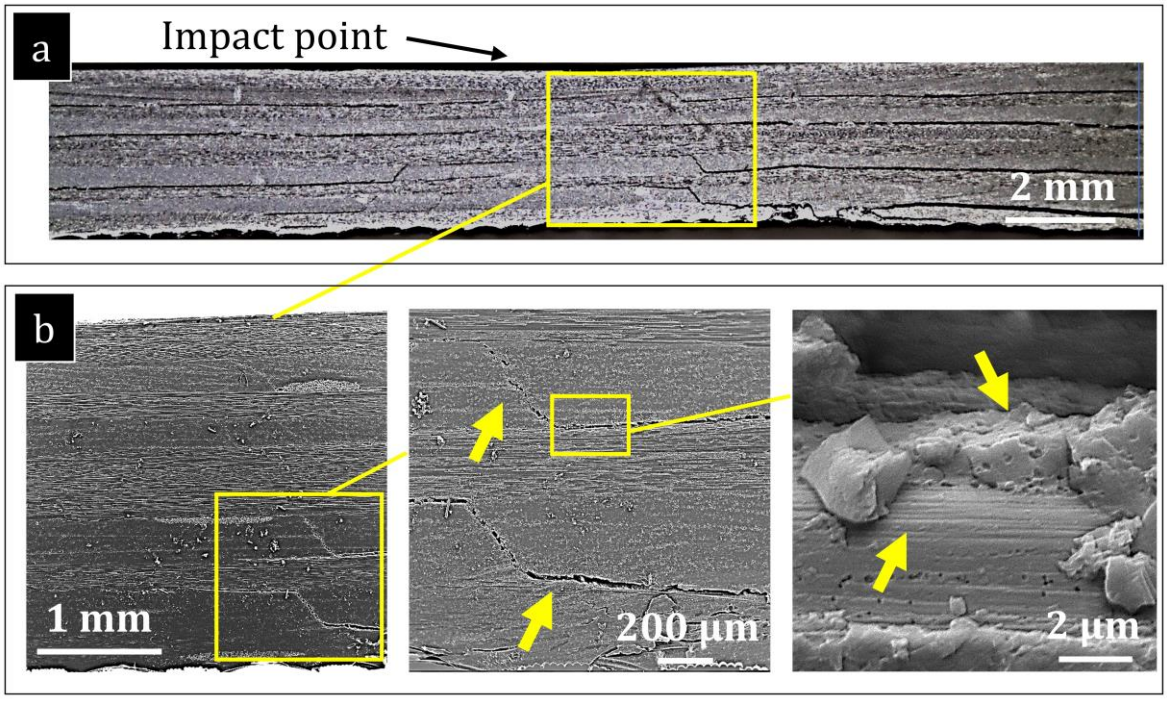

Figure 7. 14| The microstructural observations of the CSR10 laminate under transverse impact with 10 J energy: (a) the cross-sectional fracture surface features of the CSR10 laminate, (b) micrographs indicating the shear matrix cracks and delamination failures with residual cavitated matrix on the carbon fibre surface.

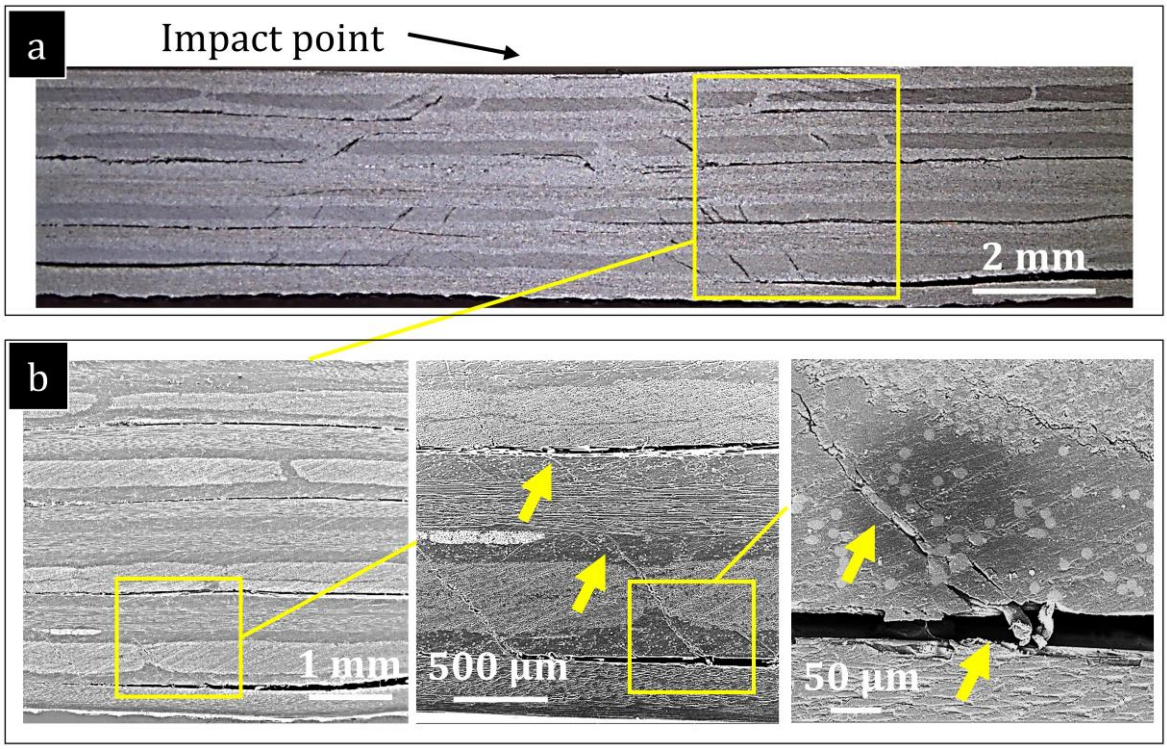

Figure 7. 15| The microstructural observations of the PPS20 laminate under transverse impact with 10 J energy: (a) the cross-sectional fracture surface features of the PPS20 laminate, (b) micrographs indicating the shear matrix cracks with debonded PPS fibres and delamination propagation along resin-rich region between PPS veils and carbon fibre surfaces.

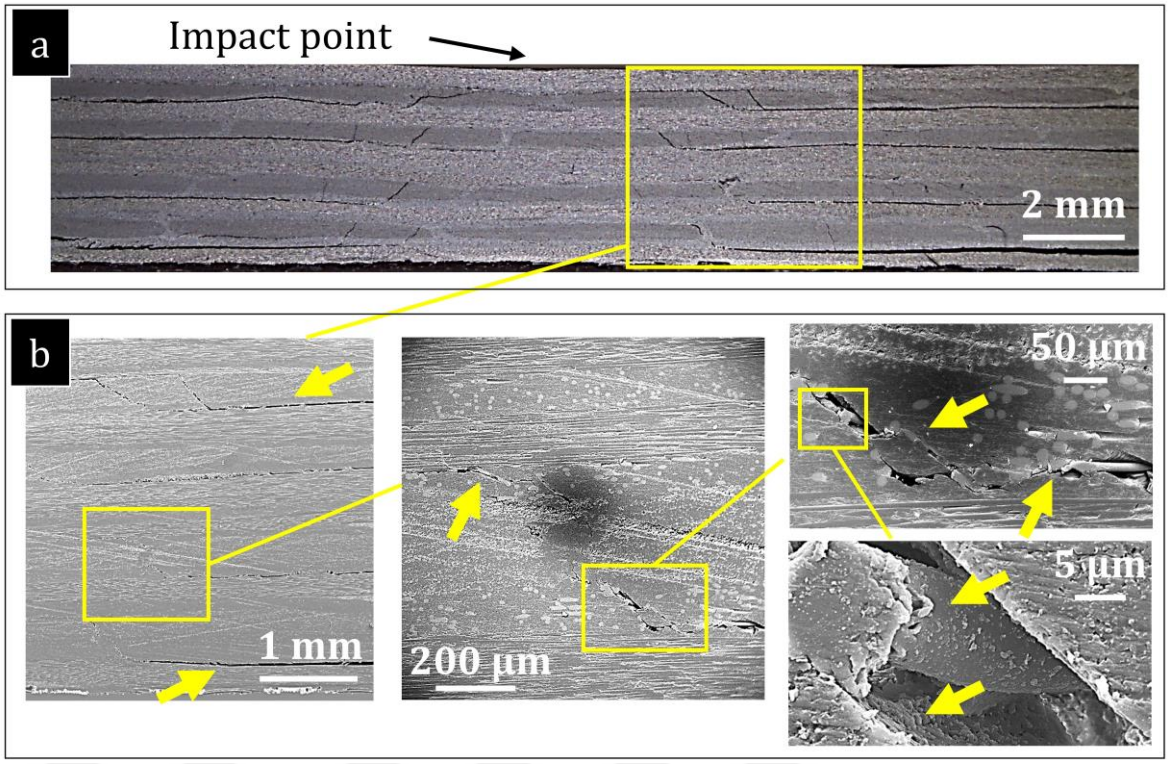

Figure 7. 16| The microstructural observations of the hybrid laminate under transverse impact with 10 J energy: (a) the cross-sectional fracture surface features of the hybrid laminate, (b) micrographs indicating the shear matrix cracks with debonded PPS fibres and delamination failures along resin-rich region between PPS veils and carbon fibre surfaces, as well as cavitated epoxy and smooth surface of the PPS fibre.

7.4. Discussions

The drop-weight low-velocity impact tests were performed in two phases. In the first phase, relatively low impact damage at 2 J, 3 J, and 4 J was introduced and it was found that the impact damage threshold can be increased with PPS veils. In the second phase, the low-velocity impact damage resistance of the composite laminates was examined at varying impact levels (*i.e.* 2.5 J, 5 J, 7.5 J and 10 J) to understand the fracture mechanisms leading to the impact resistance for the composite laminates. This section presents the relationship between the toughness and impact properties of the laminates.

Table 7. 1 presents the threshold contact (F_{th}) and maximum contact (F_{max}) forces after the threshold values generated under transverse impact with each impact level. This table indicates that CSR content with 10 wt% in the epoxy hardly influenced the F_{th} and F_{max}. In addition, over a 30% increase in F_{th} was obtained from the PPS20 and hybrid laminates with impacts at 5 J and 7.5 J (the PPS20 and hybrid laminates exhibit no

sudden drops in load-time and load-displacement curves for 2.5 J impact, see Figure 7. 7 and Figure 7. 8) whereas F_{max} generation of these laminates is close to the base laminates. This indicates that the toughening mechanisms achieved from the PPS veils are transferred to the impact properties for the PPS20 and hybrid laminates until delamination failure is generated but not for the delamination propagation under transverse impact.

Table 7. 1| The threshold and maximum contact forces, *i.e.* F_{th} and F_{max}, respectively, generated under transverse impact with varying energies in the base, CSR10, PPS20 and hybrid laminates (The values between brackets indicate the variation of the contact force values of the laminates compared to that of the base laminates).

Impact Energy Material Acronym	F_{th} (N)	F_{max} (N)
2.5 J		
Epoxy (Base)	3.37 ± 0.05	2.56 ± 0.07
Epoxy + CSR 10 wt% (CSR10)	3.16 ± 0.05 (-6%)	2.46 ± 0.04 (-4%)
Epoxy + 20 g/m^2 PPS (PPS20)	-	3.94 ± 0.02 (54%)
Epoxy + CSR 10% + 20 g/m^2 PPS veil (Hybrid)	-	3.57 ± 0.07 (39%)
5 J		
Epoxy (Base)	3.52 ± 0.2	3.75 ± 0.15
Epoxy + CSR 10 wt% (CSR10)	3.10 ± 0.2 (-12%)	3.48 ± 0.11 (-7)
Epoxy + 20 g/m^2 PPS (PPS20)	4.49 ± 0.34 (27%)	3.91 ± 0.13 (4%)
Epoxy + CSR 10% + 20 g/m^2 PPS veil (Hybrid)	4.11 ± 0.16 (17%)	3.82 ± 0.08 (2%)
7.5 J		
Epoxy (Base)	3.38 ± 0.20	4.62 ± 0.07
Epoxy + CSR 10 wt% (CSR10)	3.35 ± 0.17 (-1%)	4.11 ± 0.10 (-11%)
Epoxy + 20 g/m^2 PPS (PPS20)	4.62 ± 0.19 (37%)	4.79 ± 0.09 (4%)
Epoxy + CSR 10% + 20 g/m^2 PPS veil (Hybrid)	4.49 ± 0.26 (33%)	4.55 ± 0.20 (-2%)
10 J		
Epoxy (Base)	3.48 ± 0.24	4.96 ± 0.07

Epoxy + CSR 10 wt% (CSR10)	3.41 ± 0.45 (-2%)	4.84 ± 0.09 (-2%)
Epoxy + 20 g/m^2 PPS (PPS20)	4.62 ± 0.27 (33%)	5.35 ± 0.11 (8%)
Epoxy + CSR 10% + 20 g/m^2 PPS veil (Hybrid)	4.83 ± 0.30 (39%)	5.12 ± 0.13 (3%)

Among the investigated laminates, the hybrid laminates exhibited the lowest damage area (see Figure 7.10) . Section 7.2.1 indicates that the impact damage threshold of the hybrid laminates is between 3 J and 4 J. Also, Figure 7. 2 indicates that there is no further contact load increase for the hybrid laminates under impact loading after delamination is introduced while PPS20 laminates experienced a load increase after the delamination threshold. Therefore, the delamination threshold of the hybrid laminates is higher than the PPS20 laminates. These also suggest that higher energy is required to initiate delamination for the hybrid laminates when compared to the other laminates. On the other hand, the inelastic energy values are shown in Figure 7.10 and this figure indicates that hybrid laminates absorbed the highest inelastic energies compared to the other laminates. Also, the difference between the inelastic energy values of the hybrid and the other laminates is increasing with increasing energy. For higher impact energies, all interfaces experience delamination failure and the hybrid laminates require more energy for delamination initiation. C-scan results (Figure 7. 12) also confirm that the Y-attenuation profile of the hybrid laminates exhibits a progressive decrease with 5 J impact and the Y-attenuation profile of the hybrid laminates exhibits sharp decreases with 7.5 J and 10 J impacts. Progressive decreases indicate that delamination failure is higher at the bottom layers of laminates due to the tension component of bending moment. Sharp decreases represent that multiple delamination failures extended within impact damage areas and delamination failures were introduced at each interlaminar region for the hybrid laminates with 7.5 J and 10 J impact levels. When the micrographs obtained from the hybrid laminates (Figure 7.16) are compared with the micrographs obtained from the PPS toughened laminates (Figure 7.15), it can be said that the hybrid toughening influences energy dissipation and leads to more interaction with PPS fibres due to the crack tip branching.

$G_{I,C}$ values (Table 5. 1) of the laminates are correlated with the threshold impact energy (the energy induced to the laminates until the threshold values are reached) and the $G_{II,R}$ values (Table 6. 1) of the laminates are correlated with the E_i/A_d (ratio of the

inelastic energies and impact damage area), as seen in Figure 7. 17. Figure 7. 17a indicates a trend of increasing E_{th} with increasing $G_{I,C}$. These results suggest that the transfer of the mode-I toughening mechanisms to the impact properties was established until the delamination threshold was reached. On the other hand, Figure 7. 17b indicates that the correlation between $G_{II,R}$ and the E_i/A_d ratios was only obtained for the base and CSR10 laminates (E_i/A_d ratios are decreasing with decreasing $G_{II,R}$). Although significant improvement in $G_{II,R}$ was observed from the PPS20 laminates, E_i/A_d ratios are similar to the base laminates except for 2.5 J impact. (*i.e.* PPS20 laminates predominantly elastically responded to the impact at 2.5 J as seen in Figure 7. 7a and Figure 7. 8a). When compared to the hybrid laminates with the base laminates, slight increases in the E_i/A_d ratios were obtained while the significant improvement was obtained in $G_{II,R}$ (215%). Thus, these findings indicate that the transfer of the toughening mechanisms via PPS veils and the hybrid use of the PPS veils and CSR particle content to the impact properties of the laminates is limited. F_{max} values also confirm the inefficient transfer of the toughening mechanism to the impact response of the PPS20 and hybrid laminates (F_{max} values of the PPS20 and hybrid laminates are close to that of the base laminates). The delamination initiation phenomenon might be one of the reasons. In interlaminar fracture toughness (ILFT) testing, delamination growth was initiated from just behind the release film (*i.e.* introduce pre-cracks) but there is no factor manipulating the delamination initiation when transverse impact was induced to the laminates. Also, micrographs obtained from the PPS and hybrid laminates confirm that the crack tip propagated along the resin-rich region between veils and carbon fibre lamina and PPS toughening mechanisms were only developed with the shear crack formation under the transverse impact (see Figure 7. 15 and Figure 7. 16 for the PPS20 and hybrid laminates, respectively). On the other hand, the interlaminar fracture toughness performance of the composite laminates can be rate-dependent due to the viscoelastic behaviour of epoxy resins. The loading rate is significantly higher in impact loading compared to the loading rate applied in the ILFT tests. Some researchers reported that an increase in loading rate can decrease the mode-I and mode-II fracture properties of the unidirectional composite laminates [218–222].

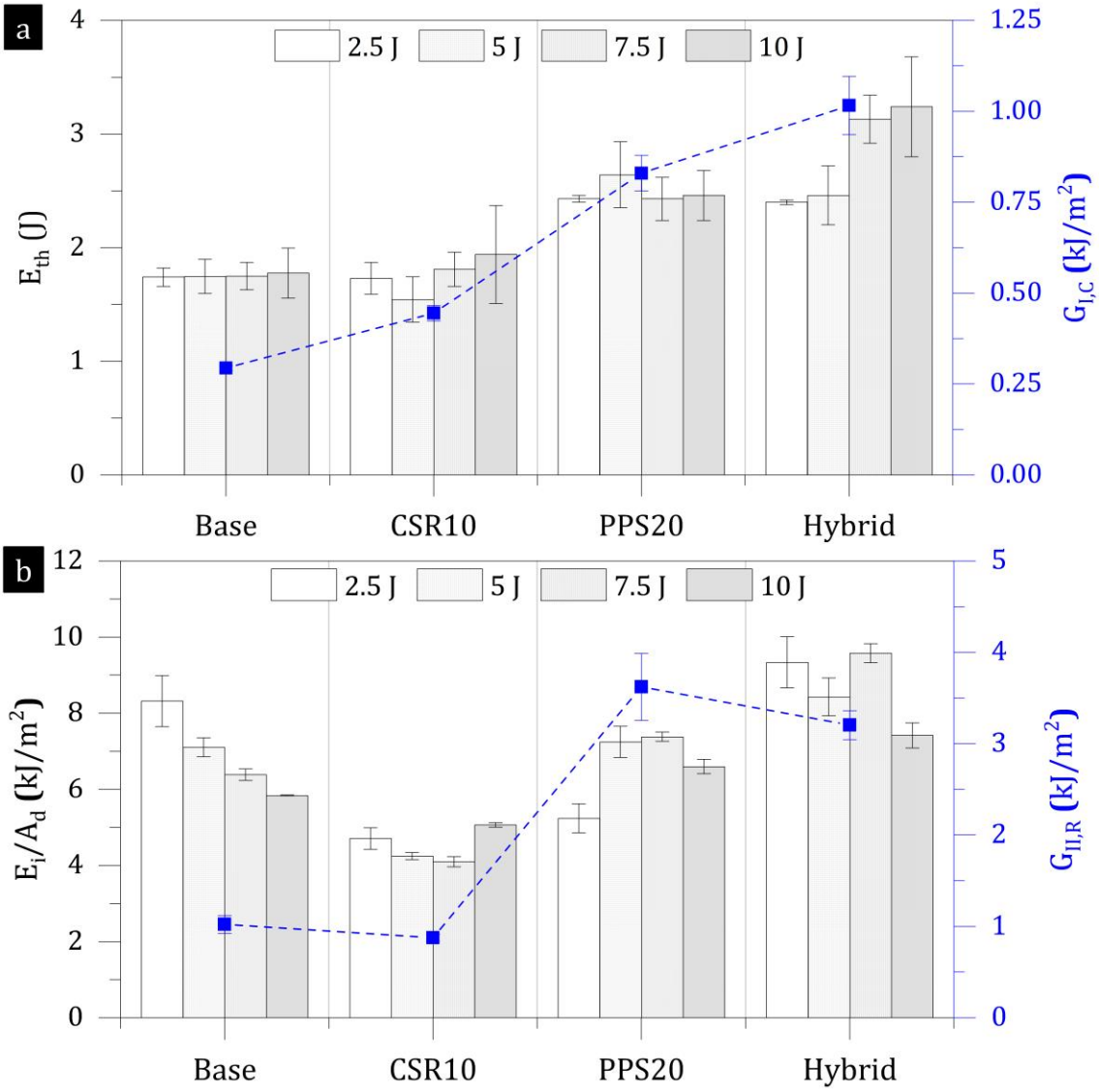

Figure 7. 17| | (a) Correlation between the threshold energies induced to the laminates, *i.e.* E_{th}, with mode-I initiation fracture energies, *i.e.* $G_{I,C}$, and (b) correlation between the ratio of the inelastic energies and impact damage area, *i.e.* E_i/A_d, with mode-II propagation fracture energies, *i.e.* $G_{II,C}$.

7.4. Conclusions

Chapter 7 investigates the influence of the hybrid use of the CSR particle content and PPS veils on the low-velocity impact response of composite laminates. The conclusions below are drawn in this chapter:

- *The influence of the CSR particle content:* The adverse effect of the CSR particle incorporation was observed. CSR10 laminates with 10 wt% CSR particle content hardly affected the contact force generations (see Table 7. 1). When

compared to the base laminates, the impact damage area of the CSR10 laminates is higher by ~70%, ~65%, ~60% and ~12% for 2.5 J, 5 J, 7.5 J and 10 J impact, respectively.

- *The influence of the PPS veil:* PPS veil presence postponed the impact damage threshold for the PPS20 and hybrid laminates (see Figure 7. 1 and Figure 7. 2). A significant improvement in F_{th} was achieved from the PPS20 laminates (by ~28%, ~37% and ~32% for 5 J, 7.5 J and 10 J impact, respectively, as seen in Table 7. 1). In addition, the impact damage area was suppressed with the PPS veils (~6%, ~12% and ~11% for 5 J, 7.5 J and 10 J impact, respectively, see Figure 7. 11). However, the PPS fibres did not contribute to the impact response of the PPS20 laminates after delamination failure was introduced. Thus, the F_{max} values of the PPS20 laminates are similar to the base laminates.
- *The influence of CSR particle content and PPS veil together:* Although the adverse effect of CSR particle content in the epoxy, the hybrid use of the PPS veils and CSR particles significantly suppressed the impact damage area (~15%, ~27% and ~12% for 5 J, 7.5 J and 10 J impact, respectively, as seen Figure 7. 11). In addition, the hybrid laminates can maintain the structural integrity under impact loading better than the other laminates (see Figure 7. 9b). The main difference between the hybrid and PPS laminates is that the hybrid laminates require higher energy to initiate delamination failure under the transverse impact, thus less impact energy was transferred for delamination propagation (Figure 7. 17). This also confirms the change in the energy dissipation toughening mechanisms of the hybrid laminates with the use of the PPS veils and CSR particle content together. The micrographs obtained from the hybrid laminates also indicate the crack tip branching during shear crack development, which promotes PPS fibre-based toughening mechanisms such as debonding. However, the crack propagation along resin-rich regions between the veils and carbon fibre surfaces indicates the inefficient transfer of the PPS fibre-based toughening mechanisms to the impact response of the hybrid laminates once delamination is initiated (Figure 7. 16). The maximum contact force generation after the delamination threshold of the hybrid laminates is similar to that of the base laminates, which also confirms the limited transfer of the toughening mechanisms to the impact properties of the laminates after the delamination threshold (Table 7. 1).

This study indicates that the toughening mechanisms via PPS veils can be transferred to enhance the impact properties of the PPS20 and hybrid laminates. The impact properties of the laminates with PPS veils were governed by $G_{I,C}$ until delamination initiation (see 7. 17a). Due to the limited transfer of the toughening mechanisms to the impact properties for the PPS20 and hybrid laminates, once delamination failure is introduced, no correlation was observed between the E_i/A_d ratio and $G_{II,R}$ (see Figure 7. 17b).

In summary, the use of the PPS veils and CSR particle content together can provide further improvement in the impact properties for the hybrid laminates compared to the PPS20 laminates, until the delamination threshold is reached. The impact damage area for the hybrid laminates was substantially suppressed as the hybrid laminates require higher energy to initiate delamination compared to the other laminates investigated in this study. However, the high strain rate in impact loading and inefficient transfer of the energy dissipation toughening mechanisms with PPS veils exhibit no significant influence on the impact properties after the delamination threshold is reached.

CHAPTER 8: Post-impact Compression Response of Hybrid Toughened Composite Laminates

8.1. Introduction

The impact damage tolerance of the hybrid toughened composite laminates is presented in this chapter. The out-of-plane low-velocity impact damage tolerance of the base, CSR10, PPS20 and hybrid toughened laminates were characterised by measuring post-impact compressive strengths for varying impact energy levels (*i.e.* 2.5 J, 5 J, 7.5 J and 10 J impact levels) following to Prichard and Hogg protocol [108]. After the mechanical tests, the composite laminates were sectioned and the fracture surfaces of undamaged and damaged composite laminates were investigated with SEM. The results obtained from the mechanical tests were also correlated with the fracture toughness properties of the composite laminates.

8.2. Compression and CAI Test Results

Due to the PPS veil presence at each interface of the composite laminates, the physical properties of the composite laminates are different. The physical properties of the base, CSR10, PPS20 and hybrid laminates are given in Table 8. 1. The properties of the manufactured test specimens, *i.e.* fibre volume fractions, thickness, density and void content, were characterised according to ASTM D792 [223] and ASTM 3171 [224] standards. The measured carbon fibre volume fraction and the thickness of the base laminates are ~54% and 3.14 mm, respectively. The carbon fibre volume ratio and thickness of CSR10 laminates are similar to the base laminates (~52% and ~3.20 mm, respectively). PPS veil presence at each interface for the carbon fibre laminates resulted in a ~0.7 mm increase in laminate thickness, thus the carbon fibre volume ratio of PPS20 laminates decreases from 54% to 42%. For the hybrid toughened laminates, the thickness increment is ~0.9 mm compared to the base laminates and the resulting carbon fibre volume ratio is calculated as 41%.

The normalised compressive stress and strain curves of the undamaged and damaged base, CSR10, PPS20 and hybrid laminates are given in Figure 8. 1. For comparability, the compressive strength values were normalised with the carbon fibre volume ratio

for undamaged and damaged composite laminates. Sharp decreases in the loading slopes indicate a brittle response of the composite laminates under compressive loading and Figure 8. 1 indicates the brittle behaviour of the undamaged (Figure 8. 1a) and damaged composite laminates under transverse impact with varying energies (*i.e.* 5 J and 10 J as seen in Figure 8. 1b and Figure 8. 1c, respectively).

Table 8. 1| The physical properties (*i.e.* carbon fibre volume ratio, laminate thickness, density and void fraction) of the base, CSR10, PPS20 and hybrid laminates.

Laminate type	Carbon fibre volume ratio (v_f)	Laminate thickness (mm)	Density (g/cm^3)	Void fraction
Epoxy (Base)	0.54 ± 0.01	3.14 ± 0.07	1.43 ± 0.02	0.016
Epoxy + CSR 10 wt% (CSR10)	0.52 ± 0.01	3.20 ± 0.08	1.42 ± 0.10	0.025
Epoxy + 20 g/m^2 PPS (PPS20)	0.42 ± 0.01	3.84 ± 0.07	1.37 ± 0.02	0.023
Epoxy + CSR 10% + 20 g/m^2 PPS veil (Hybrid)	0.41 ± 0.03	4.06 ± 0.14	1.35 ± 0.03	0.012

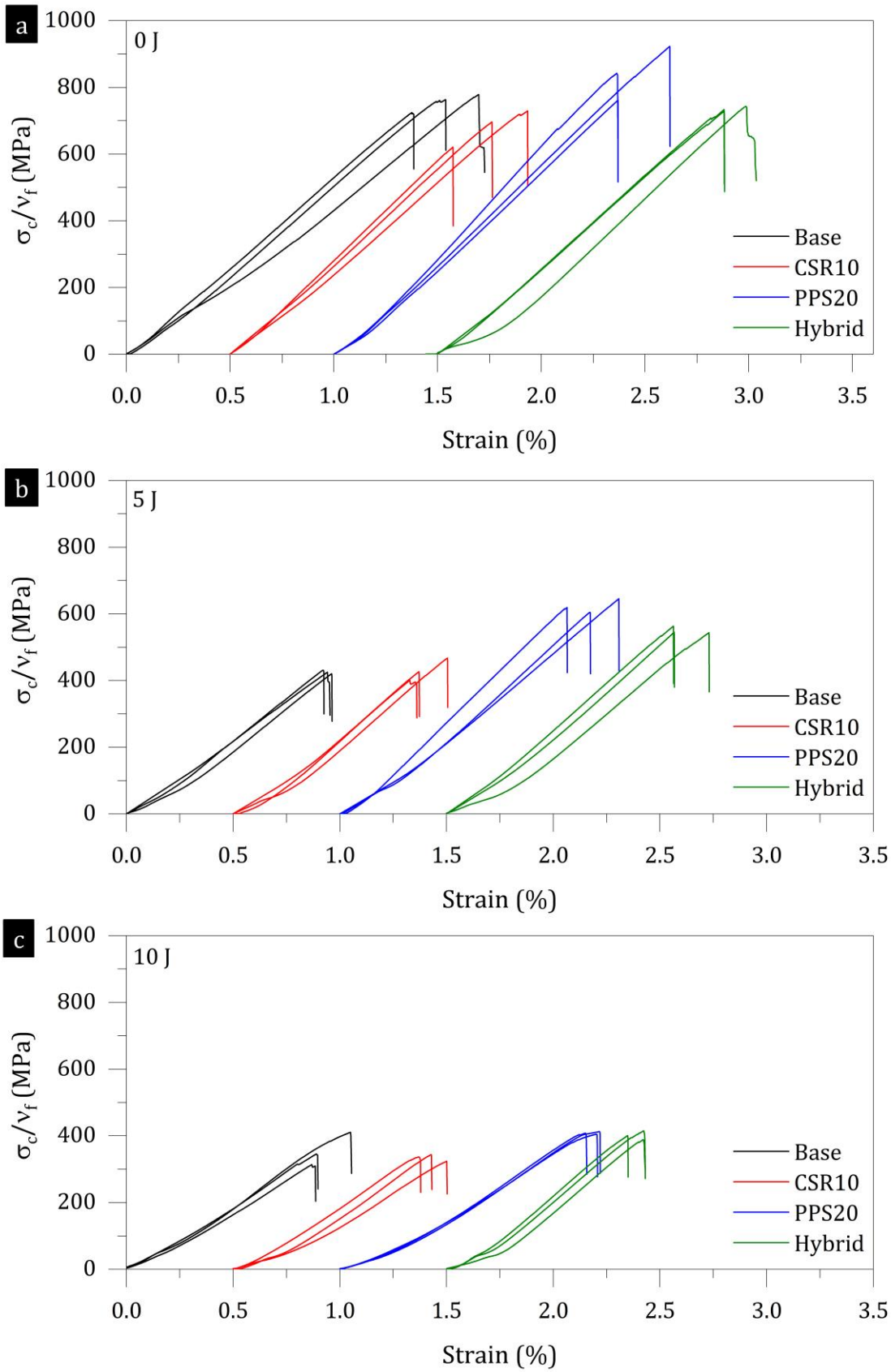

Figure 8. 1| The normalised compressive stress and strain curves of the base, CSR10, PPS20 and hybrid laminates with varying impact: (a) 0 J, (b) 5 J and (c) 10 J.

Figure 8. 2 demonstrates the σ_{uc}/υ_f and the residual compressive strength values (the compressive strength ratio of the damaged laminates to the undamaged laminates) for the laminates corresponding to the impact energy. Figure 8. 2a indicates that the highest σ_{uc}/υ_f was obtained from the PPS20 laminates followed by the base, hybrid and CSR10 laminates when the undamaged laminates are compared. Also, the σ_{uc}/υ_f of the undamaged hybrid laminates is lower than the PPS20 laminates, and the σ_{uc}/υ_f of the CSR10 laminates is lower than that of the base laminates. This suggests that CSR particle content negatively influenced the σ_{uc}/υ_f of the undamaged CSR10 and hybrid laminates. Furthermore, the post-impact compressive strength of the base laminates significantly drops from ~750 MPa to ~250 MPa with 2.5 J impact, then linearly falls until ~330 MPa for 10 J impact. The σ_{uc}/υ_f of the CSR10 laminates falls from ~680 MPa to ~335 MPa for 10 J impact. However, the σ_{uc}/υ_f of the CSR10 laminates is significantly higher compared to the base laminates for 2.5 J impact. The highest σ_{uc}/υ_f were obtained from the PPS20 laminates for each impact level and the σ_{uc}/υ_f of the PPS20 laminates drops linearly from ~840 MPa to ~410 MPa. Similarly, the σ_{uc}/υ_f of the hybrid laminates drops linearly from ~735 MPa to ~400 MPa. Figure 8. 2b demonstrates the residual compressive strength corresponding to the impact energy. This graph indicates the highest loss was observed from the base laminates for each impact level (drops until ~45%).On the other hand, the highest residual strength was observed from the hybrid laminates (*i.e.* especially for 7.5 J and 10 J impacts), which can be related to the introduced impact damage area for these laminates (see Figure 7. 11).

The normalised compression modulus (obtained from the slope of the stress-strain curves) and strain to failure values of the laminates are given in Figure 8. 3. Figure 8. 3a indicates that the lowest compression modulus (~52 GPa) was observed from the base laminates when undamaged laminates are compared. Each laminate can maintain the compression modulus for 2.5 J, 5 J, and 7.5 J impacts. However, the base, CSR10 and PPS10 laminates exhibited significant drops (up to 42 GPa) for 10 J impact, and the hybrid laminates only exhibited a slight drop. Figure 8. 3b indicates the strain to failure values ratio corresponding to the impact energies for the laminates. This graph indicates that the strain to failure value of the undamaged base laminate is ~1.65% whereas that of the CSR10, PPS20 and hybrid laminates is ~1.45%. The strain to failure values of the base and CSR10 laminates significantly decreases with increasing impact

energy whereas that of the PPS20 and hybrid laminates are higher than the base laminates for 2.5 J, 5 J, and 7.5 J impacts. For 10 J impact, a slight increase in the strain to failure values was observed for the base and CSR10 laminates. For PPS20 laminates, the strain to failure value increases from ~1.2% to ~1.35%. On the other hand, the strain to failure value of the hybrid laminates was shown to be decreased for 10 J impact.

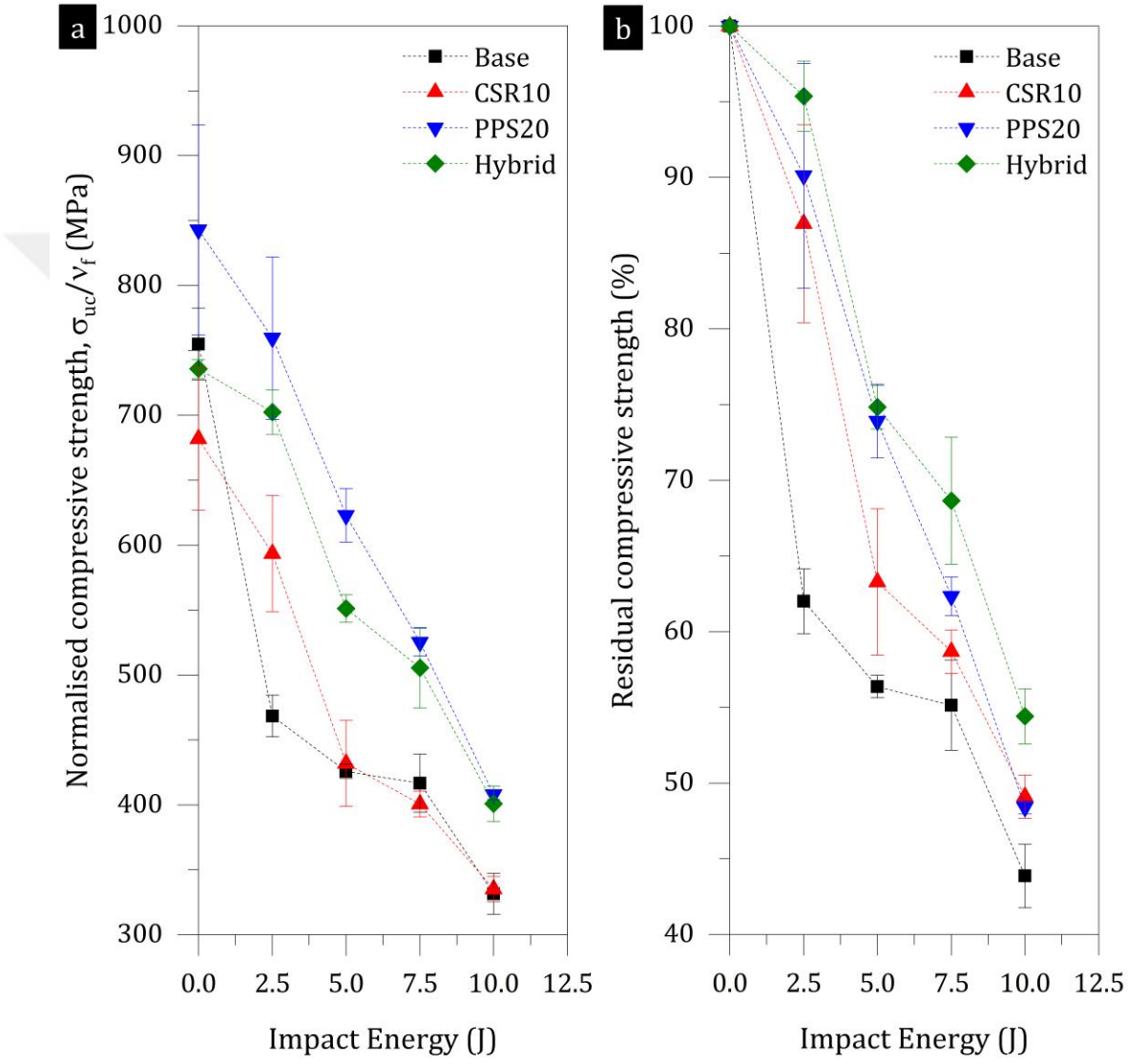

Figure 8. 2| (a) Comparison of the normalised compressive strength, *i.e.* $\sigma_{u,c}/v_f$, with impact energy and (b) the residual compressive strength values obtained from the composite laminates corresponding to the impact energies.

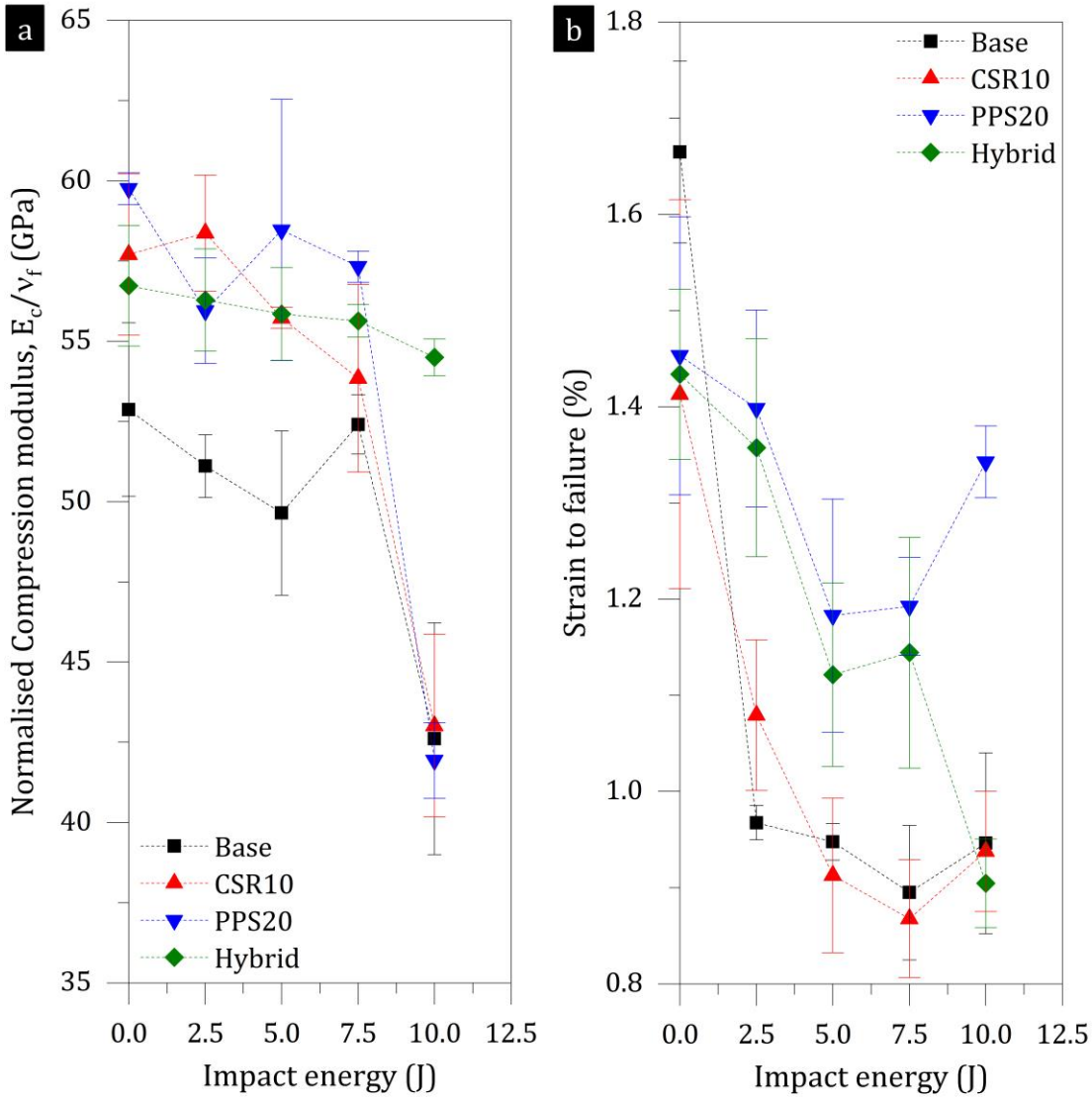

Figure 8. 3| (a) Comparison of the normalised compressive modulus of the laminates, *i.e.* E_c/v_f, (b) the strain to failure values of the laminates under compression loading corresponding to the impact energy.

8.3. Compressive Toughening Mechanisms

After compression tests were performed, the undamaged and damaged composite laminates were sectioned through the length and cross-sectional failure surfaces of the laminates were examined with SEM to provide insight into sub-laminar micro and macro-crack failures. The post-mortem failure observation of the undamaged base, CSR10, PPS20 and hybrid laminate is presented in Figures 8. 4 – 8. 7. These figures

indicate the catastrophic failure of the composite laminates under compression loading, which confirms their brittle response (see Figure 8. 1a).

Figure 8. 4a indicates shear driven compressive failures, delamination and matrix crushing obtained from the base laminate. Figure 8. 4b demonstrates the kink band formation and the ruptured carbon fibres due to kink band formation. Also, clean surfaces of the carbon fibres indicate weak adhesion between carbon fibres and the matrix interface.

Figure 8. 5a indicates that the CSR10 laminates predominantly experienced transverse shear fractures. In comparison to the base laminate, the CSR10 laminate includes less level of matrix crushing. The kink band formation and delamination failures as well as a residual matrix with cavitated CSR particles on the carbon fibre surfaces obtained from the fracture surface of the CSR10 laminate are given in Figure 8. 5b.

The cross-sectional fracture surface of the undamaged PPS20 laminates can be seen from Figure 8. 6a. The PPS20 laminates exhibited transverse shear cracks, delamination and matrix cracking. Delamination failure with bridged PPS fibre and transverse shear crack is given in Figure 8. 6b. Also, clean surfaces of the PPS fibres indicate that PPS fibres can easily debond and pull out due to the fibre bridging failure mechanisms.

The cross-sectional fracture surface of the hybrid toughened composite laminate is given in Figure 8. 7a. Figure 8. 7b indicates the compressive shear cracks, delamination failures, and a kink band formation. This figure also suggests that an extensive number of debonded and broken PPS fibres was achieved from the hybrid toughened composite laminates. Figure 8. 7b also exposes the smooth surface of the PPS fibres and cavitated CSR particles within the epoxy, which indicates that PPS fibres can easily debond from the matrix.

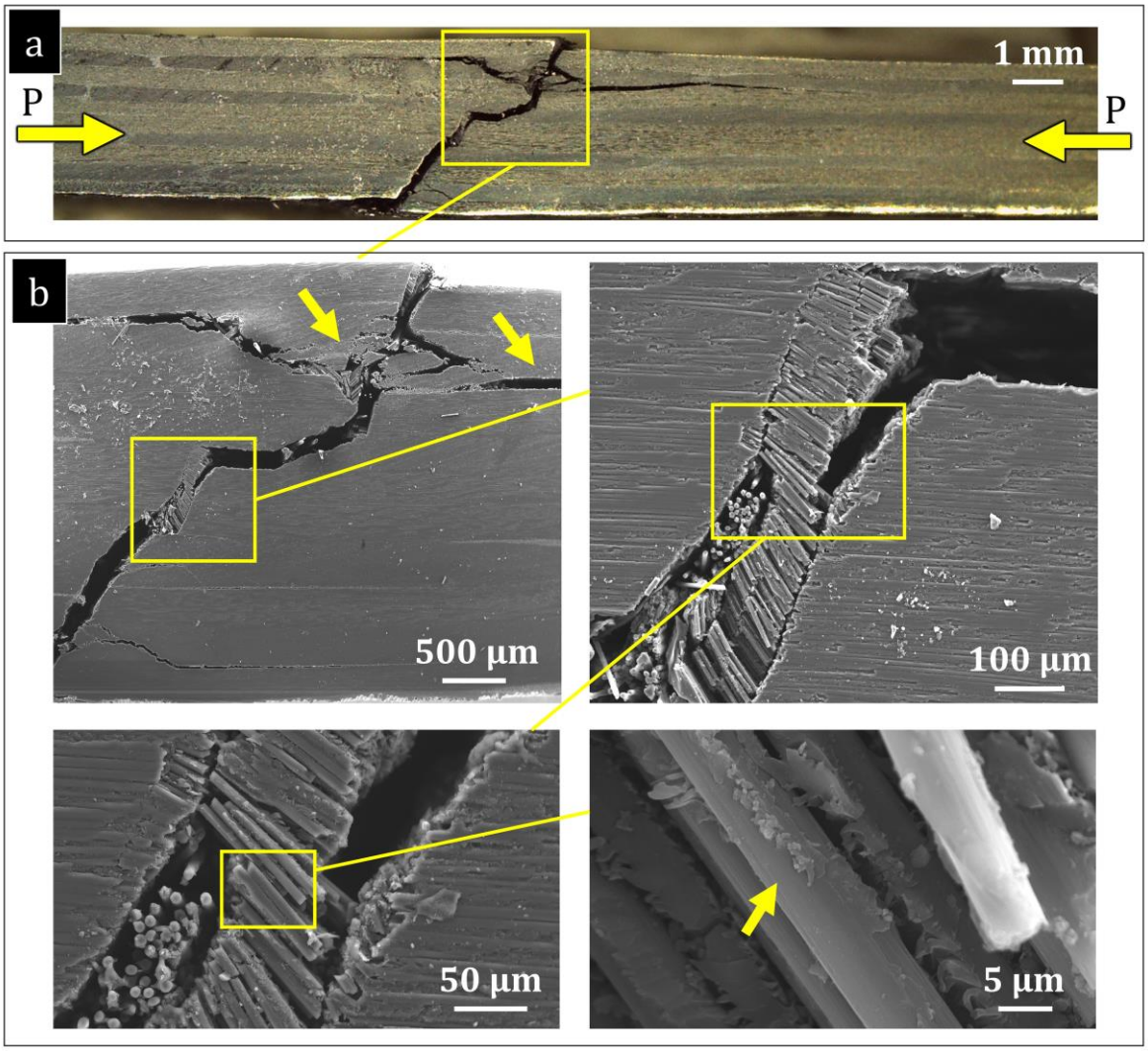

Figure 8. 4| The cross-sectional fracture surface observation of the undamaged base laminate under compression loading: (a) the cross-sectional fracture surface features, and (b) micrographs indicating transverse shear crack with delamination, matrix crushes, kind band formation, and ruptured carbon fibres.

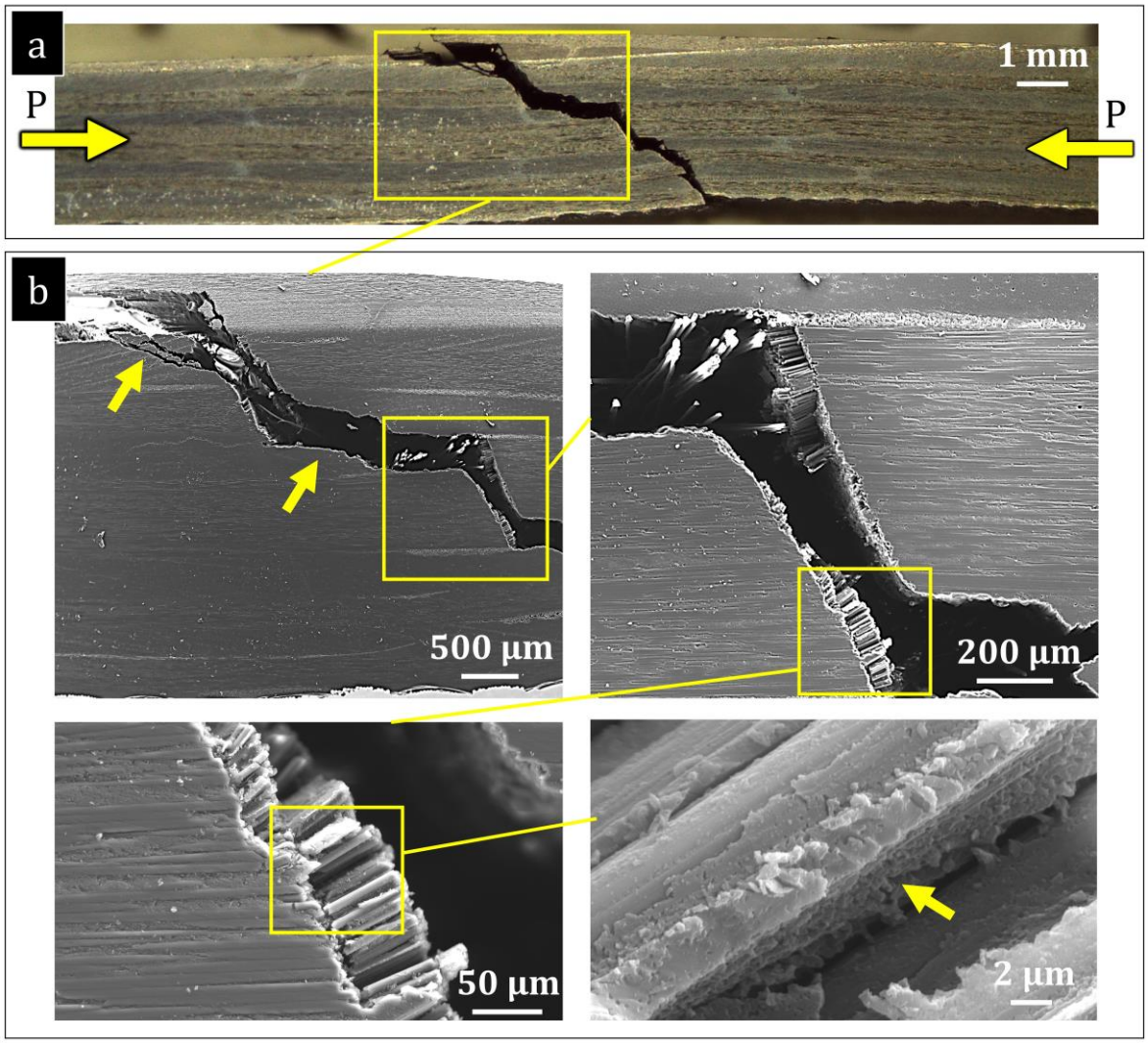

Figure 8. 5| The cross-sectional fracture surface observation of the undamaged CSR10 laminate under compression loading: (a) the cross-sectional fracture surface features, and (b) micrographs indicating transverse shear crack with delamination, matrix crushes, kind band formation, ruptured carbon fibres, and residual cavitated epoxy resin on the carbon fibre surface.

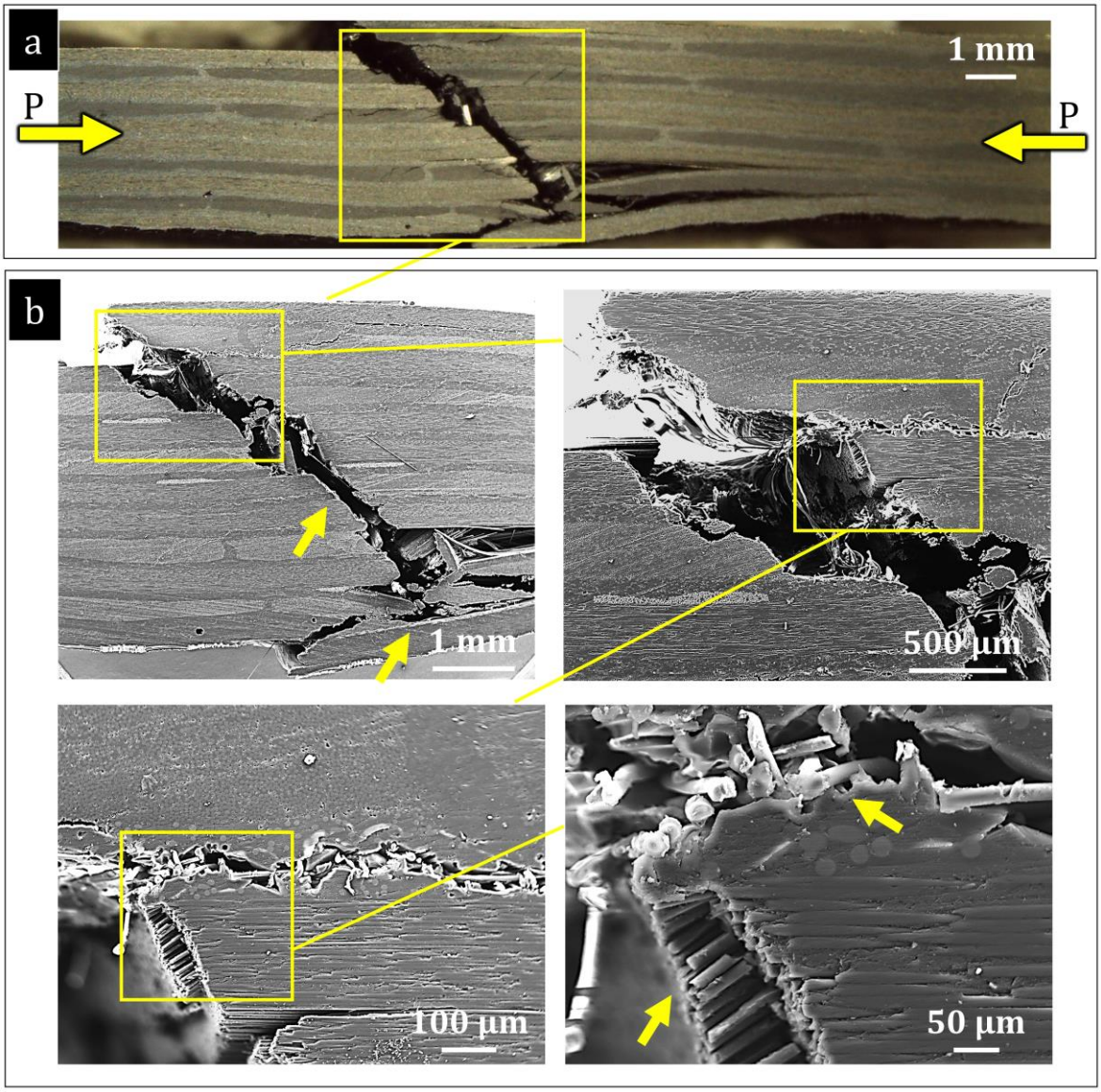

Figure 8. 6| The cross-sectional fracture surface observation of the undamaged PPS20 laminate under compression loading: (a) the cross-sectional fracture surface features, and (b) micrographs indicating transverse shear crack with delamination, matrix crushes, debonded and broken PPS fibres within the interlaminar region, smooth surface of the PPS fibres, kink band formation and ruptured carbon fibres.

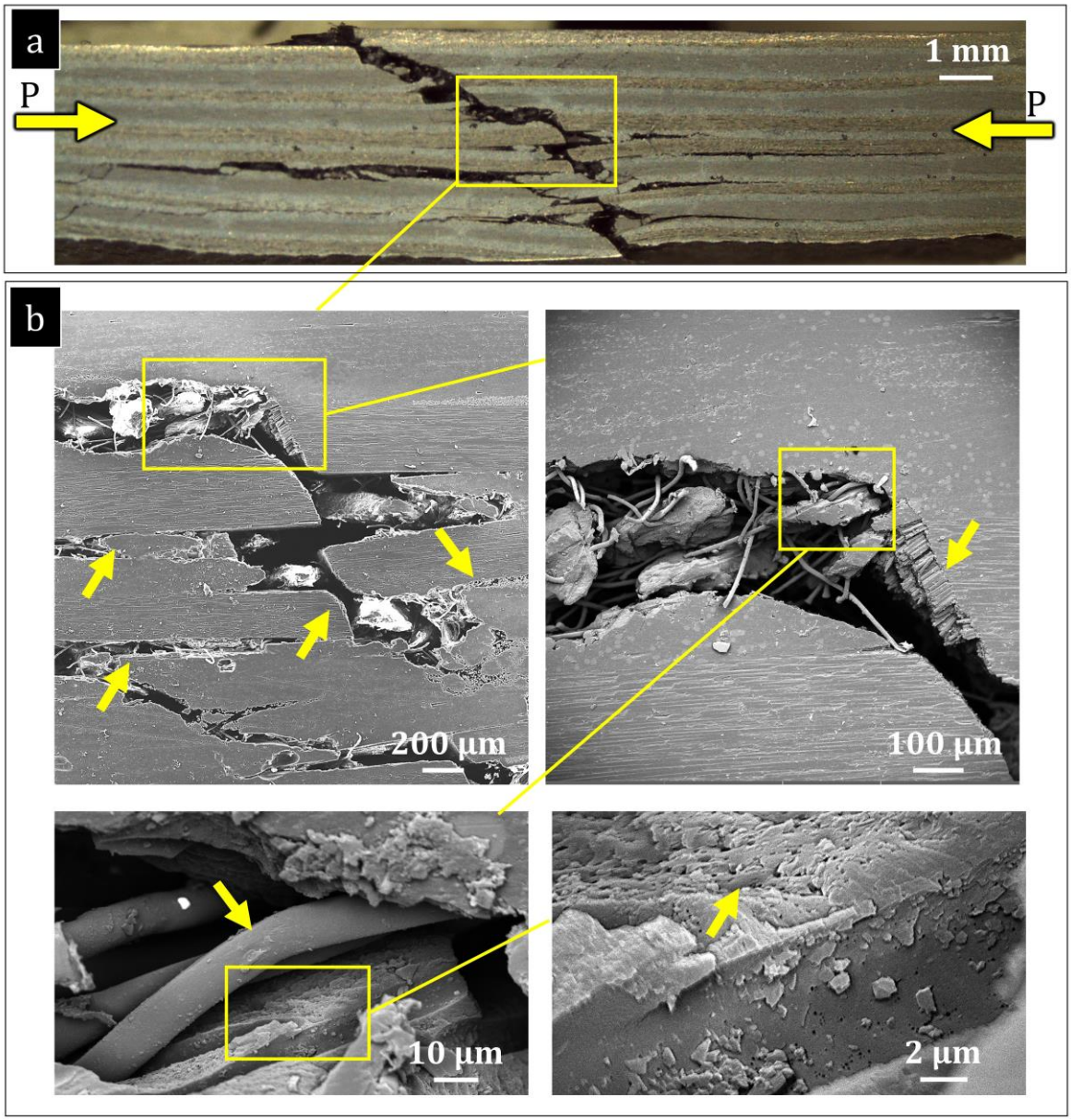

Figure 8. 7| The cross-sectional fracture surface observation of the undamaged hybrid laminate under compression loading: (a) the cross-sectional fracture surface features, and (b) micrographs indicating transverse shear cracks with delamination, matrix crushes, kink band formation, ruptured carbon fibres, debonded and broken PPS fibres within the interlaminar region, smooth surface of the PPS fibres and rough surface of the cavitated epoxy resin.

8.4. CAI Toughening Mechanisms

The compressive failure mechanisms of the damaged composite laminates with 10 J transverse impact were also observed to understand the difference leading to a loss in load-carrying capability after impact damage for the laminates. The cross-sectional failure features obtained from the damaged base, CSR10, PPS20 and hybrid laminates are given in Figures 8.8 – 8. 11. These figures indicate catastrophic failures of the

laminates and confirm the brittle response of the composite laminates under CAI loading (see Figures 8. 1b and -c).

The cross-sectional fracture surface of the damaged base laminate is given in Figure 8. 8a. This figure indicates that the damaged base laminates experienced the growth of the delamination at the upper layers beneath the impact point. The micrographs obtained from the damaged base laminates (Figure 8. 8) indicate the clear surface of the carbon fibre surface and the glassy surface of the untoughened epoxy resin.

The fracture surface obtained from the damaged CSR10 laminate indicates delamination failure at multiple interlaminar regions, which suggests delamination growth to the regions beneath the impact point as seen in Figure 8. 9a. The micrographs (see Figure 8. 8b) exhibit a residual matrix with cavitated CSR particles on the carbon fibre surfaces. It is also revealed that both the damaged base (Figure 8. 8) and CSR10 (Figure 8. 9) laminates for the 10 J impact level do not contain kink band formations, unlike the undamaged base (Figure 8. 4) and CSR10 (Figure 8. 5) laminates. This indicates that both laminates experienced delamination growth due to the local buckling of the delaminated layers under compression loading. With the failure mechanisms exposed (Figure 8. 9) and mechanical test results (Figure 8. 1), it can be stated that the propagation of the delamination failures predominantly causes the loss in the load-carrying capability for the damaged base and CSR10 laminates.

The cross-sectional failure surface of the PPS20 laminates obtained with optical microscopy is given in Figure 8. 10a. Figure 8. 10b indicates the compressive failure mechanisms of the damaged PPS20 laminate are carbon fibre breakage at the top layers due to the transverse shear, PPS fibre bridging, delamination along the resin-rich region between the carbon fibre reinforced layer and PPS veil toughened interlaminar region, and kink band formations. When compared to the base laminate (Figure 8. 8), carbon fibre fractures with kink bands and transverse shear cracks indicate better load transfer through carbon fibres for the PPS20 laminates.

The cross-sectional fracture surface of the hybrid toughened composite laminate is given in Figure 8. 11a. Matrix cracks, PPS fibre bridging and kind band formation were observed from the micrographs obtained from the damaged hybrid toughened laminate, as seen in Figure 8. 11b. The delamination growth occurred along the resin-rich region between carbon fibre surfaces and the hybrid toughened interlaminar

region, unlike the undamaged hybrid laminate response under compression loading (Figure 8. 7). However, PPS fibre-based toughening mechanisms were stimulated during transverse shear crack development. Figure 8. 11b also exposes the rough surface of the epoxy due to the CSR particle cavitation and smooth surface of the PPS fibres. In comparison to the damaged PPS laminate, the damaged hybrid laminate experienced fibre breakage at each layer (Figure 8. 11a) whereas the damaged PPS20 laminate experienced fibre breakages at the top layers (Figure 8. 10a). The fractographical investigations (Figure 8. 11) together with compressive test results (Figure 8. 2b) indicate that the use of PPS veils with CSR particle content influenced the energy dissipation mechanisms of the composite laminates, thus the post-impact residual properties of the hybrid laminates were improved.

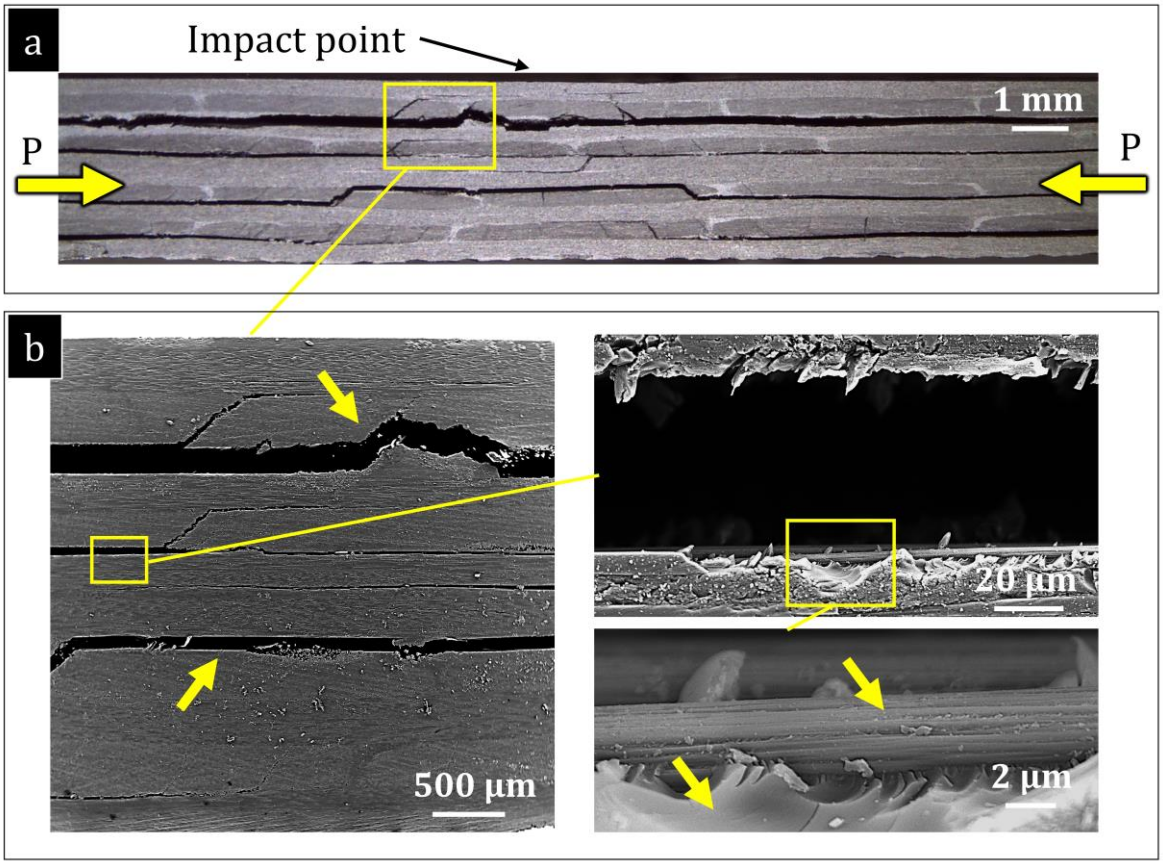

Figure 8. 8| The cross-sectional fracture surface observation of the base laminate under compression loading after the transverse impact with 10 J energy: (a) cross-sectional fracture surface features, and (b) micrographs indicating delamination, glassy surface of the epoxy resin and the carbon fibre surface.

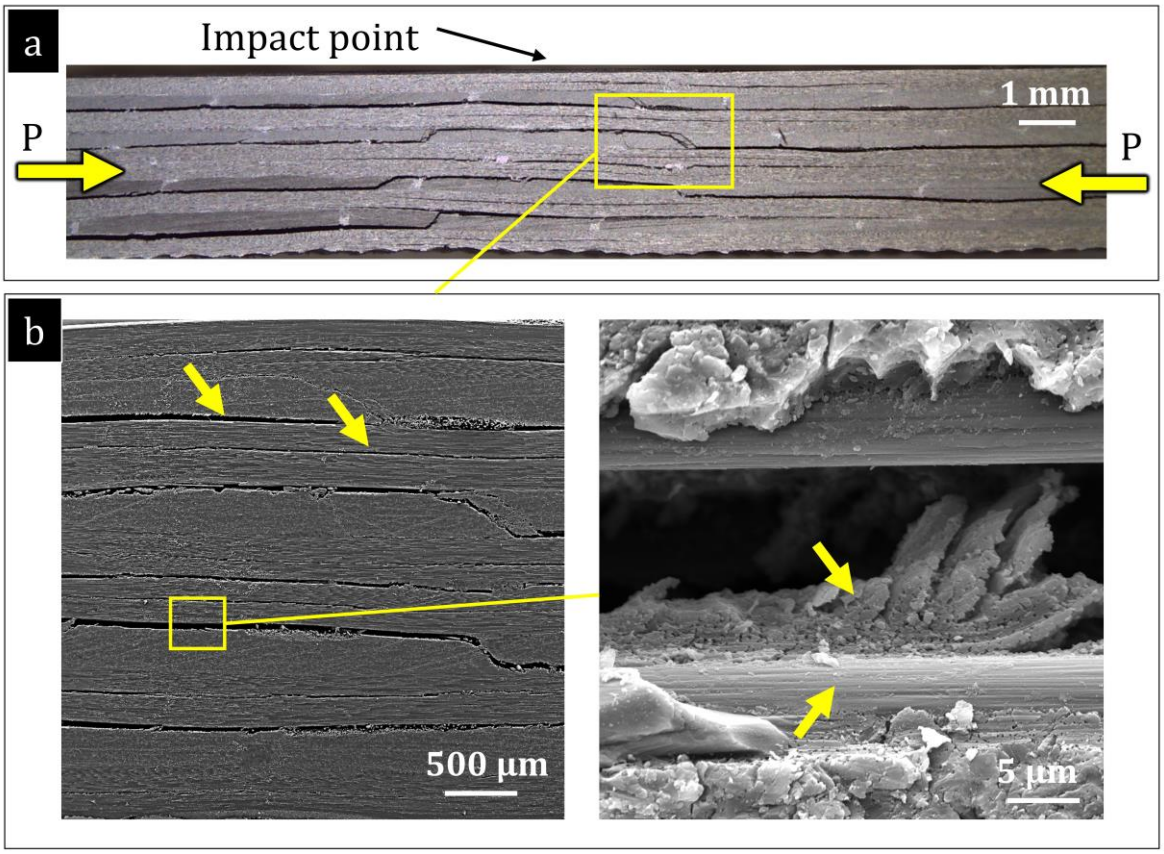

Figure 8. 9| The cross-sectional fracture surface observation of the CSR10 laminate under compression loading after the transverse impact with 10 J energy: (a) cross-sectional fracture surface features, and (b) micrographs indicating delamination growth and residual cavitated epoxy on the carbon fibre surface.

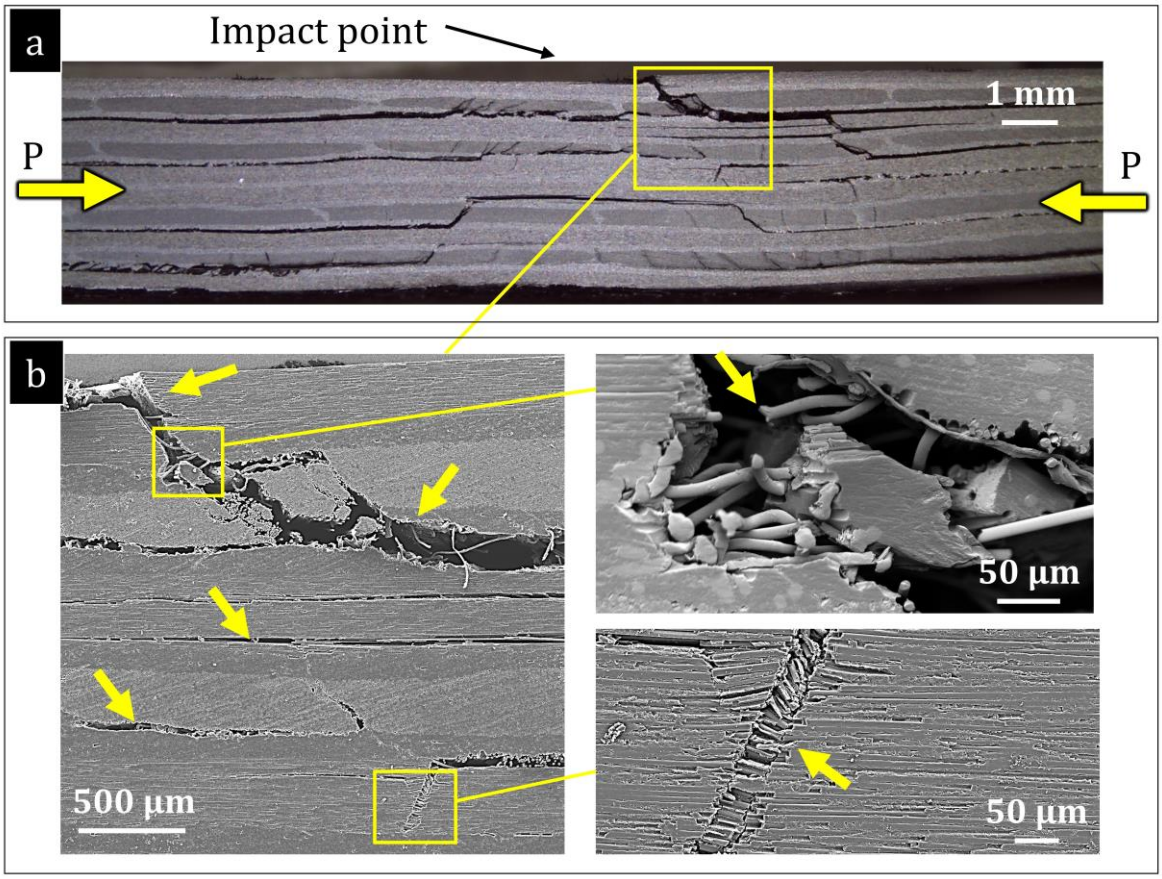

Figure 8. 10| The cross-sectional fracture surface observation of the PPS10 laminate under compression loading after the transverse impact with 10 J energy: (a) cross-sectional fracture surface features, and (b) micrographs indicating debonded and broken PPS fibres due to the shear cracks, delamination growth along the resin-rich region between PPS veils and carbon fibre surfaces, and broken carbon fibres.

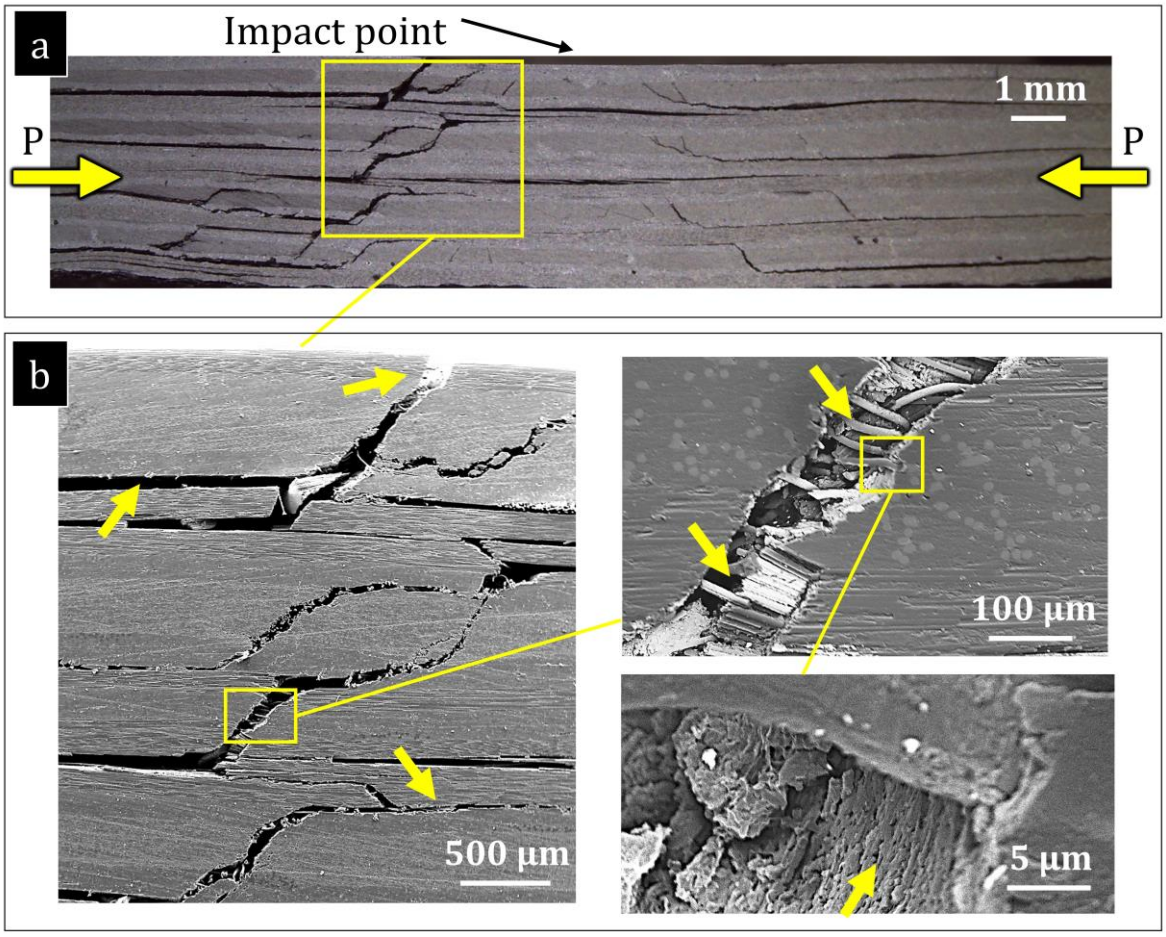

Figure 8. 11| The cross-sectional fracture surface observation of the hybrid laminate under compression laoding after the transverse impact with 10 J energy: (a) cross-sectional fracture surface features, and (b) micrographs indicating debonded PPS fibres due to the shear cracks, delamination growth along the resin-rich region between PPS veils and carbon fibre surfaces, broken carbon fibres and rough surface of the cavitated epoxy.

8.5. Discussions

The use of CSR particles and PPS veils together changes the energy dissipation of the laminates under impact loading and provides further improvement in mode-I fracture energies. In parallel, the impact damage threshold is also improved with the hybrid toughening strategy. On the other hand, the mode-II fracture properties of the hybrid laminates are lower than the PPS laminates, which is because of the adverse effect of the CSR particle content. The adverse effect of the CSR particle content on the CSR10 laminates was observed under impact loading (CSR10 laminates experienced the highest impact damage area, see Figure 7. 11). In addition, the micrographs obtained from the PPS20 and hybrid laminates indicate that the crack tip followed resin rich region between veils and neighbouring lamina. Therefore, the transfer of the mode-II

fracture properties to impact properties was limited for the PPS20 and hybrid laminates for once delamination failure is initiated. This section is discussed how the toughening mechanisms obtained from the combination of the CSR particle content and the veils together affect the post-impact properties of laminates.

The compression test results of the undamaged laminates indicate that CSR particle content adversely affects the ultimate compressive strength of the CSR10 and hybrid laminates (*i.e.* σ_{uc}/υ_f of the undamaged CSR is lower than σ_{uc}/υ_f of the base, and σ_{uc}/υ_f of the undamaged hybrid laminates is lower than the σ_{uc}/υ_f of the undamaged PPS20 laminates, see Figure 8. 2a). It is also shown that the base laminates exhibited compressive strength loss up to ~60% for 10 J impact damage (see Figure 8. 2b). The CSR particle content in the epoxy improved the low-velocity impact damage tolerance for the composite material system investigated in this study and the CSR10 laminates exhibited compressive strength loss up to 50% for 10 J impact (see Figure 8. 2b), although the CSR10 laminates include higher damage area than the base laminates (Figure 7. 11a). On the other hand, the residual compressive strength loss of the PPS20 is ~50% for 10 J impact damage (see Figure 8. 2b), which is similar to CSR10 laminates. However, the post-impact properties of the PPS20 laminates outperformed that of the CSR10 laminates for 5 J and 7.5 J impact damage, which can be due to the significant reduction in impact damage area at 5 J and 7.5 J (Figure 7. 11a). Also, microstructural investigations confirm that PPS veil presence at the interfaces changes the post-impact compression response of the PPS20 laminates (transverse shear cracks were observed at the top layer of the damaged PPS20 laminates and the PPS fibre toughening mechanisms were predominantly established with shear crack formations, see Figure 8. 10). The highest impact damage tolerance was observed to be achieved from the hybrid toughened laminates (see Figure 8. 2b), which shows that synergistic toughening mechanisms were established for the hybrid laminates. The results of this study refer that the introduction of cavitation in the epoxy with CSR particle incorporation enhances the impact damage tolerance of the CSR10 laminates, despite the moderate reduction in ultimate compressive strength for the undamaged laminates (Figure 8. 2).

As compression loading leads to the opening of the delaminated regions, the correlation between the residual compressive strength values and measured mode-I fracture propagation energies for the investigated composite laminates are given in

Figure 8. 12. This figure suggests that the low-velocity transverse impact damage tolerance of the composite laminates is correlated to mode-I fracture propagation energies of the laminates (*i.e.* higher residual compressive strength was obtained for the laminates with higher mode-I fracture energies). This indicates that the post-impact compressive properties of the laminates are predominantly governed by the mode-I fracture properties of the laminates. However, the achieved improvement in the fracture energies is not proportional compared to the achieved enhancement in the post-impact compression properties for the composite laminates (*e.g.* over 200% improvement is achieved in G_{IC} and G_{IR} from the hybrid laminates as seen in Table 5. 1, and compressive strength loss after impact is ~45% for 10 J impact for the hybrid laminates whereas that is ~60% for the base laminates, see Figure 8. 2b). Firstly, this can be attributed to the dependency of the post-impact properties on the impact properties. The loading rate is significantly higher in the impact tests compared to the loading rate applied in the ILFT tests and the interlaminar fracture properties of the composite laminates can be strain rate dependent. Therefore, a high strain rate can be a diminishing factor for the transfer of the fracture properties to the impact, thus that can influence the post-impact properties of composite laminates [218–222]. Also, the crack growth path can be another reason for the limited transfer of the fracture toughness properties to the post-impact properties of composite laminates. The fractographical observations indicate that PPS based toughening mechanisms (*e.g.* debonding and breakage) were obtained during transverse shear crack development whereas the crack tip did not propagate within the veil toughened interlaminar region during delamination formation under impact loading (*i.e.* delamination growth occurred from the resin-rich region along between carbon fibre surfaces and the interlaminar toughened interface, see Figure 7. 15 and Figure 7. 16 for the PPS20 and hybrid laminates, respectively). Therefore, the crack tip hardly experienced the PPS fibre toughening mechanisms during crack tip propagation within the veils under transverse impact. Also, early crack propagation occurred through resin-rich regions between the veils and carbon fibre surfaces in the PPS20 and hybrid laminates due to the impact loading resulted in the propagation of the crack tip along the resin-rich regions between the veils and carbon fibre lamina. The PPS fibre-based toughening mechanisms were only developed when the transverse shear cracks were established (see Figure 8. 10 and Figure 8. 11 for the PPS20 and hybrid laminates, respectively), which can also be responsible for the limited transfer of the toughening properties to

the post-impact compression properties. Similarly, several studies indicate that the crack growth path is a significant parameter influencing the fracture properties for micro-fibre veil toughened composite laminates [44,48].

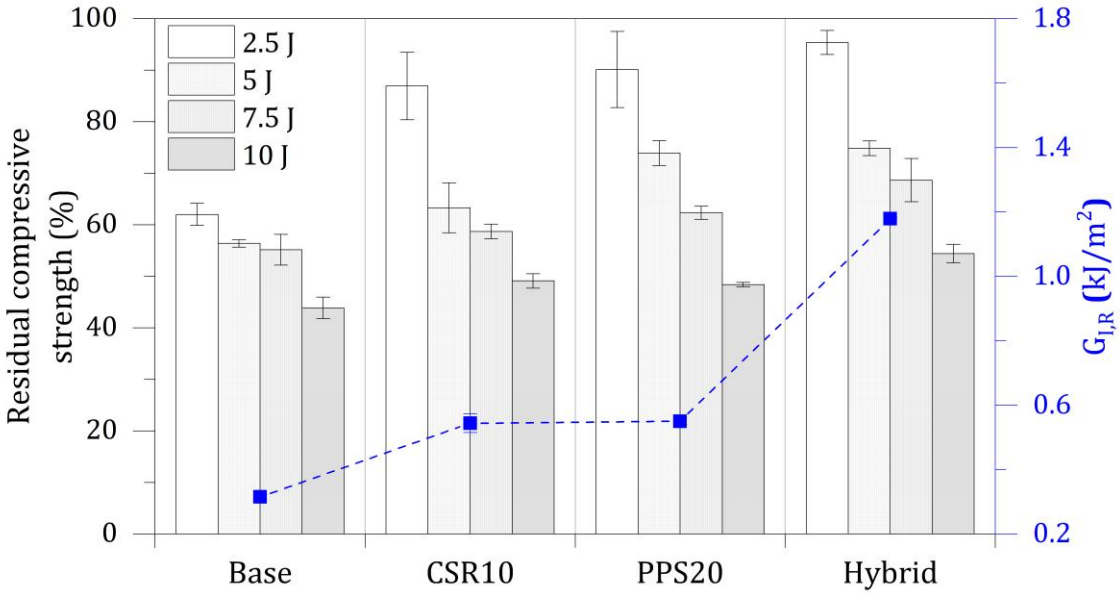

Figure 8. 12| Correlation of the residual compressive strength with mode-I propagation energies ($G_{I,R}$) of the base, CSR10, PPS20 and hybrid laminates.

8.6. Conclusions

Chapter 8 investigates how the use of PPS veils with CSR particles content influences the post-impact response of the composite laminates. The conclusions below are drawn in this chapter:

- *The influence of the CSR particle content*: The residual post-impact properties of the CSR10 laminates are higher than that of the base laminates (Figure 8. 2b). However, 10 wt% CSR particle content in the epoxy slightly reduced the compressive strength of the undamaged CSR10 laminates compared to the undamaged base laminates (Figure 8. 2a). The micrographs taken from the CSR10 laminates confirm the cavitation of the CSR particles (Figure 8. 5 and Figure 8. 9 for the micrographs of the undamaged and damaged CSR10 laminates, respectively).
- *The influence of the PPS veil:* The highest compressive strength values were obtained from the PPS20 laminates for each impact level (Figure 8. 2a). The

micrographs taken from the PPS20 laminates suggest that the presence of the PPS veils at each interface changes the post-impact response of the PPS20 laminates. The PPS20 laminates exhibited shear cracks at the top layers (see Figure 8. 10) whereas the base laminates experienced delamination propagation to the region beneath the impact point under compression loading (Figure 8. 8). The residual compressive strength is higher for each impact level compared to the base laminates (see Figure 8. 2b).

- *The influence of the CSR particle content and PPS veil together:* A moderate reduction in the compressive strength was observed for the undamaged hybrid laminates when compared to the undamaged PPS20 laminates (Figure 8. 2a). However, the residual compressive strength linearly decreases until ~55% for 10 J impact, which is higher than the other laminates for each impact level (Figure 8. 2b). The micrographs obtained from the damaged hybrid laminates confirm that transverse shear cracks with carbon fibre breakages and PPS fibre toughening mechanisms (*e.g.* debonding and breakages) at each layer (see Figure 8. 11) whereas the damaged PPS20 laminates exhibited the shear cracks only at the top layers (see Figure 8. 10). Therefore, the use of the CSR particle content together with PPS veils changes the energy dissipation mechanisms.

This chapter indicates that CSR particle content adversely affected the compressive strength of the CSR10 (*i.e.* lower than the base laminates) and hybrid laminates (*i.e.* lower than the PPS20 laminates). However, the residual strength of the laminates with CSR particle content is higher than the counterpart laminates without CSR particle content. Therefore, the introduction of the cavitation in the epoxy with the CSR particle content improved the impact damage tolerance of the laminates. With the PPS veil presence, the laminates behaved stiffer under compression loading and significant improvement was achieved in the compressive strength (Figure 8. 3). The hybrid toughening approach can provide further improvement in residual compressive strength for the laminates, although a moderate reduction in compressive strength at each impact level compared to the PPS20 laminates (Figure 8. 2b). Also, it is indicated that the laminates with higher mode-I fracture properties offered better impact damage tolerance (see Figure 8. 12). However, the limited transfer of the toughening performance to the impact damage tolerance was observed due to the crack growth along the resin-rich region between carbon fibre lamina and PPS veils.

CHAPTER 9: Conclusions And Suggestions for Future Works

9.1. Conclusions

This study was performed to investigate the influence of the hybrid use of the CSR particle content and PPS veils on the interlaminar fracture, impact and post-impact properties of composite laminates. For the material system investigated, following conclusions are made:

- The PPS veil toughened laminates outperformed PEI veil toughened laminates because easily debonded PPS fibres promoted toughening mechanisms (*e.g.* debonding and breakage) and developed relatively high crack resistance. However, both PEI and PPS veil toughened laminates experienced crack tip migration, which results in significant improvement for the crack initiation (~12% and ~80% for the PEI and PPS laminates, respectively) but slight improvement for the crack propagation (~3% and ~18% for the PEI and PPS laminates, respectively).
- The hybrid laminates were toughened with the 20 g/m^2 PPS veils and 10 wt% CSR particle content to investigate the influence of hybrid use of CSR particle and PPS veils on mode-I fracture properties. It is shown that 10 wt% CSR particle content in the epoxy influenced the crack propagation path in mode-I. The laminates with 10 wt% CSR particle content exhibited a rising R-curve under mode-I loading (~50% and ~70% improvement for the crack initiation and propagation, respectively). Also, the laminates with 20 g/m^2 PPS veils exhibited a decreasing R-curve. The crack tip initially propagated within the veils, then migrated towards the neighbouring lamina. The use of the PPS veils together with CSR particles altered the crack tip propagation path. The crack tip partly propagated from the veil partly from the neighbouring lamina. Thus, the hybrid use of the 20 g/m^2 PPS veils and 10 wt% CSR particle content developed further improvement for the hybrid laminates in mode-I fracture energies. When compared to the base laminates, the mode-I fracture energies of the hybrid toughened laminates are higher by ~245% and ~275% for the crack initiation and propagation, respectively.
- 10 wt% CSR particle content changed the crack tip propagation path in mode-II and the crack tip followed the interlaminar region while the base laminates

experienced crack migration towards neighbouring lamina. The laminates with 10 wt% CSR particle content exhibited a flat R-curve and adversely affected the mode-II properties of the CSR10 laminates (~35% and ~15% reduction for the crack initiation and propagation compared to the base laminates, respectively). On the other hand, the laminates with 20 g/m^2 PPS veils exhibited slightly rising R-curves, then falls until reaching steady-state region. The mode-II fracture properties of the PPS20 laminates were significantly enhanced (~150% and ~255% improvement for the crack initiation and propagation, respectively). The hybrid use of the CSR particle content with 20 g/m^2 PPS veils also adversely influenced the mode-II fracture properties of the hybrid laminate. The crack tip propagated without considerable migration towards neighbouring lamina. Among investigated composite material systems, only the hybrid laminates exhibited rising R-curves and a considerable improvement was achieved (~64% and ~215% for the crack initiation and propagation, respectively) in mode-II.

- The adverse effect of the CSR particle content was observed for the CSR10 laminates under impact loading. The laminates with 10 wt% CSR particle content exhibited no significant difference in F_{th} and F_{max} generations. However, the impact damage area of the CSR10 laminates is higher than the base laminates (~70%, ~65%, ~60% and ~12% for 2.5 J, 5 J, 7.5 J and 10 J impact). On the other hand, the PPS veils increased the delamination resistance of the PPS20 laminates under impact loading (no major failure was observed for 2.5 J impact) and the impact damage area was suppressed with PPS veils (~6%, ~12% and ~11% for 5 J, 7.5 J and 10 J impact, respectively). F_{th} was increased by ~28%, ~37% and ~32% for 5 J, 7.5 J and 10 J impact, respectively. F_{max} generation was hardly influenced for the PPS20 laminates, which can be due to the crack tip propagation along the resin-rich region between the veils and carbon fibre surfaces. The PPS fibre debonding and breakage was predominantly observed with the shear cracks. Similarly, the impact damage resistance of the hybrid laminates was increased and no significant impact damage area was observed at the 2 J impact level. The use of the CSR particle content with PPS veils suppressed impact damage area by ~15%, ~27% and ~12% for 5 J, 7.5 J and 10 J impacts, respectively. Also, the F_{th} generation of the hybrid laminates was increased by ~17%, ~32% and ~38% for 5 J, 7.5 J and 10

J impact, respectively. No significant improvement was achieved in the F_{max} generation from the hybrid laminates. The use of the PPS veils with CSR particle content changed the energy dissipation under impact loading for the hybrid laminates. PPS fibre debonding within shear cracks exhibited crack tip branching. Similar to the PPS20 laminates, the hybrid laminates exhibited crack propagation along the resin-rich region between the veils and carbon fibre surfaces. Therefore, the PPS fibres did not contribute to the impact response of the hybrid laminates after delamination failure was initiated. It is also shown that the impact resistance of the composite laminates was predominantly governed by the mode-I fracture properties until delamination initiation. After delamination was initiated in the laminates, the transfer of the fracture properties to the impact properties became limited due to the delamination propagation along the resin-rich region between veils and carbon fibres for the hybrid laminates.

- A significant reduction in the residual compressive strength values was observed from the base laminates (~38%, ~44%, ~45% and ~56% loss in CAI for 2.5 J, 5 J, 7.5 J and 10 J impact, respectively). The residual compressive strength values of the CSR10 laminates is higher than the base laminates (~13%, ~37%, ~41% and ~51% loss in CAI for 2.5 J, 5 J, 7.5 J and 10 J impact, respectively), although the CSR10 laminates include higher impact damage area compared to the base laminates. However, the compressive strength of the undamaged CSR10 laminates is slightly lower than that of the base laminates. The compressive strength values of the undamaged and damaged PPS20 laminates are higher than the other laminates for each impact level. Also, a significant improvement was achieved in the residual strength values from the PPS20 laminates (~10%, ~26%, ~38% and ~52% loss in CAI for 2.5 J, 5 J, 7.5 J and 10 J impact, respectively). The highest residual compressive strength was obtained from the hybrid laminates (~5%, ~25%, ~32% and ~45% loss in CAI strength for 2.5 J, 5 J, 7.5 J and 10 J impact, respectively). 10 wt% CSR particle content incorporation also resulted in a reduction in the compressive strength of the undamaged hybrid laminates compared to the undamaged PPS20 laminates. Post-impact studies clearly indicate that the hybrid use of the 20 g/m^2 PPS veils and 10 wt% CSR particle content can provide further improvement in residual compressive strength for the hybrid laminates despite

a moderate reduction in compressive strength values because of CSR particle content. Also, the post-impact properties of the laminates are predominantly correlated with the mode-I fracture energies. However, the improvement in mode-I properties and post-impact properties for the hybrid laminates are not proportional.

9.2. Future Works

- The untoughened (base) laminates experienced crack tip propagation from the interlaminar region to the neighbouring intralaminar region under mode-I loading. Also, the base laminates were interleaved with thermoplastic veils with high adhesion (PEI) and poor adhesion (PPS). In parallel, both interleaved laminates experienced crack tip migration from the veil toughened region to the neighbouring lamina. Therefore, numerical investigations can be performed to provide a better understanding of the crack tip migration from the veil to the neighbouring lamina.
- The impact damage introduced in the laminates was detected with ultrasonic C-scanning in this study. However, ultrasonic C-scanning technique is not capable to detect matrix cracking and fibre fractures. Microstructural observations require the sectioning of laminates with a saw, which can deform the fracture surface of laminates. For this reason, the laminates can be scanned with computed tomography to get a better insight into the damage.
- This study focusses on the interlaminar fracture, impact and post-impact properties of NCF composites toughened with the hybrid approach. The influence of the hybrid toughening approach on composites with different fibre architectures can be examined.
- Mode-I and mode-II fracture properties, impact and the post-impact response of the hybrid laminates were investigated in this study. The influence of the hybrid toughening mechanisms on fatigue properties can be investigated.

REFERENCES

[1] Katnam KB, Da Silva LFM, Young TM. Bonded repair of composite aircraft structures: A review of scientific challenges and opportunities. Progress in Aerospace Sciences 2013;61:26–42. https://doi.org/10.1016/j.paerosci.2013.03.003.

[2] Sela N, Ishai O. Interlaminar fracture toughness and toughening of laminated composite materials: a review. Composites 1989;20:423–35. https://doi.org/10.1016/0010-4361(89)90211-5.

[3] Katnam KB, Dalfi H, Potluri P. Towards balancing in-plane mechanical properties and impact damage tolerance of composite laminates using quasi-UD woven fabrics with hybrid warp yarns. Composite Structures 2019;225:111083. https://doi.org/10.1016/j.compstruct.2019.111083.

[4] Selver E, Potluri P, Hogg P, Soutis C. Impact damage tolerance of thermoset composites reinforced with hybrid commingled yarns. Composites Part B: Engineering 2016;91:522–38. https://doi.org/10.1016/J.COMPOSITESB.2015.12.035.

[5] Andrew JJ, Srinivasan SM, Arockiarajan A, Dhakal HN. Parameters influencing the impact response of fiber-reinforced polymer matrix composite materials: A critical review. Composite Structures 2019;224:111007. https://doi.org/10.1016/j.compstruct.2019.111007.

[6] Prevorsek DC, Chin HB, Bhatnagar A. Damage tolerance: design for structural integrity and penetration. Composite Structures 1993;23:137–48. https://doi.org/10.1016/0263-8223(93)90018-L.

[7] Vieille B, Casado VM, C B. About the impact behavior of woven-ply carbon fiber-reinforced thermoplastic- and thermosetting-composites: A comparative study. Composite Structures 2013;101:9–21. https://doi.org/10.1016/J.COMPSTRUCT.2013.01.025.

[8] Vieille B, Casado VM, Bouvet C. Influence of matrix toughness and ductility on the compression-after-impact behavior of woven-ply thermoplastic- and thermosetting-composites: A comparative study. Composite Structures 2014;110:207–18. https://doi.org/10.1016/j.compstruct.2013.12.008.

[9] Hongkarnjanakul N, Bouvet C, Rivallant S. Validation of low velocity impact modelling on different stacking sequences of CFRP laminates and influence of fibre failure. Composite Structures 2013;106:549–59. https://doi.org/10.1016/J.COMPSTRUCT.2013.07.008.

[10] Davies GAO, Zhang X. Impact damage prediction in carbon composite structures. International Journal of Impact Engineering 1995;16:149–70. https://doi.org/10.1016/0734-743X(94)00039-Y.

[11] Stegschuster G, Pingkarawat K, Wendland B, Mouritz AP. Experimental determination of the mode i delamination fracture and fatigue properties of thin 3D woven composites. Composites Part A: Applied Science and Manufacturing 2016;84:308–15. https://doi.org/10.1016/j.compositesa.2016.02.008.

[12] Tanzawa Y, Watanabe N, Ishikawa T. Interlaminar fracture toughness of 3-D orthogonal interlocked fabric composites. Composites Science and Technology 1999;59:1261–70. https://doi.org/10.1016/S0266-3538(98)00167-5.

[13] Guénon VA, Chou TW, Gillespie JW. Toughness properties of a three-dimensional carbon-epoxy composite. Journal of Materials Science 1989;24:4168–75. https://doi.org/10.1007/BF01168991.

[14] Dransfield K, Baillie C, Mai Y-W. Improving the delamination resistance of CFRP by stitching—a review. Composites Science and Technology 1994;50:305–17. https://doi.org/10.1016/0266-3538(94)90019-1.

[15] Tan K, Watanabe N, Iwahori Y. Stitch fiber comparison for improvement of interlaminar fracture toughness in stitched composites. Journal of Reinforced Plastics and Composites 2011;30:99–109. https://doi.org/10.1177/0731684410383065.

[16] Dransfield KA, Jain LK, Mai YW. On the effects of stitching in CFRPs - I. Mode I delamination toughness. Composites Science and Technology 1998;58:815–27. https://doi.org/10.1016/S0266-3538(97)00229-7.

[17] Mouritz AP. Review of z-pinned composite laminates. Composites Part A: Applied Science and Manufacturing 2007;38:2383–97. https://doi.org/10.1016/J.COMPOSITESA.2007.08.016.

[18] Pegorin F, Pingkarawat K, Daynes S, Mouritz AP. Influence of z-pin length on the delamination fracture toughness and fatigue resistance of pinned composites. Composites Part B: Engineering 2015;78:298–307. https://doi.org/10.1016/j.compositesb.2015.03.093.

[19] Liu HY, Yan W, Mai YW. Z-pin bridging force in composite delamination. European Structural Integrity Society 2003;32:491–502. https://doi.org/10.1016/S1566-1369(03)80119-X.

[20] Cartié DDR, Troulis M, Partridge IK. Delamination of Z-pinned carbon fibre reinforced laminates. Composites Science and Technology 2006;66:855–61. https://doi.org/10.1016/j.compscitech.2004.12.018.

[21] Chang P, Mouritz AP, Cox BN. Properties and failure mechanisms of z-pinned laminates in monotonic and cyclic tension. Composites Part A: Applied Science and Manufacturing 2006;37:1501–13. https://doi.org/10.1016/j.compositesa.2005.11.013.

[22] Callus PJ, Mouritz AP, Bannister MK, Leong KH. Tensile properties and failure mechanisms of 3D woven GRP composites. Composites Part A: Applied Science and Manufacturing 1999;30:1277–87. https://doi.org/10.1016/S1359-835X(99)00033-0.

[23] Kim JK, Sham ML. Impact and delamination failure of woven-fabric composites. Composites Science and Technology 2000;60:745–61. https://doi.org/10.1016/S0266-3538(99)00166-9.

[24] Farley GL, Smith BT, Maiden J. Compression Response of Thick Layer Composite Laminates with Through-the-Thickness Reinforcement. Journal of Reinforced Plastics and Composites 1992;11:787–810. https://doi.org/10.1177/073168449201100705.

[25] Mouritz AP, Cox BN. Mechanistic approach to the properties of stitched laminates. Composites Part A: Applied Science and Manufacturing 2000;31:1–27. https://doi.org/10.1016/S1359-835X(99)00056-1.

[26] Gnaba I, Legrand X, Wang P, Soulat D. Through-the-thickness reinforcement for composite structures: A review. Journal of Industrial Textiles 2018:152808371877229. https://doi.org/10.1177/1528083718772299.

[27] Beylergil B, Tanoğlu M, Aktaş E. Effect of polyamide-6,6 (PA 66) nonwoven veils on the mechanical performance of carbon fiber/epoxy composites. Composite Structures 2018;194:21–35. https://doi.org/10.1016/J.COMPSTRUCT.2018.03.097.

[28] Bagheri R, Marouf BT, Pearson RA. Rubber-Toughened Epoxies: A Critical Review. Polymer Reviews 2009;49:201–25. https://doi.org/10.1080/15583720903048227.

[29] Yan C, Xiao K, Ye L, Mai YW. Numerical and experimental studies on the fracture behavior of rubber-toughened epoxy in bulk specimen and laminated composites. Journal of Materials Science 2002;37:921–7. https://doi.org/10.1023/A:1014335511515.

[30] Pearson RA, Yee AF. Influence of particle size and particle size distribution on toughening mechanisms in rubber-modified epoxies. Journal of Materials Science 1991;26:3828–44. https://doi.org/10.1007/BF01184979.

[31] Becu L, Maazouz A, Sautereau H, Gerard JF. Fracture behavior of epoxy polymers modified with core-shell rubber particles. Journal of Applied Polymer Science 1997;65:2419–31. https://doi.org/10.1002/(SICI)1097-4628(19970919)65:12<2419::AID-APP14>3.0.CO;2-W.

[32] Marouf BT, Pearson RA, Bagheri R. Anomalous fracture behavior in an epoxy-based hybrid composite. Materials Science and Engineering A 2009;515:49–58. https://doi.org/10.1016/j.msea.2009.03.028.

[33] Abadyan M, Khademi V, Bagheri R, Haddadpour H, Kouchakzadeh MA, Farsadi M. Use of rubber modification technique to improve fracture-resistance of hoop wound composites. Materials and Design 2009;30:1976–84. https://doi.org/10.1016/j.matdes.2008.09.001.

[34] Kim DS, Cho K, Kim JK, Park CE. Effects of particle size and rubber content on fracture toughness in rubber-modified epoxies. Polymer Engineering & Science 1996;36:755–68. https://doi.org/10.1002/pen.10463.

[35] Zeng Y, Liu H-Y, Mai Y-W, Du X-S. Improving interlaminar fracture toughness of carbon fibre/epoxy laminates by incorporation of nano-particles 2011. https://doi.org/10.1016/j.compositesb.2011.04.036.

[36] Klingler A, Bajpai A, Wetzel B. The effect of block copolymer and core-shell rubber hybrid toughening on morphology and fracture of epoxy-based fibre reinforced composites. Engineering Fracture Mechanics 2018;203:81–101. https://doi.org/10.1016/j.engfracmech.2018.06.044.

[37] Awang Ngah S, Taylor AC. Toughening performance of glass fibre composites with core–shell rubber and silica nanoparticle modified matrices. Composites Part A:

Applied Science and Manufacturing 2016;80:292–303. https://doi.org/10.1016/J.COMPOSITESA.2015.10.036.

[38] Maazouz A, Sautereau H, Gérard JF. Toughening of epoxy networks using pre-formed core-shell particles or reactive rubbers. Polymer Bulletin 1994;33:67–74. https://doi.org/10.1007/BF00313475.

[39] Giannakopoulos G, Masania K, Taylor AC. Toughening of epoxy using core–shell particles. Journal of Materials Science 2011;46:327–38. https://doi.org/10.1007/s10853-010-4816-6.

[40] Ratna D. Phase separation in liquid rubber modified epoxy mixture. Relationship between curing conditions, morphology and ultimate behavior. Polymer (Guildf) 2001;42:4209–18. https://doi.org/10.1016/S0032-3861(00)00798-9.

[41] Yasaee M, Bond IP, Trask RS, Greenhalgh ES. Mode i interfacial toughening through discontinuous interleaves for damage suppression and control. Composites Part A: Applied Science and Manufacturing 2012;43:198–207. https://doi.org/10.1016/j.compositesa.2011.10.009.

[42] Dikshit V, Somen KB, Joshi CS. Multiscale Polymer Composites: A Review of the Interlaminar Fracture Toughness Improvement. Fibers 2017;5:38. https://doi.org/10.3390/fib5040038.

[43] Beckermann GW, Pickering KL. Mode I and Mode II interlaminar fracture toughness of composite laminates interleaved with electrospun nanofibre veils. Composites Part A: Applied Science and Manufacturing 2015;72:11–21. https://doi.org/10.1016/J.COMPOSITESA.2015.01.028.

[44] Del Saz-Orozco B, Ray D, Stanley WF. Effect of thermoplastic veils on interlaminar fracture toughness of a glass fiber/vinyl ester composite. Polymer Composites 2017;38:2501–8. https://doi.org/10.1002/pc.23840.

[45] Brugo T, Palazzetti R. The effect of thickness of Nylon 6,6 nanofibrous mat on Modes I–II fracture mechanics of UD and woven composite laminates. Composite Structures 2016;154:172–8. https://doi.org/10.1016/J.COMPSTRUCT.2016.07.034.

[46] Beylergil B, Tanoğlu M, Aktaş E. Enhancement of interlaminar fracture toughness of carbon fiber-epoxy composites using polyamide-6,6 electrospun nanofibers. Journal of Applied Polymer Science 2017;134:45244. https://doi.org/10.1002/app.45244.

[47] Kuwata M, Hogg PJ. Interlaminar toughness of interleaved CFRP using non-woven veils: Part 1. Mode-I testing. Composites Part A: Applied Science and Manufacturing 2011;42:1551–9. https://doi.org/10.1016/J.COMPOSITESA.2011.07.016.

[48] Quan D, Bologna F, Scarselli G, Ivankovic A, Murphy N. Interlaminar fracture toughness of aerospace-grade carbon fibre reinforced plastics interleaved with thermoplastic veils. Composites Part A: Applied Science and Manufacturing 2020;128:105642. https://doi.org/https://doi.org/10.1016/j.compositesa.2019.105642.

[49] Ramirez VA, Hogg PJ, Sampson WW. The influence of the nonwoven veil architectures on interlaminar fracture toughness of interleaved composites. Composites Science and Technology 2015;110:103–10. https://doi.org/10.1016/j.compscitech.2015.01.016.

[50] Quan D, Bologna F, Scarselli G, Ivanković A, Murphy N. Mode-II fracture behaviour of aerospace-grade carbon fibre/epoxy composites interleaved with thermoplastic veils. Composites Science and Technology 2020;191:108065. https://doi.org/10.1016/j.compscitech.2020.108065.

[51] García-Rodríguez SM, Costa J, Rankin KE, Boardman RP, Singery V, Mayugo JA. Interleaving light veils to minimise the trade-off between mode-I interlaminar fracture toughness and in-plane properties. Composites Part A: Applied Science and Manufacturing 2020;128:105659. https://doi.org/10.1016/j.compositesa.2019.105659.

[52] Quan D, Alderliesten R, Dransfeld C, Murphy N, Ivanković A, Benedictus R. Enhancing the fracture toughness of carbon fibre/epoxy composites by interleaving hybrid meltable/non-meltable thermoplastic veils. Composite Structures 2020;252:112699. https://doi.org/10.1016/j.compstruct.2020.112699.

[53] Wong DWY, Zhang H, Bilotti E, Peijs T. Interlaminar toughening of woven fabric carbon/epoxy composite laminates using hybrid aramid/phenoxy interleaves. Composites Part A: Applied Science and Manufacturing 2017;101:151–9. https://doi.org/10.1016/j.compositesa.2017.06.001.

[54] Kuwata M, Hogg PJ. Interlaminar toughness of interleaved CFRP using non-woven veils: Part 2. Mode-II testing. Composites Part A: Applied Science and Manufacturing 2011;42:1560–70. https://doi.org/10.1016/j.compositesa.2011.07.017.

[55] Quan D, Deegan B, Alderliesten R, Dransfeld C, Murphy N, Ivanković A, et al. The influence of interlayer/epoxy adhesion on the mode-I and mode-II fracture response of carbon fibre/epoxy composites interleaved with thermoplastic veils. Materials and Design 2020;192:108781. https://doi.org/10.1016/j.matdes.2020.108781.

[56] Quan D, Mischo C, Binsfeld L, Ivankovic A, Murphy N. Fracture behaviour of carbon fibre/epoxy composites interleaved by MWCNT- and graphene nanoplatelet-doped thermoplastic veils. Composite Structures 2020;235:111767. https://doi.org/10.1016/j.compstruct.2019.111767.

[57] Mallick PK. Fiber-reinforced composites : materials, manufacturing, and design. Boca Raton: CRC Press; 2008.

[58] Hull Derek, Clyne TW. An introduction to composite materials. Cambridge University Press; 1996.

[59] Warren AS. Developments and Challenges for Aluminum - A Boeing Perspective. MATERIALS FORUM, vol. 28, Proceedings of the 9th International Conference on Aluminium Alloys; 2004, p. 24–31.

[60] Campbell FC. Structural composite materials. Ohio: ASM International; 2010.

[61] Gay D, Hoa SV (Suong V), Tsai SW. Composite materials : design and applications. CRC Press; 2003.

[62] Barbero EJ. Introduction to Composite Materials Design. Third Edit. CRC Press; 2017.

[63] Bank LC. Composites for Construction: Structural Design with FRP Materials - Lawrence C. Bank . John Wiley & Sons; 2006.

[64] Wilkinson AN, Ryan AJ. Polymer processing and structure development. Kluwer Academic Publishers; 1999.

[65] Chang IY, Lees JK. Recent Development in Thermoplastic Composites: A Review of Matrix Systems and Processing Methods. Journal of Thermoplastic Composite Materials 1988;1:277–96. https://doi.org/10.1177/089270578800100305.

[66] Cantwell WJ, Morton J. The impact resistance of composite materials — a review. Composites 1991;22:347–62. https://doi.org/10.1016/0010-4361(91)90549-V.

[67] Pilato LA, Michno MJ. Advanced Composite Materials. Springer Berlin Heidelberg; 1994. https://doi.org/10.1007/978-3-662-35356-1_1.

[68] Chawla KK. Matrix Materials. Composite Materials, New York, NY: Springer New York; 2012, p. 73–103. https://doi.org/10.1007/978-0-387-74365-3_3.

[69] Jefferson AJ, Arumugam V, Dhakal H. Repair of Polymer Composites. 1st Edition. Woodhead Publishing; 2018.

[70] Soutis C. Carbon fiber reinforced plastics in aircraft construction. Materials Science and Engineering: A 2005;412:171–6. https://doi.org/10.1016/J.MSEA.2005.08.064.

[71] Campbell FC. Manufacturing processes for advanced composites. Elsevier; 2004.

[72] Richardson MOW, Wisheart MJ. Review of low-velocity impact properties of composite materials. Composites Part A: Applied Science and Manufacturing 1996;27:1123–31. https://doi.org/10.1016/1359-835X(96)00074-7.

[73] Campbell FC. Manufacturing Technology for Aerospace Structural Materials. 2006.

[74] Dutton S, Kelly D, Baker A. Composite Materials for Aircraft Structures, Second Edition. American Institute of Aeronautics and Astronautics; 2004. https://doi.org/10.2514/4.861680.

[75] Soutis C. Fibre reinforced composites in aircraft construction. Progress in Aerospace Sciences 2005;41:143–51. https://doi.org/10.1016/J.PAEROSCI.2005.02.004.

[76] Sathishkumar T, Satheeshkumar S, Naveen J. Glass fiber-reinforced polymer composites – a review. Journal of Reinforced Plastics and Composites 2014;33:1258–75. https://doi.org/10.1177/0731684414530790.

[77] Graham-Jones J, Summerscales J. Marine Applications of Advanced Fibre-Reinforced Composites. Elsevier Inc.; 2015. https://doi.org/10.1016/C2013-0-16504-X.

[78] Sinmazçelik T, Avcu E, Bora MÖ, Çoban O. A review: Fibre metal laminates, background, bonding types and applied test methods. Materials and Design 2011;32:3671–85. https://doi.org/10.1016/j.matdes.2011.03.011.

[79] Moussavi-Torshizi SE, Dariushi S, Sadighi M, Safarpour P. A study on tensile properties of a novel fiber/metal laminates. Materials Science and Engineering A 2010;527:4920–5. https://doi.org/10.1016/j.msea.2010.04.028.

[80] Baj J. Advanced Fibre-Reinforced Polymer (FRP) Composites for Structural Applications - 1st Edition. Woodhead Publishing; 2013.

[81] Miravete A. 3-D textile reinforcements in composite materials. Woodhead Publishing Ltd; 1999.

[82] Oelsner GH. Handbook of Weaves. Dover Publications; 1952.

[83] Adanur S. Handbook of weaving. CRC Press; 2000. https://doi.org/10.1201/9780429135828.

[84] Cox BN, Flanagan G. Handbook of analytical methods for textile composites. NASA Contractor Report 4750; 1997.

[85] Mariatti M, Nasir M, Ismail H, Naslr M. Influence of Different Woven Geometry and Ply Effect in Woven Thermoplastic Composite Behaviour-Part 2. International Journal of Polymeric Materials 2000;47:499–512. https://doi.org/10.1080/00914030008035083.

[86] Rudd CD, Long AC, Kendall KN, Mangin C. Liquid Moulding Technologies: Resin Transfer Moulding, Structural Reaction Injection Moulding and Related Processing Techniques. Woodhead Publishing; 1997.

[87] Rudov-Clark S, Mouritz AP, Lee L, Bannister MK. Fibre damage in the manufacture of advanced three-dimensional woven composites. Composites Part A: Applied Science and Manufacturing 2003;34:963–70. https://doi.org/10.1016/S1359-835X(03)00213-6.

[88] Todor MP, Bulei C, Kiss I. Composite materials manufacturing using textile inserts with natural origins fibres. IOP Conference Series: Materials Science and Engineering 2018;393:012088. https://doi.org/10.1088/1757-899X/393/1/012088.

[89] Saleh MN, El-Dessouky HM. 3D Woven Composites: From Weaving to Manufacturing. In: Khanna R, Cayumil R, editors. Recent Developments in the Field of Carbon Fibers, InTech; 2018. https://doi.org/10.5772/intechopen.71346.

[90] Cherif C. The Textile Process Chain and Classification of Textile Semi-finished Products. Textile Materials for Lightweight Constructions, Berlin, Heidelberg: Springer Berlin Heidelberg; 2016, p. 9–35. https://doi.org/10.1007/978-3-662-46341-3_2.

[91] Tanwer AK. Mechanical Properties Testing of Uni-directional and Bi-directional Glass Fibre Reinforced Epoxy Based Composites. International Journal of Research in Advent Technology 2014;2.

[92] Zhang D, Sun Y, Chen L, Pan N. A comparative study on low-velocity impact response of fabric composite laminates. Materials and Design 2013;50:750–6. https://doi.org/10.1016/j.matdes.2013.03.044.

[93] Bru T. Behaviour and material properties of composites for crash modelling. CHALMERS UNIVERSITY OF TECHNOLOGY, 2016.

[94] Erden S, Ho K. Fiber reinforced composites. Fiber Technology for Fiber-Reinforced Composites 2017:51–79. https://doi.org/10.1016/B978-0-08-101871-2.00003-5.

[95] Hoa S V. Principles of manufacturing of composite materials. Lancaster: DEStech Publications; 2009.

[96] Hull D, Shi YB. Damage mechanism characterization in composite damage tolerance investigations. Composite Structures 1993;23:99–120. https://doi.org/10.1016/0263-8223(93)90015-I.

[97] Baker AA, Jones R, Callinan RJ. Damage tolerance of graphite/epoxy composites. Composite Structures 1985;4:15–44. https://doi.org/10.1016/0263-8223(85)90018-2.

[98] Sierakowski RL, Newaz GM. Damage tolerance in advanced composites. Technomic Pub. Co; 1995.

[99] Vogelesang LB, Vlot A. Development of fibre metal laminates for advanced aerospace structures. Journal of Materials Processing Technology 2000;103:1–5. https://doi.org/10.1016/S0924-0136(00)00411-8.

[100] Larsson F. Damage tolerance of a stitched carbon/epoxy laminate. Composites Part A: Applied Science and Manufacturing 1997;28:923–34. https://doi.org/10.1016/S1359-835X(97)00063-8.

[101] Naik NK, Ramasimha R, Arya H, Prabhu S V., ShamaRao N. Impact response and damage tolerance characteristics of glass-carbon/epoxy hybrid composite plates. Composites Part B:Engineering 2001;32:565–74. https://doi.org/10.1016/S1359-8368(01)00036-1.

[102] Bingyan Y, Bo T, Yunsen H, Jeremy S, Xiaozhi H. Improving impact resistance and residual compressive strength of carbon fibre composites using un-bonded non-woven short aramid fibre veil. Composites Part A: Applied Science and Manufacturing 2019;121:439–48. https://doi.org/10.1016/J.COMPOSITESA.2019.04.006.

[103] Sasikumar A, Trias D, Costa J, Blanco N, Orr J, Linde P. Impact and compression after impact response in thin laminates of spread-tow woven and non-crimp fabrics. Composite Structures 2019;215:432–45. https://doi.org/10.1016/J.COMPSTRUCT.2019.02.054.

[104] Davies GAO, Hitchings D, Zhou G. Impact damage and residual strengths of woven fabric glass/polyester laminates. Composites Part A: Applied Science and Manufacturing 1996;27:1147–56. https://doi.org/10.1016/1359-835X(96)00083-8.

[105] Sanchez-Saez S, Barbero E, Zaera R, Navarro C. Compression after impact of thin composite laminates. Composites Science and Technology 2005;65:1911–9. https://doi.org/10.1016/j.compscitech.2005.04.009.

[106] Cantwell WJ, Curtis PT, Morton J. An assessment of the impact performance of CFRP reinforced with high-strain carbon fibres. Composites Science and Technology 1986;25:133–48. https://doi.org/10.1016/0266-3538(86)90039-4.

[107] Hogg PJ, Bibo GA. Impact and damage tolerance. Mechanical Testing of Advanced Fibre Composites, Elsevier; 2000, p. 211–47. https://doi.org/10.1533/9781855738911.211.

[108] Prichard JC, Hogg PJ. The role of impact damage in post-impact compression testing. Composites 1990;21:503–11. https://doi.org/10.1016/0010-4361(90)90423-T.

[109] Leonard F, Withers PJ, Léonard F, Shi Y, Soutis C, Pinna C. Impact damage characterisation of fibre metal laminates by X-ray computed tomography, 2014, The Conference on Industrial Computed Tomography.

[110] Vaidya UK. Impact response of laminated and sandwich composites. CISM International Centre for Mechanical Sciences, Courses and Lectures, vol. 526, Springer International Publishing; 2011, p. 97–191. https://doi.org/10.1007/978-3-7091-0523-8_4.

[111] Sjoblom PO, Hartness JT, Cordell TM. On Low-Velocity Impact Testing of Composite Materials. Journal of Composite Materials 1988;22:30–52. https://doi.org/10.1177/002199838802200103.

[112] Shivakumar KN, Elber W, Illg W. Prediction of low-velocity impact damage in thin circular laminates. AIAA Journal 1985;23:442–9. https://doi.org/10.2514/3.8933.

[113] Abrate S. Impact on Laminated Composite Materials. American Society of Mechanical Engineers, 1991. https://doi.org/10.1115/1.3119500.

[114] Liu D, Malvern LE. Matrix Cracking in Impacted Glass/Epoxy Plates. Journal of Composite Materials 1987;21:594–609. https://doi.org/10.1177/002199838702100701.

[115] Olsson R. Mass criterion for wave controlled impact response of composite plates. Composites Part A: Applied Science and Manufacturing 2000;31:879–87. https://doi.org/10.1016/S1359-835X(00)00020-8.

[116] Challenger KD. The damage tolerance of carbon fiber reinforced composites-A workshop summary. Composite Structures 1986;6:295–318. https://doi.org/10.1016/0263-8223(86)90025-5.

[117] Kim J-K, MacKay DB, Mai Y-W. Drop-weight impact damage tolerance of CFRP with rubber-modified epoxy matrix. Composites 1993;24:485–94. https://doi.org/10.1016/0010-4361(93)90018-4.

[118] Belingardi G, Vadori R. Low velocity impact tests of laminate glass-fiber-epoxy matrix composite material plates. International Journal of Impact Engineering 2002;27:213–29. https://doi.org/10.1016/S0734-743X(01)00040-9.

[119] Sultan MTH, Worden K, Staszewski WJ. Impact damage characterisation of composite laminates using a statistical approach. Composites Science and Technology 2012;72:1108–20. https://doi.org/10.1016/J.COMPSCITECH.2012.01.019.

[120] Shyr TW, Pan YH. Impact resistance and damage characteristics of composite laminates. Composite Structures 2003;62:193–203. https://doi.org/10.1016/S0263-8223(03)00114-4.

[121] Aktaş M, Ersen Balcioğlu H, Aktaş A, Türker E, Emin Deniz M. Impact and post impact behavior of layer fabric composites. Composite Structures 2012;94:2809–18. https://doi.org/10.1016/j.compstruct.2012.04.008.

[122] Zhang X, Hounslow L, Grassi M. Improvement of low-velocity impact and compression-after-impact performance by z-fibre pinning. Composites Science and Technology 2006;66:2785–94. https://doi.org/10.1016/J.COMPSCITECH.2006.02.029.

[123] Davies GAO, Olsson R. Impact on composite structures. The Aeronautical Journal 2004;108:541–63. https://doi.org/10.1017/S0001924000000385.

[124] Olsson R. Low- and medium-velocity impact as a cause of failure in polymer matrix composites. Failure Mechanisms in Polymer Matrix Composites 2012:53–78. https://doi.org/10.1533/9780857095329.1.53.

[125] Choi HY, Downs RJ, Chang F-K. A New Approach toward Understanding Damage Mechanisms and Mechanics of Laminated Composites Due to Low-Velocity Impact: Part I—Experiments. Journal of Composite Materials 1991;25:992–1011. https://doi.org/10.1177/002199839102500803.

[126] Choi HY, Wu H-YT, Chang F-K. A New Approach toward Understanding Damage Mechanisms and Mechanics of Laminated Composites Due to Low-Velocity Impact: Part-II Analysis. Journal of Composite Materials 1991;25:1012–38. https://doi.org/10.1177/002199839102500804.

[127] Liu D. Impact-Induced Delamination—A View of Bending Stiffness Mismatching. Journal of Composite Materials 1988;22:674–92. https://doi.org/10.1177/002199838802200706.

[128] Joshi SP, Sun CT. Impact induced fracture initiation and detailed dynamic stress field in the vicinity of the impact. American Society og Composites 2nd Tech. Conf, American Society og Composites 2nd Tech. Conf; 1987, p. 177–85.

[129] Varelidis PC, McCullough RL, Papaspyrides CD. The effect on the mechanical properties of carbon/epoxy composites of polyamide coatings on the fibers. Composites Science and Technology 1999;59:1813–23. https://doi.org/10.1016/S0266-3538(99)00039-1.

[130] Chua CK, Wong CH, Yeong WY. Benchmarking for Additive Manufacturing. Standards, Quality Control, and Measurement Sciences in 3D Printing and Additive Manufacturing, Elsevier; 2017, p. 181–212. https://doi.org/10.1016/b978-0-12-813489-4.00008-8.

[131] Tada H, Paris PC, Irwin GR. Introductory Information. The Stress Analysis of Cracks Handbook, Third Edition, ASME Press; 2000, p. 1–38. https://doi.org/10.1115/1.801535.ch1.

[132] Farahmand B. Linear Elastic Fracture Mechanics (LEFM) and Applications. Fracture Mechanics of Metals, Composites, Welds, and Bolted Joints, Springer US; 2001, p. 52–117. https://doi.org/10.1007/978-1-4615-1585-2_2.

[133] Dowling NE. Mechanical behavior of materials : engineering methods for deformation, fracture, and fatigue. Pearson; 2013.

[134] Hyung Yun Choi, Chang F-K. A Model for Predicting Damage in Graphite/Epoxy Laminated Composites Resulting from Low-Velocity Point Impact. Journal of Composite Materials 1992;26:2134–69. https://doi.org/10.1177/002199839202601408.

[135] Walker L, Sohn M-S, Hu X-Z. Improving impact resistance of carbon-fibre composites through interlaminar reinforcement. Composites Part A: Applied Science and Manufacturing 2002;33:893–902. https://doi.org/10.1016/S1359-835X(02)00010-6.

[136] Masters JE. Correlation of impact and delamination resistance in interleafed laminates. In: Matthews FL, Buskell NCR, Hodgkinson JM, Morton J, editors. Proc Sixth int Conf on Composite Mater/Second European Conf on Composite Materials, vol. 3, Elsevier Applied Science Publiscation; 1987, p. 96–107.

[137] Salpekar SA. Analysis of delamination in cross ply laminates initiating from impact induced matrix cracking. 1991.

[138] Sheng L. Quasi-impact damage initiation and growth of thick-section and toughened composite materials. International Journal of Solids and Structures 1994;31:3079–98. https://doi.org/10.1016/0020-7683(94)90042-6.

[139] Sheng L, Kutlu Z, Chang fu K. Matrix Cracking and Delamination in Laminated Composite Beams Subjected to a Transverse Concentrated Line Load: Http://DxDoiOrgManchesterIdmOclcOrg/101177/002199839302700501 2016;27:436–70. https://doi.org/10.1177/002199839302700501.

[140] Friedrich K, Walter R, Carlsson LA, Smiley AJ, Gillespie JW. Mechanisms for rate effects on interlaminar fracture toughness of carbon/epoxy and carbon/PEEK composites. Journal of Materials Science 1989;24:3387–98. https://doi.org/10.1007/BF01139070.

[141] Yao L, Alderliesten R, Zhao M, Benedictus R. Bridging effect on mode i fatigue delamination behavior in composite laminates. Composites Part A: Applied Science and Manufacturing 2014;63:103–9. https://doi.org/10.1016/j.compositesa.2014.04.007.

[142] Phillips DC, Wells GM. The stability of transverse cracks in fibre composites. Journal of Material Science Letters 1982;1:321–4.

[143] Davies P, Casari P, Carlsson LA. Influence of fibre volume fraction on mode II interlaminar fracture toughness of glass/epoxy using the 4ENF specimen. Composites Science and Technology 2005;65:295–300. https://doi.org/10.1016/J.COMPSCITECH.2004.07.014.

[144] Hojo M, Matsuda S, Tanaka M, Ochiai S, Murakami A. Mode I delamination fatigue properties of interlayer-toughened CF/epoxy laminates. Composites Science and Technology 2006;66:665–75. https://doi.org/10.1016/j.compscitech.2005.07.038.

[145] Wambua PM, Anandjiwala AR. A Review of Preforms for the Composites Industry. Journal of Industrial Textiles 2011;40:310–33. https://doi.org/10.1177/1528083709092014.

[146] Chen HP, Jang BZ. Failure mechanisms of 2-D and 3-D woven fiber reinforced polymer composites. Polymer Composites 1995;16:125–34. https://doi.org/10.1002/pc.750160204.

[147] Mouritz AP, Baini C, Herszberg I. Mode I interlaminar fracture toughness properties of advanced textile fibreglass composites. Composites Part A: Applied Science and Manufacturing 1999;30:859–70. https://doi.org/10.1016/S1359-835X(98)00197-3.

[148] Bibo GA, Hogg PJ, Kemp M. Mechanical characterisation of glass- and carbon-fibre-reinforced composites made with non-crimp fabrics. Composites Science and Technology 1997;57:1221–41. https://doi.org/10.1016/s0266-3538(97)00053-5.

[149] Mouritz AP, Leong KH, Herszberg I. A review of the effect of stitching on the in-plane mechanical properties of fibre-reinforced polymer composites. Composites Part A: Applied Science and Manufacturing 1997;28:979–91. https://doi.org/10.1016/S1359-835X(97)00057-2.

[150] Liu L, Wang P, Legrand X, Soulat D. Investigation of mechanical properties of tufted composites: Influence of tuft length through the thickness reinforcement. Composite Structures 2017;172:221–8. https://doi.org/10.1016/J.COMPSTRUCT.2017.03.099.

[151] Dell 'anno G, Treiber JWG, Partridge IK. Manufacturing of composite parts reinforced through-thickness by tufting. Robotics and Computer Integrated Manufacturing 2015;37:262–72. https://doi.org/10.1016/j.rcim.2015.04.004.

[152] Yan W, Liu HY, Mai YW. Mode II delamination toughness of z-pinned laminates. Composites Science and Technology 2004;64:1937–45. https://doi.org/10.1016/j.compscitech.2004.02.008.

[153] M'membe B, Gannon S, Yasaee M, Hallett SR, Partridge IK. Mode II delamination resistance of composites reinforced with inclined Z-pins. Materials and Design 2016;94:565–72. https://doi.org/10.1016/j.matdes.2016.01.051.

[154] Pegorin F, Pingkarawat K, Mouritz AP. Comparative study of the mode I and mode II delamination fatigue properties of z-pinned aircraft composites. Materials and Design 2015;65:139–46. https://doi.org/10.1016/j.matdes.2014.08.072.

[155] Dai SC, Yan W, Liu HY, Mai YW. Experimental study on z-pin bridging law by pullout test. Composites Science and Technology 2004;64:2451–7. https://doi.org/10.1016/j.compscitech.2004.04.005.

[156] Cartié DDR, Cox BN, Fleck NA. Mechanisms of crack bridging by composite and metallic rods. Composites Part A: Applied Science and Manufacturing 2004;35:1325–36. https://doi.org/10.1016/j.compositesa.2004.03.006.

[157] Rezai A, Cartie D, Partridge I, Irving P, Ashton T, Negre P, et al. Interlaminar Damage Resistance of Z-Fibre Reinforced Structural CFRP, Beijing: 2001, p. 25–9.

[158] Tong L, Mouritz AP, Bannister M. 3D Fibre Reinforced Polymer Composites - 1st Edition. Elsevier Science; 2002.

[159] Jain LK, Mai YW. Determination of mode II delamination toughness of stitched laminated composites. Composites Science and Technology 1995;55:241–53. https://doi.org/10.1016/0266-3538(95)00089-5.

[160] Jain LK, Dransfield KA, Mai Y-W. On the effects of stitching in CFRPs—II. Mode II delamination toughness. Composites Science and Technology 1998;58:829–37. https://doi.org/10.1016/S0266-3538(97)00186-3.

[161] Sankar B V., Sharma SK. Mode II delamination toughness of stitched graphite/epoxy textile composites. Composites Science and Technology 1997;57:729–37. https://doi.org/10.1016/S0266-3538(97)00032-8.

[162] Velmurugan R, Solaimurugan S. Improvements in Mode I interlaminar fracture toughness and in-plane mechanical properties of stitched glass/polyester composites.

Composites Science and Technology 2007;67:61–9. https://doi.org/10.1016/j.compscitech.2006.03.032.

[163] Yoshimura A, Nakao T, Yashiro S, Takeda N. Improvement on out-of-plane impact resistance of CFRP laminates due to through-the-thickness stitching. Composites: Part A Journal 2008;39:1370–9. https://doi.org/10.1016/j.compositesa.2008.04.019.

[164] Yudhanto A, Lubineau G, Ventura IA, Watanabe N, Iwahori Y, Hoshi H. Damage characteristics in 3D stitched composites with various stitch parameters under in-plane tension. Composites Part A: Applied Science and Manufacturing 2015;71:17–31. https://doi.org/10.1016/j.compositesa.2014.12.012.

[165] Dell'Anno G, Cartié DD, Partridge IK, Rezai A. Exploring mechanical property balance in tufted carbon fabric/epoxy composites. Composites Part A: Applied Science and Manufacturing 2007;38:2366–73. https://doi.org/10.1016/J.COMPOSITESA.2007.06.004.

[166] Jin FL, Li X, Park SJ. Synthesis and application of epoxy resins: A review. Journal of Industrial and Engineering Chemistry 2015;29:1–11. https://doi.org/10.1016/j.jiec.2015.03.026.

[167] Mohan P. A Critical Review: The Modification, Properties, and Applications of Epoxy Resins. Polymer-Plastics Technology and Engineering 2013;52:107–25. https://doi.org/10.1080/03602559.2012.727057.

[168] Liu S, Chevali VS, Xu Z, Hui D, Wang H. A review of extending performance of epoxy resins using carbon nanomaterials. Composites Part B: Engineering 2018;136:197–214. https://doi.org/10.1016/j.compositesb.2017.08.020.

[169] Sultan JN, Liable RC, Mcgarry FJ. Microstructure of two-phase polymers. Appl Polym Symp 1971;16:127–36.

[170] Thomas R, Yumei D, Yuelong H, Le Y, Moldenaers P, Weimin Y, et al. Miscibility, morphology, thermal, and mechanical properties of a DGEBA based epoxy resin toughened with a liquid rubber. Polymer (Guildf) 2008;49:278–94. https://doi.org/10.1016/j.polymer.2007.11.030.

[171] Akbari R, Beheshty MH, Shervin M. Toughening of dicyandiamide-cured DGEBA-based epoxy resins by CTBN liquid rubber. Iranian Polymer Journal (English Edition) 2013;22:313–24. https://doi.org/10.1007/s13726-013-0130-x.

[172] Quan D, Ivankovic A. Effect of core-shell rubber (CSR) nano-particles on mechanical properties and fracture toughness of an epoxy polymer. Polymer (Guildf) 2015;66:16–28. https://doi.org/10.1016/j.polymer.2015.04.002.

[173] Pearson RA, Yee AF. Toughening mechanisms in thermoplastic-modified epoxies: 1. Modification using poly(phenylene oxide). 1993.

[174] Gao F, Jiao G, Lu Z, Ning R. Mode II Delamination and Damage Resistance of Carbon/Epoxy Composite Laminates Interleaved with Thermoplastic Particles. Journal of Composite Materials 2007;41:111–23. https://doi.org/10.1177/0021998306063356.

[175] Pearson RA. Toughening Epoxies Using Rigid Thermoplastic Particles, 1993, p. 405–25. https://doi.org/10.1021/ba-1993-0233.ch017.

[176] Liang JZ. Toughening and reinforcing in rigid inorganic particulate filled poly(propylene): A review. Journal of Applied Polymer Science 2002;83:1547–55. https://doi.org/10.1002/app.10052.

[177] Chaudhary S, Surekha P, Kumar D, Rajagopal C, Roy PK. Amine-functionalized poly(styrene) microspheres as thermoplastic toughener for epoxy resin. Polymer Composites 2015;36:174–83. https://doi.org/10.1002/pc.22927.

[178] Kinloch AJ, Yuen ML, Jenkins SD. Thermoplastic-toughened epoxy polymers. JOURNAL OF MATERIALS SCIENCE 1994;29:3781–90.

[179] Park S-J, Li K, Jin F-L. Thermal Stabilities and Mechanical Interfacial Properties of Polyethersulfone-modified Epoxy Resin. Journal of Industrial and Engineering Chemistry 2005;11:720–5.

[180] Zucchi IA, Galante MJ, Williams RJJ. Comparison of morphologies and mechanical properties of crosslinked epoxies modified by polystyrene and poly(methyl methacrylate)) or by the corresponding block copolymer polystyrene-b-poly(methyl methacrylate). Polymer (Guildf) 2005;46:2603–9. https://doi.org/10.1016/j.polymer.2005.02.012.

[181] Rico M, López J, Montero B, Bellas R. Phase separation and morphology development in a thermoplastic-modified toughened epoxy. European Polymer Journal 2012;48:1660–73. https://doi.org/10.1016/j.eurpolymj.2012.07.007.

[182] Xie XL, Mai YW, Zhou XP. Dispersion and alignment of carbon nanotubes in polymer matrix: A review. Materials Science and Engineering R: Reports 2005;49:89–112. https://doi.org/10.1016/j.mser.2005.04.002.

[183] Youhong T, Ye L, Zhong Z, Friedrich K. Interlaminar fracture toughness and CAI strength of fibre-reinforced composites with nanoparticles – A review. Composites Science and Technology 2013;86:26–37. https://doi.org/10.1016/J.COMPSCITECH.2013.06.021.

[184] Kinloch AJ, Mohammed ARD, Taylor AAC, Sprenger AS, Egan AD. The interlaminar toughness of carbon-fibre reinforced plastic composites using “hybrid-toughened” matrices. https://doi.org/10.1007/s10853-006-0130-8.

[185] Wetzel B, Rosso P, Haupert F, Friedrich K. Epoxy nanocomposites - fracture and toughening mechanisms. Engineering Fracture Mechanics 2006;73:2375–98. https://doi.org/10.1016/j.engfracmech.2006.05.018.

[186] Zainol Abidin MS, Herceg T, Greenhalgh ES, Shaffer M, Bismarck A. Enhanced fracture toughness of hierarchical carbon nanotube reinforced carbon fibre epoxy composites with engineered matrix microstructure. Composites Science and Technology 2019;170:85–92. https://doi.org/10.1016/j.compscitech.2018.11.017.

[187] Almuhammadi K, Alfano M, Yang Y, Lubineau G. Analysis of interlaminar fracture toughness and damage mechanisms in composite laminates reinforced with sprayed multi-walled carbon nanotubes. Materials and Design 2014;53:921–7. https://doi.org/10.1016/j.matdes.2013.07.081.

[188] Siddiqui NA, Woo RSC, Kim J-K, Leung CCK, Munir A. Mode I interlaminar fracture behavior and mechanical properties of CFRPs with nanoclay-filled epoxy matrix. Composites Part A: Applied Science and Manufacturing 2007;38:449–60. https://doi.org/10.1016/J.COMPOSITESA.2006.03.001.

[189] Xu Y, Hoa S Van. Mechanical properties of carbon fiber reinforced epoxy/clay nanocomposites. Composites Science and Technology 2008;68:854–61. https://doi.org/10.1016/j.compscitech.2007.08.013.

[190] Johnsen BB, Kinloch AJ, Mohammed RD, Taylor AC, Sprenger S. Toughening mechanisms of nanoparticle-modified epoxy polymers. Polymer (Guildf) 2007;48:530–41. https://doi.org/10.1016/J.POLYMER.2006.11.038.

[191] Gojny FH, Wichmann MHG, Köpke U, Fiedler B, Schulte K. Carbon nanotube-reinforced epoxy-composites: Enhanced stiffness and fracture toughness at low nanotube content. Composites Science and Technology 2004;64:2363–71. https://doi.org/10.1016/j.compscitech.2004.04.002.

[192] Fiedler B, Gojny FH, Wichmann MHG, Nolte MCM, Schulte K. Fundamental aspects of nano-reinforced composites. Composites Science and Technology 2006;66:3115–25. https://doi.org/10.1016/j.compscitech.2005.01.014.

[193] Wang K, Chen L, Wu J, Toh ML, He C, Yee AF. Epoxy nanocomposites with highly exfoliated clay: Mechanical properties and fracture mechanisms. Macromolecules 2005;38:788–800. https://doi.org/10.1021/ma048465n.

[194] Shelimov KB, Esenaliev RO, Rinzler AG, Huffman CB, Smalley RE. Purification of single-wall carbon nanotubes by ultrasonically assisted filtration. Chemical Physics Letters 1998;282:429–34. https://doi.org/10.1016/S0009-2614(97)01265-7.

[195] Wu CL, Zhang MQ, Rong MZ, Friedrich K. Tensile performance improvement of low nanoparticles filled-polypropylene composites. Composites Science and Technology 2002;62:1327–40. https://doi.org/10.1016/S0266-3538(02)00079-9.

[196] Nash NH, M YT, McGrail PT, Stanley WF. Inclusion of a thermoplastic phase to improve impact and post-impact performances of carbon fibre reinforced thermosetting composites — A review. Materials & Design 2015;85:582–97. https://doi.org/10.1016/J.MATDES.2015.07.001.

[197] Nash NH, Ray D, Young TM, Stanley WF. The influence of hydrothermal conditioning on the Mode-I, thermal and flexural properties of Carbon/Benzoxazine composites with a thermoplastic toughening interlayer. Composites Part A: Applied Science and Manufacturing 2015;76:135–44. https://doi.org/10.1016/j.compositesa.2015.04.023.

[198] O'Donovan K, Ray D, McCarthy MA. Toughening effects of interleaved nylon veils on glass fabric/low-styrene-emission unsaturated polyester resin composites. Journal of Applied Polymer Science 2015;132:n/a-n/a. https://doi.org/10.1002/app.41462.

[199] Fitzmaurice K, Ray D, Mccarthy MA. PET interleaving veils for improved fracture toughness of glass fibre/low-styrene-emission unsaturated polyester resin composites. Journal of Applied Polymer Science 2016;133:n/a-n/a. https://doi.org/10.1002/app.42877.

[200] Beylergil B, Tanoğlu M, Aktaş E. Experimental and statistical analysis of carbon fiber/epoxy composites interleaved with nylon 6,6 nonwoven fabric interlayers. Journal of Composite Materials 2020:002199832092774. https://doi.org/10.1177/0021998320927740.

[201] Zhang J, Lin T, Wang X. Electrospun nanofibre toughened carbon/epoxy composites: Effects of polyetherketone cardo (PEK-C) nanofibre diameter and interlayer thickness. Composites Science and Technology 2010;70:1660–6. https://doi.org/10.1016/J.COMPSCITECH.2010.06.019.

[202] Ramirez VA. Effect of nonwoven veil architectures on interlaminar fracture toughness of interleaved composites. The University of Manchester, 2015.

[203] ASTM D5528 - 13 Standard Test Method for Mode I Interlaminar Fracture Toughness of Unidirectional Fiber-Reinforced Polymer Matrix Composites.

[204] Johnson W, Masters J, O'Brien T, O'Brien T, Martin R. Round Robin Testing for Mode I Interlaminar Fracture Toughness of Composite Materials. Journal of Composites Technology and Research 1993;15:269. https://doi.org/10.1520/CTR10379J.

[205] Shokrieh MM, Rajabpour-Shirazi H, Heidari-Rarani M, Haghpanahi M. Simulation of mode I delamination propagation in multidirectional composites with R-curve effects using VCCT method. Computational Materials Science 2012;65:66–73. https://doi.org/10.1016/J.COMMATSCI.2012.06.025.

[206] Martin RH, Davidson BD. Mode II fracture toughness evaluation using four point bend, end notched flexure test. Plastics, Rubber and Composites Processing and Applications 1999;28:401–6. https://doi.org/10.1179/146580199101540565.

[207] Schuecker C, Davidson BD. Evaluation of the accuracy of the four-point bend end-notched flexure test for mode II delamination toughness determination. Composites Science and Technology 2000;60:2137–46. https://doi.org/10.1016/S0266-3538(00)00113-5.

[208] Hodgkinson JM. Mechanical testing of advanced fibre composites. CRC Press; 2000.

[209] Adams RD, Cawley P. A review of defect types and nondestructive testing techniques for composites and bonded joints. NDT International 1988;21:208–22. https://doi.org/10.1016/0308-9126(88)90333-1.

[210] Joffe R, Mattsson D, Modniks J, Varna J. Compressive failure analysis of non-crimp fabric composites with large out-of-plane misalignment of fiber bundles. Composites Part A: Applied Science and Manufacturing, vol. 36, Elsevier; 2005, p. 1030–46. https://doi.org/10.1016/j.compositesa.2004.10.028.

[211] Shipsha A, Hallström S, Burman M. Effect of stacking sequence and bundle waviness in quasi-isotropic NCF composites subjected to compression. Composites Part B: Engineering 2019;178:107423. https://doi.org/10.1016/j.compositesb.2019.107423.

[212] Wu Z, Yi XS, Wilkinson A. Interlaminar fracture toughness of carbon fibre/RTM6-2 composites toughened with thermoplastic-coated fabric reinforcement. Composites Part B: Engineering 2017;130:192–9. https://doi.org/10.1016/j.compositesb.2017.08.003.

[213] Asp LE, Olsson R. Assessment of Evaluation Methods for the Mixed-Mode Bending Test. Article in Journal of Composites Technology and Research 1999. https://doi.org/10.1520/CTR10611J.

[214] Armanios EA, Asp LE, Sjögren BA. Delamination Growth and Thresholds in a Carbon/Epoxy Composite Under Fatigue Loading Design and Application of multifunctional composite materials in large ship structures View project Momentum View project. Article in Journal of Composites Technology and Research 2001. https://doi.org/10.1520/CTR10914J.

[215] Albertsen H, Ivens J, Peters P, Wevers M, Verpoest I. Interlaminar fracture toughness of CFRP influenced by fibre surface treatment: Part 1. Experimental results. Composites Science and Technology 1995;54:133–45. https://doi.org/10.1016/0266-3538(95)00048-8.

[216] Lee SM. Mode II delamination failure mechanisms of polymer matrix composites. Journal of Materials Science 1997;32:1287–95. https://doi.org/10.1023/A:1018552506085.

[217] Bhudolia SK, Joshi SC. Low-velocity impact response of carbon fibre composites with novel liquid Methylmethacrylate thermoplastic matrix. Composite Structures 2018;203:696–708. https://doi.org/10.1016/J.COMPSTRUCT.2018.07.066.

[218] Machado JJM, Marques EAS, Campilho RDSG, da Silva LFM. Mode I fracture toughness of CFRP as a function of temperature and strain rate. Journal of Composite Materials 2017;51:3315–26. https://doi.org/10.1177/0021998316682309.

[219] Machado JJM, Marques EAS, Campilho RDSG, da Silva LFM. Mode II fracture toughness of CFRP as a function of temperature and strain rate. Composites Part B: Engineering 2017;114:311–8. https://doi.org/10.1016/j.compositesb.2017.02.013.

[220] Zabala H, Aretxabaleta L, Castillo G, Aurrekoetxea J. Loading rate dependency on mode I interlaminar fracture toughness of unidirectional and woven carbon fibre epoxy composites. Composite Structures 2015;121:75–82. https://doi.org/10.1016/j.compstruct.2014.11.001.

[221] Smiley AJ, Pipes RB. Rate Effects on Mode I Interlaminar Fracture Toughness in Composite Materials. Journal of Composite Materials 1987;21:670–87. https://doi.org/10.1177/002199838702100706.

[222] Smiley AJ, Pipes RB. Rate sensitivity of mode II interlaminar fracture toughness in graphite/epoxy and graphite/PEEK composite materials. Composites Science and Technology 1987;29:1–15. https://doi.org/10.1016/0266-3538(87)90033-9.

[223] ASTM D792-20 Standard Test Methods for Density and Specific Gravity (Relative Density) of Plastics by Displacement.

[224] ASTM D3171-22 Standard Test Methods for Constituent Content of Composite Materials.